Universitat Autònoma de Barcelona

Emerging many-body phenomena in Raman-dressed ultracold atoms

Josep Cabedo Bru

Emerging many-body phenomena in Raman-dressed ultracold atoms

Josep Cabedo Bru

Submitted in fulfillment of
the requirements for the degree of
Doctor of Physics

Thesis supervisor:
Dr. Alessio Celi

Departament de Física
Universitat Autònoma de Barcelona

Bellaterra, Gener 2022

A la meva família

Acknowledgments

A risc de caure en clixés, he de dir que la redacció d'aquesta tesi representa per a mi la culminació d'un llarg procés d'assoliment acadèmic i, sobretot, personal. En un projecte d'anys i tants esforços, no és estrany que hi hagi trobat alts i baixos i moments desafiants. Lluny de poder-me queixar, però, al llarg de tot aquest camí he tingut la sort d'estar acompanyat de moltes persones fantàstiques que, no només han fet possible que aquest viatge hagi arribat a bon port, sinó que l'han convertit en tota una experiència enriquidora, vibrant i divertida. Que menys, doncs, que dirigir-los unes paraules d'agraïment.

Primer de tot vull donar les gràcies a l'Alessio, i per moltíssimes raons. La primera, és clar, per haver dirigit la meva recerca i per saber-me comunicar tants coneixements de física i del món acadèmic. A la vegada, és la persona amb qui més hores he treballat, i la veritat és que la seva passió per la física s'encomana. I més enllà dels aspectes professionals i acadèmics, he gaudit moltíssim de la seva companyia al llarg d'aquests últims anys en les tertúlies dels dinars i dels cafès, i també jugant a futbol! A més té una memòria sorprenent i d'ell en pots aprendre pràcticament de qualsevol tema. Li he d'agrair, també, que en els moments de dificultat, el seu optimisme, la seva paciència i la seva entrega hagin sigut claus perquè les coses anessin sortint bé.

Quan cursava el grau, sempre tenia la sensació que em faltaven moltíssimes coses per entendre, de només haver vist la punta de l'iceberg de la física. Si bé comprenc ara que aquesta sensació no marxarà mai del tot –per sort la física és molt més complexa del que desitja un estudiant de grau quan s'enfronta als exàmens– el doctorat ha estat, i amb diferència, l'època on m'he sentit personalment més realitzat amb els meus estudis. Per aquest motiu, entre molts d'altres, estic agraït al Jordi i a la Verònica, que em vau convèncer d'emprendre aquesta aventura i em vau oferir la possibilitat de fer el doctorat al grup. Ells em van guiar en els meus primers passos per aquest peculiar món de la ciència, que em tenia ben confós. Crec que és universalment reconeguda la manera en

com els dos combinen la professionalitat més absoluta amb aquest tracte tan proper que et fa sentir com a casa. Una prova d'això és la "QAOS family": qui hi entra ja no en surt.

Comentava al començament que en un camí tan llarg i desafiant s'hi troben alts i baixos. Doncs precisament en un d'aquests baixos em va aparèixer el meu bon amic i millor persona, col·laborador i coautor, el Joan. Em va ajudar moltíssim en el punt més difícil del doctorat, i des d'aleshores hem compartit una bona pila de moments, que espero que es continuïn acumulant. Les col·laboracions científiques amb ell han sigut divertidíssimes, inclús quan les coses "no sortien". A més, com que no en teníem prou, encara ens engrescàvem a repassar les matèries de la física d'on coixejàvem més i a discutir-les energèticament. Haig de destacar també els passejos que fèiem per estirar les cames durant les jornades intensives de feina i tots els dinars i "cafès" compartits (tot i que ell no en prenia, de cafè). Per tot això, i més, sempre li estaré agraït.

També vull mostrar el meu agraïment als professors del grup d'Òptica, que sempre s'han mostrat disposats a ajudar-me en el que feia falta. Al Francesc, que sempre que ha fet falta ha donat un cop de mà en la preparació de les classes de laboratori, i amb qui he col·laborat en moltes activitats de divulgació. A l'Àngel, amb qui ha sigut un plaer compartir docència. Al Gaspar, de qui, a més, en guardo un excel·lent record com a professor quan jo era estudiant de grau. I també al Juan i a la Marifí, que han contribuït a crear un excel·lent ambient de treball. També vull dedicar unes paraules en memòria del Ramón i del Todor, als qui trobem tots molt a faltar, i als qui agraeixo els anys compartits.

Al llarg d'aquests anys com a estudiant de doctorat, sempre he pogut presumir de companys de despatx. El Gerard P. i el Gerard Q., amb qui més tram del camí he compartit, els he d'agrair el seu bon humor i l'ambient immillorable que han creat en el despatx. Són gent molt interessant, i en les converses diàries durant les petites pauses, els cafès i els dinars hem cobert un amplíssim repertori de temes i també hem rigut molt. En aquest sentit, també estic agraït al Juanlu, el Poeta Cuántico, que ens ha inspirat a tots amb el seu art i la seva perseverança. Coincidíem més esporàdicament, però quan ho fèiem ell sempre venia carregat d'anècdotes divertides. També vull agrair-los els moments compartits als "clàssics": a la Irene, a l'Albert i al Haolin. Amb ells, juntament amb els Gerards, m'ho he passat molt bé organitzant activitats de divulgació. I també als companys de despatx arribats més recentment, l'Eulàlia i al David. Finalment, dono les gràcies també al Joan P. per la bona rebuda i l'ajuda quan vaig arribar al grup, i al Dani, amb qui va ser un plaer coincidir uns mesos. I també a l'Àlex, que malgrat no haver coincidit directament, sempre ha contagiat el seu entusiasme en les seves visites esporàdiques i en les trobades de la "QAOS family".

Of course, I am also grateful to all the collaborators, besides Alessio, Jordi, Verònica and Joan, that I have had the pleasure to work with. I would like to specially mention Prof. Leticia Tarruell, who has always shed light to the experimental side of our research, and from whom I have learned a lot in this sense, and also Prof. Yongping Zhang.

To the latter, I would like to express my gratitude for inviting and hosting me in his research group in Shanghai University during my stay abroad. Beyond the academic collaboration, he made sure the stay was a wonderful and lasting experience. In this regard, I am also grateful to Zhiqian, Qian, Jin Su, Huaxin and the rest of the students I shared office with, and also to Jingjun, Tangyou, and the rest of the neighbors in front. They all helped me a lot during the stay and made me feel at home.

I also want to thank Profs. Pasquale Calabrese and Matteo Rizzi for their positive reviews, and Profs. Anna Sanpera, Luis Santos and Ian B. Spielman for agreeing to be part of my PhD thesis committee.

Finalment, vull expressar el meu més profund agraïment als meus pares i al meu germà, als qui dedico aquesta tesi, pel seu suport tan incondicional. I per descomptat també a la Mònica, la meva companya de vida, que em fa tan feliç. Amb ella he crescut i après moltíssimes coses durant tota aquesta etapa tan especial de la meva vida. Em fa tota la il·lusió del món compartir les següents que vindran.

Josep Cabedo Bru
Bellaterra, Gener de 2022.

List of publications

The research contained in this thesis is supported by the following publications:

Chapter 3: Coherent spin mixing via spin-orbit coupling in Bose gases

1. J. Cabedo, J. Claramunt, A. Celi, Y. Zhang, V. Ahufinger and J. Mompart, *Coherent spin mixing via spin-orbit coupling in Bose gases*, Phys. Rev. A **100**, 063633 (2019).

Chapter 4: Dynamical preparation of stripe states in spin-orbit coupled gases

2. J. Cabedo, J. Claramunt and A. Celi, *Dynamical preparation of stripe states in spin-orbit-coupled gases*, Phys. Rev. A **104**, L031305 (2021).

Chapter 5: Excited-state quantum phase transitions in spin-orbit-coupled Bose gases

3. J. Cabedo and A. Celi, *Excited-state quantum phase transitions in spin-orbit-coupled Bose gases*, Phys. Rev. Res. **3**, 043215 (2021).

Chapter 6: Effective frustrated quantum magnetism from spin-orbit coupling in 1D optical lattices

4. J. Cabedo, J. Claramunt, J. Mompart, V. Ahufinger and A. Celi, *Effective triangular ladders with staggered flux from spin-orbit coupling in 1D optical lattices*, Eur. J. Phys. D **74**, 123 (2020).

5. L. Barbiero*, J. Cabedo*, M. Lewenstein, L. Tarruell and A. Celi, *Simulating frustrated quantum magnetism with Bose ladders in a synthetic gauge field*, in preparation (2022).

Contents

Acknowledgments . . . iii
List of publications . . . vii

1 Preface **1**
Outline of the thesis . . . 6

2 Theoretical frameworks **9**
2.1 Light-matter interaction in alkali atoms . . . 10
2.1.1 The dipole interaction . . . 10
2.1.2 Atomic structure of alkali metals . . . 11
2.1.3 Off-resonant dipole coupling: the scalar and vector light shifts . . . 14
2.1.4 Optical dipole trapping of neutral atoms . . . 17
2.1.5 Raman dressing . . . 18
2.1.6 Note on laser cooling . . . 22
2.2 Ultracold Bose gases with synthetic spin-orbit coupling . . . 25
2.2.1 Many-body treatment of ultracold Bose gases . . . 25
2.2.2 Mean-field treatment of a Bose-Einstein condensate . . . 31
2.2.3 The Raman-dressed gas: synthetic spin-orbit coupling . . . 37
2.3 Quantum magnetism with ultracold atoms in optical lattices . . . 43
2.3.1 Ultracold atoms in periodic optical potentials . . . 45
2.3.2 Tight-binding regime: the Bose-Hubbard model . . . 47
2.3.3 Atomic degrees of freedom as synthetic lattice dimensions: artificial magnetic fields . . . 52
2.4 Note on numerical simulations . . . 54

3 Coherent spin mixing via spin-orbit coupling in Bose gases **55**
3.1 Introduction . . . 56
3.2 Physical system . . . 58

3.2.1 Synthetic SOC . . . 58
3.2.2 Momentum-space triple-well band . . . 59
3.2.3 Many-body Hamiltonian . . . 60
3.3 Tight-binding approximation . . . 64
3.4 Properties of the tight-binding Hamiltonian . . . 68
3.4.1 Spectral properties of $\hat{H}_{t.b.}$ . . . 68
3.4.2 Dynamical properties of $\hat{H}_{t.b.}$ . . . 73
3.4.3 Experimental considerations . . . 75
3.5 Conclusion . . . 79

4 Dynamical preparation of stripe states in spin-orbit-coupled gases 81
4.1 Introduction . . . 82
4.2 The Raman-dressed gas as an artificial spinor gas . . . 83
4.2.1 Low-energy effective field theory . . . 85
4.2.2 Collective spin model . . . 89
4.3 Dynamical preparation of stripe states . . . 92
4.3.1 Phase diagram of the collective spin model . . . 92
4.3.2 Phases of the dressed gas as a pseudospin model . . . 94
4.3.3 The FS phase as an excited state . . . 97
4.3.4 Dynamical preparation of FS states: Gross-Pitaevskii results . . . 98
4.4 Experimental considerations . . . 103
4.5 Conclusions . . . 107

5 Excited state quantum phase transitions in spin-orbit-coupled Bose gases 109
5.1 Introduction . . . 110
5.1.1 Background and motivation . . . 110
5.1.2 The Raman-dressed gas as an artificial spinor gas . . . 112
5.2 ESQPs in SOC gases . . . 114
5.2.1 The Excited-Stripe phase . . . 116
5.2.2 The ES phase: Gross-Pitaevskii results . . . 119
5.2.3 Signature of the BA' ESQP . . . 122
5.2.4 Quench excitation of stripe states as a dynamical quantum phase transition . . . 125
5.3 Quench excitation of ES states via coherent spin-mixing . . . 127
5.3.1 Two-step quench scheme: few-mode predictions . . . 127
5.3.2 Excitation of ES states: Gross-Pitaevskii results . . . 129
5.4 Conclusions . . . 133

6 Effective frustrated quantum magnetism in a synthetic ladder 135
6.1 Introduction . . . 136
6.1.1 Quantum magnetism in semi-synthetic flux ladders . . . 137

6.1.2 Frustrated quantum magnetism in bosonic ladders 138
6.2 Tunable ladder physics in 1D lattices with SOC 140
6.2.1 Effective quasi-particle from Raman dressing 141
6.3 The spin-1/2 case: an effective triangular ladder with staggered flux . . . 143
6.4 Frustrated quantum magnetism with dressed ultracold atoms 149
6.5 Experimental implementation and detection of the frustrated phases . . . 154
6.5.1 Current structures of the frustrated phases 154
6.5.2 Measuring the observables of the effective model 161
6.5.3 Comment on experimental scales 164
6.6 Conclusions 167

7 Conclusions and outlook **169**
Outlook and future directions 172

CHAPTER 1

Preface

The arguably most rich and often less understood phenomena in physics arise from the interplay and the competition of interactions between many separate constituents. From high-temperature superconductivity to the phase diagram of quantum chromodynamics (QCD) at high density of fermions, the understanding of a great deal of phenomena in both condensed matter and high-energy physics relies on solving the so-called many-body problem. However, the numerical simulation of many-body systems is faced with a major difficulty: the configuration space of a many-body quantum system increases exponentially with the number of constituents. Even the simplest of the toy models, such as the spin-$\frac{1}{2}$ Heisenberg model, can not be solved by brute-force diagonalization by any realistic supercomputer when the size of the system increases just above few tens of particles. This fundamental issue has been long acknowledged, and, as early as 1982, Richard Feynman famously envisioned an alternative route to address the many-body problem [1]: could the quantum systems of interest be efficiently simulated by other quantum systems? This is the basic idea behind quantum simulation, where the relevant degrees of freedom of the system under scrutiny are encoded into those of a well-controlled and accessible system, the quantum simulator. The degrees of freedom in the simulator are also to evolve quantum mechanically, and thus expected to exhibit features such as superposition and entanglement of their quantum states. In 1996, Seth Lloyd proved in a seminal work [2] that the time evolution from any arbitrary Hamiltonian with local interactions could be efficiently simulated by repeatedly acting a series of local time-evolution operators in a so-called universal quantum simulator. The error of the simulation could in principle be made arbitrarily small by increasing the number of local operations, with the resulting total time scaling polynomially with the size of the simulated system, and not exponentially as is expected for a classical simulation, thus

making the problem computationally tractable. Since then, great efforts have been made in order to realize reliable experimental platforms upon which to perform quantum simulation. While to date a general-purpose quantum simulator, i.e. a quantum computer, is still far out of technical reach, great advances have been made in the simulation of specific models, where only the access to restricted families of local operations are required [3]. Conventionally, simulators are classified into digital and analog. The former execute algorithms composed of elementary steps or quantum gates in the so-called Trotter decomposition of the time-evolution operators. In the latter class, the system is evolved with a global Hamiltonian that mimics that of the model of interest, rather than with a sequence of local operations. Analog simulators sacrifice versatility for an enhanced robustness and scalability, and are immune to errors associated with the Trotter expansion of the Hamiltonian. They have been the object of a huge body of research over the past two decades and a variety of classically hard problems have already been explored in analog simulators. These include the equilibration and thermalization of quantum systems [4–7], the dynamics and the correlations in quantum phase transitions [8, 9] and dynamical phase transitions [10, 11], or the magnetic order in strongly-correlated Hubbard models [12–14], to mention a few. In practice, though, the digital-analog dichotomy is rather loose, with hybrids of the two categories being commonly built [15]. Due to the rapid development of quantum simulation techniques, wider classes of problems are progressively becoming in reach of quantum simulators [16].

To be operative, a quantum simulator demands that at least three fundamental features are fulfilled [17]. To start, the system needs to be able to accurately load the initial state required for the simulation. During the time-evolution, be it digital or analog, the system must preserve to a large extent the quantum coherence of the evolved states, and follow the targeted equations of motion which, ideally, should not admit efficient simulations with classical computations. And finally, at the end of the time-evolution, the prepared state needs to allow a precise interrogation with projective measurements that suitably characterize the observables of interest. Typically, measurements that are robust against the appearance of many errors, such as the magnetization in a set of spins, are targeted, rather than a full tomography of the prepared quantum state. The resources required for the latter task would scale exponentially with the size of the system size, even when the preparation time does it polynomially. To date, quantum simulations have been proposed and tested in many different experimental platforms. Most prominently, with large tunability and precise readout, these include superconducting circuits [18–21], trapped ions [22–25], cold atoms trapped in arrays of optical tweezers [26–28] and ultracold atoms [29–31], each exhibiting a competitive edge on different tasks and facing their own experimental challenges.

Regardless of the platform of choice for its implementation, there remains an open question regarding the use of quantum simulators. How are we to know that the simulations work properly when the simulated systems are out of reach of the analytical and numerical methods available? There is no definitive answer to this question yet, with the

falsifiability of quantum simulators being an active field of research. Naturally, the most basic step in the calibration of a simulator is to benchmark the apparatus against simulations for which theoretical predictions can be made. Besides the direct reproduction of results obtained with analytical and numerical computations, faulty simulations could be inferred from the violation of fundamental bounds and properties that the system is known to obey, even when it is not possible to simulate it classically [32]. Beyond that, the next simplest approach is to test the simulations by comparing the outputs from different platforms. The fact that similar sources of error may be shared across platforms strongly encourages the development of as many technologies as possible [33].

At its current proof-of-concept stage, quantum simulation is filled with technical challenges to be overcome, and its exploration alone has been motivating a huge body of theoretical research. The aim of such theoretical efforts is multifold: to make more refined predictions to be tested in the ever-improving simulators that are being built, to design novel protocols that widen the set of tools available to implement in the different experimental platforms, or to give insights on the results that are obtained along the way. Of course, in the theoretical side of the benchmark process, one needs to predict the behavior of quantum many-body systems. Luckily, in most situations the full configuration space of a many-body system needs not be considered, and several families of many-body problems can be addressed in approximate ways with conventional computation methods. Very often, the dynamics of a low-lying family of energy eigenstates is enough to account for the description of the observed many-body phenomena. Furthermore, the Hilbert space can be significantly reduced by independently addressing the different symmetry sectors of the Hamiltonian [34]. In other situations, safe assumptions can be made by which the relevant states of the system are restricted to a small subset of states. For instance, numerical methods based on tensor networks [35], such as the density-matrix renormalization group [36] approach, assume that the lowest energy eigenstates lie within a low-entanglement corner of the Hilbert space –a property that rigorously holds for 1D gapped systems [37]. Many weakly-correlated systems admit a mean-field treatment. For instance, under the right conditions, ultracold atoms can form a condensate, where a large fraction of the atoms macroscopically occupy one or few single-particle state. In several applications, the condensate can be well treated within the classical field formalism of the Gross-Pitaevskii equation [38], where the many-body behavior is captured by the appearance of nonlinearities in the differential equations that govern the fields. Other popular methods include density functional theory [39], best used in the absence of strong correlations, and the more powerful stochastic quantum Monte Carlo algorithms [40].

Over the last two decades, the blossoming of quantum simulation has pushed the boundaries of our understanding in many scientific disciplines, ranging from the atomic, molecular and optical physics to information theory, computer science and device engineering. With the holy-grailesque quest for an operating universal quantum computer [41] as the ultimate goal in the long run, the developing of efficient techniques for the

harnessing of quantum systems has become a prominent field of research. This multidisciplinary effort hopes to deliver game-changing technologies in the future [42]. Moreover, quantum technologies are not restricted to the fields of simulation and computation. Enhancements beyond the limits of classical systems are also fervently pursued in fields such as quantum sensing [43] and quantum metrology [44, 45], where the properties of quantum states, such as squeezing and entanglement, are exploited to overcome conventional bounds to the precision of the measurements [46], and also in quantum communication, where entangled pairs of photons are used in information-theoretically secure key distribution protocols [47, 48]. Amid this simultaneously fascinating and intimidating scope, the modest results presented in this thesis deal with a rather specific, yet related, subject. This dissertation explores theoretically phenomena that arise from the interplay between light-dressing and interatomic interactions in ultracold atomic systems, with potential applications to both the simulation of exotic physics and quantum metrology.

Quantum gases of ultracold atoms are found amongst the most developed and studied platforms in quantum science and technology. They are characterized by naturally accommodating a large number of particles in the experiments, from hundreds to millions of interacting atoms of both bosonic and fermionic species. Ultracold atoms are cooled down to temperatures close to the absolute zero, which is possible thanks to impressive advances in the cooling and trapping of neutral atoms [49, 50]. While the small resulting energy scales can be a drawback for tasks that require computational speed, ultracold gases can be very well isolated, and large coherence times be attained. In turn, their slow dynamics allows for the time-resolved control of the parameters of the system in shorter times than their characteristic timescales, which is very attractive for the simulation of complex processes. This enables, for instance, the direct probing of nonequilibrium dynamics [4, 51, 52]. Crucially, ultracold gases can be manipulated and probed with electromagnetic fields in myriad ways [53]. A wide range of their properties can be tuned with high precision, including the effective dimensionality of the gas [54, 55] and the geometry of the simulated models [56–59], the strength and sign of the interatomic interactions via Feshbach resonances [60–63], and the effective spin size of the atoms, which can be controlled independently from their bosonic or fermionic nature. Owing to such a versatility, experiments with ultracold atoms can simulate a broad diversity of models [64]. When loaded into optical lattices [30, 31, 65, 66], they can emulate Hamiltonians of relevance in solid state physics in a natural way, such as the paradigmatic Hubbard model. In the continuum, bulk-gas experiments can realize a variety of phenomena of interest [67], with the crossover between weak coupling Bardeen-Cooper-Schrieffer pairing to a Bose-Einstein condensate of tightly bound pairs in Fermi gases with attractive interactions [68, 69] as a paradigmatic example, and also study transport properties [70]. With atom numbers as large as few millions, these systems allow for a precise exploration of thermodynamic behavior [71, 72]. And beyond quantum simulation, the coherent manipulation of gases of ultracold atoms is actively investigated in the field of quantum metrology. By exploiting interatomic interactions,

entangled states with a very large number of particles can be generated in Bose-Einstein condensates, to be exploited for phase estimation in interferometry protocols [73].

Because ultracold atoms are charge-neutral, they only couple to gauge fields via their dipole moments. An immediate challenge posed by the quantum gas as a platform for simulation is, thus, to find ways to emulate the effects of gauge fields on charged matter. To fully simulate gauge theories, which could address very challenging problems in particle physics such as quark confinement, chiral symmetry breaking, and the phase diagram of QCD, dynamical gauge fields are required. Their realization has proven very hard since gauge theories must satisfy local gauge invariance, i.e. the Gauss law. Still, their implementation is actively researched theoretically [74–76], with some recent experimental efforts [77–79] starting to pave the way in this promising direction. In the meantime, nonetheless, a wealth of interesting phenomena related to the behavior of nonrelativistic particles in the presence of static gauge fields has been successfully translated into ultracold atomic systems following various approaches. In these, the engineered fields themselves are not dynamical variables, describing instead the action of effective classical external fields. The earliest examples of synthetic gauge fields in ultracold gases are the effective magnetic fields induced in bulk atomic gases that are set into rotation [80], as demonstrated by the observation of quantized vortices in Bose-Einstein condensates [81, 82] and in a condensate of Fermi pairs [83]. Alternatively, employing light-dressing schemes [84, 85] can partly avoid the substantial heating generated by the rotation-based implementations. For instance, artificial magnetic fields can be generated in a Raman-dressed gas in the presence of a bias magnetic field gradient [86]. In the lattice, Peierls phases leading to Aharonov-Bohm fluxes have been achieved in diverse ways: Floquet-engineered in periodically driven lattices [87], via Raman-assisted tunneling in magnetically tilted lattices [88, 89] and in super lattices [90, 91], an also in quasi 2D ladder-like systems using Raman-coupled synthetic dimensions [92, 93] in 1D lattices [94–96]. Relevantly, the engineering of Peierls phases in 2D square lattices realizes the Harper–Hofstadter model [97] in a way that allows strong magnetic field regimes to be easily accessed. This enables the experimental exploration of its topological properties and the quantum Hall response [94–96, 98–100]. Further topologically non-trivial models have been realized [101] by exploiting different ladder geometries. A prominent example is the experimental realization [102] of the Haldane model [103], where Chern bands occur in the absence of net Aharonov-Bohm fluxes. At the same time, synthetic forms of spin-orbit-coupling interaction have been realized in ultracold gases by exploiting Raman coupling, both in the continuum by directly coupling two internal states [104–106], or in a superlattice by using Raman-assisted tunneling [107, 108]. In condensed matter systems, spin-orbit coupling is strongly connected to a variety of phenomena, such as the spin-Hall effect [109] or topological insulators [110, 111] and superconductors [111, 112]. In degenerate quantum gases, spin-orbit coupling gives rise to novel and intriguing phases that can go beyond those found in conventional condensed matter systems [113, 114].

In many of the current experimental implementations of gauge physics in ultracold

atomic systems, Raman dressing stands as a key ingredient to provide spatially-varying phase terms and level couplings in the required spatial and temporal scales. Interestingly, Raman coupling has been shown to modify the properties of the scattering processes that take place in the gas. These effects have been studied mostly in the context of the stabilization of the magnetic-like ground state phases of the weakly coupled gas [104, 115], and also as a collision-induced decay mechanism in stronger coupling regimes [116, 117]. In this thesis, we will explore further this rich interplay, and focus on two regimes of the Raman-coupled gas where the many-body behavior can be tackled with different numerical approaches. In both scenarios, we will derive effective models where the dressed gas is described at low energies in terms of the interactions of single-particle dressed states. Through these effective models, we will be able to spot regimes of parameters of the Raman-coupled gas where phenomena of interest can take place, to be later numerically explored via exact diagonalization, Runge-Kutta methods, the Gross-Pitaevskii equation or density-matrix renormalization group methods. In bulk weakly-dressed and weakly-interacting spin-1 Bose gases [118], we will see that the interplay between superfluidity, interatomic interactions and the induced spin-orbit coupling gives access to the coherent exploration of phenomena of relevance such as supersolidity [119], macroscopic entanglement [73] and dynamical [120] and excited [121] quantum phase transitions. These aspects will be treated in a simple unified framework where the spin-1 Raman-dressed gas is thought of as an undressed spinor gas with tunable spin-changing collisions [122–124]. In the lattice, Raman dressing is one of the most popular routes for the realization of Aharonov-Bohm fluxes, both in laser-assisted tunneling proposals and in schemes that exploit synthetic dimensions. In this regard, we will investigate the one-dimensional synthetic flux ladder in a regime of strong Raman coupling and strong synthetic flux. There, we will show that the system effectively realizes a frustrated triangular ladder model [125]. In presence of strong interatomic interactions, we will see that the Hamiltonian is able to hold phases that are characteristic of frustrated spin models built on triangular geometries.

Outline of the thesis

The thesis is organized as follows:

Chapter 2 briefly introduces the theoretical models that are employed in the remainder of the thesis. We start by covering relevant aspects of light-atom interaction, with emphasis on the scalar and vector light shifts resulting from off-resonant dipole coupling. These are used, respectively, to generate the optical trapping potentials and the Raman dressing exploited in the experimental implementations of the investigated systems. We next review the theoretical treatment of an interacting spinor Bose gas, and discuss some of its properties in the presence of Raman dressing. Finally, the basics of ultracold atoms in optical lattices are reviewed, and the synthetic dimension approach to simulate quantum magnetism therein is introduced.

Chapter 3 explores the interplay between Raman dressing and two-body elastic collisions in a weakly-coupled spin-1 Bose gas. In particular, we study the emergence of coherent spin-mixing dynamics in a SU(3)-symmetric gas [122] in a regime where near-resonant spin-changing collisions are mediated by two-photon Raman processes. Remarkably, the strength of the spin-mixing collisions can be tuned with the intensity of the Raman beams. The effects of such a dynamics are identified by following an unconventional tight-binding approximation in quasi-momentum space, in which only three low-energy dressed states are taken into account. We discuss the properties of the resulting Hamiltonian, which shares many similarities to the one describing a spinor condensate with nonsymmetric collisions.

Chapter 4 expands the description of the Raman-dressed gas as an effective spinor gas with tunable spin-changing collisions away from the previously considered tight-binding regime. Following a perturbative treatment of the weakly-dressed field Hamiltonian, we find an analytical equivalence at the quantum level between the two systems across the low-energy landscape. Through this equivalence, we then introduce the description of the dressed condensate as a collective pseudospin degree of freedom, which provides a simple framework to understand the quantum phases of the gas and its dynamics. Such a collective spin picture allows us to design a novel protocol to dynamically prepare the ferromagnetic stripe phase of the spin-orbit coupled gas [123]. In the protocol, the supersolid-like stripe states are prepared by driving initially spin-polarized states across a quantum phase transition in the most excited state manifold of the effective model. There, the characteristic parameters that stabilize the phase are scaled up, enhancing both its robustness and its accessibility.

Chapter 5 proposes the Raman-dressed spin-1 Bose gase as a novel platform to explore dynamical and excited-state quantum phase transitions. By using the collective spin model derived in the previous chapter, we identify excited-state quantum phases of the Raman-dressed gas that are in direct correspondence to those recently found in undressed spinor gases [124]. Due to spin-orbit coupling, the phases of the dressed system are further characterized by the spatial properties of the many-body wavefunction. We show that a detection protocol based on these properties could facilitate the experimental observation of the excited phases. At the same time, we describe a robust quench preparation of stripe states with large density modulations that exploits the dynamical properties of the excited phases.

Chapter 6 considers the exploration of frustrated magnetic phases with a Raman-dressed spin-$\frac{1}{2}$ Bose gas loaded into a one-dimensional optical lattice. We show that, for strong Raman coupling, the Hamiltonian written in terms of the lowest-band dressed states describes an effective triangular Bose ladder with staggered flux and on-site interactions. There, both the strength of the flux and the ratio of the arm and rung currents can be easily tuned with the parameters of the Raman dressing [125]. Through the effective model, we identify regimes of parameters where the original Hamiltonian realizes

different phases that are characteristic of frustrated XX spin models. We discuss the experimental signatures of the phases and their potential realization and detection in experiments with ultracold atoms.

Chapter 7 concludes the thesis by summarizing the results presented and briefly discusses further perspectives.

CHAPTER 2

Theoretical frameworks

In this introductory chapter, we provide an overview of the theoretical frameworks in which the research presented in this thesis is embedded, and briefly present the main concepts and tools that will be employed. Accordingly, the chapter is organized in three different sections, each covering a fundamental building block of the systems investigated in the thesis. In Sec. 2.1, we review the basic mechanisms of light-matter interaction that are exploited for the manipulation of ultracold atoms, with special emphasis on the most commonly employed alkali-metal family. In Sec. 2.2 we discuss the theoretical treatment of the many-body problem in ultracold Bose gases, and review the properties of the system in the presence of Raman dressing. Finally, in Sec. 2.3 we introduce the powerful framework of ultracold atoms in optical lattices, and present a simple approach to simulate quantum magnetism with such systems. As a general remark, it should be stressed that the motivation behind this introductory chapter is not to provide a detailed textbook course on the various subjects covered. Rather, the chapter is set to establish a minimum background for the non-expert reader to aid the understanding of the following chapters, in which the original results compiled in the thesis are presented.

This chapter is written with a special emphasis on conveying a sense of scale for the intricate interactions between the different ingredients that come to play in the light-dressed ultracold atomic systems that will be investigated. Eventually, we will model the coherent dynamics of atomic clouds that have been cooled down to quantum degeneracy, with characteristic energy scales in the order of 10^2 Hz to 10^3 Hz. Considering optical atomic transitions in alkali species as our starting point, with characteristic frequencies in the order of 10^{14} Hz, that is a remarkable journey to make. Such a fascinating journey has mandatory stops at the fine structure splitting scale, a few orders below, at the hyperfine structure splitting scale, around $\sim 10^9$ Hz for the ground state, at the natural

line width of the first-excited electronic state and at the Zeeman shifts, both in the order of 10^6 to 10^7 Hz, and the single-photon recoil energy $\sim 10^3$ to 10^4 Hz. And beyond that, this thesis will explore many-body processes that act perturbatively over metastable solutions that are well defined in the condensate energy scales, at frequencies as low as few to few tens of Hz! Such a disparity in the characteristic time scales is what allows the use of specific techniques that address independently the different energy sectors in these systems, a key feature for the efficient simulation of quantum systems.

2.1 Light-matter interaction in alkali atoms

We start this chapter by briefly reviewing the aspects of the interaction between atoms and electromagnetic fields that will be of relevance to the results presented in following chapters. We will focus, in particular, on the coupling between optical light fields and the ground state atomic levels of alkali-metal species. The harnessing of such a rich interaction has been crucial to the development of atom cooling and trapping techniques [126–128], which eventually lead to the experimental realization of the Bose-Einstein condensate (BEC) in 1995 [129–131]. Furthermore, it has been proven a prolific tool to further control ultracold atomic systems and engineer a myriad of phenomena in such a versatile platform [30].

2.1.1 The dipole interaction

While the nonionized atoms that we consider are charge neutral, they still interact with external electric fields via dipole interaction. Most of the features of this interaction that are relevant to the trapping and manipulation of ultracold atoms can be well described in a semiclassical picture. There, the atom is treated quantum-mechanically, but the light is described by a classical field theory. The semi-classical light-matter interaction framework is remarkably accurate for high intensity light fields, and has been very successful in explaining phenomena that extend beyond the predictions of classical physics, including Rabi oscillations, multi-photon transitions or light shifts [132].

We consider the simplest scenario, where an atom is dressed by a monochromatic light field $\mathbf{E}(\mathbf{r}, t) = \mathbf{E}_0 \cos(\mathbf{k}\cdot\mathbf{r} - \omega_L t)$, oscillating at angular frequency ω_L. Consider now two electronic orbitals $|i\rangle$ and $|j\rangle$ of the outer shell, that are separated by an energy split $\hbar\omega_0$. In the presence of the field, the levels are coupled through the dipole interaction, given by the Hamiltonian

$$\hat{H}_{\text{dip}} = -\hat{\mathbf{d}}\cdot\mathbf{E}, \tag{2.1}$$

with $\hat{\mathbf{d}} = -e\sum_k \hat{\mathbf{r}}_k$, being the electric dipole moment operator. Here, e the charge of the electron and $\hat{\mathbf{r}}_j$ are the position operators of the electrons relative to the center of mass of the atom. For illustrative purposes, we neglect the effects of higher order multipolar and magnetic interaction terms. Since the atom radius is much smaller than the wavelength of light in the regimes that we will consider, we neglect, for now, the spatial dependence

of the electric field, in the so-called electric dipole approximation. In the bare basis, the dipole potential can be written as

$$\hat{V}_{\rm dip}(t) = \sum_{ij} \Omega_{ij} \cos(\omega_L t)|i\rangle\langle j| + \text{H.c.}, \tag{2.2}$$

where $\Omega_{ij} = -\mathbf{d}_{ij}\cdot\mathbf{E_0}/\hbar$ is the Rabi frequency of the transition, with $\mathbf{d}_{ij} = -e\sum_k \langle i|\hat{\mathbf{r}}_k|j\rangle$. The dipole elements $\mathbf{d}_{ij}$ will depend on the characteristics of the electronic orbitals that are involved in the transition. Observe that for orbitals with the same parity, such an interaction is null. This includes, of course, the self-coupling interaction for symmetric or antisymmetric states. While simplistic, this picture underlines the basic mechanism behind atom-light interaction. As we will see, such a model is able to capture the mechanism behind optical trapping. The picture can be extended to account for the simultaneous coupling of several atomic levels, where various fields with different polarizations may be involved, and used to describe the two-photon processes that are essential to a central ingredient of this thesis: the Raman dressing. Not surprisingly, though, the precise way by which the different electronic levels are actually coupled in real atom species is rather complex, and it strongly depends on the structure of the atomic species. Henceforth, we will restrict ourselves to the alkali metal family. We next review some fundamental aspects of their structure.

2.1.2 Atomic structure of alkali metals

Generally speaking, the low-energy spectroscopic properties of atoms stem from the electrons in the outer open shell. Here, we will use the conventional notation $n^{2S+1}L_J$ to refer to orbitals of the outer electrons with principal quantum number n, orbital angular momentum $\mathbf{L}$ and total angular momentum $\mathbf{J} = \mathbf{L} + \mathbf{S}$, where $\mathbf{S}$ is the spin of the total spin in the outer shell. Typically, the letters $\mathcal{S}, \mathcal{P}, \mathcal{D}, ...$ are used to denote the orbitals with $L = 0, 1, 2, ...$ The alkali metal family includes the atomic species in the first group to the left of the periodic table. With only one valence electron in an s-orbital $n^2\mathcal{S}_{1/2}$ as ground state, alkali atoms exhibit a relatively simple internal state structure and they all share a host of similar atomic and chemical properties. Most relevantly to the content of this thesis, the electronic ground state and the lowest lying family of excited states across the alkali family are resonantly coupled via dipole interaction in the optical range of the electromagnetic field spectrum. This feature is experimentally very convenient, since it allows the manipulation of the atoms in their ground state with laser light, which can be used to cool and spatially trap them, and to tune their properties.

In Fig. 2.1, we show the level diagram of ^{87}Rb, which includes the two lowest-lying families of energy eigenstates, with $n = 5$ and $L = 0$ in the ground state, and $n = 5$ and $L = 1$ in the first excited family. In the latter, the spin-orbit interaction $A_{\rm fs}\hat{\mathbf{L}}\cdot\hat{\mathbf{S}}$ between the electronic spin and the the orbital momentum lifts the degeneracy between different states with angular momentum $L = 1$, resulting in the fine structure splitting of the $\mathcal{P}$ level. The vertical red arrows highlight the electronic transitions $n^2S_{1/2} \to n^2\mathcal{P}_{1/2}$ and

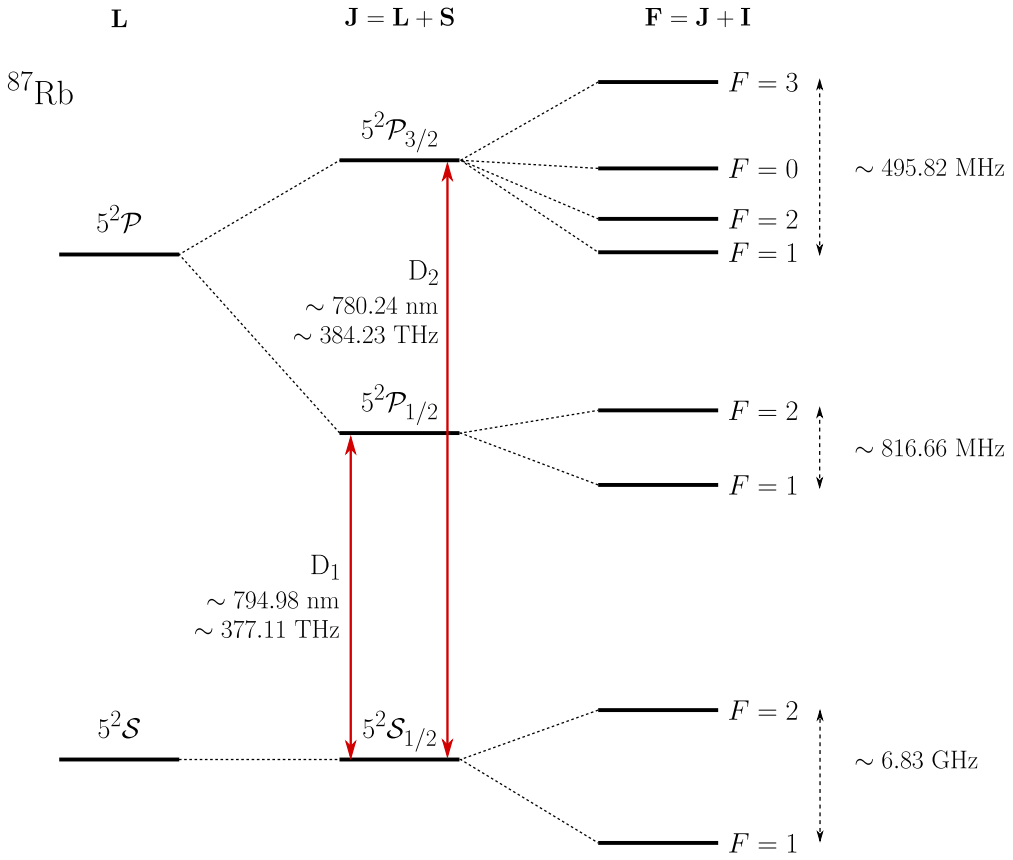

Figure 2.1: Level diagram of the lowest electronic levels of a ^{87}Rb atom (energies not to scale), including the outer shell orbitals $n^2\mathcal{S}$ and $n^2\mathcal{P}$. The red arrows highlight the transitions $n^2S_{1/2} \rightarrow n^2\mathcal{P}_{1/2}$ and $n^2S_{1/2} \rightarrow n^2\mathcal{P}_{3/2}$ that correspond to the D_1 and D_2 spectral lines.

$n^2S_{1/2} \rightarrow n^2\mathcal{P}_{3/2}$, which are commonly referred to as the D_1 and D_2 lines, respectively. The designation letter D in these Fraunhofer lines stems from them being first identified as the sodium doublet, with the notation having been extended to all the transitions between the ground state and the fine-structure-split first excited manifold of alkali atoms. For ^{87}Rb, the corresponding equivalent wavelengths for such transitions are 794.98nm and 790.24nm [133], which, as anticipated, are found within the optical range of the spectrum and can be targeted with diode lasers in the laboratory. Similarly, the coupling between the total angular momentum of the electron and the spin of the nucleus $A_{\text{hfs}}\hat{\mathbf{J}} \cdot \hat{\mathbf{I}}$ further splits the fine structure into hyperfine levels of total angular momentum $F = J + I$ [134]. In ^{87}Rb, the nuclear spin is given by $I = 3/2$, and the lowest hyperfine manifold includes 3 degenerate eigenstates with total angular momentum $F = 1$ and 5 eigenstates with $F = 2$.

Notice in Fig. 2.1 the energy separation between the different scales associated with each of these angular momentum coupling processes. While the states with different

orbital angular momentum L have a separation of several hundreds of THz, the fine structure splitting in ^{87}Rb is found in the order of few THz (and it is amongst the largest across the alkali family). Finally, the hyperfine splitting is roughly 3 orders of magnitude smaller than the fine structure splitting of the $5^2\mathcal{P}$ orbital. Such a large scale separation is fundamental to a *clean* addressing and manipulation of the atomic levels with electromagnetic beams. The same level structure is shared amongst all alkali species, albeit the transition frequencies vary significantly due to the large differences they exhibit in the nuclear mass. For instance, the D lines of sodium have characteristic transition wavelenghts around 589 nm [135]. On the other hand, even among different isotopes of the same species, the nuclear spin $\mathbf{I}$ takes different values, which determines the total angular momentum of the hyperfine states and the width of the energy splitting. As an example, the truly stable isotope of Rubidium, ^{85}Rb, has a nuclear spin $I = 5/2$ [136], which results into a $F = 2$ ground state with a smaller hyperfine splitting (in experiments with ultracold alkali atoms, however, the choice of isotope is motivated largely by the s-wave scattering properties of the different isotopes [137]).

In the presence of an external static magnetic field, which sets a privileged axis that we arbitrarily set along the $\hat{z}$ direction, the degeneracy between eigenstates with the same total angular momentum is lifted due to the magnetic dipole interaction

$$\hat{H}_B = \boldsymbol{\mu} \cdot \mathbf{B} = \frac{\mu_\mathrm{B}}{\hbar}\left(g_L \hat{L}_z + g_S \hat{S}_z + g_I \hat{I}_z\right) B_z \simeq \frac{\mu_\mathrm{B}}{\hbar}\left(g_J \hat{J}_z + g_I \hat{I}_z\right) B_z, \tag{2.3}$$

where $\boldsymbol{\mu}$ is the total magnetic dipole of the atom, $\mu_\mathrm{B} = \frac{e\hbar}{2m_\mathrm{e}}$ is the Borh magneton (m_e denotes the mass of the electron). The coefficients g_L, g_S and g_I are the electron orbital, electron spin, and nuclear gyromagnetic factors that weigh in the corresponding contributions to the total magnetic dipole moment. Typically, the fine structure splitting in alkali atoms is much larger than the characteristic energies associated with the magnetic shifts, and J remains a good quantum number for the total angular momentum of the electron. Hence the approximate equality in (2.3), where

$$g_J \simeq 1 + \frac{J(J+1) - L(L+1) + S(S+1)}{2J(F+1)} \tag{2.4}$$

is the effective Landé factor associated with the total electronic angular momentum, which depends on the different electronic angular momentum quantum numbers.

In general, therefore, the atomic eigenstates will be given by superpositions of the bare basis states $|J, m_J, I, m_I\rangle$, where m_J and m_I are the $\hat{J}_z$ and $\hat{I}_z$ projection quantum numbers. This picture is simplified further in the weak bias magnetic field regime, where the magnetic dipole Hamiltonian can be treated as a perturbation to the bare Hamiltonian. There, the total angular momentum basis states $|F, m_F\rangle$ can be kept as a good approximation of the eigenbasis. We then can write

$$\hat{H}_B \simeq \frac{\mu_\mathrm{B}}{\hbar} g_F \hat{F}_z B_z, \tag{2.5}$$

with

$$g_F = g_J \frac{F(F+1) - I(I+1) + J(J+1)}{2F(F+1)} + g_I \frac{F(F+1) + I(I+1) - J(J+1)}{2F(F+1)}. \tag{2.6}$$

This regime, where the perturbative action of the bias field lifts the degeneracy with a linear shift $\Delta E_{m_F} = \frac{\mu_B}{\hbar} g_F m_F$, is the so-called linear Zeeman regime of the atom-magnetic field interaction. Along this thesis, we will keep ourselves within this regime (with the exclusion of the experimental proposal discussed at the end of chapter 6) and consider the states $|F, m_F\rangle$ in a hyperfine manifold as the relevant internal states of the atoms in an ultracold cloud. They will serve as effective spin degrees of freedom, to be further manipulated with laser light via electric dipole interaction. It is worth noting, though, that shifts beyond the linear regime of the magnetic interaction (essentially the quadratic Zeeman shift) will nonetheless play a major role in the manipulation of the *spin* states, despite its characteristic energies being several orders of magnitude smaller than the shifts at the linear order.

2.1.3 Off-resonant dipole coupling: the scalar and vector light shifts

As sketched in Sec. 2.1.1, a neutral atom interacts with an external electric field mainly via the dipole interaction. Alkali atoms can be approximately described by a simple dipole formed by the single outer shell electron, with charge e, and the rest of the atom, which can be approximated to a point-like particle of charge $-e$ located at the center of mass of the atom. In this situation, the dipole Hamiltonian for a monochromatic field simply reads

$$\hat{H}_{\text{dip}} = -e \sum_j \hat{r}_j E_j \cos(\phi_j - \omega_L t). \tag{2.7}$$

Here, we have introduced the phases of the field ϕ_j along each spatial direction $j = x, y, z$, which allows us to account for nonlinear polarizations of the dressing field.

We will tackle off-resonant electric dipole transitions involving the $n^2\mathcal{S}$ ground state and the first excited $n^2\mathcal{P}$ orbital, separated by an energy that we label with $\hbar\omega_0$. It will be sufficient to include the FS of the atom, since we will consider that the detuning from resonance, while small relative to the transition frequency ω_0, is much larger than the hyperfine structure splitting. Therefore, the undressed atom can be described the truncated Hamiltonian

$$\hat{H}_{\text{at}} = \hbar\omega_0 \hat{P}_{\mathcal{P}} + \frac{A_{\text{fs}}}{\hbar^2} \hat{\mathbf{L}} \cdot \hat{\mathbf{S}}. \tag{2.8}$$

Here, $\hat{P}_{\mathcal{P}} = \frac{\hat{\mathbf{L}}^2}{2\hbar^2}$ is the projector onto the $n^2\mathcal{P}$ subspace (we neglect the occupation of higher excited orbitals). Likewise, we conveniently define the projector to the $n^2\mathcal{S}$ state, $\hat{P}_{\mathcal{S}} = 1 - \frac{\hat{\mathbf{L}}^2}{2\hbar^2}$.

It is often the case that $\omega_0 + \omega_L \gg |\omega_0 - \omega_L|$. In this conditions, the Hamiltonian $\hat{H} = \hat{H}_{at} + \hat{H}_{\text{dip}}$ can be written in a time-independent form following a time-dependent unitary transformation $\hat{H}' = \hat{U}\hat{H}\hat{U}^\dagger - i\hbar\hat{U}\frac{\partial}{\partial t}\hat{U}^\dagger$, with $\hat{U} = \hat{P}_{\mathcal{S}} + \hat{P}_{\mathcal{P}} e^{i\omega_L t}$, and simultaneously neglecting the resulting fast-oscillating contributions to the Hamiltonian, which oscillate at ω_L and $2\omega_L$. This is the so-called rotating wave approximation (RWA). Doing so, the dressed Hamiltonian is given by $\hat{H}' = \hat{H}'_{at} + \hat{H}'_{\text{dip}}$, where the rotated dipole and atomic

terms read

$$\hat{H}'_{\rm at} = \Delta \hat{P}_{\mathcal{P}} + \frac{A_{\rm fs}}{\hbar^2}\hat{\mathbf{L}}\cdot\hat{\mathbf{S}}, \tag{2.9}$$

and

$$\hat{H}'_{\rm dip} \simeq \frac{e}{2}\sum_j \left(\tilde{E}_j \hat{P}_{\mathcal{P}}\hat{r}_j\hat{P}_{\mathcal{S}} + H.c.\right), \tag{2.10}$$

respectively. The latter is written in terms of the positive and negative frequency Fourier components of $\mathbf{E}(\mathbf{r},t)$, given by $\tilde{E}_j^* = E_j e^{-i\phi_j}$ and $\tilde{E}_j = E_j e^{i\phi_j}$, respectively. These are complex quantities that incorporate the time-independent contributions to the oscillating phase terms $\propto e^{\pm i(\phi_j - \omega_L t)}$. Notice that the transformed atomic Hamiltonian remains time-independent, but in the rotated basis the $n^2\mathcal{S}$ amd $n^2\mathcal{P}$ subspaces are separated instead by the detuning from resonance $\Delta = \hbar(\omega_0 - \omega_L)$. The RWA is very accurate when both $\omega_L \sim \omega_0$, so that $\Delta \ll \hbar\omega_0$, and the coupling energies $\langle i|\hat{H}'_{\rm dip}|j\rangle$ are much smaller than ω_0. In experiments with light-dressed alkali atoms the latter is guaranteed, since $\omega_0/2\pi$ is in the order of hundreds of THz.

Since we will restrict ourselves to the off-resonant coupling between $n^2\mathcal{S}$ and $n^2\mathcal{P}$ states, we will also require that $\Delta \gg \langle i|\hat{H}'_{\rm dip}|j\rangle$. In this situation, the perturbative effect of the dipole Hamiltonian over the ground state manifold can be described following the adiabatic elimination [138–140] of the excited states

$$\hat{H}_{\rm eff} = -\hat{P}_{\mathcal{S}}\hat{H}'_{\rm dip}\hat{H}'^{-1}_{\rm at}\hat{H}'_{\rm dip}\hat{P}_{\mathcal{S}} = -\frac{1}{4}\sum_{jk}\tilde{E}_j^*\hat{D}_{jk}\tilde{E}_k. \tag{2.11}$$

In this way, the effect of the off-resonant dipole coupling is captured by the rank-2 tensor

$$\hat{D}_{jk} = e^2\hat{P}_{\mathcal{S}}\hat{r}_j\hat{P}_{\mathcal{P}}\hat{H}'^{-1}_{\rm at}\hat{P}_{\mathcal{P}}\hat{r}_k\hat{P}_{\mathcal{S}} \tag{2.12}$$

that acts on the ground state subspace, which can be decomposed into a scalar (rank-0 tensor), vector (rank-1 tensor) and a rank-2 tensor contributions. While a general expression of such an operator for an arbitrary atomic transition is rather complex, when restricted to the $n^2\mathcal{S}$ and $n^2\mathcal{P}$ fine structure states of alkali atoms, a simpler form can be obtained (see [85] for a detailed derivation), which reads

$$\hat{D}_{jk} = \frac{|\mathbf{d}_{01}|^2}{9}\left(\frac{2}{\Delta_2}+\frac{1}{\Delta_1}\right)\left[\delta_{jk} + i\epsilon_{jkl}\frac{2\Delta_{\rm FS}}{\hbar(2\Delta_1+\Delta_2)}\hat{J}_l\right]\hat{P}_{\mathcal{S}}, \tag{2.13}$$

and which includes only a scalar and a vector components. Here $\Delta_{\rm FS} = 3A_{\rm fs}/2$ is the fine structure splitting and $\Delta_1 = \hbar\omega_0 - A_{\rm fs} - \hbar\omega_L$ and $\Delta_1 = \hbar\omega_0 + A_{\rm fs}/2 - \hbar\omega_L$ are the detunings from the $n^2\mathcal{S}_{1/2} \to n^2\mathcal{P}_{1/2}$ and $n^2\mathcal{S}_{1/2} \to n^2\mathcal{P}_{3/2}$ transitions, respectively (the D_1 and D_2 lines shown in Fig. 2.1). The prefactor

$$|\mathbf{d}_{01}|^2 = e^2\sum_{m'_l}|\langle l=0|\hat{\mathbf{r}}|l'=1,m'_l\rangle|^2 \tag{2.14}$$

includes the dipole matrix elements $e\langle l,m_l|\mathbf{r}|\hat{l',m'_l}\rangle$ that couple the eigenstates $|l,m_l\rangle$ of $\mathbf{L}^2$ and $\hat{L}_z$ within the $n^2\mathcal{S}$ and $n^2\mathcal{P}$ manifolds, with eigenvalues $l(l+1)\hbar^2$ and $\hbar m_l$, respectively.

By inserting (2.13) into (2.11), we obtain the expression of the light shift Hamiltonian

$$\hat{H}_{\text{eff}} = \alpha^{(0)} \left(\tilde{\mathbf{E}}^* \cdot \tilde{\mathbf{E}} \right) + i \frac{\alpha^{(1)}}{\hbar} \left(\tilde{\mathbf{E}}^* \times \tilde{\mathbf{E}} \right) \cdot \hat{\mathbf{J}}, \tag{2.15}$$

where

$$\alpha^{(0)} = -\frac{|\mathbf{d}_{01}|^2}{36} \left(\frac{2}{\Delta_2} + \frac{1}{\Delta_1} \right), \tag{2.16}$$

$$\alpha^{(1)} = \alpha^{(0)} \frac{2\Delta_{\text{FS}}}{2\Delta_1 + \Delta_2}. \tag{2.17}$$

are the scalar and vector polarizabilities, respectively. Since we restrict ourselves to the effects of the dressing onto the ground state manifold of the atom, in (2.15) we have omitted the explicit inclusion of the projector to the ground state, which will be assumed for the rest of the section.

Finally, we now recover the presence of an external static magnetic field. As argued in Sec. 2.1.2, fo a weak bias field, F can be maintained as a good quantum number and the states $|F, m_F\rangle$ as a good approximation to the actual eigenbasis elements. In these conditions, the magnetic dipole interaction translates into a correction $\sim \frac{\mu_{\text{B}} g_F}{\hbar} \mathbf{F} \cdot \mathbf{B}$ to the hyperfine levels. Moreover, realize that the vector light shits in (2.15) can be regarded as an additional magnetic field

$$\mathbf{B}_{\text{eff}} = i \frac{\alpha^{(1)}}{\mu_{\text{B}} g_J} \left(\tilde{\mathbf{E}}^* \times \tilde{\mathbf{E}} \right), \tag{2.18}$$

acting on the gas. Notice that, with the amplitudes $\mathbf{E}$ being complex quantities, the cross product $\mathbf{E}^* \times \mathbf{E}$ can take nonzero values. As long as the level shifts that result from $\mathbf{B}_{\text{eff}}$ are much smaller than the hyperfine structure splitting, we can treat this effective field the same exact way as we did for $\mathbf{B}$, and write

$$\hat{H}_{\text{eff}} \simeq \alpha^{(0)} \left(\tilde{\mathbf{E}}^* \cdot \tilde{\mathbf{E}} \right) + \frac{\mu_{\text{B}} g_F}{\hbar} \left(\mathbf{B} + \mathbf{B}_{\text{eff}} \right) \cdot \hat{\mathbf{F}} + \frac{A_{\text{hfs}}}{\hbar^2} \hat{\mathbf{J}} \cdot \hat{\mathbf{I}}, \tag{2.19}$$

Where we have introduced back the fine structure interaction $\propto \mathbf{J} \cdot \mathbf{I}$. In the results presented in this thesis, we will restrict ourselves to a single hyperfine manifold with fixed total angular momentum (typically $F = 1$, in the case of ^{87}Rb), and such a term can be disregarded as a global energy shift within the dressed manifold.

Equation (2.19) summarizes the way a near-resonant oscillating electric field interacts with an alkali atom. Most relevant to this thesis, we will see some immediate applications of the light shift Hamiltonian. These include the realization of effective light-induced spatial trapping potentials, which exploits the scalar part of the light shift. At the same time, a variety of spin-dependent potentials can originate from the vector contribution. Next we briefly review the fundamental mechanism behind the optical trapping of atoms.

2.1.4 Optical dipole trapping of neutral atoms

Let us consider now a dressed atom described by the Hamiltonian (2.15) in which the dressing field is linearly polarized. Then, the vector contribution to is null, and the perturbative action of the dipole Hamiltonian yields the ac-Stark shift of the ground state energy levels. Let us further consider that $|\Delta| \gg \Delta_{\mathrm{FS}}$, so that we have $\Delta_2 \sim \Delta_1 \sim \Delta$, and the fine structure can be ignored. The resulting dressed Hamiltonian reads

$$\hat{H}_{\mathrm{eff}} = -\frac{|\mathbf{d}_{01}|^2}{6\epsilon_0 c}\frac{I}{\Delta}, \tag{2.20}$$

where ϵ_0 is the vacuum permittivity, c is the speed of light and $I = \frac{\epsilon_0 c}{2}|\tilde{\mathbf{E}}|^2$ is the light intensity.

While we have ignored the spatial dependence of the dressing fields (the dipole approximation) in the derivation of (2.15), the same results can be used to treat nonhomogeneous intensity distributions as long as they are spatially modulated with wavelengths that are much larger than the atomic dipole characteristic lengths. If we consider a spatially dependent intensity profile $I(\mathbf{r})$, the light shift (2.20) describes a scalar potential

$$V_s(\mathbf{r}) \propto -I(\mathbf{r})/\Delta. \tag{2.21}$$

The dressed atoms are then subject to the dipole force $F_{\mathrm{dip}} = -\nabla V_s(\mathbf{r})$, and are attracted to the local maxima of the spatial intensity profile for red-detuned beams, that is $\Delta > 0$, and to the local minima in the case of blue-detuned beams, with $\Delta < 0$. Therefore, via the dipole interaction, neutral atoms can be manipulated and trapped with light beams. In the simplest realization of an optical dipole trap [141], the intensity profiles to create three-dimensional confinement potentials can be obtained from shining focused Gaussian red detuned laser beams. Likewise, periodic trapping potentials, known as optical lattices, can be created from the spatial interference patterns created by the superposition of coherent light beams. Ultracold atoms loaded in optical lattices offer a rich and versatile platform to simulate a rich variety of quantum models. Their fundamental aspects will be briefly discussed in Sec. 2.3.

It should be noted that the dressed eigenstates are actually a mixture of the bare atomic states, and the trapped atoms have a small but nonzero occupation of the bare excited $n\mathcal{P}$ orbitals. At the same time, even in the absence of a dressing field, the two states are coupled through the dipole interaction with the electric field vacuum. This unavoidably result in spontaneous emission processes from the excited to the ground state. It is worth noting that such processes go beyond the semi-classical description of light, with the quantization of the electromagnetic modes being required to properly describe them [132]. Phenomenologically, though, they can be often treated by including decay rates in the semiclassical equations. In each spontaneous emission process a photon is emitted in a random direction, and, due to momentum conservation, the emitting atom experiences a recoil momentum kick in the opposite direction. Over time, this is translated into an increase in the mean kinetic energy of the atoms in the dressed sample,

at a rate $\Gamma_{\text{heat}} = 2E_r\Gamma_{\text{sp}}$, where $E_r = \frac{\hbar^2 k_r^2}{2m_a}$ is the single-photon recoil energy, with k_r being the wavevector of the emitted photon and m_a the mass of the atom, and where Γ_{sp} is the rate of the spontaneous emission processes.

Luckily, in optical trapping such a heating mechanism can be largely suppressed. The rate Γ_{sp} is given by the natural linewidth Γ_{10} of the $n\mathcal{S} \to n\mathcal{P}$ transition times the projection squared of the dressed eigenstates into the bare $n\mathcal{P}$ manifold, the latter being proportional to I/Δ^2. This is quite remarkable, since it follows that $\Gamma_{\text{heat}}/V_s \propto 1/\Delta$. Thus, the heating rate can in principle be made arbitrarily small while leaving the light shift unchanged by simultaneously increasing I and Δ. Naturally, there exist practical limitations to the extent of the suppression. Yet in the dressed alkali systems we will consider, recoil heating from trapping potentials can be kept very low, and much more significant sources of heating and noise will stem from other mechanisms.

That being said, optical traps for neutral atoms can only operate at very low temperatures, due to their weak characteristic potential depths –typically below the mK. As we will elaborate further in Sec. 2.1.6 the atoms can be loaded into optical traps only after being cooled with the aid of magnetic confinement techniques [142]. The latter exploit the magnetic dipole interaction (see eq. (2.5)), and use magnetic field gradients to create state-dependent potentials. As a comparison, magnetic traps can reach potential depths as large as several hundreds of mK [143]. Optical traps, though, offer some major advantages with respect to magnetic traps. The advances in the techniques for the manipulation of coherent light, such as spatial light modulators, allow for the flexible creation of a variety of trapping geometries [144, 145]. Most relevant to the content presented in this thesis, optical traps are not sensitive to the Zeeman sublevels structure, which facilitates the experimental realization of multicomponent spinor condensates [146, 147].

2.1.5 Raman dressing

We now focus on the opposite scenario, where the vector light shift is the dominant contribution to the atom-light interaction. From (2.13), we see that by setting $\Delta_2 = -2\Delta_1$, the scalar light shift is suppressed, while the vector light shift, which is proportional to $(\Delta_1\Delta_2)^{-1}$, is maintained. The wavelength that fulfills such a condition, which we label as ω_{to}, is commonly referred to as the *tune-out* or *magic* wavelength [148]. In ^{87}Rb, for instance, the tune-out wavelength is found around 790 nm (see Fig. 2.1). In these conditions, the effect of the light dressing is the mere addition of the effective magnetic field $\mathbf{B}_{\text{eff}}$ described in equation (2.18). It should be pointed out that vector light-shift potentials can also be effectively realized away from the tune-out frequency. However, unlike the scalar contribution to the light-shift, the vector contribution far from resonance scales as Δ^{-2}. The ratio $\mathbf{B}_{\text{eff}}/\Gamma_{\text{heat}}$, thus, can not be suppressed by increasing both the detuning and the intensity of the dressing beams. By targeting frequencies above the D_2 or below the D_1 lines the heating from photon scattering is only modestly

reduced at the expenses of a non-vanishing scalar light-shift potential.

By choosing different configurations for the dressing beams, that is, their polarization and direction of propagation, the orientation of the effective field $\mathbf{B}_{\text{eff}}$ can be tuned. It is easy to show that, by aligning the effective magnetic field to the magnetic bias field $\mathbf{B}$, one can obtain spin-dependent spatial potentials. In this thesis, however, we will focus on the Raman coupling configuration, where $\mathbf{B}_{\text{eff}}$ is set perpendicular to $\mathbf{B}$. In any case, we will always consider $\mathbf{B}_{\text{eff}}$ to act perturbatively with respect to the bias field $\mathbf{B} = B_0\mathbf{e}_z$, so that the quantization axis of the angular momentum is maintained along the unit vector $\mathbf{e}_z$ set by the bias field. This is typically a good approximation even in the linear Zeeman regime, where the magnetic level shifts are found at the MHz scale. By contrast, the frequencies associated with the vector light shift lie in the range of few to few tens of kHz.

In the Raman configuration, the effective magnetic field is achieved with two counter-propagating beams with mutually orthogonal polarizations. To illustrate it, consider an atom that is dressed by a monochromatic field propagating along $\mathbf{e}_x$. The field is linearly polarized along $\mathbf{e}_y$ and oscillates with frequency $\omega_1 = \omega_L \sim \omega_{\text{to}}$ and amplitude E_1. At the same time, the atom is illuminated by an additional counter-propagating monochromatic field polarized along $\mathbf{e}_z$, with frequency $\omega_2 = \omega_L + \delta\omega_L \sim \omega_{\text{to}}$ and amplitude E_2. Both frequencies are chosen very close to the tune-out wavelength, to be able to neglect the effects of scalar light shift. At the same time, we require that both are separated by a frequency difference $\delta\omega_L \sim \omega_{\text{Z}}$ that is close to the linear Zeeman shift $\omega_{\text{Z}} = \left|\frac{\mu_{\text{B}} g_F B_0}{\hbar}\right|$ lifted by the bias field. In these conditions the electric field illuminating the atom reads

$$\mathbf{E}(\mathbf{r}, t) = \left(E_1\mathbf{e}_y e^{ik_1 x} e^{-i\omega_L t} + E_2\mathbf{e}_z e^{-i(k_2 x + \delta\omega_L t)} e^{-i\omega_L t} + \text{c.c.}\right), \tag{2.22}$$

where $k_j = \omega_j/c$. We reintroduce here the spatial dependence of the electric field, which was omitted in the atomic dipole approximation taken in Sec. 2.1. Since we will eventually consider an atomic cloud where the atoms are sparsely distributed over distances much larger than the wavelengths of the fields $2\pi/k_j$, such a dependency needs to be taken into account. It will indeed play a major role.

Previously, we had assumed monochromatic light, with just a negative and a positive complex component of $\mathbf{E}$. However, with two slightly mutually detuned electric beams, the electric field (2.22) has now four nonzero Fourier components at $\pm\omega_1$ and $\pm\omega_2$, which will results in a time-dependent light-shift potential. We can incorporate the frequency difference into the complex amplitude $\tilde{\mathbf{E}}$ to write

$$\tilde{\mathbf{E}} = E_1\mathbf{e}_y e^{ik_1 x} + E_2\mathbf{e}_z e^{-i(k_2 x + \delta\omega_L t)}. \tag{2.23}$$

From (2.23) and (2.18), it follows that

$$\mathbf{B}_{\text{eff}} = \mathbf{e}_x \frac{2\alpha^{(1)} E_1 E_2}{\mu_{\text{B}} g_J} \sin\left((k_1 + k_2)x + \delta\omega_L t\right). \tag{2.24}$$

In this way, the light-shift Hamiltonian within a given Zeeman manifold with total spin F can be written as

$$\hat{H}_{\text{eff}} \simeq \frac{\sqrt{2}\Omega}{\hbar} \sin\left(2k_r x + \delta\omega_L t\right) \hat{F}_x - \omega_{\text{Z}} \hat{F}_z + \frac{\epsilon}{\hbar^2} \hat{F}_z^2, \tag{2.25}$$

where we have introduced the Raman coupling strength

$$\Omega = \frac{\sqrt{2}\alpha^{(1)} E_1 E_2 g_F}{g_J}, \tag{2.26}$$

and where we define $k_r = (k_1 + k_2)/2 \simeq k_1 \simeq k_2$. The last term in Hamiltonian (2.25) was not included in the expression (2.19) given for the general case. It accounts for the quadratic contribution to the Zeeman shifts which will be very relevant henceforth.

Similarly as considered in Sec. 2.1.3, we can eliminate the time dependency of Hamiltonian (2.25) by applying another time-dependent transformation $\hat{H}'_{\text{eff}} = \hat{U}_2 \hat{H}_{\text{eff}} \hat{U}_2^\dagger - i\hbar \hat{U}_2 \frac{\partial}{\partial t} \hat{U}_2^\dagger$, with $\hat{U}_2 = \exp(-i\delta\omega_L t \hat{F}_z)$, and taking again the RWA to eliminate the terms oscillating at $\delta\omega_L$ and $2\delta\omega_L$. This results into the time-independent dressing Hamiltonian

$$\hat{H}'_{\text{eff}} \simeq \frac{\Omega}{\sqrt{2}\hbar} \left(\sin(2k_r x) \hat{F}_x - \cos(2k_r x) \hat{F}_y \right) + \frac{\delta}{\hbar} \hat{F}_z + \frac{\epsilon}{\hbar^2} \hat{F}_z^2, \tag{2.27}$$

where $\delta = \hbar\delta\omega_L - \hbar\omega_{\text{Z}}$ is the detuning energy from Raman resonance. Notice that the first RWA could be taken on the basis that the field frequency was much larger than the detuning from resonance, which set the relevant energy scale, that is $\omega_L \gg |\Delta| = |\omega_0 - \omega_L|$. Similarly, the second RWA is justified as long as $\hbar\delta\omega_L \sim \hbar\omega_{\text{Z}}$ is large compared to the characteristic kinetic energy scales. This is indeed the case in ultracold gases, with typical temperatures below the μK, and so thermal energies in the order of few to few tens of kHz (see Sec. 2.1.6). As we will discuss in Sec. 2.2, the kinetic energies in bosonic gases can even be much smaller when a condensate is formed. The Raman Hamiltonian in equation (2.27) describes a position-dependent Zeeman field that precesses helically in the x-y plane with a subwavelength period of π/k_r. At any position, the precessing field is transverse to the quantization axis $\mathbf{e}_z$. Hence, when close to resonance, Raman coupling is able to drive transitions between m_F and $m_F \pm 1$ Zeeman sublevels. A Raman transition is a two-photon process, where the initial state is off-resonantly coupled to an intermediate state in the excited $n^2\mathcal{P}$ manifold, which is in turn off-resonantly coupled to the final state. Since the excited-state transition is far off-resonant, the actual occupation of the excited manifold in the Raman dressed atom is kept negligible. Such a process is schematically represented in Fig. 2.2. Notice that, while we consider the linear regime of the magnetic dipole interaction, with $\omega_{\text{Z}}/2\pi \sim 10^7$ Hz, the quadratic contributions to the magnetic shifts, with $\epsilon/h \sim 10^4 \ll \omega_{\text{Z}}$ Hz, can still be large compared to the coupling strength Ω, and thus render the Raman transitions off-resonant even at $\delta = 0$. In fact, the quadratic Zeeman shift will play a major role in the following chapters, where we will consider that two pairs of Zeeman sublevels are coupled with independent Raman transitions. This can be efficiently achieved using three laser beams when the magnetic

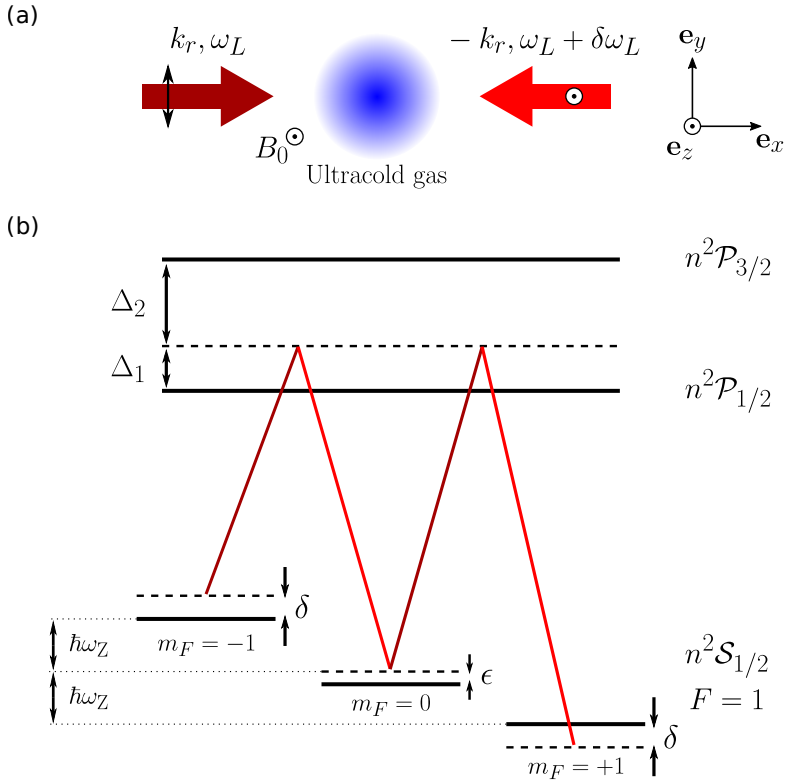

Figure 2.2: (a) Sketch of the experimental realization of Raman dressing in alkali atoms. Two counter-propagating linearly polarized beams, with mutually orthogonal polarizations, illuminate an ultracold atomic cloud. Their frequencies are adjusted near the tune-out frequency $\omega_{\rm to}$ of the scalar light shift, where the detunings from the D_1 and the D_2 lines fulfill $2\Delta_1 \simeq -\Delta_2$. The frequencies of the beams are shifted by an amount $\delta\omega_L$, which is set close to the energy separation between the Zeeman sublevels, whose degeneracy is lifted by a bias magnetic field $B_0\mathbf{e}_z$. As a result, the Zeeman sublevels in the ground state manifold become coupled via dipole interaction mediated by far-off-resonant transitions to an excited state. (b) Corresponding level diagram for an atom with a $F = 1$ ground state, such as ^{87}Rb or ^{41}K (energies are not to scale). The dashed lines indicate the energies involved in the off-resonant couplings from each beam, which are represented by colored solid lines. The energy shift $\delta = \hbar\delta\omega_L - \hbar\omega_L$ indicates the detuning from resonance of the two-photon Raman transitions. Due to a small quadratic Zeeman shift, the $m_F = 0$ level is effectively shifted by an amount $-\epsilon$.

field is sufficiently strong to separate well the resonant frequencies of each transition [118].

As we will see in Sec. 2.2, due to the spatial dependence of Raman transitions, the effect of Raman dressing in an ultracold atomic gas can be interpreted as a synthetic form of spin-orbit coupling interaction in otherwise neutral atoms. Before discussing the spin-orbit-coupled Raman-dressed ultracold gas, next we briefly review the basics

of another fundamental application that exploits the dipole light-atom interaction: the cooling of neutral atoms.

2.1.6 Note on laser cooling

Contrarily to the off-resonant, weakly dissipative light-shifts employed to create optical potentials, the dissipative regime of the dipole interaction is exploited in the laser cooling of neutral atoms. The main idea behind laser cooling is to modify the momentum distribution in the atomic sample via controlling the momentum exchanged between the electromagnetic field and the atoms. The simplest, and perhaps most fundamental of the cooling mechanisms is the so-called Doppler cooling [149]. In a nutshell, Doppler cooling exploits the spatially uniform distribution of the emitted photons in the spontaneous emission processes. The momentum transferred to the atom after a sufficiently large number of these processes is zero. After many cycles of absorption and spontaneous emission, the net momentum transferred from the electromagnetic field to the atoms in the gas comes from the absorption processes. Remarkably, the absorption rate depends on the detuning from resonance, and the latter depends in turn on the velocity $\mathbf{v}$ of the atoms relative to the light source due to the Doppler effect. With this in mind, a net velocity-dependent scattering force $\mathbf{F}_{\text{scatt}} \propto -\mathbf{v}$ can be created by using pairs of counter-propagating beams, in a configuration known as optical molasses [150]. The working principle of optical molasses is rather simple: the gas is illuminated with slightly red-detuned laser fields. Hence, an atom that moves towards one of the lasers experiences an incoming beam from such a laser that is Doppler shifted closer to resonance, while the beam coming from the opposite side is shifted further from resonance. Needless to say, the situation is reversed when the atom moves in the opposite direction. Therefore, the illuminated atoms undergo on average more absorption processes that oppose their motion, which results in an effective damping force. With three pairs of counter-propagating beams, the scattering force can act over the three spatial dimensions. Overtime, its presence leads to a decrease of the mean kinetic energy of the atoms, i.e. the cooling of the atomic cloud.

At the same time, laser cooling typically incorporates techniques that exploit the magnetic dipole interaction. Through the Zeeman effect, a spatially dependent bias magnetic field produces a m_F-dependent scalar potential (see Sec. 2.1.2), and thus a detuning from resonance that depends on the position of the atoms. In a first cooling stage, a Zeeman slower configuration is commonly employed [151]. There, a magnetic field gradient provides the required spatially varying level shifts so that the atoms are continuously kept in resonance with the absorption processes as they move forward and their velocity decreases. In this way, throughout the process a large dipole force is maintained on the atoms, where otherwise the atomic transitions would quickly go off-resonant. The sample is then simultaneously cooled further and spatially confined in a magneto-optical trap (MOT) [152]. In a MOT, optical molasses are used in combination with a quadrupole magnetic field gradient that provides a static detuning gradient. The

gradient is adjusted so that the atoms that move away from the center of the trap have a larger probability to undergo absorption processes from the laser beam that opposes their motion. On average, this adds a restoring contribution $\propto -\mathbf{r}$ to the scattering force, trapping the atoms in a damped harmonic oscillator.

However, the same mechanism that enables Doppler cooling in the first place, the spontaneous emission, also establishes a minimum temperature that the atoms can reach. The momentum transferred from spontaneous emission averages to zero, but the emitted photons increase on average the kinetic energy of the atoms. Therefore, while the laser fields create the restoring force $\mathbf{F}_{\text{scatt}}$, they are also a source of heating. The cooling force removes energy at a rate $\mathbf{F}_{\text{scatt}}\cdot\mathbf{v}$ that is proportional to the velocity of the atoms squared. Contrarily, for low velocities the heating rate from spontaneous emission is independent of the velocity, with $\Gamma_{\text{heat}} \sim 4E_r\Gamma$, where Γ is the natural line width, or decay rate, of the targeted excited state. Eventually, the atom-light system reaches a steady state where heating and the cooling rates are balanced around a certain kinetic energy. There exist an optimal value for the detuning Δ at which the equilibrium is reached at the lowest possible temperature, given by $k_{\text{B}}T_{\text{D}} = \hbar\Gamma/2$, where $k_{\text{B}} = 1.380649 \times 10^{-23}$ J$\cdot K^{-1}$ is the Boltzmann constant. This is the so-called Doppler cooling limit [153]. For instance, with the natural line widths of the D_1 and D_2 lines found roughly at 6 MHz [133], the corresponding Doppler temperature is found around 140μK. A temperature in the order of 10^{-4}K could appear to be a rather low one. However, the results presented in this thesis deal with light-dressed ultracold atomic systems in the BEC phase [38]. In a bosonic gas, achieving condensation requires simultaneously a low temperature and a large density. This condition is often expressed in terms of the phase space density $\rho = n\lambda_{\text{dB}}^3$, where $\lambda_{\text{dB}} = h/\sqrt{2\pi m_a k_{\text{B}} T}$ is the thermal de Broglie wavelength, and n and T are the atom density and the temperature of the gas, respectively. Condensation occurs for values of ρ above a certain critial value around $\rho_c \sim 1$, roughly where the thermal wavelength equals the average distance between particles, so that the individual atomic wavefunctions start to overlap significantly. To give a sense of scale, for the atoms in the atomic beam ρ is in the order of 10^{-10} [143], ten orders of magnitude below the critical condition. In laser cooling, which uses resonant light, an increase in atomic density is strongly constrained by the reabsorption of the scattered light, which causes interatomic repulsion, and by an enhanced atom-atom collision rate, both leading to heating and atom loss. Eventually, to achieve such a dramatic increase in phase space density, one needs to cool atomic vapors down to temperatures typically below the μK. The Doppler cooling limit, therefore, misses that mark by several orders of magnitude.

All the same, the extreme conditions required for condensation can be experimentally achieved by using a combination of various techniques, besides Doppler cooling. First and foremost, a scheme known as Sisyphus cooling [154, 155] permits laser cooling way below the Doppler temperature. The mechanism, also known as polarization gradient cooling, was discovered after W. Phillips et al. found out they were achieving lower-than-expected temperatures in the laboratory [156]. As it soon became clear, the multilevel

structure of the atomic level manifolds, which was ignored in the previously considered two-level model of the atoms, had a major part to play. Its role was signalled by the critical sensitivity of the achieved temperatures to the applied magnetic bias field and to the polarization of the laser beams. In essence, Sisyphus cooling relies on the creation of polarization gradients using orthogonal polarizations for the counter-propagating beams in the optical molasses. Doing so produces light shifts that oscillate at subwavelength scale and that affect the m_J sublevels differently. Selection rules for the transitions involving the different sublevels of the ground and excited manifolds ensure that, at a given position, the optical pumping from the highest energy states to the lowest is statistically favored. On average, thus, the atoms are found themselves *climbing up* a potential barrier as they travel along the polarization gradient, losing kinetic energy on the way. This mechanism allows the atoms to be cooled to much lower temperatures than those predicted by the two-level model of the Doppler cooling [126]. The theoretical limit in the Sisyphus cooling scheme is set by the recoil temperature $T_{\text{recoil}} = 2E_r/k_{\text{B}}$. With ^{87}Rb, and using the D_2 transition, this yields a temperature of $T_{\text{recoil}} \sim 360$nK. However, such a limit is technically never achieved in the laboratory, with the samples *only* effectively cooled down to the order of the μK, while preserving the atomic density. To go sub-μK and achieve the right conditions for condensation, that is, a sufficiently large phase space density, even further efforts are required. The final step involves switching off the MOT and loading the cooled atomic cloud into a confining potential. Once loaded, the trap depth is ramp down so that the trapped atoms with higher kinetic energy have a larger probability to leave the trap. This approach is commonly referred to as evaporative cooling [50]. A fraction of the atoms is lost in the process, but the remainder can reach temperatures in the order of tens to hundreds of nK. If the ramp is properly tuned, the resulting phase space density is increased by the end of the process, reaching the suitable conditions for the realization of experiments with ultracold atoms.

Needless to say, all the mechanisms sketched above are far more intricate in an actual experimental setup. A full sequence to achieve condensation includes many additional stages and considerations. For instance, the inclusion of additional fields is required to correct for the off-resonant population transfer to non-targeted ground state sublevels, or to remove atoms that populate non-trappable states in a magnetic trap. At the same time, no source of light is truly monochromatic, and the availability of high intensity coherent light sources with a narrow bandwidth around the required wavelengths is therefore crucial, as is their accurate calibration. Most importantly, to reach the ultracold regime, the samples need to be extremely well isolated from the surrounding environment. Eventually, an almost perfect vacuum needs to be created to keep the background pressure as low as 10^{-9} to 10^{-10} Pa, and great efforts have to be put into minimizing the different sources of electromagnetic noise and the calibration uncertainties. A detailed exploration of the various techniques used to cool and trap ultracold atoms is, however, beyond the scope of this thesis. A comprehensive review on such a fascinating topic can be found, for instance in [143]. The purpose behind this brief venture into

the field of laser cooling is –aside to provide the non-expert reader with a basic notion of the fundamental mechanisms at play– to convey a sense of scale and to emphasize the landmark that the achievement of degenerate quantum gases with laser-cooled alkali atoms has supposed in the road to achieve coherent control over quantum matter. Laser cooling, initially set out to improve atomic clocks, proved an essential ingredient to the eventual controlled preparation of a BEC, which, impressive as it is, is nowadays routinely achieved in laboratories across the world –and even in an Earth-orbiting research lab [157]. Not surprisingly, these remarkable achievements were awarded with two Nobel prizes in 1997 and in 2001. The first one was awarded to Steven Chu, Claude Cohen-Tannoudji and William D. Phillips *for development of methods to cool and trap atoms with laser light* [126–128], and the second one to Eric A. Cornell, Wolfgang Ketterle and Carl E. Wieman *for the achievement of Bose-Einstein condensation in dilute gases of alkali atoms, and for early fundamental studies of the properties of the condensates* [158, 159]. Henceforth, in this thesis we will take the trapped ultracold atomic cloud as our starting point, and focus on the exploitation of the dipole interaction described in this section to engineer synthetic spin-orbit coupling and magnetic fields.

2.2 Ultracold Bose gases with synthetic spin-orbit coupling

The previous section reviewed the most fundamental ingredient behind the manipulation of ultracold atoms: the dipole light-atom interaction. With the electromagnetic fields treated as position- and time-dependent corrections to the bare atomic Hamiltonian in a semiclassical description, the problem so far has been presented at the single-atom level. Yet this thesis explores the dynamics that results from the interplay between Raman dressing and cold collisions in an ultracold atomic cloud. Accordingly, in this section we introduce the basic frameworks that will be employed along the thesis to describe these phenomena. First, we will establish the fundamental framework to treat the many-body problem of an ultracold gas of N interacting atoms in Sec. 2.2.1, with especial emphasis on the case of alkali species with $F = 1$ in the lowest hyperfine state. Next, we will briefly sketch the basic notions of the phenomenon of Bose-Einstein condensation in Sec. 2.2.2, where we will also review the mean-field treatment of an ultracold gas in the condensate phase. Finally, in Sec. 2.2.3 we will apply the discussed frameworks to the case of a Raman-dressed spinor gas, where we will see that the dressing can effectively induce a synthetic form of spin-orbit coupling in the gas.

2.2.1 Many-body treatment of ultracold Bose gases

We consider a dilute ultracold gas formed by N identical atoms held in a confining potential. The atoms in the gas interact with each other via low-energy scattering processes. As briefly elaborated in the previous section, the ultracold regimes that are experimentally accessible with neutral atoms are achieved at temperatures in the nK

regime. The critical phase space density necessary for condensation is reached in this temperature range with typical atomic densities between $n \sim 10^{13}$ and $n \sim 10^{14}$ cm^{-3}. While such densities are large when compared to the ones required to optimize the cooling processes in the MOT, ultracold atomic clouds are still impressively dilute –as a reference, dry air at room temperature (20°C) and 1 atm has a number density close to 10^{19} cm^{-3}. For alkali atoms in their electronic ground state and at such low densities, the mean distance between the atoms, $d = n^{-1/3}$, is much larger than the the range of the atom-atom interactions, r_0, i.e.

$$r_0 \ll d, \tag{2.28}$$

Inequality (2.28) is the so-called diluteness condition. When (2.28) is fulfilled, the amplitude of the scattering processes that involve simultaneously more than two atoms is negligible. Hence, the interactions in the gas are well described by two-body interaction potentials.

Remarkably, the expression for such two-body potentials in the ultracold regime can be written in a very simple form. To achieve condensation, the gas needs to be cooled down to quantum degeneracy (more details in Sec. 2.2.2), which is roughly achieved when thermal de Broglie wavelength $\lambda_{\mathrm{dB}} = h/\sqrt{2\pi m_a k_{\mathrm{B}} T}$ is of the order of the interatomic separation d, or, equivalently, when the phase space density fulfills

$$\rho = n\lambda_{\mathrm{dB}}^3 \sim 1. \tag{2.29}$$

Combining condition (2.29) with the diluteness criterion (2.28), and using the relation $p_{th} = h/\lambda_{\mathrm{dB}}$ between the thermal momentum and the de Broglie wavelength, one finds that the characteristic values of the momentum in the gas must satisfy

$$\frac{p\, r_0}{\hbar} \ll 1. \tag{2.30}$$

At such small momenta and densities, it is safe to assume that all atom-atom interactions taking place in the gas are well described by asymptotic s-wave scattering processes [160]. In such processes, the scattering amplitude is independent of the momentum of the particles involved in the collision and of the specific shape of the two-body potential. The potential can then be characterized simply by a scalar parameter, the scattering length. In general, its value is sensitive to the Zeeman sublevel structure of the involved atoms [161], and is also dependent on external magnetic [60, 61] and electric fields [62, 63] through Feshbach resonances. Along this thesis we will consider alkali atoms in the lower hyperfine manifold of the electronic ground state, with total angular momentum F. The hyperfine energy split to the highest manifold is several orders of magnitude larger than the characteristic energies of ultracold collisions (see Fig. 2.1). Hence, the internal structure of the atoms described in *Sec.* 2.1 is not altered in the presence of interactions, and atoms in the lowest hyperfine manifold can not be excited the higher manifold via collisions. Taking all these considerations into account, and fruther assuming that collisions are invariant under rotations in the hyperfine spin space, we can approximate

the expression for the two-body potential for each pair ij of atoms at positions $\mathbf{r}$ and $\mathbf{r}'$ to [162]

$$U^{(i,j)}(|\mathbf{r}-\mathbf{r}'|) \simeq \delta(\mathbf{r}-\mathbf{r}')\frac{4\pi\hbar^2}{m_a}\sum_{\mathcal{F}=0}^{2F} a_{\mathcal{F}}\hat{\mathcal{P}}_{\mathcal{F}}, \tag{2.31}$$

where a_F is the scattering length of atoms colliding in the total spin $\mathcal{F}$ (the composition of the spins of the two colliding atoms) channel, and $\hat{\mathcal{P}}_{\mathcal{F}} = \sum_{M_{\mathcal{F}}=-\mathcal{F}}^{\mathcal{F}} |\mathcal{F}, M_{\mathcal{F}}\rangle\langle\mathcal{F}, M_{\mathcal{F}}|$ is the projector of the states of the incoming and outcoming spin pairs into the subspace of total spin $\mathcal{F}$.

With all these considerations, we can now construct the many-body Hamiltonian for the gas. Quantum particles are fundamentally indistinguishable and, as a consequence, only two types of physically meaningful many-body product states can be constructed: those that are symmetric with respect to the interchange of any two particles and those that are antisymmetric. The particles described by the symmetric states are called bosons, and the ones described by anti-symmetric states are called fermions. According to the spin-statistics theorem [163], particles are classified into these two categories depending on their spin. Such a relation, of relativistic origin, states that integer-spin particles are bosons and half-integer–spin particles are fermions. This result also applies to composite systems, such as atoms, which behave as bosons or fermions according to their total angular momentum. In this thesis we restrict ourselves to the study of bosonic atomic species, which, as we will cover in Sec. 2.2.2, can form a BEC. The Hilbert space of a bosonic many-body system is, therefore, the symmetric subspace of the product space of N single-particle Hilbert spaces. Accordingly, the operators acting on the states of the system are restricted to the symmetric subset of all operators acting on the product Hilbert space.

We will treat the many-body problem within the conventional second quantization or number representation formalism, in which all operators are written in terms of products of creation and annihilation operators. These operators are best defined through their action upon the occupation number or Fock basis states. Let us consider an arbitrary set of states $\{|j\rangle\}$, with $j = 1, 2, 3, ...$, that form an orthonormal basis of a given single-particle Hilbert space $\mathcal{H}^{(1)}$. We can define a bosonic Fock state $|n_1, n_2, n_3, \ldots\rangle \equiv \prod_{\otimes j=1} |n_j\rangle$ as the $(N = \sum_{j=1} n_j)$-particle state given by the normalized superposition of all permutations of product states with n_j particles in each single-particle state $|j\rangle$. The set of all Fock states form an orthonormal basis of the bosonic Fock space $\mathcal{H}_{\mathrm{S}}^{\mathrm{F}}$, which is the extended Hilbert space that spans over all bosonic states of arbitrary numbers of particles. It can be written as the direct sum of the Hilbert spaces for all the different number of particles

$$\mathcal{H}_{\mathrm{S}}^{\mathrm{F}} = \mathcal{H}^{(0)} \oplus \mathcal{H}^{(1)} \oplus \mathcal{H}_{\mathrm{S}}^{(2)} \oplus \mathcal{H}_{\mathrm{S}}^{(3)} \cdots, \tag{2.32}$$

where $\mathcal{H}_{\mathrm{S}}^{(j)}$ is the subspace of symmetrized j-particle states. Naturally, the subspaces of 0 and 1 particles can not be symmetrized or antisymmetrized. The subspace $\mathcal{H}^{(0)}$ contains only one vector state, the so-called vacuum state, commonly labelled by $|0\rangle$. It

should be stressed that, while the vacuum state contains no particles, it is not a zero vector, and it has the standard normalization $\langle 0|0\rangle = 1$.

We label the annihilation operator for the state $|k\rangle$ by $\hat{a}_k^\dagger$. Its action couples the m-particle to the $(m-1)$-particle subspaces of the Fock space in the following way

$$\hat{a}_k|n_1, n_2, \ldots, n_k, \ldots, n_s\rangle = \sqrt{n_k}|n_1, n_2, \ldots, (n_k - 1), \ldots, n_s\rangle. \tag{2.33}$$

By taking the Hermitian conjugate of (2.33), and acting the resulting operator at each side on $|n_1', n_2', \ldots, n_k', \ldots, n_s'\rangle$ it is immediate seen that

$$\hat{a}_k^\dagger|n_1, n_2, \ldots, n_k, \ldots, n_s\rangle = \sqrt{n_k + 1}|n_1, n_2, \ldots, (n_k + 1), \ldots, n_s\rangle. \tag{2.34}$$

In this way, the corresponding creation operator for the state $|k\rangle$ is given by the Hermitic conjugate $\hat{a}_k^\dagger$ of the annihilation operator. As expected, $\hat{a}_k^\dagger$ couples the m-particle to the $(m+1)$-particle subspaces. These definitions can be directly extended to the corresponding operators for any single-particle state. Notice that the application of a creation operator to the vacuum state yields the corresponding single-particle state, so we can equal $|j\rangle = \hat{a}_j^\dagger|0\rangle$. Likewise, $\hat{a}_j|j\rangle = |0\rangle$. Relevantly, the annihilation operator acting upon the vacuum state returns the zero vector, i.e., $\hat{a}_j|0\rangle = 0$. It is also worth mentioning that we can construct the Hermitian number operators $\hat{n}_j = \hat{a}_j^\dagger\hat{a}_j$ from the creation and annihilation operators. All Fock states are eigenvectors of the number operators $\hat{n}_j$, with their eigenvalues given by the occupation of the corresponding states $|j\rangle$

$$\hat{n}_k|n_1, n_2, \ldots, n_k, \ldots, n_s\rangle = n_k|n_1, n_2, \ldots, n_k, \ldots, n_s\rangle. \tag{2.35}$$

Finally, using expressions (2.33) and (2.34), is easy to show that $\hat{a}_k^\dagger$ operators fulfill the so-called bosonic commutation relations, given by

$$[\hat{a}_j^\dagger, \hat{a}_k] = \delta_{jk} \quad \text{and} \quad [\hat{a}_j^\dagger, \hat{a}_k^\dagger] = [\hat{a}_j, \hat{a}_k] = 0, \tag{2.36}$$

for any j, k.

Let us now review the way the operators acting in the physical subspace can be written in terms of bosonic operators. Any arbitrary m-particle operator $\hat{U}_m$ acting on the space of N identical bosonic particles must be symmetric under the permutation of all particle pairs. Hence, we can generally write them as

$$\hat{U}_m = \frac{1}{m!}\sum_P \sum_{\oplus 1 \le i_1 < \cdots < i_m}^{N} \hat{U}^{(P(i_1),\ldots,P(i_m))}, \tag{2.37}$$

with $m < N$ and where $\hat{U}^{(i_1,\ldots,i_m)}$ represents a m-particle operator acting on the subset of the product space of the $i_1, \ldots, i_m$ particles. The sum over P runs over the permutations

of the indices of $\hat{U}^{(i_1,\ldots,i_m)}$. Expanding expression (2.37) in the $\{|s\rangle\}$ eigenbasis yields

$$\hat{U}_m = \frac{1}{m!}\sum_{j_1,\ldots,j_m}\sum_{k_1,\ldots,k_m}\Bigg[\langle j_1|\cdots\langle j_m|\hat{U}^{(1,\ldots,m)}|k_1\rangle\cdots|k_m\rangle \sum_{P}\sum_{\oplus 1\le i_1<\cdots<i_m}^{N}|j^{(i_1)}_{P(1)}\rangle\cdots|j^{(i_m)}_{P(m)}\rangle\langle k^{(i_1)}_{P(1)}|\cdots\langle k^{(i_m)}_{P(m)}|\Bigg], \tag{2.38}$$

where the projectors $|j^{(i_l)}\rangle\langle k^{(i_l)}|$ act on the Hilbert space of the i_l particle. Observe that, due to their indistinguishability, particle interactions are the same for all groups of m particles, and hence the components of $\hat{U}^{(i_1,\ldots,i_m)}$ factor out and the operator is written in terms of the m-particle operator $\hat{U}^{(1,\ldots,m)}$. From (2.38) we can write the m-particle operator in terms of bosonic operators by using the following identity

$$\sum_{P}\sum_{\oplus 1\le i_1<\cdots<i_m}^{N}|j^{(i_1)}_{P(1)}\rangle\cdots|j^{(i_m)}_{P(m)}\rangle\langle k^{(i_1)}_{P(1)}|\cdots\langle k^{(i_m)}_{P(m)}| = \hat{a}^\dagger_{j_1}\cdots\hat{a}^\dagger_{j_m}\hat{a}_{k_1}\cdots\hat{a}_{k_m}, \tag{2.39}$$

which holds only when the operator in the left-hand side is restricted to act within the subspace of the symmetric states of the N-particle product space (see [164] for a detailed proof). In this way, we can write the second-quantized expression for any arbitrary m-particle operator as

$$\hat{U}_m = \frac{1}{m!}\sum_{j_1,\ldots,j_m}\sum_{k_1,\ldots,k_m}\langle j_1|\cdots\langle j_m|\hat{U}^{(1,\ldots,m)}|k_1\rangle\cdots|k_m\rangle\hat{a}^\dagger_{j_1}\cdots\hat{a}^\dagger_{j_m}\hat{a}_{k_1}\cdots\hat{a}_{k_m}. \tag{2.40}$$

Having the symmetry considerations built-in, the second quantization formalism is a powerful tool that allows to write the many-body operators in a compact way that does not depend on the total number of particles, and which greatly simplifies the manipulations of multi-particle states. Fundamentally, such a simplification originates from the vast reduction in the size of the many-body Hilbert space due to the indistinguishability of the particles. For our purposes, we will consider the set of states $\{|\mathbf{r}_m\rangle\}$ that form an orthogonal basis of the single-atom subspace. We choose the basis elements $|\mathbf{r}_m\rangle$ to describe an atom located at $\mathbf{r}$ with internal state $|F,m\rangle$, with $\langle\mathbf{r}_m|\mathbf{r}'_{m'}\rangle = \delta(\mathbf{r}-\mathbf{r}')\delta_{mm'}$. By using the result in equation (2.40), we can straightforwardly write any arbitrary one-body operator $\hat{V}_1$ as

$$\hat{V}_1 = \sum_{mm'}\int\int d\mathbf{r}\,d\mathbf{r}'\,\langle\mathbf{r}_m|\hat{V}^{(1)}|\mathbf{r}'_{m'}\rangle\hat{\Psi}^\dagger_m(\mathbf{r})\hat{\Psi}_{m'}(\mathbf{r}'), \tag{2.41}$$

where $\langle\mathbf{r}_m|\hat{V}^{(1)}|\mathbf{r}'_{m'}\rangle$ is the matrix element of the corresponding single-particle operator. Here, $\hat{\Psi}^\dagger_m(\mathbf{r})$ and $\hat{\Psi}_{m'}(\mathbf{r}')$ are corresponding bosonic creation and annihilation operators for the states $|\mathbf{r}_m\rangle$ and $|\mathbf{r}'_{m'}\rangle$. The bosonic commutation relations in this particular case, where the indexes $\mathbf{r}$ are not discrete and the sum is replaced by an integration, are expressed as

$$\left[\hat{\Psi}_m(\mathbf{r}),\hat{\Psi}^\dagger_{m'}(\mathbf{r}')\right] = \delta(\mathbf{r}-\mathbf{r}')\delta_{mm'} \;\text{ and }\; \left[\hat{\Psi}_m(\mathbf{r}),\hat{\Psi}_{m'}(\mathbf{r}')\right] = \left[\hat{\Psi}^\dagger_m(\mathbf{r}),\hat{\Psi}^\dagger_{m'}(\mathbf{r}')\right] = 0, \tag{2.42}$$

where the Kroennecker operator $\delta_{\mathbf{r}\mathbf{r}'}$ is *replaced* by a Dirac delta function $\delta(\mathbf{r}-\mathbf{r}')$.

Let us apply these results to the Hamiltonian of a gas of bosonic atoms of mass m_a in an arbitrary potential $V_{mm'}(\mathbf{r})$. The single-particle Hamiltonian can be written in terms of the first-quantized position and momentum operators $\hat{\mathbf{r}}$ and $\hat{\mathbf{p}}$ as

$$\hat{H}^{(1)} = \frac{\hat{\mathbf{p}}^2}{2m_a} + \hat{V}, \tag{2.43}$$

with $\hat{V} = \sum_{mm'} V_{mm'}(\hat{\mathbf{r}})|F,m\rangle\langle F,m'|$. By using expression (2.41), we can construct the many-body noninteracting Hamiltonian from the single-particle operator $\hat{H}^{(1)}$, which yields

$$\hat{H}_{\text{n.i.}} = \sum_{mm'} \int d\mathbf{r}\, \hat{\Psi}^\dagger_m(\mathbf{r}) \left[\frac{-\hbar^2\nabla^2}{2m_a}\delta_{mm'} + V_{mm'}(\mathbf{r})\right] \hat{\Psi}_{m'}(\mathbf{r}). \tag{2.44}$$

It is left to write the contribution to the many-body Hamiltonian that accounts for the interatomic interactions. As argued above, for an ultracold atomic cloud we just need to consider isotropic binary interaction operators $\hat{U}^{(1,2)}$ that fulfill

$$\langle \mathbf{r}_m|\langle \mathbf{r}'_{m'}|\hat{U}^{(1,2)}|\mathbf{r}''_{m''}\rangle|\mathbf{r}'''_{m'''}\rangle \simeq \delta(\mathbf{r}-\mathbf{r}')\delta(\mathbf{r}-\mathbf{r}'')\delta(\mathbf{r}'-\mathbf{r}''')C^{m,m'}_{m'',m'''}, \tag{2.45}$$

with

$$C^{m,m'}_{m'',m'''} = \frac{4\pi\hbar^2}{m_a}\sum_{\mathcal{F}=0}^{2F} a_{\mathcal{F}}\langle F,m|\langle F,m'|\hat{\mathcal{P}}_{\mathcal{F}}|F,m''\rangle|F,m'''\rangle. \tag{2.46}$$

From (2.40) and (2.45), it follows that

$$\hat{H}_{\text{int}} \simeq \sum_{mm'm''m'''} \int d\mathbf{r}\, C^{m,m'}_{m'',m'''}\hat{\Psi}^\dagger_m(\mathbf{r})\hat{\Psi}^\dagger_{m'}(\mathbf{r})\hat{\Psi}_{m''}(\mathbf{r})\hat{\Psi}_{m'''}(\mathbf{r}), \tag{2.47}$$

Henceforth, we will stick to atomic species with total angular momentum $F=1$ in the lowest hyperfine state, such as ^{87}Rb or ^{41}K, where the composite spin of an atomic pair can only take the values $\mathcal{F}=0,2$. In this situation, by explicitly computing the Clebsch-Gordan coefficients $\langle \mathcal{F}, M_{\mathcal{F}}|(|F=1,m\rangle\otimes|F=1,m'\rangle)$ and grouping the resulting terms, the expression (2.47) for the interaction Hamiltonian can be compactly written as

$$\hat{H}^{(F=1)}_{\text{int}} \simeq \int d\mathbf{r}\left(\frac{g_s}{2}(\hat{\mathbf{\Psi}}^\dagger\hat{\mathbf{\Psi}})^2 + \frac{g_a}{2\hbar}\sum_j(\hat{\mathbf{\Psi}}^\dagger\hat{F}_j\hat{\mathbf{\Psi}})^2\right), \tag{2.48}$$

where we introduce *spinor* field operator $\hat{\mathbf{\Psi}} = (\hat{\Psi}_{-1},\hat{\Psi}_0,\hat{\Psi}_1)^T$. Here $\hat{F}_j \in \{\hat{F}_x,\hat{F}_y,\hat{F}_z\}$ are the spin-1 matrices. The interaction coefficients g_s and g_a read

$$g_s = 4\pi\hbar^2(a_0+2a_2)/3m \text{ , and } g_a = 4\pi\hbar^2(a_2-a_0)/3m, \tag{2.49}$$

and group the different four-operator contributions into a *spin*-symmetric and a non-symmetric term, respectively [165].

In this way, a weakly-interacting ultracold atomic gas of bosonic species in a $F = 1$ ground state can be described by the following many-body Hamiltonian

$$\hat{H}^{(F=1)} = \int d\mathbf{r} \left[\hat{\mathbf{\Psi}}^\dagger \left(\frac{-\hbar^2 \nabla^2}{2m_a} + \hat{V} \right) \hat{\mathbf{\Psi}} + \frac{g_s}{2} (\hat{\mathbf{\Psi}}^\dagger \hat{\mathbf{\Psi}})^2 + \frac{g_a}{2\hbar} \sum_j (\hat{\mathbf{\Psi}}^\dagger \hat{F}_j \hat{\mathbf{\Psi}})^2 \right]. \tag{2.50}$$

Such a second-quantized expression for the Hamiltonian of a spin-1 spinor gas is the starting point of the research presented in this thesis. However, while the second-quantization formalism allows for deceptively simple looking expressions, in most situations it is not possible to perform full numerical simulations of such a model. As discussed in chapter 1, many-body Hilbert spaces increase in size exponentially with the total number of particles, and the problems quickly become untreatable as the number is increased. In order to numerically investigate ultracold atomic systems, further assumptions about the solutions need to be made. In this thesis, three main approaches will be taken to reduce the size many-body problem to treatable regimes. In the simplest approach, we will assume that the energy densities are kept below a certain threshold during the dynamics of the many-body system. The occupation of the high-energy single-particle states is then neglected, and the second-quantized many-body Hamiltonian is constructed upon the truncated basis instead. Such a procedure, for instance, is fundamental for an efficient simulation of ultracold atoms in deep optical lattices (see Sec. 2.3), where the truncation of the single-particle space is straightforward. In chapters 3 to 5, few-mode truncations will be employed to investigate numerically the pseudospin dynamics induced by ultracold collisions in the Raman dressed atomic cloud. Yet these truncations are still insufficient when the number of atoms and/or modes considered is further increased. Far more sophisticated numerical methods are then required. In chapter 6, we will use the density-matrix renormalization group approach [166], which is valid when the solutions are found in a low-entanglement sector of the Hilbert space. Finally, in chapter 4 and chapter 5 we will investigate the same pseudospin dynamics in the condensate. Due to the nature of bosonic statistics, a condensate can be described by a mean-field theory, which we review next, and where almost the entirety of the many-body degrees of freedom are neglected.

2.2.2 Mean-field treatment of a Bose-Einstein condensate

Bose-Einstein condensation is the collapse of a macroscopic fraction of the particles in an ensemble into their ground state, which can occur for many-body systems of bosons at thermal equilibrium for sufficiently low temperatures. In many bosonic systems, the onset of the macroscopic occupation takes place at a finite critical temperature, defining a phase transition into a condensate phase. Having a single state macroscopically occupied, the Bose-Einstein condensate constitutes a state of matter that exhibits distinctive properties. Most notably, the fraction of particles in the condensate is described by a wavefunction that exhibits long-range phase coherence, giving rise to superfluidity [167]. Its occurrence is understood from the statistics of bosonic particles at low temperature.

The thermal distributions of indistinguishable quantum particles can be easily derived from a maximum entropy principle [168], which, by construction, minimizes the amount of a priori information assumed in the distribution. For an ensemble of noninteracting bosons at thermal equilibrium with a bath, one finds that the following distribution for the average occupation n_s of the single-particle states of energy E_s

$$n_s = \frac{1}{\exp(\beta E_s) - 1}. \tag{2.51}$$

Equation (2.51) is commonly referred to as the Planck distribution, since it was originally developed to describe the spectral density of electromagnetic radiation emitted by a black body in thermal equilibrium. Here, β is the coldness or thermodynamic beta at the equilibrium, which fixes the ratio between the increase in the entropy and in the total energy of the ensemble-bath compound system. Very often, it is expressed rather in terms of the thermodynamic temperature T as $\beta = (k_{\mathrm{B}}T)^{-1}$.

For massive particles at low energies, we can further assume that the total number of particles is conserved in the statistical ensemble. Then, the distribution n_s has to satisfy the additional constraint $\sum_s n_s = N$, and the Bose-Einstein distribution is found instead

$$n_s = \frac{1}{\exp[\beta(E_s - \mu)] - 1}. \tag{2.52}$$

Here, μ is the chemical potential, that is, the energy cost of adding a particle to the total number N. Observe that, at large temperatures (small β), the mean occupation of the states is much smaller than 1, and so $\exp[\beta(E_s - \mu)] \gg 1$. In this situation, the distribution is well approximated by the Boltzmann distribution $n(E_j) = \exp[-\beta(E_s - \mu)]$, which describes an ensemble of identical yet distinguishable particles at thermal equilibrium. At sufficiently low temperatures, however, distinguishable and indistinguishable particles behave in markedly different ways, and the -1 term in the denominator in the right-hand side of (2.52) has major consequences. Due to such a term, μ necessarily has to fulfill that $\mu \leq E_s \leq E_0$, where E_0 is the energy of the ground state, in order to have $n(E_s) \geq 0$ for any state s. This condition is fundamental to the phenomeon of Bose-Einstein condensation, since it implies that, as $\mu \to E_0$, the occupation of the lowest energy state becomes unbounded (see Fig. 2.3(a)), while the maximum occupation for all other states is bounded to $n_{s\neq 0}^{\max} = \frac{1}{\exp\beta(E_s - E_0) - 1}$. Therefore, at a finite β, the maximum number of particles that can be in the excited states is given by

$$N_{\mathrm{c}} = \sum_{s>0} n_s^{\max} = \sum_{s>0} \frac{1}{\exp\beta(E_s - E_0) - 1}. \tag{2.53}$$

If N is increased beyond the critical value N_{c}, all the extra atoms $N - N_{\mathrm{c}}$ must necessarily populate the ground state, where the occupation is not bounded. At the same time, the critical population N_{c} is an increasing function of the temperature. Hence, by equaling the total number of particles N to N_{c}

$$N = N_{\mathrm{c}} = \sum_{s>0} \frac{1}{\exp\frac{E_s - E_0}{k_{\mathrm{B}}T_{\mathrm{c}}} - 1}, \tag{2.54}$$

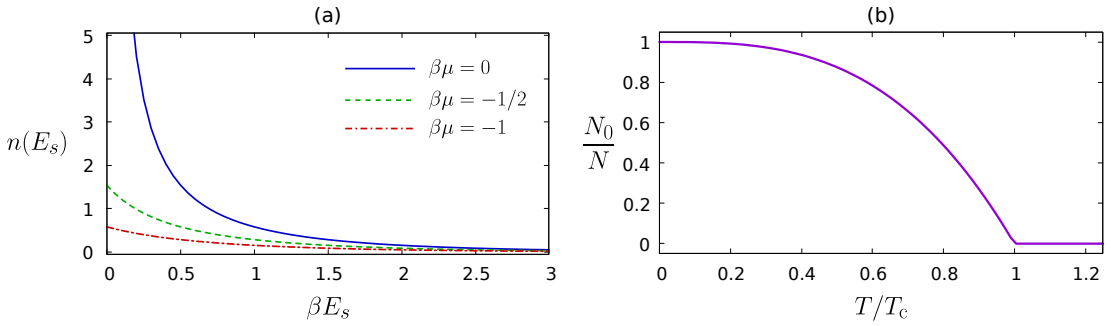

Figure 2.3: (a) Average occupation of the states with energy E_s predicted by the Bose-Einstein distribution as a function of βE_s and for several values of the chemical potential μ. Without loss of generality, the ground state energy is set to $E_0 = 0$, for which $\mu \leq 0$. (b) Fraction of atoms occupying the ground state as a function of the temperature for an ensemble of noninteracting bosons in a 3D harmonic potential at thermal equilibrium. The temperature is scaled to the critical temperature $T_c = \hbar(\omega_x\omega_y\omega_z N)^{-1/3}$.

we can implicitly define a critical temperature T_c below which the atoms start to occupy macroscopically the ground state. This macroscopically occupied state is what constitutes the BEC. However, notice that in order to have $T_c > 0$, the sum in the right-hand side of (2.54) needs to be bounded. This is not generally granted for any arbitrary Hamiltonian. The explicit expression for T_c will depend on the specific characteristics of the single-particle spectrum $\{E_j\}$. Of relevance to the research presented in this thesis, for a gas of noninteracting bosons held in a three-dimensional harmonic potential, the critical temperature is found to be

$$k_B T_c = 0.94\hbar\bar{\omega}N^{1/3}, \tag{2.55}$$

where $\bar{\omega} = (\omega_x\omega_y\omega_z)^{1/3}$ is the geometric mean of the harmonic trap frequencies along the x, y, z-direction. The critical temperature defines a second-order phase transition in the thermodynamic limit. The thermodynamic limit in such a system can be properly defined by simultaneously taking $N \to \infty$ and $\bar{\omega} \to 0$ while keeping $N\bar{\omega}$ constant [169]. There, the condensate fraction, or relative occupation of the ground state, can be expressed in terms of T_c as

$$\frac{N_0}{N} = 1 - \frac{N_c}{N} = \begin{cases} 1 - \left(\frac{T}{T_c}\right)^3, & \text{for } T < T_c, \\ 0, & \text{for } T > T_c, \end{cases} \tag{2.56}$$

where N_0 is the occupation of the ground state. The condensate fraction of the harmonically trapped gas is shown in Fig. 2.3(b) as a function of the temperature. The ratio N_0/N vanishes for temperatures above T_c, and increases continuously as T is decreased below T_c. Its derivative with respect to the temperature changes nonanalytically at T_c, signaling the second-order phase transition into the BEC phase.

In a typical condensate of $N \sim 10^5$ atoms in an isotropic potential with $\omega \sim 2\pi \times 150$ Hz, the critical temperature in the absence of interatomic interactions is found around

$T_c \sim 300$ nK. While the critical temperature in this example is way below the μK, it needs to be stressed that it is still much higher than the temperature associated with the single-particle energy gap, $T_{sp} = \hbar\omega/k_B \sim 7$ nK. Together with the critical behavior in the thermodynamic limit, this huge difference illustrates how Bose-Einstein condensation is a completely different phenomenon than the macroscopic occupation of the ground state that is expected for distinguishable particles as the temperature is brought to $T < T_{sp}$. The intrinsic indistinguishability of the particles lies, therefore, at its core. As a side note, it is worth noting that particles with half-integer spin obey fermionic statistics, which forbid the multiple occupation of the same single-particle quantum state, and therefore can not directly form a condensate. However, interacting fermions may form bosonic pairs or molecules that can condensate given the right conditions. Not long after the first realization of a degenerate Fermi gas [170], Bose-Einstein condensation of paired fermions was achieved [171, 172]. And soon after, the crossover between a Bardeen-Cooper-Schrieffer state of Cooper momentum pairs, with long pairing distances, to a BEC formed by bosonic molecular pairs was observed [68, 69]. In condensed matter systems, bosonic pair formation plays a fundamental role in the phenomenon of superconductivity [173].

The theory of Bose-Einstein condensation can be extended to describe weakly interacting Bose gases. In fact, in real systems, the survival of the long-range phase coherence of the macroscopic wavefunction against external perturbations relies on the interatomic interactions. As discussed in Sec. 2.2.1, ultracold atoms interact with each other mainly via s-wave scattering processes. Yet, even at low densities, weak interactions can suppose a marked departure from the ideal gas scenario. One immediate consequence of interactions is that the real gas does not have infinite compressibility. In order to achieve the critical condition for condensation, it is not enough in general to simply increase N above the value of N_c predicted by the noninteracting theory. As densities are increased, higher-energy scattering processes become increasingly more relevant, which result in a larger atom loss rate from the trap. That being said, at typical condensate densities $\sim 10^{14}$ cm^{-3}, the critical temperatures in real alkali gases are found very close to the value predicted for the ideal gas [174, 175]. To properly treat the problem in the presence of interactions, however, a more sophisticated analysis is required. For an detailed discussion of the weakly interacting Bose gas, see for instance [38].

For our purposes, it will suffice to assume that a critical temperature T_c still exists in the presence of weak interactions, and that a condensate is formed for temperatures below T_c. We consider that the temperature is sufficiently low so that a large fraction of the atoms is found at the condensate state. By using the second-quantization formalism introduced in Sec. 2.2.1, we can express the state of the condensate part of the gas in an arbitrary orthonormal basis $\{|j\rangle\}$ as

$$|\phi_0\rangle = |N_0, \boldsymbol{\alpha}\rangle = \frac{1}{\sqrt{N_0!}} \left(\sum_j \alpha_j \hat{a}_j^\dagger \right)^{N_0} |0\rangle \,, \tag{2.57}$$

with $\sum_j |\alpha_j|^2 = 1$. The many-body state (2.57) describes the macroscopic occupation of an arbitrary single-particle state $|\boldsymbol{\alpha}\rangle = \sum_j \alpha_j |j\rangle$ with $1 \ll N_0 < N$ atoms. It is a projective coherent states, which fulfills

$$\frac{1}{\sqrt{N_0}} \hat{a}_j \, |N_0, \boldsymbol{\alpha}\rangle \overset{N_0 \to \infty}{\longrightarrow} \alpha_j \, |N_0 - 1, \boldsymbol{\alpha}\rangle \,, \tag{2.58}$$

for any j. Since we assume that the Hamiltonian preserves the total number of particles, it can only include particle-preserving operators of the form $(\hat{a}_i^\dagger)^{k_i} \cdots (\hat{a}_j^\dagger)^{k_j} \hat{a}_s^{q_s} \cdots \hat{a}_r^{q_r}$, with $\sum_l k_l = \sum_l q_l = M$. Thus, considering the result (2.58), the expected value for these operators when acting on the ansatz state (2.57) fulfills

$$\frac{1}{N_0^M} \langle \phi_0 | (\hat{a}_i^\dagger)^{k_i} \cdots (\hat{a}_j^\dagger)^{k_j} \hat{a}_s^{q_s} \cdots \hat{a}_r^{q_r} | \phi_0 \rangle \overset{N_o \to \infty}{\longrightarrow} \frac{N_0!}{N_0^M (N_0 - M)!} (\alpha_i^*)^{k_i} \cdots (\alpha_j^*)^{k_j} \alpha_s^{q_s} \cdots \alpha_r^{q_r} , \tag{2.59}$$

while the higher moments vanish. The prefactor in the right-hand-side of (2.59) converges to 1 as the ratio M/N_0 goes to zero. In our many-body problem, we consider up to 2-body operators, and so $M \leq 4$. Hence, for large N_0 we can then safely make the substitutions

$$\hat{a}_j \overset{N_0 \to \infty}{\longrightarrow} \sqrt{N_0} \alpha_j \;, \quad \hat{a}_j^\dagger \overset{N_0 \to \infty}{\longrightarrow} \sqrt{N_0} \alpha_j^* , \tag{2.60}$$

and replace the bosonic operators in the quantum theory by the scalar quantities. The condensate is well described by a mean-field complex-valued wavefunction $\phi_0(j) = \sqrt{N_0}\alpha_j$. The condensate wavefunction $\phi_0(j)$ is normalized to the number of particles in the condensate, $\sum_j |\phi(j)|^2 = N_0$. It is commonly referred to as the order parameter of the condensate phase, in connection to the term used in the theory of superfluidity.

Naturally, the set of complex numbers $\{\phi(j)\}$ describes only the fraction of atoms within the condensate, and, strictly speaking, even there it only does so properly in the thermodynamic limit. A more accurate mean-field treatment for the weakly-interacting gas involves the replacement $\hat{a}_j \to \alpha_j + \delta\hat{a}_j$, where the expansion includes a non-condensed component $\delta\hat{a}_j$ of the operators, which can account for the fluctuations in the condensed fraction of the gas that arise due to atomic interactions. Typically, $\delta\hat{a}_j$ is treated as a perturbation to compute elementary excitations of a gas. In chapter 4 and chapter 5, we will employ the mean-field treatment of a BEC to describe macroscopic variations of the condensate wavefunction over time, $\phi_0(j,t)$, after quenches in the Hamiltonian. We will assume that the temperature is sufficiently low so that the depletion of the condensate is comparatively small, and disregard the role of the non-condensed excitations. Hence, for our purposes the zeroth order of the approximation will suffice.

With these considerations in mind, we can write the zeroth order theory for the BEC of an ultracold spin-1 gas by directly substituting the field operators $\hat{\boldsymbol{\Psi}}(\mathbf{r})$ in the many-body Hamiltonian (2.50) with a condensate wavefunction $\boldsymbol{\psi}(\mathbf{r}) = (\psi_{-1}(\mathbf{r}), \psi_0(\mathbf{r}), \psi_1(\mathbf{r}))^T$.

This yields the following energy functional

$$E[\boldsymbol{\psi}] \simeq \int d\mathbf{r} \left(\frac{\hbar^2}{2m_a} |\nabla \boldsymbol{\psi}|^2 + \boldsymbol{\psi}^* \hat{V} \boldsymbol{\psi} + \frac{g_s}{2} |\boldsymbol{\psi}|^4 + \frac{g_a}{2\hbar} \sum_j (\boldsymbol{\psi}^* \hat{F}_j \boldsymbol{\psi})^2 \right), \tag{2.61}$$

Such a substitution is safe only when there are no nonlocal terms in the effective interaction Hamiltonian, which would make quantum correlations relevant. In ultracold atomic gases, this is actually granted by the conditions for diluteness (2.28) and quantum degeneracy (2.29) discussed at the beginning of Sec. 2.2.1, which led to the s-wave scattering potential (2.31). It should be remarked that, despite ultracold gases being weakly-interacting, the interaction energy in the condensate is by no means negligible. In fact, it can easily be the case that the interaction energy is much larger than the kinetic energy, while at the same time the atomic density still fulfills the diluteness condition.

With the commutation relations having been trivialized, the energy functional in (2.61) describes a classical theory for the fields ψ_j. The canonical momentum associated with each $\psi_j(\mathbf{r})$ is simply $\Pi_j(\mathbf{r}) = i\hbar\psi_j^*(\mathbf{r})$, from which we can construct the classical action

$$S = \int dt \int d\mathbf{r} \left(\Pi_j \frac{d\psi_j}{dt} \right) - \int dt E. \tag{2.62}$$

By imposing the stationary condition $\delta S = 0$ on the action (2.62), we obtain the corresponding Hamilton's equations for the fields

$$i\hbar \frac{d\psi_j}{dt} = \frac{\delta E}{\delta \psi_j^*}, \tag{2.63}$$

where $\frac{\delta}{\delta \psi_j}$ indicates the variational derivative with respect to ψ_j. Equation (2.63) is the Gross-Pitaevskii equation (GPE) [176, 177], a nonlinear Schrödinger field equation commonly employed to describe a BEC at temperatures close to the absolute zero [38]. By explicitly developing the right-hand side terms in (2.63), we obtain the following system of coupled equations

$$\begin{aligned}
i\hbar \frac{\partial \psi_1}{\partial t} &= \sum_j H_{1j}^{(1)} \psi_j + g_s |\boldsymbol{\psi}|^2 \psi_1 + g_a \left[\left(|\boldsymbol{\psi}|^2 - 2|\psi_{-1}|^2 \right) \psi_1 + \psi_{-1}^* \psi_0 \psi_0 \right], \\
i\hbar \frac{\partial \psi_0}{\partial t} &= \sum_j H_{0j}^{(1)} \psi_j + g_s |\boldsymbol{\psi}|^2 \psi_0 + g_a \left[\left(|\boldsymbol{\psi}|^2 - |\psi_0|^2 \right) \psi_0 + \psi_0^* \psi_1 \psi_{-1} \right], \\
i\hbar \frac{\partial \psi_{-1}}{\partial t} &= \sum_j H_{-1j}^{(1)} \psi_j + g_s |\boldsymbol{\psi}|^2 \psi_{-1} + g_a \left[\left(|\boldsymbol{\psi}|^2 - 2|\psi_1|^2 \right) \psi_{-1} + \psi_1^* \psi_0 \psi_0 \right],
\end{aligned} \tag{2.64}$$

which describe the zero-temperature mean-field dynamics of a spin-1 spinor condensate. Here, $H_{ij}^{(1)} = -\frac{\hbar^2 \nabla^2}{2m_a} \delta_{ij} + V_{ij}(\mathbf{r})$. Alternatively, the GPE can be derived from the expression for the time dependence of the field operators in the Heisenberg picture. Indeed, by writing the Heisenberg equation $i\hbar \frac{d}{dt} \hat{\Psi}_j = [\hat{\Psi}_j, \hat{H}^{(F=1)}]$ for the evolution of the fields $\hat{\Psi}_j$ and using the commutation relations for the bosonic operators, one immediately arrives

at equations (2.64) after making the substituion $\hat{\mathbf{\Psi}}(\mathbf{r},t) \to \boldsymbol{\psi}(\mathbf{r},t)$ into the resulting Heisenber equations. In this thesis, we will numerically solve the GPE to compute the dynamics of a Raman-dressed spin-1 spinor gas. In the presence of the dressing, the single-particle terms $H_{ij}^{(1)}$ in equations (2.64) will include the Raman light-shift potentials described in Sec. 2.1.5. We next review the effects of such an inclusion.

Before doing so, an important aspect should be clarified. So far, we have relied on the assumption that ansatz (2.57) is the correct description of the ground state of the condensate, that is, that only one single-particle state is macroscopically occupied. For multicomponent or spinor condensates, however, this may not be the case, and the condensate can be *fragmented* [147]. Depending on the interaction between the different components, the system may favor the occupation of more than one single-particle state, so that the true many-body state reads

$$|\phi\rangle = \prod_m \frac{1}{\sqrt{N_m!}} \hat{b}_m^{\dagger\, N_m} |0\rangle \,, \tag{2.65}$$

with $\sum_m N_m \leq N$ and where $\hat{b}_m^\dagger$ creates a particle in some single-particle state $|\phi_m\rangle = \sum_j \alpha_j^{(m)} \hat{a}_j^\dagger$. The fragmentation of the ground state is often expressed as the number of nonzero eigenvalues λ_i of the one-body density matrix $\rho_{jk}^1 = \langle \hat{a}_j^\dagger \hat{a}_k \rangle$. Clearly, for ansatz (2.57), there is only one nonzero eigenvalue of ρ^1, with $\lambda_0 = N_0$. Its corresponding eigenvector is the order parameter $\phi_0(j)$. In general, though, many eigenmodes $\phi_m(j)$ can have nonzero eigenvalues. Only when $\lambda_m \gg 1$ for all nonzero eigenvalues, we can safely recover the mean-field description and use the GPE to describe the dynamics of the system. This issue regarding fragmentation will be of relevance in chapter 4 and chapter 5, where in certain circumstances the mean-field solutions will need to be cross-checked by the predictions of truncated few-mode quantum models.

2.2.3 The Raman-dressed gas: synthetic spin-orbit coupling

Let us consider now an ultracold $F = 1$ spinor gas dressed by counter-propagating laser beams in a Raman configuration as described in Sec. 2.1.5. At the regimes considered, where the magnetic bias field fulfills $\mathbf{B} \gg \mathbf{B}_{\text{eff}}$, both the kinetic and the interaction energy in the ultracold gas are orders of magnitude smaller than the magnetic shifts of the Zeeman levels. Therefore, the light-shift potentials described in Sec. 2.1 are not modified significantly by the presence of weak interatomic interactions, and we can introduce them straightforwardly to the many-body Hamiltonian (2.50). With this in mimd, let us leave aside, for now, the interacting and the trapping contributions to the Hamiltonian, and focus solely on the dressed single-particle Hamiltonian $\hat{H}^{(1)} = \frac{\hbar^2 \mathbf{k}^2}{2m_a} + \hat{H}'_{\text{eff}}$. Here, $\hat{H}'_{\text{eff}}$ is the vector light-shift potential from equation (2.27) that describes an effective

periodic transverse Zeeman field. Expressed in matrix form, $\hat{H}^{(1)}$ reads

$$\hat{H}^{(1)} = \begin{pmatrix} \frac{\hbar^2\hat{\mathbf{k}}^2}{2m_a} + \delta + \epsilon & \frac{\Omega}{2}e^{i(2k_r\hat{x}+\theta)} & 0 \\ \frac{\Omega}{2}e^{-i(2k_r\hat{x}+\theta)} & \frac{\hbar^2\hat{\mathbf{k}}^2}{2m_a} & \frac{\Omega}{2}e^{i(2k_r\hat{x}+\theta)} \\ 0 & \frac{\Omega}{2}e^{-i(2k_r\hat{x}+\theta)} & \frac{\hbar^2\hat{\mathbf{k}}^2}{2m_a} - \delta + \epsilon \end{pmatrix}, \tag{2.66}$$

where θ is an arbitrary constant phase shift. Remind that δ is the detuning from Raman resonance and ϵ the shift due to the quadratic contribution of the Zeeman effect (see Sec. 2.1.5). Unlike δ, ϵ can only take positive values.

Hamiltonian (2.66) can be written in a position-independent form in a frame that rotates with the effective magnetic field $\hat{H}'_{\text{eff}}$, related to the unrotated frame by the unitary transformation

$$\hat{U}_3 = \exp(-i(2k_r\hat{x} + \theta)\hat{F}_z/\hbar). \tag{2.67}$$

Naturally, such a transformation is position-dependent, and the terms $\exp(2k_r\hat{x})$ do not commute with the momentum operators in the diagonal entries of (2.66). In fact, $\hat{U}_3$ acts as an internal-state- or spin-dependent momentum shift, and we can express the rotated Hamiltonian in terms of the shifted quasimomentum $\hat{\mathbf{q}}$, which fulfills $(\hat{\mathbf{q}} - 2k_r\mathbf{e}_x\hat{F}_z/\hbar)^2 = \exp(-i2k_r\hat{x}\hat{F}_z/\hbar)\hat{\mathbf{k}}^2\exp(i2k_r\hat{x}\hat{F}_z/\hbar)$. The resulting rotated Hamiltonian reads

$$\hat{H}_q^{(1)} = \hat{U}_3\hat{H}_{\text{eff}}\hat{U}_3^\dagger \quad = \begin{pmatrix} \frac{\hbar^2(\hat{\mathbf{q}}-2k_r\mathbf{e}_x)^2}{2m_a} + \delta + \epsilon & \frac{\Omega}{2} & 0 \\ \frac{\Omega}{2} & \frac{\hbar^2\hat{\mathbf{q}}^2}{2m_a} & \frac{\Omega}{2} \\ 0 & \frac{\Omega}{2} & \frac{\hbar^2(\hat{\mathbf{q}}+2k_r\mathbf{e}_x)^2}{2m_a} - \delta + \epsilon \end{pmatrix}. \tag{2.68}$$

In the rotated frame, the kinetic terms in the diagonal entries are shifted in a spin-dependent manner. Observe also that the dressed kinetic Hamiltonian breaks Galilean invariance. Indeed, the terms that result from applying a boost $x \to x - v_0 t$, $q_x \to q_x - m_a v_0/\hbar$ to Hamiltonian (2.68) can not be eliminated by a gauge transformation $\exp(i\frac{m_a v_0}{\hbar}x)$. Instead, an additional Zeeman term proportional to the velocity of the moving frame appears, which reminds the spin-orbit coupling (SOC) interaction that electrons experience in solid-state systems.

At its core, the interaction between internal (spin) and external (orbital) degrees of freedom has a relativistic origin. By taking the non-relativistic limit of the Dirac equation that describes a free electron in an electromagnetic field, the Zeeman interaction $\boldsymbol{\mu}\cdot\mathbf{B} = -\frac{g_s e}{2m_e}\mathbf{S}\cdot\mathbf{B}$ between the spin of the electron $\mathbf{S}$ and a magnetic field $\mathbf{B}$ arises, where e and m_e are the charge and the mass of the electron. In the atom, such an interaction originates the fine-structure splitting discussed in Sec. 2.1.2. There, due to the way electromagnetic fields transform under Lorentz transformations, the electric field created by the nucleus is translated into a velocity-dependent magnetic field in the rest frame of the electrons. This results in a correction to their energy that is proportional to $\mathbf{S}\cdot\mathbf{L}$. Similarly, in a solid, nonzero net static electric fields can originate from inhomogeneities in its structure. When moving, the charged particles experience a magnetic field $\mathbf{B}_{\text{rest}}$ in their rest frame that is proportional to its momentum. At the linear order of the

resulting Zeeman interaction $\mu \cdot \mathbf{B}_{\text{rest}}$, the general expression for the two-dimensional SOC interaction in a solid reads

$$\hat{H}_{\text{SOC}} = \alpha(k_x\sigma_y - k_y\sigma_x) + \beta(k_x\sigma_y + k_y\sigma_x), \tag{2.69}$$

where σ_j are the Pauli matrices. The coefficients α and β are the strengths of the Rashba- [178] and Dresselhaus-type [178] of SOC, respectively. Fundamentally, both kinds of SOC emerge from the breaking of spatial symmetries in the structure of the solid.

SOC plays a fundamental role in many condensed matter phenomena, including the spin-Hall effect [109], topological insulators [110, 111] and topological superconductors [111, 112], and applications such as spintronics [179]. Yet being characteristic of charged matter, SOC does not naturally emerge in experiments with ultracold atoms, which are charge-neutral. However, notice that the dressed Hamiltonian (2.68) does include terms linearly proportional to q_j that describe momentum-dependent Zeeman shifts, similar those appearing in the SOC Hamiltonian (2.69). The direct analogy to the SOC in condensed matter systems is made the most evident if we take $\delta \sim \epsilon \gg \Omega$ in (2.68). In these conditions, the Zeeman state $|F = 1, m = 0\rangle$ is far off-resonantly coupled to highest-energy Zeeman state $|F = 1, m = 1\rangle$, as long as the characteristic kinetic energy in the atomic cloud is also much smaller than ϵ. In the regimes considered, where ϵ is in the order of tens of kHz, such condition is granted in ultracold atomic systems. We can then assume that the state $|F = 1, m = 1\rangle$ will not be significantly populated during the dynamics of the system. With only two relevant internal states, $|F = 1, m = 0\rangle$ and $|F = 1, m = -1\rangle$, the single-particle Hamiltonian effectively reduces to

$$\begin{aligned}\hat{H}_q^{(1)} &\simeq \begin{pmatrix} \frac{\hbar^2(\hat{\mathbf{q}}-k_r\mathbf{e}_x)^2}{2m_a} + \delta'/2 & \frac{\Omega}{2} \\ \frac{\Omega}{2} & \frac{\hbar^2(\hat{\mathbf{q}}+k_r\mathbf{e}_x)^2}{2m_a} - \delta'/2 \end{pmatrix} \\ &= \frac{\hbar^2\hat{\mathbf{q}}^2}{2m_a} - \frac{\hbar^2 k_r}{m_a}\hat{q}_x\sigma_z + \frac{\Omega}{2}\sigma_x + \frac{\tilde{\delta}}{2}\sigma_z + E_r. \end{aligned} \tag{2.70}$$

Here $\tilde{\delta} = \delta - \epsilon$ and $E_r = \frac{\hbar^2 k_r^2}{2m_a}$ is the single-photon recoil energy from the Raman beams. Without loss of generality, we have shifted the origin of the quasimomentum by $-k_r\mathbf{e}_x$ and the energies by $\tilde{\delta}/2$. The Pauli matrices σ_j act on the Zeeman subspace spanned by $|F = 1, m = 0\rangle$ and $|F = 1, m = -1\rangle$. Indeed, Hamiltonian (2.70) is equivalent to the one describing a spin-$\frac{1}{2}$ particle with equal contributions from the Rashba and Dresselhaus SOC interactions ($\alpha = \beta = -\frac{\hbar^2 k_r}{2m_a}$) along the $x - z$ plane. The particle is further subject to an effective transverse magnetic field $\propto \Omega$ that couples the two spin states. Such a coupling is detuned from resonance by a constant Zeeman shift δ' and a momentum-dependent one from the SOC interaction.

The mechanism behind such a synthetic form of spin-orbit coupling in ultracold atoms lies at the nonzero exchange of momentum between the electric field and the atom during the two-photon transitions that couple the Zeeman states. In conventional materials, the single-photon recoil momentums and energies exchanged are negligible,

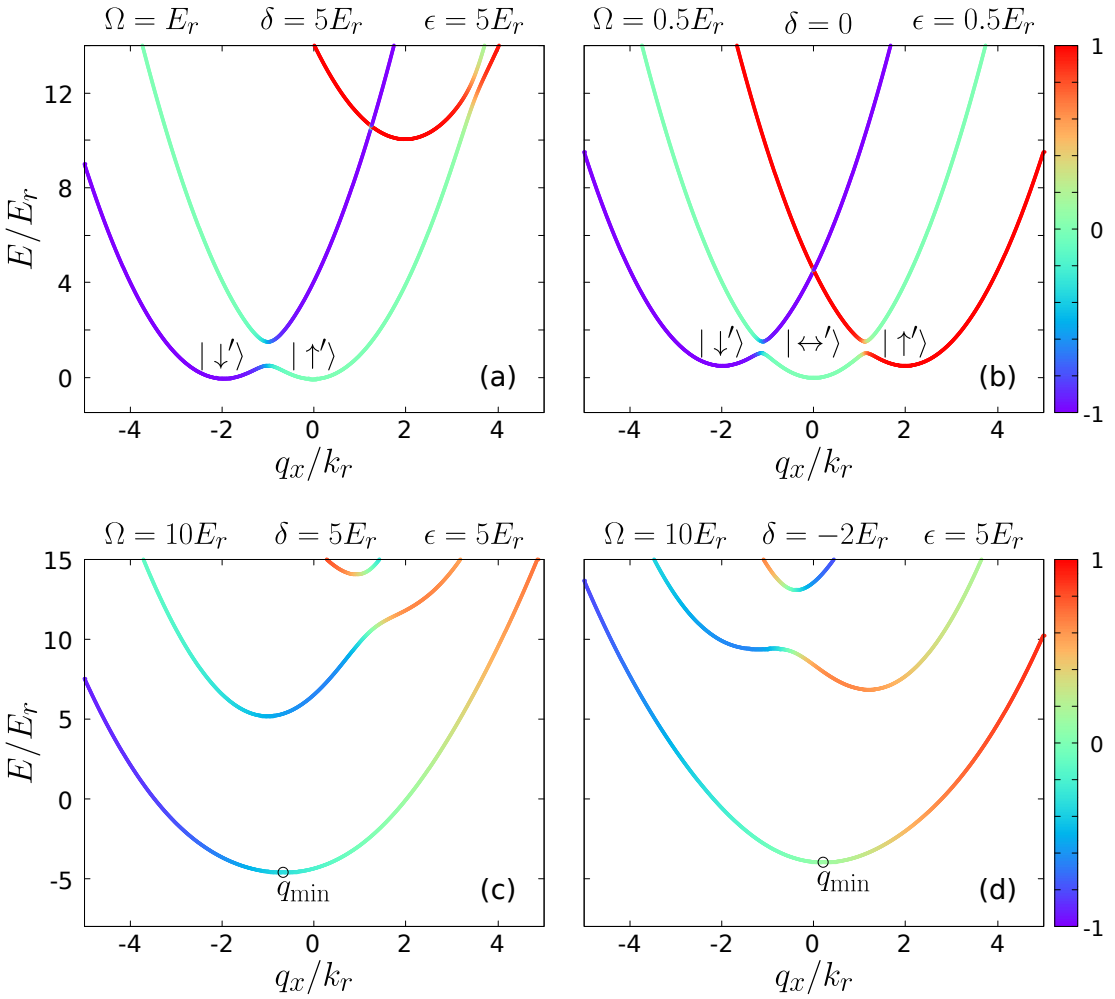

Figure 2.4: Eigenvalues of Hamiltonian (2.68), which describes a free particle in the presence of Raman dressing, as a function of q_x and for different values of the dressing parameters. In all cases we set $q_y = q_z = 0$. The color texture of the bands indicates the mean axial polarization $\langle \hat{F}_z \rangle$ in the corresponding eigenstate.

and so are the derived SOC-like effects. However, in ultracold atoms, with characteristic kinetic energies way below E_r, comparatively strong regimes of SOC can be realized in this way. Remarkably, in the implementation of SOC in ultracold atomic systems, the strengths of both the effective SOC and magnetic interactions in Hamiltonian can be easily tuned to a wide range of parameters. The former can be adjusting with the angle of incidence of the Raman beams, reaching its maximum $|\alpha| = E_r/k_r$ when they are counter-propagating, and the latter can be controlled with the intensity and the detunings of the laser beams. This enhaced tunability offers the possibility to engineer a variety of phenomena in the dressed gas. To illustrate it, we show in Fig. 2.4 the energy bands of the dressed system for various regimes of parameters. The three energy bands are obtained as a funtion of the quasimomentum $\mathbf{q}$ simply by diagonalizing the

translation-invariant Hamiltonian $\hat{H}_q$ in equation (2.68). The dressed bands exhibits interesting properties, such as spin texture, anisotropy or the formation of local minima. The number and position of the minima and the strength of the spin gradients can be adjusted with the dressing parameters Ω, δ and ϵ. Fig. 2.4(a) shows the band in the parameter regime that realizes effective spin-$\frac{1}{2}$ SOC, with $\delta = \epsilon \gg \Omega$, where the lower energy states only populate significantly two spin states $m = 0$ and $m = -1$. For $\Omega < 4E_r$, the lowest band has a characteristic double well shape, with two almost orthogonal dressed spin states $|\uparrow', \downarrow'\rangle$ sitting at each minima. In Fig. 2.4(b), Ω, δ and ϵ are all set smaller than the recoil energy. The band has a triple-well shape and the system describes a spin-1 particle with a generalized spin-1 SOC interaction. Finally, when $\Omega > 4E_r$, the lowest band exhibits only a single minimum. The position of the minimum depends on the values of the dressing parameters, as exemplified by Fig. 2.4(c) and Fig. 2.4(d).

These three scenarios illustrate simple ways by which the same dressed system can realize different physics. For instance, the latter configuration can realize an effective interaction with an electromagnetic field in ultracold atoms. Indeed, with the lowest band minimum shifted to $q_{\min}(\Omega, \delta, \epsilon)\mathbf{e}_x$, the dispersion band around the minimum can be approximated to

$$E(\mathbf{q}) \approx \frac{\hbar^2(\mathbf{q} - \mathbf{A})^2}{2m_a^*}, \tag{2.71}$$

which has the same from of the Hamiltonian describing a charged particle moving in an electromagnetic field, with $\mathbf{A} = A_x e_x^e = \hbar q_{\min}\mathbf{e}_x$ acting as a vector potential and m_a^* being the effective mass of the atoms. Due to the modified shape of the dispersion relation [180], m_a^* deviates from the actual atomic mass. By making the detuning spatially varying, a synthethic magnetic field $\mathbf{B}_{\text{synth}} = \nabla \times \mathbf{A}(\mathbf{r}) \neq 0$ can be realized in this way [181]. In [86], the formation of vortices due to the action of such a synthetic field was observed. Likewise, synthetic electric fields have been achieved by introducing a time dependence to δ so that $\mathbf{E}_{\text{synth}} = \partial\mathbf{A}/\partial t \neq 0$ [182]. Remarkably, the Raman-dressed gas not only exemplifies that phenomena characteristic of charged matter can be simulated with ultracold atoms (for a comprehensive review on the realization of synthetic gauge fields in light-dressed ultracold atoms see [85], and also [183]), but it also provides a platform to engineer effective physics beyond any analog in real condensed matter physics. For example, the realization of SOC in a BEC [104] opened the possibility to study spin-orbit-coupled superfluids with ultracold atoms. Spin-orbit-coupled Bose gases have attracted a significant theoretical [115, 184–198] and experimental attention [107, 108, 116, 118, 199–207] over the last decade. BECs with SOC exhibit many interesting properties that arise from their nontrivial dispersion bands, such as anisotropy in the excitation spectrum and in the sound velocity and roton modes [189, 192, 202, 208, 209]. In a rich interplay with interactomic interactions, synthetic SOC has been shown, for instance, to lead to effective ranged interactions, signalled by the appearance of higher-order partial wave contributions to the scattering distribution [116], and to the stabilization of a *stripe* phase [115, 185, 186, 192, 198], a ferromagnetic-like spin-miscible regime with super-

solid-like properties that have been recently probed [108, 207]. The lack of Galilean invariance was probed in [203], by measuring the response of the SOC gas loaded into a translating optical lattice. The SOC scheme has also been realized in degenerate Fermi gases [105, 106, 117, 210]. where SOC has been shown to modify the pairing properties of strongly-interacting fermions [211]. Moreover, several schemes have been proposed for the realization of two- [187, 188, 191, 194] and three-dimensional SOC [190] in ultracold gases, with the former eventually achieved with both bosonic [204, 206] and fermionic [212] species.

At the same time, this framework generalizes the notion of SOC to spins larger than 1/2 [195, 196]. In chapters 3 to 5, we will focus on the spin-1 spin-orbit-coupled Bose gas in the weakly-coupled regime, where the Hamiltonian exhibits a triple minima in the lowest band (see Fig. 2.4(b)). We will interpret the dressed states located at the vicinity of the minima as spin degrees of freedom, and study the emergence of dressing-enabled two-body spin-mixing collisions [122–124] that couple the three effective spin states $|\uparrow'\rangle|\downarrow'\rangle \longleftrightarrow |\leftrightarrow'\rangle|\leftrightarrow'\rangle$. However, these processes become relevant only very near to resonance, which will require that the three band minima become nearly degenerate. Yet it is clear that, due to the presence of the quadratic Zeeman shift ϵ, a single Raman transition can not resonantly couple both pairs of spin states. Triple degeneracy requires, thus, bringing the quadratic Zeeman shift ϵ to zero, which is incompatible with the requirement of a nonzero magnetic bias field. Alternatively, such a condition can be met if two Raman frequencies $\delta\omega_{-1,0}$ and $\delta\omega_{0,1}$ (from two different pairs of counter-propagating beams) are employed instead [118]. To avoid a large cross-coupling between the two transitions, a relatively large bias field is employed, so that the resonant conditions for the $|F, m = -1\rangle \leftrightarrow |F, m = 0\rangle$ transition, at $\delta\omega_{-1,0} \sim \hbar\omega_z + \epsilon$, and the $|F, m = 0\rangle \leftrightarrow |F, m = 1\rangle$ transition, at $\delta\omega_{0,1} \sim \hbar\omega_z - \epsilon$, are energetically well separated. Keep in mind, though, that by doing so the two characteristic frequencies show up in the time-dependent vector light-shift. By setting both Raman coupling strengths equal, we now have (compare to (2.25))

$$\hat{H}_{\text{eff}} \simeq \frac{\sqrt{2}\Omega}{\hbar}\left(\sin\left(2k_r x + \delta\omega_{-1,0}t\right) + \sin\left(2k_r x + \delta\omega_{0,1}t\right)\right)\hat{F}_x - \omega_{\text{Z}}\hat{F}_z + \frac{\epsilon}{\hbar^2}\hat{F}_z^2. \tag{2.72}$$

As was done in Sec. 2.1.5, following a time-dependent transformation, the fast oscillating terms with frequencies $\pm 2\delta\omega_{-1,0}$, $\pm 2\delta\omega_{0,1}$ and $\pm(\delta\omega_{-1,0} + \delta\omega_{0,1})$ can be eliminated with the RWA. Likewise, by applying the unitary transformation (2.67), the resulting Hamiltonian takes a translationally invariant form

$$\hat{H}_q^{(1)} = \frac{\hbar^2}{2m_a}\left(\hat{\mathbf{q}} - 2k_r\hat{F}_z\mathbf{e}_x\right)^2 + \frac{\Omega}{\sqrt{2}}\hat{F}_x + \delta'\hat{F}_z + \epsilon'\hat{F}_z^2 + \hat{V}(t), \tag{2.73}$$

where

$$\delta' = \frac{\hbar\delta\omega_{-1,0} + \hbar\delta\omega_{0,1}}{2} - \hbar\omega_{\text{Z}}, \text{ and } \quad \epsilon' = \frac{\hbar\delta\omega_{-1,0} - \hbar\delta\omega_{0,1}}{2} - \epsilon, \tag{2.74}$$

Observe, however, that the time dependency of the resulting Hamiltonian is not eliminated entirely, as a cross-coupling contribution $\hat{V}(t)$ remains, which includes slow-oscillating terms with frequencies $\pm\Delta\omega = \pm\frac{1}{2}(\delta\omega_{-1,0} - \delta\omega_{0,1})$. It should be noted that,

near resonance, $\hbar\Delta\omega$ is of the order of ϵ, which can easily be much larger than the recoil energy in the gas. Thus, we expect the effects of such cross-coupling to be small. Its precise effect can be computed from Floquet theory (see [118]), which gives an intensity-dependent shift to the effective quadratic Zeeman strength ϵ'. The cross-coupling could in principle be arbitrarily minimed by increasing the strength of the bias field, and so ϵ. In practice, there is a trade-off between a reduced cross-coupling and an increase in the magnetic fluctuations at larger fields.

In this discussion of the Raman dressed gas, we have intentionally omitted the inclusion of the trapping potential in $H^{(1)}$, and restricted the analysis to the noninteracting regime, so that the Hamiltonian admits a translation-invariant form $H^{(1)}$, where the characteristic free-particle dressed bands illustrate the rich phenomenology of the SOC gas. Following the recipe from Sec. 2.2.1, the dressed and trapped many-body Hamiltonian is straightforwardly obtained in the rotated frame

$$\begin{aligned}\hat{H} = &\int d\mathbf{r}\hat{\mathbf{\Psi}}^\dagger \left(\frac{-\hbar^2(\nabla - 2k_r\hat{F}_z\mathbf{e}_x)^2}{2m_a} + \frac{1}{2}m_a\omega_t^2\mathbf{r}^2 + \frac{\Omega}{\sqrt{2}}\hat{F}_x + \delta'\hat{F}_z + \epsilon'\hat{F}_z^2 + \hat{V}(t) \right) \hat{\mathbf{\Psi}} \\ &+ \int d\mathbf{r} \left(\frac{g_s}{2}(\hat{\mathbf{\Psi}}^\dagger\hat{\mathbf{\Psi}})^2 + \frac{g_a}{2\hbar}\sum_j (\hat{\mathbf{\Psi}}^\dagger\hat{F}_j\hat{\mathbf{\Psi}})^2 \right),\end{aligned} \tag{2.75}$$

where the phase terms from the rotation (2.67) cancel out in all the quartic contributions $\hat{\Psi}_i^\dagger\hat{\Psi}_j^\dagger\hat{\Psi}_k\hat{\Psi}_l$ that show up in the interaction Hamiltonian. In chapters 3 to 5, we will use the two-Raman-dressed and trapped Hamiltonian (2.75) to describe the resonant regimes discussed above. To avoid confusion, several notation choices taken there should be clarified. The parameters ϵ' and δ' in the Hamiltonian will be labelled by ϵ and δ, and often referred to as the detuning and the quadratic Zeeman strength, but they will still refer to the parameters in equation (2.74) appearing in the two-Raman-dressing scheme. Moreover, we will omit the explicit time dependency by just including the corresponding Floquet shifts in the values of ϵ. Similarly, the quasimomentum $\mathbf{q}$ will be labeled as a conventional momentum $\mathbf{k}$. And finally, we will conveniently use the adimentional scaled spin-1 matrices $\hat{F}'_j = \hat{F}_j/\hbar$, which will nonetheless be labelled by unprimed characters.

2.3 Quantum magnetism with ultracold atoms in optical lattices

Ultracold atomic gases loaded in optical lattices, provide an extraordinary platform for simulation of complex condensed matter phenomena in a clean environment [30, 31]. In a nutshell, optical lattices are generated by superimposing pairs of counter-propagating laser beams, which create tunable periodic distributions of intensity out of their interference pattern. As reviewed in Sec. 2.1, atoms in contact with off-resonant light fields can be trapped around maxima or minima of the intensity pattern via the dipole interaction.

In this way, a large variety of periodic potentials may be generated from the spatially modulated light fields , where trapped atoms can bound to the potential minima and behave in a similar fashion to that of electrons in a crystal. There is, however, an immediately apparent caveat to the realization of such synthetic crystals. The lattice spacing attainable with laser-generated lattices are in the order of 10^2 nm, with potential depths below the μK. The characteristic scales are, therefore, many orders of magnitude away from those found in electronic systems. Still, thanks to the astonishing advances in cooling techniques (see the brief discussion in Sec. 2.1.6), temperatures low enough for the dressed atoms to fall trapped to optical potentials became experimentally attainable. Crucially, the synthetic crystal potential from the optical lattice downplays the relative weight of the effective kinetic energy in the ultracold gas, which opens the door to the realization of strongly correlated regimes even with very dilute, weakly-interacting gases. Finally, the high vacuum created in experiments with ultracold atoms, together with the low heating associated with the nondissipative optical dipole trapping interaction, allows for very long coherence times, which can compensate for the drastically reduced energy scales in the simulated models.

Ultracold atoms in optical lattices constitute, therefore, a direct analog simulator of solid-state models, which benefits from an unparalleled scalability and a large degree of tunabilty and addressability, even down to site-resolved manipulations. The depth of the trapping potential and the lattice geometry can both be adjusted with the laser beams. Moreover, different atomic species can be trapped, both bosonic and fermionic, and additional electromagnetic fields can be employed to modify the properties of the trapped atoms. Such unprecedented degree of control has opened new possibilities to realize synthetic systems that can even go beyond mere analogies to those found in conventional condensed matter. In this section we review some basic aspects of ultracold atoms in optical lattices. In Sec. 2.3.1 we start with a brief summary of the fundamental ideas behind the treatment of particles in periodic potentials, and sketch the notion of band structure. In Sec. 2.3.2 we describe the framework employed to treat the many-body problem in the so-called tight-binding regime, where the Hilbert space of the system is truncated to one or few single-particle states per lattice site. Interatomic interactions can then be added perturbatively. In this regime, the system is well described by the Hubbard Hamiltonian, a paradigmatic framework that describes strongly correlated phenomena in solid-state systems. Finally, we introduce the notion of synthetic dimensions in the lattice in Sec. 2.3.3, and how they provide a useful tool to simulate quantum magnetism phenomena with ultracold atoms. We can take as definition of quantum magnetism any quantum spin models. Quantum spin models emerge naturally in the low energy description of strongly-correlated Hubbard model, for instance in the hard-core-boson limit of the Bose Hubbard model. These fundamental notions are later employed in chapter 6.

2.3.1 Ultracold atoms in periodic optical potentials

Let us consider the electric field generated by a pair of counter-propagating light beams. In the simplest scenario, let the two fields be monochromatic, with the same modulus, frequency and polarization, and write $\mathbf{E}_1 = \mathbf{E}_0 \cos(k_l x - \omega_l t)$ and $\mathbf{E}_2 = \mathbf{E}_0 \cos(k_l x + \omega_l t)$. Their superposition forms a stationary wave $\mathbf{E}_l = \mathbf{E}_1 + \mathbf{E}_2 = 2\mathbf{E}_0 \cos(k_l x) \cos(\omega_l t)$. Due to the electric dipole interaction, an atom subject to the field $\mathbf{E}_l$ experiences a light-shift potential $V(x)$ proportional to the intensity and inversely proportional to the detuning from resonance (see Sec. 2.1.4). Dropping a constant term, we can write

$$V(x) = \frac{V_0}{2} \cos(2k_l x), \tag{2.76}$$

where $V_0 \propto -\frac{|\mathbf{d}|^2 |\mathbf{E}_0|^2}{\Delta}$. Here, $|\mathbf{d}|$ and Δ are, respectively, the dipole coupling strenght and the detuning from resonance of the targeted atomic transition.

The potential $V(x)$ is periodic, with periodicity $d = \pi/k_l$. From Bloch's theorem, we know periodicity constraints the form of the eigenfunctions $\psi(x)$ of the atom in the potential, which fulfill

$$\hat{H}\psi(x) = \left(-\frac{\hbar^2}{2m_a} \frac{\partial^2}{\partial x^2} + V(x) \right) \psi(x) = E\psi(x). \tag{2.77}$$

To treat the problem, let us consider a system of finite size Ld, with L minima in the potential. There we can fix the boundary condition $\psi(-Ld/2) = \psi(Ld/2) = 0$ and expand the solutions in the discrete Fourier basis

$$\psi(x) = \sum_k \tilde{\psi}_k \exp(ikx), \tag{2.78}$$

with $k = j\frac{2\pi}{Ld}$, $j \in \mathbb{Z}$. Spatially truncating the potential modifies the expression (2.76) of the potential. However, since we will consider $L \gg 1$, we can neglect the additional Fourier components of $V(x)$ that stem from the truncation and write

$$V(x) \simeq \frac{V_0}{4} \left(e^{i\frac{2\pi}{d}x} + e^{-i\frac{2\pi}{d}x} \right). \tag{2.79}$$

By introducing (2.78) and (2.79) into (2.77), multiplying each side by $e^{-ik'x}$ and integrating over x, we obtain the following relation between the components $\tilde{\psi}'_k$

$$\frac{\hbar^2 k'^2}{2m_a} \tilde{\psi}_{k'} + \frac{V_0}{4} \left(\tilde{\psi}_{k'-\frac{2\pi}{d}} + \tilde{\psi}_{k'+\frac{2\pi}{d}} \right) = E\tilde{\psi}_{k'}, \tag{2.80}$$

for all k'. Equation (2.80) couples the components $\tilde{\psi}_k$ with momenutm k to the set of components $\tilde{\psi}_{k+\Delta k}$ that are shifted in momentum by an amount $\Delta = l\frac{2\pi}{d}$, $l \in \mathbb{Z}$. This allows to identify independent the sets of coupled components by a quasimomentum $-\pi/d \leq q < \pi/d$, an write $\tilde{\psi}_q^{(l)} = \tilde{\psi}_{q+l\frac{2\pi}{d}}$. This has important consequences. The set of

suitable values $q = -\frac{\pi}{d} + j\frac{2\pi}{Ld}$, $j = 0, 1..., L-1$ within the range $[-\pi/d, \pi/d)$, is known as the first Brillouin zone. The energy eigenstates for each set q will be of the form

$$\tilde{\Psi}_{n,q}(x) = e^{iqx} u_{n,q}(x), \tag{2.81}$$

with

$$u_{n,q}(x) = \sum_l \tilde{\psi}^{(l)}_{n,q} e^{il\frac{2\pi}{d}x}. \tag{2.82}$$

Including only Fourier components with momentum $l\frac{2\pi}{d}$, the functions $u_{n,q}$ fulfill $u_{n,q}(x+d)u_{n,q}(x)$. Thus, the solutions of the particle in a periodic potential are given by plane waves with wavevector $k = q$, modulated by a function with the same period as the potential. This is Bloch's theorem, central to the theory of band structure. In principle, l is not bounded, and hence solving the eigenproblem problem requires to solve at each q an infinite set of coupled equations

$$\frac{\hbar^2(q + l\frac{2\pi}{d})^2}{2m_a}\tilde{\psi}^{(l)}_q + \frac{V_0}{4}(\tilde{\psi}^{(l-1)}_q + \tilde{\psi}^{(l+1)}_q) = E\tilde{\psi}^{(l)}_q. \tag{2.83}$$

The kinetic term $\frac{\hbar^2(q+l\frac{2\pi}{d})^2}{2m_a}$, though, diverges as $|l| \to \infty$, and so it is safe to assume that the low energy solutions of (2.83) do not significantly populate components with $|l|$ larger than a certain threshold value $l_{\max}$. In this way, we can obtain the lowest eigenenergies an eigenvectors from a truncated Hamiltonian $\hat{H}^{l_{\max}}$ that includes the $2l_{\max}+1$ lowest momentum states from each set q. The Hamiltonian is block-diagonal, so we can write $\hat{H}^{l_{\max}} = \prod_{\otimes q} \hat{H}^{l_{\max}}_q$, with

$$\hat{H}^{l_{\max}}_q = \sum_{l=-l_{\max}}^{l_{\max}} \frac{\hbar^2(q + l\frac{2\pi}{d})^2}{2m_a}|q,l\rangle\langle q,l| + \sum_{l=-l_{\max}}^{l_{\max}-1} \frac{V_0}{4}\left(|q,l\rangle\langle q,l+1| + |q,l+1\rangle\langle q,l|\right). \tag{2.84}$$

Here $|q,l\rangle$ is the ket representation of the state with momentum $q + l\frac{2\pi}{d}$.

By diagonalizing (2.84), we obtain the truncated expressions for the $2l_{\max}+1$ lowest energy eigenvalues and eigenstates for each quasimomentum q. One can easily check that the M-lowest eigenstates converge quickly as $l_{\max}$ is increased past M. We label the eigenvalues at each q by $E_n(q)$, with $n = 0, 1, 2, ..., l\max+1$ and $E_n > E_m$ for $n > m$. The sets of energies $E_n(q)$ at a given n constitute the n_{th} energy band of the system. In Fig. 2.5, we plot the five lowest energy bands for $L = 50$ and for different values of V_0. We scale the energies to the single-photon recoil energy $E_l = \frac{\hbar^2 k_l^2}{2m_a}$ from the lattice beams. For $V_0 = 0$, the system reduces to a free-particle in a box of size Ld, and the solutions are simply given by the kinetic energies. As V_0 is increased, the free solutions start to hybridize, and an energy gap between the different bands is formed. Notice that, in the limit $L \to \infty$, the discretization size $\frac{2\pi}{Ld}$ of the allowed momenta vanishes, and the bands $E_n(q)$ become continuous functions of the quasimomenutm q. Still, the band gaps are preserved, which means that continuous families of eigenenergies are separated by energy ranges with no solutions.

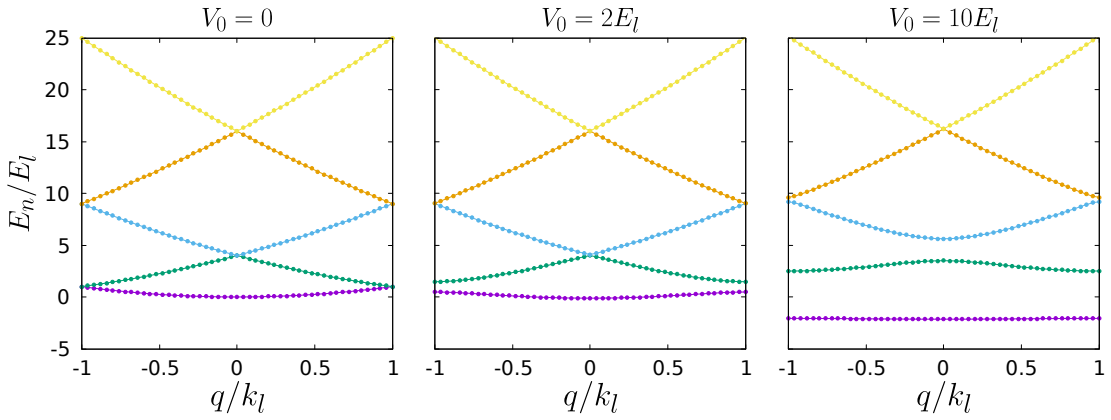

Figure 2.5: Eigenvalues of the lattice Hamitonian (2.84) for $L = 50$ and for different values of the potential depth V_l.

2.3.2 Tight-binding regime: the Bose-Hubbard model

To treat the many-body problem, we use the second-quantization formalism (see Sec. 2.2.1). The noninteracting Hamiltonian can be written as

$$\hat{H}_{\text{n.i.}} = \sum_{q\in \text{BZ}} E_n(q)\tilde{\hat{a}}^\dagger_{n,q}\tilde{\hat{a}}_{n,q}, \tag{2.85}$$

where BZ denotes the first-Brillouin zone, and $\tilde{\hat{a}}_{n,q}$ are the bosonic operators of the Bloch modes. The Bloch functions $\tilde{\Psi}_{n,q}(x) = \langle x|\tilde{\hat{a}}^\dagger_{n,q}|0\rangle$ describe states that are delocalized in position space. To treat the interactomic interactions, which are of local nature in ultracold gases, it is convenient to perform the following rotation into the Wannier basis

$$\hat{a}^\dagger_{n,j} = \frac{1}{\sqrt{L}}\sum_{q\in \text{BZ}} \tilde{\hat{a}}^\dagger_{n,q} e^{-iqx_j}, \tag{2.86}$$

where $x_j = jd$ is the position of the j_{th} minima of the optical potential, or lattice site. We then can write

$$\hat{H}_{\text{n.i.}} = \sum_n \sum_{q\in \text{BZ}} E_n(q)\tilde{\hat{a}}^\dagger_{n,q}\tilde{\hat{a}}_{n,q} = -\sum_{n,i,j} J_n(i-j)\hat{a}^\dagger_{n,i}\hat{a}_{n,j}, \tag{2.87}$$

where

$$J_n(i-j) = -\frac{1}{L}\sum_{q\in \text{BZ}} e^{-iq(x_i-x_j)}E_n(q). \tag{2.88}$$

Observe that coefficients $J_n(i-j)$ are given by the discrete Fourier component $(j-i)d$ of the n_{th} energy band. The zeroth component $J_n(0)$ gives minus the band average energy $\overline{E}_n = \frac{1}{L}\sum_{q\in \text{BZ}} E_n(q)$. The remainder give the tunneling rate between the i_{th} and j_{th} Wannier modes in the n_{th} band, which can be written explicitly in terms of the Wannier wavefunctions $w_{n,j}(x) = \langle x|\hat{a}^\dagger_{n,j}|0\rangle = \frac{1}{\sqrt{L}}\sum_{q\in \text{BZ}} \tilde{\Psi}_{n,q}(x)e^{-iqx_j}$ as

$$J_n(i-j) = -\int dx\, w^*_{n,j}(x)\left(-\frac{\hbar^2}{2m_a}\frac{\partial^2}{\partial x^2} + V(x)\right) w_{n,i}(x). \tag{2.89}$$

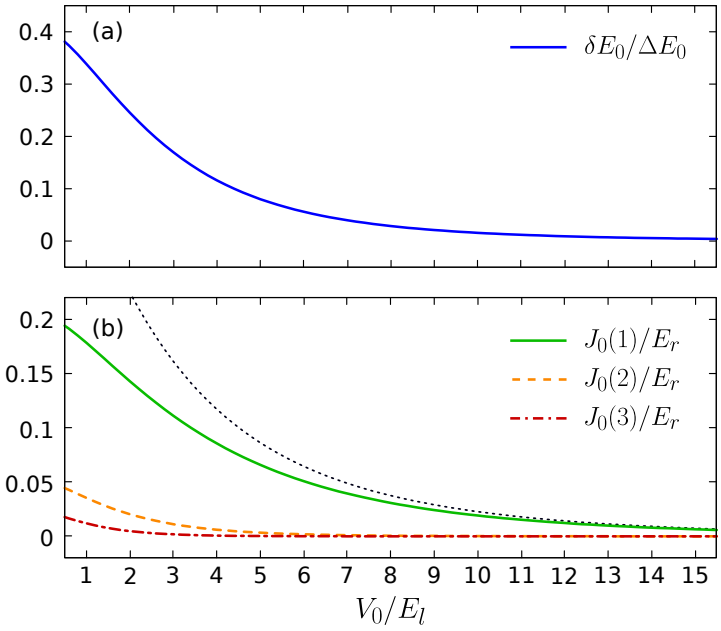

Figure 2.6: (a) Ratio between the bandwidth δE_0 and the mean interband energy ΔE_0 of the lowest band as a function of V_0. (b) Tunneling coefficients $J_0(l)$ with $l = 1$ (green solid line), $l = 2$ (orange dashed line) and $l = 3$ (red dash-dotted line). The black dotted line shows the values of the approximated expression for $J_0(1)$ from equation (2.95).

If the potential $V(x)$ is symmetric, we have $J_n(i-j) = J_n(j-i)$, for any i, j.

As V_0 is increased, the Wannier functions $w_{n,j}(x)$ become increasingly more localized around the minima at x_j, and the coupling coefficients $|J_n(i-j)|$ decay exponentially with the intersite distance $|i-j|$. Hence, we can simplify further the problem by neglecting the longer distance couplings, which is equivalent to neglect the higher Fourier components of the bands. When $V_0 \gg E_r$, we can take the so-called tight-binding approximation, where all Fourier contributions to the band except for the lowest ones, $J_n(0)$ and $J_n(\pm 1)$, are neglected. The modes are then tightly located at their central lattice site, only coupled to the modes centered at the nearest neighbor (NN) sites. In these conditions, the bands are approximated to $E_n(q) \sim -J_n(0) - J_n(1)(e^{iqd} + e^{-iqd}) = \overline{E}_n - \delta E_n \cos(qd)$, where $\delta E_n = 4J_n(1)$ is the bandwidth of the band. For a given V_0, the accuracy of the tight-binding approximation depends on the band index n, being less accurate as n is increased. It can be considered when the interband energies $\Delta E_n = |\overline{E}_{n+1} - \overline{E}_n|$ are very large compared to the intraband energies $|\delta E_n|$.

In this thesis, we will focus on the regime where ΔE_0 is very large compared to both δE_0 and the characteristic energies of trapped ultracold atoms, typically below 1μK. The low energy landscape is then well described by a truncated Hamiltonian that includes

only the lowest band states $w_{0,j}$ in the the tight-binding approximation

$$\hat{H}_{\text{n.i.}} \simeq -\sum_j \left[J_0(1)(\hat{a}^\dagger_{0,j}\hat{a}_{0,j+1} + \text{H.c}) + \overline{E}_0 \hat{n}_{0,j} \right], \tag{2.90}$$

where $\hat{n}_i = \hat{a}^\dagger_i \hat{a}_i$. Roughly, this regime is realized when $V_0 \gtrsim 5E_l$, where the band gap is at least one order of magnitude larger than the bandwidth, as shown in Fig. 2.6(a). The largest tunneling coefficients $J_0(l)$ are shown in Fig. 2.6(b). With these considerations, we introduce now the many-body interactions. In order to preserve the lowest-band truncation, we require the interaction energy per particle to be much smaller than ΔE_0. Henceforth, we will drop the band index $n = 0$ from the labelling of lowest band modes. Likewise we will relabel $J_0(1) \equiv J$ and $\overline{E}_0 \equiv \mu$. Considering s-wave interactions with scattering length a, the interacting Hamiltonian truncated to the lowest band reads

$$\hat{H}_{\text{int}} \simeq \frac{2\pi\hbar^2 a}{m_a} \sum_{ijkl} \int d\mathbf{r} \omega_i^*(\mathbf{r})\omega_j^*(\mathbf{r}')\delta(\mathbf{r}-\mathbf{r}')\omega_k^*(\mathbf{r})\omega_l^*(\mathbf{r}')\hat{a}_i^\dagger \hat{a}_j^\dagger \hat{a}_k \hat{a}_l. \tag{2.91}$$

Despite considering a lowest-band truncation and contact s-wave interactions, the general expression for the interactions is fairly complex and describes a variety of processes. The largest contributions are given by on-site interaction process $\propto \hat{n}_i(\hat{n}_i - 1)$, followed by NN and Next-NN couplings. The latter include density-dependent NN- and Next-NN-tunneling processes $\propto \hat{a}_i^\dagger \hat{a}_i \hat{a}_i^\dagger \hat{a}_j$, density-density NN-interactions $\propto \hat{n}_i \hat{n}_j$ and atom-pair NN-tunnelings $\propto \hat{a}_i^\dagger \hat{a}_i^\dagger \hat{a}_j \hat{a}_j$. However, the relative strengths of these contributions can not be tuned independently from one another. In fact, in the tight-binding regime $V_0 \gtrsim 5E_l$, all the NN contributions are much smaller than the on-site ones and can be safely neglected. Then

$$\hat{H}_{\text{int}} \sim \frac{U}{2} \sum_i \hat{n}_i(\hat{n}_i - 1), \qquad \text{with } U = \frac{4\pi\hbar^2 a}{m_a} \int d\mathbf{r} |\omega_i(\mathbf{r})|^4. \tag{2.92}$$

So far we have considered the simplest scenario of a one-dimensional (1D) periodic potential resulting from the standing wave generated by two counter-propagating beams. By superimposing independent standing waves in different spatial directions, the generalization to two- (2D) and three-dimensional (3D) lattices is straightforward. By adjusting the pairs of beams to have very close frequencies and intensities, square and cubic lattices can be created. Typically, the beams from different standing waves are chosen with mutually orthogonal polarization in order to minimize their interference. At the same time, the beams are also slightly detuned with acousto-optical modulators. In this way, any residual interference oscillates very fast with respect to the time scales of the trapped atoms, and is effectively averaged to zero, while the wavevectors $k_{x,y,z} \simeq k_l$ are not significantly modified [213]. The number of NN in these configurations is given by $2D$, where D is the number of spatial dimensions. To unify the treatment, the summation $\sum_j$ runs over all the sites in the lattice, and the summation over nearest neightbors is indicated with $\sum_{\langle ij \rangle}$, independently of the dimensionality of the lattice. In this way,

ultracold atoms trapped in an optical lattice potential can be described in a compact way by the tight-binding, lowest-band Hamiltonian

$$\hat{H}_{\mathrm{BH}} = -J \sum_{\langle ij \rangle} \hat{a}_i^\dagger \hat{a}_j + \frac{U}{2} \sum_j \hat{a}_j^\dagger \hat{a}_j^\dagger \hat{a}_j \hat{a}_j + \mu \sum_j \hat{n}_j. \tag{2.93}$$

A simple analytical expression for the on-site interaction strength U can be obtained by considering the Taylor expansion of the lattice potential $V(\mathbf{r})$ around site at $\mathbf{r}_j$. In the deep lattice regime ($V_0 \gg E_l$), we can truncate the expansion to second order $V(\mathbf{r}-\mathbf{r}_j) = -\frac{V_0}{2} + \frac{1}{2} m_a \omega_{\mathrm{t.b.}}^2 (\mathbf{r}-\mathbf{r}_j)^2 + O(\mathbf{r}-\mathbf{r}_j)^4$, with $\hbar\omega_{\mathrm{t.b.}} = 2\sqrt{V_0 E_l}$, and approximate the tight-binding modes to harmonic oscillator modes. For the ground state, one finds

$$\frac{U}{E_l} \propto (V_0/E_l)^{D/4}. \tag{2.94}$$

On the other hand, for large $V_0 \gg E_l$ the tunneling coefficients can be approximated to [64]

$$\frac{J}{E_l} \simeq \frac{4}{\sqrt{\pi}} (V_0/E_r)^{3/4} \exp(-2\sqrt{V_0/E_l}), \tag{2.95}$$

as shown in Fig. 2.6(b). Thus, the ratio $U/J \propto (V_0/E_l)^{\frac{D-3}{4}} \exp(2\sqrt{V_0 E_l})$ can be easily tuned by adjusting the depth of the potential, or, equivalently, the intensity of the lattice beams. Essentially, this highlights a fundamental feature of ultracold atoms in optical lattices: the kinetic contribution to the effective Hamiltonian can be almost arbitrarily suppressed, which allows the realization of strongly correlated regimes, granted that the temperatures can be kept sufficiently small.

Hamiltonian (2.93) is the celebrated Hubbard model [214], applied in this case to bosonic species. In solid-state physics, the Hubbard Hamiltonian has been extensively employed to model electron dynamics and magnetic phenomena in strongly correlated electronic systems [215]. The model is able to account, e.g., for the transition between conducting and insulating systems or the superexchange antiferromagnetic coupling. Despite its apparent simplicity, many of its ramifications remain to date an open area of research. In particular, it is believed to be able to give crucial insights on high-temperature superconductivity [216–219]. In bosonic systems, already in its simplest form, the Bose-Hubbard Hamiltonian predicts a quantum phase transition from a superfluid phase (SF) to a Mott insulator (MI) phase [220]. Quantum phase transitions [221] are inherently different from their classical counterparts in that they are not driven by thermal fluctuations. In quantum systems, due to Heisenberg uncertainty relations, fluctuations persist even at zero temperature, and may become relevant enough to induce macroscopic changes in the state of a system when the parameters of the Hamiltonian are modified. As in their classical counterparts, the transitions are signaled by non-analytical changes of some macroscopic quantities in the thermodynamic limit. In the Bose-Hubbard model, the SF-MI transition is driven by the interplay between the kinetic $\propto J$ and the interacting $\propto U$ terms of the Hamiltonian. The former favors the delocalization of the wavefunctions of the atoms across the lattice sites and the formation of

a condensate ground state $|\varphi\rangle_{\mathrm{J}} = \frac{1}{\sqrt{N!}}(\frac{1}{\sqrt{L}}\sum_i \hat{a}_i^\dagger)^N|0\rangle$ that exhibits long-range phase coherence. Contrarily, the latter favors the uniform occupation of each lattice site with a well defined number of atoms $|\varphi\rangle_{\mathrm{U}} = \prod_i \frac{1}{(N/L)!}(\hat{a}_i^\dagger)^{N/L}|0\rangle$. The suppression of the atom number fluctuations implies an increase in the phase fluctuations, and coherence across sites is lost. At the same time, in this regime a nonzero excitation energy gap persists to the thermodynamic limit. The competition between these two contributions defines the transition from a SF regime dominated by atom-number fluctuations to the gapped MI regime dominated by phase fluctuation, which is predicted to occur at a critical value $\frac{1}{2D}(U/J) = 5.8$.

As shown above, the realization of model (2.93) in optical lattices, allows to control the ratio U/J with the laser intensity. Soon after the experimental achievement of Bose-Einstein condensation, the exploration of the SF to MI quantum phase transition with ultracold atoms loaded into optical lattices was proposed [222], and its experimental detection was first achieved a few years later [213]. This landmark achievement exemplified the potential of the platform for the study of strongly correlated phenomena in a controlled environment [29]. Since then, optical lattices have become an staple in ultracold atom experiments with both bosonic and fermionic [66] species, owing their enormous success in great part to the large degree of tunability of the system. For instance, by choosing properly the number of laser beams and their direction of propagation, model (2.93) can be extended to lattices with different geometries [223], including dimerized [224], triangular [56], hexagonal [57], Kagome [58] or Lieb [59] lattices. Moreover, lattice shaking techniques allow to engineer complex tunneling coefficients in the lattice [87, 225, 226], which can lead to topologically non-trivial energy bands [102, 227]. A similar effect can be achieved via laser assisted tunneling in a superlattice [90, 91] or in a tilted lattice [88, 89], where the tilt is achieved with a magnetic gradient. The Peierls phases around a the unit cell of the lattices may add up to a nonzero Aharonov-Bohm phase, which is equivalent to having a synthetic magnetic flux piercing the cells, thus realizing the Harper–Hofstadter model [97]. In combination with triangular geometries, flux lattices offer a potential playground to explore geometric frustration effects in quantum magnetism [228]. The model can be made even richer by accounting for the internal structure of the atomic species, or by loading more than one atomic species. For instance, antiferromagnetic correlations in the Hubbard model were observed in a two-component Fermi gas [229]. Recently, a tunable anisotropic realization of the Heisenberg model was achieved in a two-component bosonic lattice [230]. Also, internal-state-dependent [231] lattice potentials can be generated exploiting the vector light shift instead, as sketched in Sec. 2.1.5. At the same time, the states prepared in optical lattice systems can be accessed with multiple detection techniques. Currently, quantum-gas microscope techniques allows site-resolved measurements of particle densities [232–234] and even spins [235], making the direct measurements of spin-spin correlations possible [12, 14, 236]. We next focus on a particular extension of the Bose-Hubbard model, which is the basis of the results presented in chapter 6, and which exploits the interplay between one-dimensional

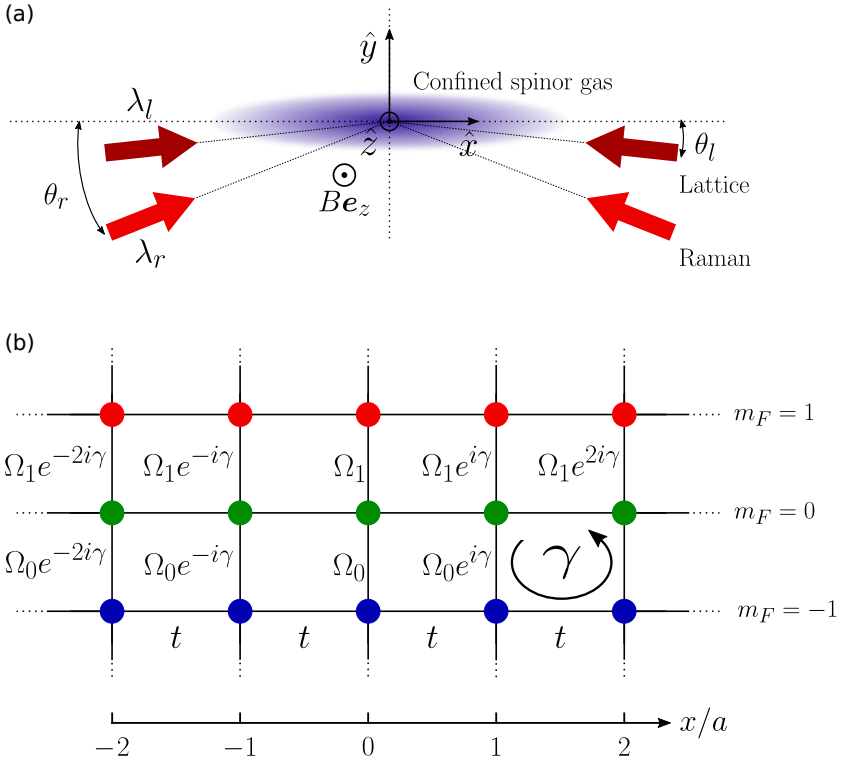

Figure 2.7: Semi-synthetic flux ladders from Raman dressing. (a) Schematic representation of the setup: a confined spinor gas is loaded into an optical lattice, generated by a pair of far-detuned laser beams with wavelength λ_l that intersect with an opening angle θ_l, which results in a lattice spacing $d = \lambda_l/(2\cos\theta_l)$. The gas is further dressed by additional laser beams with wavelength λ_r at an angle θ_r, which couple the internal states of the spinor gas via near-resonant Raman transitions, with an associated recoil momentum $k_r = 2\pi\cos\theta_r/\lambda_r$. The Zeeman levels are energetically separated by means of a perpendicular bias field $B\mathbf{e}_z$. (b) In the tight-binding regime of the gas in the lattice, the Hamiltonian describes a semi-synthetic ladder with an effective magnetic flux $\gamma = 2k_r d = \frac{\lambda_l}{\lambda_r}\frac{\cos\theta_r}{\cos\theta_l}$ piercing each plaquette.

lattice potential and Raman dressing in a spinor gas.

2.3.3 Atomic degrees of freedom as synthetic lattice dimensions: artificial magnetic fields

Let us now consider an ultracold spinor gas loaded in a 1D spin-independent optical lattice, generated with a pair of far-detuned counter-propagating laser beams that intersect with an opening angle θ_l. The lattice is characterized by the laser wavelength λ_l, which defines the lattice spacing $d = \pi/k_l$, with $k_l = 2\pi\cos\theta_l/\lambda_l$. We consider a potential depth V_0 sufficiently deep so as to realize the lowest-band tight-binding regime discussed

in Sec. 2.3.2. Furthermore, we will consider that the gas is dressed by an additional pair of Raman beams, as described in Sec. 2.1.5. We label the wavelength and opening angle of the Raman beams by λ_r and θ_r, respectively, giving an associated Raman recoil momentum $k_r = 2\pi \cos\theta_r/\lambda_r$. Raman dressing generates a helically precessing transverse magnetic field that couples the internal states with a position-dependent phase. The experimental layout is schematically represented in Fig. 2.7(a). If the strength of the couplings between internal states is small compared to the interband separation, the truncation to the lowest-band Wannier basis can be maintained, and the resulting noninteracting Hamiltonian reads

$$H_{\text{n.i.}} = \sum_{j,m} \Big(- J\hat{a}^\dagger_{j+1,m} + \Omega_{m+1} e^{-i\gamma j} \hat{a}^\dagger_{j,m+1} + \frac{1}{2}\Delta_m \hat{a}^\dagger_{j,m} \Big) \hat{a}_{j,m} + \text{H.c.}. \tag{2.96}$$

Here $\hat{a}^\dagger_{j,m}$ and $\hat{a}_{j,m}$ are, respectively, the bosonic creation and annihilation operators for the tight-binding modes at the lattice site j with internal state m. Raman dressing introduces three additional sets of parameters: Ω_m is the Raman coupling strength between the internal states m and $m+1$, Δ_m is an onsite energy shift that accounts for the Raman detuning from resonance, and $\gamma = 2k_r d = 2\pi k_r/k_l$ is the phase that the Raman coupling acquires after a distance of a lattice period d. The strength of the Raman dressing is constrained by the tight-binding consideration.

As first noted in [93], Hamiltonian (2.96) is equivalent to a 2D (quasi 1D) flux ladder. In this interpretation, the internal spin states are regarded as sites along an additional synthetic dimension [92, 237] perpendicular to the physical direction. Due to the spin states being coupled via Raman transitions, the atoms pick up a position-dependent phase $j\gamma$ when hopping along the synthetic dimension. The presence of these phase terms is equivalent to having an effective magnetic field with an Aharonov-Bohm flux of γ that pierces the plaquette of a ladder system, as illustrated in Fig. 2.7(b). The strength of the engineered magnetic flux is adjusted with the ratio between the Raman and the lattice wavevectors $k_r/k_l = \frac{\lambda_l}{\lambda_r}\frac{\cos\theta_r}{\cos\theta_l}$. Flux ladders are the minimal systems capable of exhibiting orbital quantum magnetism phenomena [238, 239], and such an implementation in 1D Raman-dressed lattices, often referred to as semi-synthetic flux ladders, is perhaps the simplest available. Both strong-field and strongly-interacting regimes can be easily achieved in this way, facilitating the exploration of the Hall response in strongly correlated quantum phases [240–242]. Key features of quantum Hall physics have been measured in experimental realizations of the model, both with bosons [94, 96] and fermions [95].

Aside from its simplicity, the main strength of this implementation is that it substantially reduces the heating produced, when compared to the most popular alternatives to realize Aharonov-Bohm phases in optical lattices. In position-space laser assisted tunneling, for instance, the amplitude of the Raman-induced complex tunneling processes is weighted down with the reduced overlap from the neighboring, instead of on-site, Wannier functions. Hence, much larger Raman coupling strengths are required there to

realize the same regimes, which increases the losses from photon scattering. There are, however, some shortcomings in the use of synthetic dimensions. The most evident limitation of the approach is that the extent of the synthetic dimension is restricted by the number of internal states that can be efficiently employed. Engineering periodic boundary conditions along the synthetic dimension is possible [243], for instance, by combining radio-frequency and Raman dressing [188], but is technically more demanding and may result in larger atom loss [244]. Not only the extent of the synthetic dimension, but also the geometry of the ladder realized is constrained by the use of synthetic dimensions. Triangular geometries, for instance, can not be directly implemented. Finally, interatomic interactions are nonlocal along the synthetic dimension, since atoms in different spin states interact locally in the same lattice site. In chapter 6, we will explore an alternative route to partially overcome these limitations. We will show that the semi-synthetic flux ladder model (2.96) in a strong coupling regime can be mapped into a flux ladder with a triangular geometry and on-site interactions [125], where the system is able to host frustrated magnetic phases.

2.4 Note on numerical simulations

All the numerical results shown in this thesis have been obtained by J. Cabedo using free software packages released under a public licence. The exact diagonalization computations shown in chapter 3 to chapter 5 have been obtained using the GSL-GNU Scientific Library [245] package, distributed under the GNU General Public License (GPL). The simulations of the GPE shown in chapter 4 and chapter 5 have used the XMDS2 package [246], also distributed under the GNU GPL. Finally, the density-matrix normalization group calculations shown in chapter 6 have used the ITensor `C++` library [247].

CHAPTER 3

Coherent spin mixing via spin-orbit coupling in Bose gases

In quantum simulation, light dressing, which is the off-resonant coupling of a target set of states to other energetically separated levels by means of electromagnetic fields, can provide a powerful means to manipulate the properties of the resulting *dressed* states. Light dressing is ubiquitous in quantum simulation across the various experimental platforms employed. The interplay between the modified properties of the dressed states and many-body interactions is of particular interest, and can offer attractive possibilities. In this direction, this chapter explores the interplay between Raman dressing and two-body collisions in a spin-1 Bose gas. Raman processes involve a relatively large momentum exchange between the electromagnetic field and the atom. Such exchange results in a momentum dependence of the scattering processes between dressed states which in turn can give rise to nontrivial correlated behavior in momentum space. To gain insights on the properties of these dressed collisions, we study the system at weak Raman coupling, and consider the effect of perturbatively adding interatomic interactions to the noninteracting solutions. To this aim, following a tight-binding approximation in quasi-momentum space, we derive a many-body Hamiltonian in which only three low-energy dressed states are considered. These dressed states act as pseudospin degrees of freedom, and are perturbatively coupled via s-wave scattering processes. The resulting effective spin-spin interacting Hamiltonian shares many properties with the one describing a spinor condensate with spin-changing collisions. Remarkably, in contrast to the intrinsic phenomena, the induced spin-mixing rate can be modified by adjusting the parameters of the Raman dressing. We discuss the properties of the spectrum of the derived Hamiltonian and its experimental signatures. Despite the simplicity of the approach taken, the presented three-state model exemplifies the potential of dressed-state physics as a tool for quantum simulation. Its predictions point out to beyond-mean-field

dynamics that could be observed in existing experimental setups, and be exploited for potential metrological applications.

The chapter is organized as follows. In Sec. 3.1, we briefly review the theoretical and experimental context that embeds the work presented in this chapter. In Sec. 3.2, we describe the Hamiltonian for a spin-1 Bose gas with Raman-induced Rashba-Dresselhaus SOC and introduce a second-quantized form for the weakly-interacting scenario following a lowest-band truncation. In Sec. 3.3, we investigate the system in the weak coupling regime, where the lowest single-particle dispersion band exhibits a triple-well shape. The spin texture in the band gives rise to effective spin-changing collision processes. Within a tight-binding approximation in the lowest band, we show that such processes act as correlated tunneling terms between the bound states. In Sec. 3.4, we explore the properties of the momentum-space tight-binding Hamiltonian. We show that the resulting dynamics of the bound states can be made analogous to that of spin-1 BEC with spin-dependent collisions. In these conditions, the dressed states can undergo coherent mixing induced by nonlinear processes that could be experimentally probed. Finally, we sumarize the conclusions of this chapter in Sec. 3.5, and outline future directions of the work.

3.1 Introduction

Over the last decade, synthetic gauge fields have been experimentally realized in neutral atom systems [84, 85], which provide a highly controllable and tunable platform for quantum many-body simulations [30]. The achievement of BECs with spin-orbit coupling (SOC) by the NIST group [104] gave rise to a huge body of theoretical and experimental research. Such spin-orbit-coupled gases are characterized by parameter-dependent nontrivial single-particle dispersion relations. In an interplay with the interatomic interactions, these yield a rich phase diagram, including a zero-momentum phase, a spin-polarized phase and a spatially modulated phase with supersolid-like properties [108, 186, 192, 248] (for supersolid phases from magnetic interactions see [249–251]). Likewise, the presence of SOC notably affects the dynamics of the gas, with an excitation spectrum exhibiting peculiar features such as anisotropy, suppression of the sound velocity or the emergence of a roton minimum in the plane-wave phase [199, 202, 205, 252]. In the simplest scenario, the engineered SOC consists of equal Rashba [178] and Dresselhaus [253] contributions. This restricted one-dimensional kind of SOC can be achieved by employing an external magnetic field and pairs of counter-propagating laser beams that couple different atomic states in a Raman configuration (see Sec. 2.2.3). More recently, Rashba SOC in 2D BECs [204, 206] and in ultracold Fermi gases [212] was achieved. While most of the research focuses on spin-$\frac{1}{2}$ gases, spin-orbit-coupled BECs with spin larger than 1/2 have been theoretically studied [195, 196] and spin-1 BECs with SOC were attained [118].

While most of the research on SOC gases involve very dilute gases, where the interac-

tions are weak and a mean-field treatment is accurate, many intriguing phenomena appear in the presence of SOC beyond the mean-field regime. This is the case, for instance, in optical lattices where, by downplaying the kinetic terms and enhancing the gas density without further losses, many-body physics at strong coupling may become experimentally accessible [64]. The experimental observation of integer quantum Hall (Hofstadter model on 2D square lattice [88, 89], and on narrow strips [94, 95, 238, 254, 255] in real or synthetic lattices [92, 93, 237]) and spin-Hall (Haldane model in honeycomb-like lattices [102, 227]) effect for noninteracting gases with synthetic gauge fields, the lattice equivalent of SOC, paves the way for the experimental realization of fractional quantum Hall effect and quantum magnetism with interacting gases. Remarkably, beyond-mean-field effects can dominate the dynamics in weakly-interacting dilute gases when mean-field effects largely cancel and lead to the stabilization of quantum droplets [256], as experimentally demonstrated for contact [257–259] and dipolar interactions [260–262].

In this chapter, we will explore a particular regime where beyond-mean-field effects become relevant to the dynamics of a weakly-interacting spin-1 Bose gas with Raman-induced artificial Rashba-Dresselhaus SOC. At weak couplings, the single-particle dispersion relation exhibits a triple-well shaped lowest band. Similarly as done in [263] for the spin-$\frac{1}{2}$ gas, we can consider the well-shaped band to act as a 3-site "lattice" in momentum space by performing a tight-binding approximation. Even in the case of SU(N)-symmetric interactions, we show that, for spin 1 and larger, the SOC-mediated spin dependence of the interactions gives rise to the appearance of correlated tunneling processes involving the tightly-bound lowest-band states, leading to a richer scenario than in the spin-$\frac{1}{2}$ case. It is worth mentioning that synthetic momentum-space lattices can also be obtained via Bragg transitions in a BEC, as proposed in [264] and experimentally realized [265–267] to simulate topological models. As shown in [268], Bose statistics can induce localized interactions in momentum space at the mean-field level. Here, we notice that nontrivial many-body physics in SOC-induced momentum space lattices emerges due to the interplay of contact binary collisions with the spin texture present in the dispersion band of a SOC Bose gas. As we will discuss in Sec. 3.4, the realization of the tight-binding condition in the "momentum-space lattice" can be challenging in an actual experiment with ultracold atoms. Still, we will show that the few particle regime of the model is accessible in state-of-the-art experiments with ultracold atoms, where key experimental signatures of the predicted dynamics, such as a coherent nonlinear spin mixing not captured by the mean-field equations, could in principle be observed in quench dynamics protocols. The model developed in this chapter provides a simple framework to understand such interplay between collisons and synthetic SOC. As we will develop further in chapter 4 and chapter 5, the results presented in this chapter can, under certain conditions, be extrapolated away from the tight-binding regime, with potential applications in metrology and in the study of many-body quantum phase transitions.

3.2 Physical system

3.2.1 Synthetic SOC

We consider a dilute spinor Bose gas subject to an external uniform bias magnetic field that we arbitrarily set along $\mathbf{e}_z$. The gas is further dressed by two pairs of counter-propagating laser beams in a Raman scheme, as realized in [118], that couple the Zeeman sublevels $\{|F, m_F\rangle\}$ of a given hyperfine manifold $F \geq 1$ in the electronic ground state. Here we label the targeted bare or uncoupled hyperfine states, which work as the spin basis, as $|s\rangle$, with $s \in \{-1, 0, 1\}$. We arbitrarily choose the direction of propagation of the dressing beams along $\mathbf{e}_x$. Each two-photon process involves a momentum exchange between the Raman fields and the atoms given by $2\hbar k_r \mathbf{e}_x$, where k_r is the single-photon recoil momentum. As it is usual, we will often compare the energy scales in the system to the single-photon Raman recoil energy, which we label as $E_r = \hbar^2 k_r^2/2m$. Here, m is the mass of the atoms in the gas.

As covered in chapter 2.2.3, the presence of Raman coupling breaks the Galilean invariance of the dressed Hamiltonian by establishing a preferred frame. Still, the kinetic Hamiltonian adopts a translationally invariant and time-independent form in a frame co-rotating and co-moving with the laser fields [195], where it reads

$$\hat{\mathcal{H}}_{\mathrm{k}} = \frac{\hbar^2}{2m}\left(\mathbf{k} - 2k_r \hat{F}_z \mathbf{e}_x\right)^2 + \frac{\Omega}{\sqrt{2}}\hat{F}_x + \delta \hat{F}_z + \epsilon \hat{F}_z^2. \tag{3.1}$$

with $\{\hbar\hat{F}_x, \hbar\hat{F}_y, \hbar\hat{F}_z\}$ being the spin-1 matrices. In Hamiltonian (3.1), the rotating wave approximation is assumed, and the two-photon Rabi frequency of both Raman processes is considered equal and labelled by Ω. Here, δ and ϵ parameterize the relative bare states energy shifts, which can be independently adjusted by controlling the detunings of the Raman lasers, as discussed in detail in Methods from [118]. Hamiltonian (3.1) effectively describes a free spin-1 Bose gas with equal contributions of Rashba and Dresselhaus type of SOC. Notice, though, that in this case the SOC canonical and mechanical momentum of each state $|s\rangle$ differ by $s2\hbar k_r$. The SOC term appearing in (3.1) is given by

$$\hat{\mathcal{H}}_{\mathrm{RD}} = -\gamma \hbar k_x \hat{F}_z, \tag{3.2}$$

with a SOC strength $\gamma = \frac{2\hbar k_r}{m}$. This term gives a linear contribution in k_x to the dispersion relation, in a way that depends on the effective spin of the particle. By construction, the 1D SOC Hamiltonian (3.2) breaks parity symmetry. Instead, it possesses invariance under the simultaneous action of parity and spin-flip operation, which we will refer to as s-parity symmetry. It is worth mentioning that this is not generally the case in artificial SOC, where the coupling between each pair of spin components can be tuned independently to the momentum degree of freedom. For simplicity, we have restricted Hamiltonian (3.1) to the scenario in which Raman momentum transfers and Rabi frequencies are set equal. In this setting, s-parity symmetry is maintained in the whole system by further fixing $\delta = 0$.

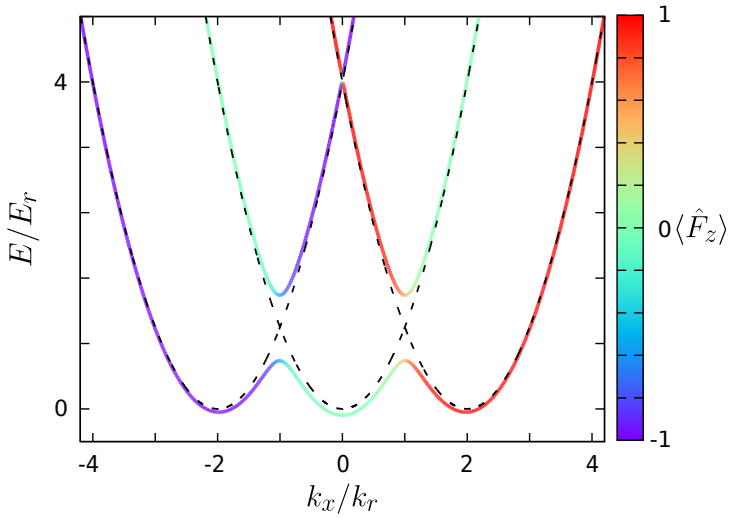

Figure 3.1: Energy bands of the Raman-dressed free gas. Dispersion bands of Hamiltonian (3.1) along the longitudinal direction $\mathbf{e}_x$ for $\Omega = 0.8E_r$, with $\delta = \epsilon = 0$. The color texture represents the expected value of the spin of the dressed states. Dashed lines show the undressed dispersion bands (at $\Omega = 0$).

3.2.2 Momentum-space triple-well band

Along the direction of propagation of the Raman fields, the energy spectrum of Hamiltonian (3.1) is characterized by three dispersion bands, that we denote by $h_0(k_x)$, $h_1(k_x)$ and $h_2(k_x)$. In the weak-coupling regime, where $\Omega < 4E_r$, and near to the two-photon resonance, $\delta, \epsilon \ll E_r$, the bare bands for the different spins hybridize most significantly at the vicinity of the crossings, which are turned into avoided crossings with a gap that increases with Ω. This results in a characteristic triple-well shape of the lowest band of the free Raman-dressed gas, as illustrated in Fig. 3.1.

Furthermore, we consider the spin-orbit-coupled gas to be spatially confined by means of an internal-state-independent potential $\hat{V}_t = \hat{V}_x(z) + \hat{V}_\perp(\mathbf{r}_\perp)$, with $\mathbf{r}_\perp = y\mathbf{e}_y + z\mathbf{e}_z$. We will consider the longitudinal potential to be quadratic in x, that is $\hat{V}_x = \frac{1}{2}m\omega_x^2\hat{x}^2$. In momentum space, the harmonic potential acts as an effective kinetic-like term in the single-particle Hamiltonian, being proportional to the second derivative of the momentum, which prevents the solutions of the system from being well-localized. It will be useful to write the Hamiltonian of the trapped single-particle system, $\hat{\mathcal{H}}_{\text{s.p.}} = \hat{\mathcal{H}}_{\text{k}} + \hat{V}_t$, in the eigenbasis of the homogeneous Hamiltonian (3.1), the so-called dressed basis. Labelling the dressed states as $\{|\varphi_0(\mathbf{k})\rangle, |\varphi_1(\mathbf{k})\rangle, |\varphi_2(\mathbf{k})\rangle\}$, we can write

$$\hat{\mathcal{H}}_{\text{s.p.}}(\mathbf{k}) = \sum_i \left(h_i(k_x) + \frac{\mathbf{k}_\perp^2}{2m} \right) |\varphi_i(\mathbf{k})\rangle \langle \varphi_i(\mathbf{k})| - \frac{1}{2}m\hbar^2\omega_x^2 \hat{\mathrm{U}}^\dagger(k_x) \frac{\partial^2}{\partial k_x^2} \hat{\mathrm{U}}(k_x) + \hat{V}_\perp, \quad (3.3)$$

where $\hat{\mathrm{U}}(k_x) = \sum_{i,j} U_{i-1,j}(k_x) |\varphi_i(\mathbf{k})\rangle \langle \varphi_j(\mathbf{k})|$ is the unitary transformation that relates the dressed basis with the uncoupled hyperfine state basis $\{|s, \mathbf{k}\rangle\}$, with $U_{s,j}(k_x) =$

$\langle s, \mathbf{k}|\varphi_j(\mathbf{k})\rangle$.

In this chapter, we want to explore the regime where the longitudinal part of the spatial potential acts as a perturbation to the free Hamiltonian, in order to preserve the triple-well structure of the effective lowest dispersion band along $\mathbf{e}_x$. Thus, we require that the longitudinal trapping strength is significantly small compared to the energy split between the two lowest bands. In this conditions, a lowest-band approximation can be safely applied: we truncate the single-particle basis to the lowest energy band states $\{|\varphi_0(\mathbf{k})\rangle\}$, neglecting the occupation of higher band states during the dynamics of the system. The lowest band states have at each quasi-momentum $\mathbf{k}$ a bare spin state composition

$$\overrightarrow{s_0}(k_x) = \sum_s U_{s,0}(k_x)\,|s\rangle \tag{3.4}$$

that depends on the strength of the Raman couplings and the detunings. For a state in the lowest band $\overrightarrow{\phi}(\mathbf{k}) = (\phi(\mathbf{k}), 0, 0)^T$, the energy due to the trapping in the $\mathbf{e}_x$ direction is given by

$$\begin{aligned}\left\langle \hat{V}_x \right\rangle_{\overrightarrow{\phi}} &= -\frac{1}{2} m\hbar^2\omega_x^2 \overrightarrow{\phi}^\dagger \hat{\mathrm{U}}^\dagger(k_x) \frac{\partial^2}{\partial k_x^2}\left(\hat{\mathrm{U}}(k_x)\overrightarrow{\phi}\right) \\ &= -\frac{1}{2} m\hbar^2\omega_x^2 \phi^* \left[\frac{\partial^2}{\partial k_x^2} - \left\|\frac{\partial \overrightarrow{s_0}}{\partial k_x}(k_x)\right\|^2\right]\phi. \end{aligned} \tag{3.5}$$

Up to second order in ω_x, the action of the trapping potential on the rotated basis is simply modified by the addition of a correction to the energy of the band states. From equations (3.3) and (3.5) it follows that, in the lowest-band approximation, the single-particle Hamiltonian is reduced to $\hat{\mathcal{H}}_{\text{s.p.}} = \hat{\mathcal{H}}_x + \hat{\mathcal{H}}_\perp$, with

$$\hat{\mathcal{H}}_\perp = \frac{\mathbf{k}_\perp^2}{2m} + \hat{V}_\perp, \tag{3.6}$$

and

$$\hat{\mathcal{H}}_x \simeq h(k_x) - \frac{1}{2} m\hbar^2\omega_x^2 \frac{\partial^2}{\partial k_x^2}. \tag{3.7}$$

Here, $h = h_0 + \frac{1}{2} m\hbar^2\omega_x^2 \left\|\frac{\partial \overrightarrow{s_0}}{\partial k_x}\right\|^2$ is the effective energy band in the dressed and trapped system. Even for relatively strong trapping, as long as the confinement is weak compared to the recoil energy, the deviation from the free-particle band near the minima is negligible, as shown in Fig. 3.2.

3.2.3 Many-body Hamiltonian

So far, we have established the noninteracting framework of the problem. Essentially, the SOC gas at weak Raman coupling strengths presents a many-wells shaped lowest dispersion band with a spin texture that can be adjusted by tuning the parameters of the Raman dressing. Given this momentum-dependence of the spin composition of the

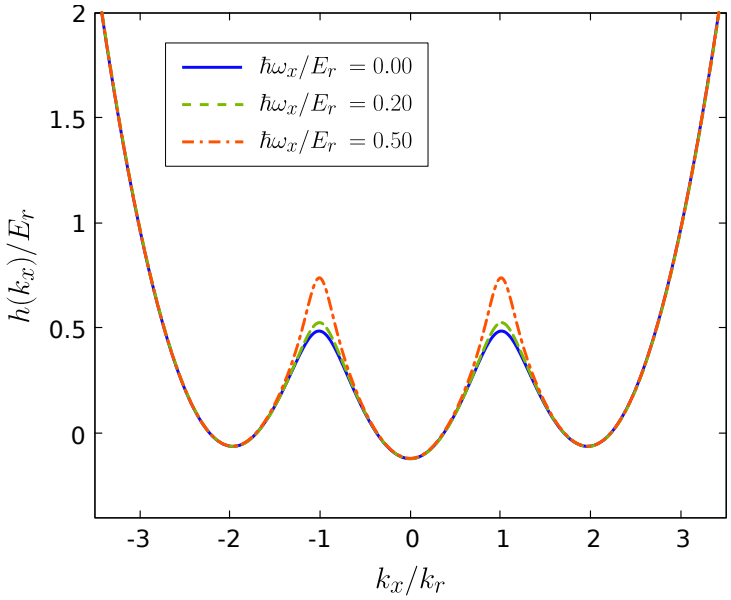

Figure 3.2: Effective lowest energy band. The addition of an external trapping potential modifies the energy of the dressed states. The effective lowest band $h(k_x)$ is plotted for $\hbar\omega_x = 0$ (blue solid line), $\hbar\omega_x = 0.2E_r$ (green dashed line) and $\hbar\omega_x = 0.5E_r$ (red dash-dotted line). In all cases, $\Omega = E_r$, $\delta = \epsilon = 0$. Even for relatively large ω_x, the states in the vicinity of the three minima are only slightly modified.

dressed states, we expect the scattering processes involving these states to have different properties than those of the undressed collisions. To gain insights on such interplay, we now consider the perturbative addition of interatomic interactions on top of the Raman-dressed framework presented.

To this aim, we construct the many-body Hamiltonian following a second quantization approach (see Sec. 2.2.1 for more details). We introduce the corresponding field operators for the band modes $\hat{\varphi}_j(\mathbf{k})$ obeying standard bosonic commutation relations: $\left[\hat{\varphi}_j(\mathbf{k}), \hat{\varphi}_k^\dagger(\mathbf{k}')\right] = \delta(\mathbf{k}-\mathbf{k}')\delta_{j,k}$, and write

$$\hat{H} = \hat{H}_{\text{n.i.}} + \hat{H}_{\text{int}}, \tag{3.8}$$

where $\hat{H}_{\text{n.i.}}$ and $\hat{H}_{\text{int}}$ stand for its noninteracting and interacting contributions, respectively. In the lowest-band approximation, the former is simply given by

$$\hat{H}_{\text{n.i.}} \simeq \int d\mathbf{k}\hat{\varphi}_0^\dagger(\mathbf{k})\hat{\mathcal{H}}_{\text{s.p.}}\hat{\varphi}_0(\mathbf{k}). \tag{3.9}$$

At low energies, the interacting Hamiltonian is obtained from the two-body interaction model [269]. Within the $F = 1$ manifold, such a Hamiltonian can be generally split into a SU(3)-symmetric and a non-symmetric contribution. For simplicity, in this chapter we will consider only the former. Qualitatively, this allows us to focus on the

phenomena that emerges directly from the interplay between two-body collisions and SOC in isolation. Quantitatively, the truncation can be justified in many situations. Very often, the symmetric contribution is much stronger than the non-symmetric one, as is the case, for instance, of ^{87}Rb [270], and the latter can be treated as a perturbation. Consistently to perturbation theory, the total spin-dependent collisions are then given by the sum of the intrinsic ones and the SOC-induced ones. As we will discuss in Sec. 3.4.3, the latter can be much larger than the former in the regimes we will consider.

Therefore, we characterize collisions simply by a single spin-independent parameter $g = 4\pi\hbar^2(a_0 + 2a_2)/3m$, where a_0 and a_2 are the scattering lengths in the $F = 0$ and $F = 2$ channels, respectively, and derive the the effective spin-dependent collisions that emerge from SOC. In this way, expressed in the bare-state basis, the interaction Hamiltonian is given by

$$\left\langle s_1, \mathbf{k}; s_2, \mathbf{k}' \right| \hat{\mathcal{H}}_{int} \left| s_3, \mathbf{k}''; s_4, \mathbf{k}''' \right\rangle = \frac{g}{2(2\pi\hbar)^3} \delta_{s_1,s_4} \delta_{s_2,s_3} \delta(\mathbf{k} + \mathbf{k}' - \mathbf{k}'' - \mathbf{k}'''), \tag{3.10}$$

resulting in the following second-quantized form

$$\hat{H}_{\text{int}} = \frac{g}{2(2\pi\hbar)^3} \sum_{s_1,s_2} \int d\mathbf{k} d\mathbf{k}' d\mathbf{q} \left(\hat{a}^\dagger_{s_1}(\mathbf{k} - \mathbf{q}) \hat{a}^\dagger_{s_2}(\mathbf{k}' + \mathbf{q}) \hat{a}_{s_2}(\mathbf{k}') \hat{a}_{s_1}(\mathbf{k}) \right), \tag{3.11}$$

where $\hat{a}_s(\mathbf{k})^\dagger$, $\hat{a}_s(\mathbf{k})$ are the creation and annihilation operators for the mode $|s, \mathbf{k}\rangle$, respectively. As long as the interaction energy per particle in the many-body system is small compared to the gap to the excited band states, the lowest-band approximation can be maintained. For the states located in the vicinity of the band minima, we require that

$$gn \ll 4E_r, \tag{3.12}$$

which is easily fulfilled in dilute ultracold Bose gases.

In this situation, we can truncate the expression of $\hat{a}_s(\mathbf{k})$ to the lowest band

$$\hat{a}_s(\mathbf{k}) = \sum_j U_{s,j}(k_x) \hat{\varphi}_j(\mathbf{k}) \simeq U_{s,0}(k_x) \hat{\varphi}_0(\mathbf{k}). \tag{3.13}$$

Finally, after inserting this approximation into (3.11) we obtain

$$\hat{H}_{\text{int}} \simeq \frac{g}{2(2\pi\hbar)^3} \int d\mathbf{k} d\mathbf{k}' d\mathbf{q} \left(\hat{\varphi}^\dagger_0(\mathbf{k} - \mathbf{q}) \hat{\varphi}^\dagger_0(\mathbf{k}' + \mathbf{q}) \hat{\varphi}_0(\mathbf{k}') \hat{\varphi}_0(\mathbf{k}) f(k_x, q_x) f(k'_x, -q_x) \right), \tag{3.14}$$

with

$$f(k_x, q_x) = \sum_s U^*_{s,0}(k_x - q_x) U_{s,0}(k_x) = \overrightarrow{s_0}(k_x - q_x) \cdot \overrightarrow{s_0}(k_x). \tag{3.15}$$

Hamiltonian (3.14) describes the scattering processes that take place between the dressed states of the lowest single-particle band. The role of SOC is immediately apparent in the expression. Despite assuming spin-symmetric interactions, notice that each

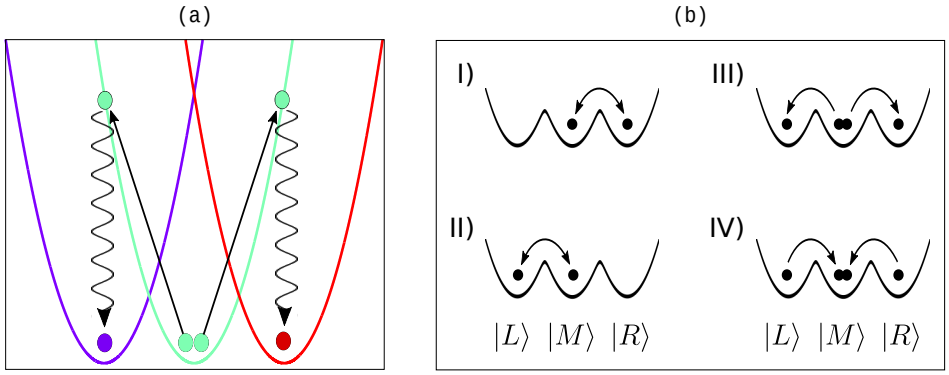

Figure 3.3: Emergence of spin-changing collisions in presence of SOC. (a) Schematic representation of a resonant collision process that couples different spin states mediated by Raman transitions (represented in wavy lines). (b) Schematic representation of the spin-changing collision processes that couple the many-body states in the Fock space spanned by the tight-binding well-states basis $|L\rangle$, $|M\rangle$ and $|R\rangle$ (see Sec. 3.3). These processes act as effective correlated tunneling processes between the bound states of the band wells.

scattering process $(\mathbf{k}, \mathbf{k}') \to (\mathbf{k} - \mathbf{q}, \mathbf{k}' + \mathbf{q})$ in the lowest band is now weighted by the overlaps of the spin states $\overrightarrow{s_0}$ of the initial and final states involved. Near the band minima, the spin overlaps decrease fast with its quasimomentum separation, which yields a certain degree of localization of the interactions in quasimomentum space. This feature is remarkable, as it directly allows to drive correlated behavior in momentum space, while otherwise totally delocalized interactions could not [265]. A similar phenomenon was exploited in [116] to create effective interactions with higher-order partial waves at low energies.

We now focus our attention in the collision processes that involve the dressed states located at the vicinity of the three band minima. While smaller, the spin overlap between states located around the different minima is nonzero. This enables resonant two-body collisions that exchange large momentum at low energies. At the same time, the particles exchange spin in the process, which is mediated by Raman photon pairs. A schematic representation of such effective spin-changing collisions is shown in Fig. 3.3(a).

Since we consider weak Raman coupling, these spin-changing scattering processes have a small amplitude that is proportional to Ω^2. Nonetheless, in the remainder of the chapter we will show that these processes can dominate the dynamics in a regime where we can apply a momentum space tight-binding approximation. In analogy to the usual treatment in position-space many-wells configurations, we will take into account only the lowest energy states of each well of the band, and interpret the collision processes depicted in Fig. 3.3(b) as a form of atom-pair tunneling processes [271] in a 3-site Hubbard model. We will see that these *well states* can be interpreted as an effective spin degree of freedom with tunable spin-mixing interactions. Relevantly, spin-mixing processes in ultracold

spinor gases have been extensively studied, with special attention to its potential for generating many-body entanglement [272–285]. The tight-binding model we develop in the next section provides a simple framework to explore further the connection between spin-orbit-coupled gases and spinor gases with spin-changing collisions [286–290].

3.3 Tight-binding approximation

The many-well lowest dispersion band of weakly-coupled Raman-dressed gases easily invites the interpretation of the low-energy physics of the system as a peculiar kind of *momentum-space optical lattice* system. To go a step further in this picture, we now account for the interatomic interactions following a tight-binding approximation, in the same fashion as done for regular Hubbard models. Essentially, we will assume that the single-particle contributions to Hamiltonian (3.8) dominate. We can then treat the interaction Hamiltonian as a perturbation to the noninteracting system, and describe the low-energy scenario within the Fock space spanned by the lowest single-particle energy states, as long as the energy per particle is significantly smaller than the energy separation between such states and the next lowest family of energy eigenstates.

This simple approach will allow us to work with a drastically reduced Hilbert space without requiring the usual mean-field treatment of the system. However, such truncation comes at a price. Keep in mind that in momentum space the role of the trapping potential is reversed: to have a set of eigenstates that are well localized at the vicinity of each band minimum and that are well separated from the remainder of the single-particle eigenstates, the trapping strength is required to be small. Yet the energy separation between this lowest set of eigenstates and the next is still linearly proportional to the trapping frequency ω_x, which can make an actual realization of a momentum space tight-binding regime challenging. We will discuss its potential realization further in the next section, and assume for now the validity of the approach.

In the weak longitudinal-trapping regime, the wavefunctions of the lowest three eigenstates of Hamiltonian (3.7) can be written as superpositions of three states localized at the vicinity of a minimum of the wells in the band. In the tight-binding approximation, we truncate the Hilbert space to just one single-particle state per site, the so-called well states, with wavefunction $\psi_i(\mathbf{p})$. Here, $i \in \{-1, 0, 1\}$, which correspond to the left-, middle- and right-well states respectively. The transverse part of the wavefunction is spin independent, so it is useful to write $\psi_i(\mathbf{p}) = \phi_i(p_x)\phi_\perp(\mathbf{p}_\perp)$. The function $\phi_i(p_x)$ is centered around the corresponding minima at $p_x = p_i$, with $p_{\pm 1} \sim \pm 2\hbar k_r$ and $p_0 = 0$. Under these considerations, we can treat many-body problem by truncating the lowest band field operator to

$$\hat{\varphi}_0(\mathbf{p}) \sim \psi_{-1}(\mathbf{p})\hat{b}_{-1} + \psi_0(\mathbf{p})\hat{b}_0 + \psi_1(\mathbf{p})\hat{b}_1, \tag{3.16}$$

where $\hat{b}_i$ is the bosonic annihilation operator for the i^{th} well-state, and substituting the expression into equations (3.9) and (3.14) for the second-quantized form of the lowest

band Hamiltonian.

Naturally, the tight-binding truncation assumes that the energy splitting between the lowest and next-lowest on-site eigenstates is sufficiently large compared to the energy per particle. This imposes a much stricter upper limit on the density of the gas in the trap. At low energies and small Ω, such splitting can be approximated to $\hbar\omega_x$, since the dispersion is close to being quadratic at the vicinity of the minima at each well. Therefore we require

$$gn \ll \hbar\omega_x \ll E_r. \tag{3.17}$$

In section 3.4.2 we discuss its experimental viability. Henceforth, we will assume that condition (3.17) holds.

With this simplification, the noninteracting contribution to the truncated Hamiltonian in this low-energy description from (3.9) reduces to

$$\hat{H}_{\text{n.i.}} \simeq \sum_i \epsilon_i \hat{N}_i - \frac{1}{2}\sum_{\langle i,j\rangle} J_{ij}\hat{b}_i^\dagger \hat{b}_j, \tag{3.18}$$

with

$$J_{ij} = -2\int dk_x \phi_j^*(k_x)\hat{\mathcal{H}}_x\phi_i(k_x), \tag{3.19}$$

$$\epsilon_i = \int d\mathbf{k}\psi_i^*(\mathbf{k})\hat{\mathcal{H}}_{\text{s.p.}}\psi_i(\mathbf{k}), \tag{3.20}$$

$$\hat{N}_i = \hat{b}_i^\dagger \hat{b}_i, \tag{3.21}$$

and where $\langle i,j\rangle$ stands for the summation on nearest neighbors.

Likewise, by substituting the truncated field operator (3.16) into (3.14), we obtain

$$\hat{H}_{\text{int}} \simeq \sum_{i,j,k,l} U_{ijkl}\hat{b}_i^\dagger \hat{b}_j^\dagger \hat{b}_k \hat{b}_l, \tag{3.22}$$

where the interacting coefficients U_{ijkl} are given by

$$U_{ijkl} = \frac{g}{2(2\pi\hbar)}\int d\mathbf{r}_\perp \left|\tilde{\phi}_\perp(\mathbf{r}_\perp)\right|^4 \int dq_x G_{il}(q_x)G_{jk}(-q_x), \tag{3.23}$$

with

$$G_{ab}(q) = \int dk_x \phi_a^*(k_x - q_x)\phi_b(k_x)f(k_x, q_x). \tag{3.24}$$

Here, $\tilde{\phi}_\perp$ is the inverse Fourier transform of the transverse mode $\phi_\perp$. It is easy to show that $G_{ab}(q) = G_{ba}(-q)$ for every index a, b, and hence

$$U_{ijkl} = U_{jilk} = U_{klij} = U_{lkji}, \quad \text{for all } i,j,k,l. \tag{3.25}$$

Furthermore from s-parity symmetry it follows

$$U_{ijkl} = U_{(-l)jk(-i)} = U_{i(-k)(-j)l} = U_{(-j)(-i)(-l)(-k)}. \tag{3.26}$$

Condition (3.17) implies that we can treat the interactions as a perturbation to the truncated noninteracting Hamiltonian and so the wave packets $\phi_i(k_x)$ will not not deviate significantly from the single-particle solutions. For weak longitudinal confinement, we can regard the momentum potential as harmonic and approximate such single-particle solutions with Gaussians of width $\sigma_x \simeq \sqrt{\frac{m\omega_x}{2\hbar}}$. With this approximation, from (3.23) and (3.24) it follows that, for $\sigma_x/k_r \ll 1$

$$U_{ijkl} \approx C_{ijkl}(\Omega) U_0 e^{-\left(\frac{k_i+k_j-k_k-k_l}{4\sigma_x}\right)^2}, \tag{3.27}$$

with

$$C_{ijkl}(\Omega) = \left(\overrightarrow{s_0}(k_i)\cdot\overrightarrow{s_0}(k_l)\right)\left(\overrightarrow{s_0}(k_j)\cdot\overrightarrow{s_0}(k_k)\right), \tag{3.28}$$

and

$$U_0 = \frac{g\langle n\rangle}{2N}. \tag{3.29}$$

Here, the coefficient $\langle n\rangle$ is the average density in the gas. Hence, as the longitudinal trapping frequency ω_x is made smaller, most coupling coefficients U_{ijkl} decrease exponentially, while those relating modes $\{\phi_i, \phi_j\}$ with $\{\phi_{i-k}, \phi_{j+k}\}$, being $|k| \in \{0, 1, 2\}$, decrease linearly. This is a direct consequence of the momentum conservation of the contact s-wave scattering processes we consider (3.10). Therefore, there always exist a certain regime for ω_x for which Hamiltonian (3.22) can be safely truncated to the much simpler form

$$\hat{H}_{\text{int}} \simeq \hat{H}^{(0)}_{\text{int}} + \sum_{i=0}^{1}\sum_{j=-1}^{0} 2U^{(1)}_{ij}\hat{b}^\dagger_{i-1}\hat{b}^\dagger_{j+1}\hat{b}_i\hat{b}_j + 2U^{(2)}_{1,-1}\hat{b}^\dagger_1\hat{b}^\dagger_{-1}\hat{b}_1\hat{b}_{-1} \tag{3.30}$$

with

$$\hat{H}^{(0)}_{\text{int}} := \sum_{i,j} U^{(0)}_{ij}\hat{b}^\dagger_i\hat{b}^\dagger_j\hat{b}_i\hat{b}_j, \tag{3.31}$$

$$U^{(k)}_{ij} := U_{(i-k)(j+k)ji}. \tag{3.32}$$

Fig. 3.4(a) illustrates the dependence of the truncation leading to expression (3.30) ω_x. It shows the ratio between the largest neglected coefficients $U_{(i\pm1)jji}$ and $U^{(1)}_{kl}$. The contributions proportional to the former can be interpreted as density-dependent tunneling-like processes. We can roughly say that the truncation is safe when $\omega_x \ll E_r$.

The factors $C_{ijkl}(\Omega)$ depend on the spin mixture of the band states around the minima. Specifically, on the spin projection of each pair of initial and final well states (see eq. (3.28)), which decreases fast with their inter-well distances $|i-l|$ and $|j-k|$. Notice that the process involving next-nearest neighbors, weighted by $U^{(2)}_{1,-1}$, is of fourth-order (corresponding to a four-photon process), and therefore scale as Ω^4. By contrast the two-photon nearest-neighbors processes scale quadratically, with $U^{(1)}_{i,j} \propto \Omega^2$. Finally, the main contribution to the on-site interaction is not mediated by Raman processes

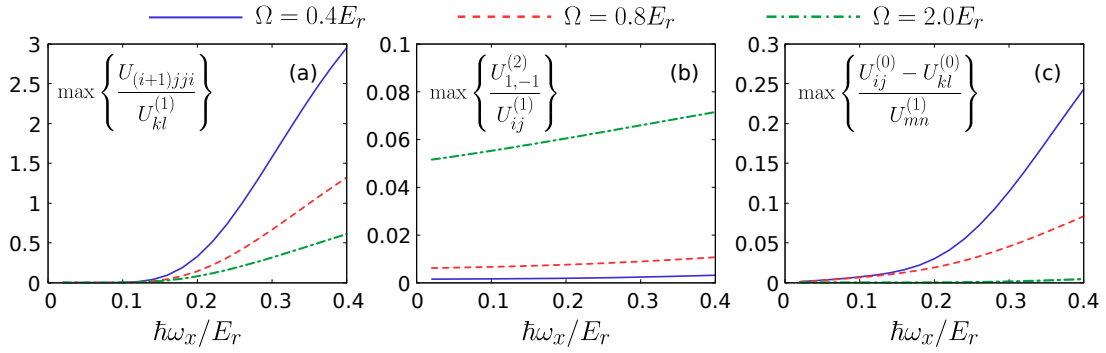

Figure 3.4: Parameters of the tight-binding interaction Hamiltonian. (a) Maximum value of the ratio between the coefficients $U_{(i+1)jji}$ and $U^{(1)}_{kl}$, for any i, j, k, l, as a function of the longitudinal trapping strength ω_x, and for $\Omega = 0.4$ (blue solid line), $\Omega = 0.4$ (red dashed line) and $\Omega = 0.4$ (green dash-dotted line). (b) Maximum value of the ratio between $U^{(2)}_{1,-1}$ and the second order interaction coefficients $U^{(1)}_{ij}$, for any i, j. (c) Maximum value of the ratio between the difference $U^{(0)}_{i,j}$ and $U^{(1)}_{ij}$, for any i, j. In all cases, the coefficients are computed using (3.27), which considers gaussian modes $\phi_i(k_x)$ with standard deviation $\sigma_x = \sqrt{m\omega_x/2\hbar}$.

and hence is of zero-order with respect to Ω. With the three kind of processes scaling differently, we can easily tune the ratio between the different coefficients. In particular, by lowering Ω, the ratio $U^{(2)}_{1,-1}/U^{(1)}_{i,j}$ can be made arbitrarily small, while maintaining the energy gap between the two lowest dispersion bands, which scales linearly. It is worth mentioning that such ratio depends weakly on the trapping frequency (see Fig. 3.4(b)).

Finally, the Hamiltonian can be further simplified by dropping the contributions $O(\Omega)$ to the zeroth order processes. These contributions decrease fast with ω_x and the ratio $U^{(0)}_{ij}/U^{(0)}_{kl}$ approaches 1 as $\hbar\omega_x/E_r$ approaches 0, for all indices i, j, k, l. All such terms can then be added up to a single contribution that depends only on the total number of particles, N

$$\hat{H}^{(0)}_{\text{int}} \overset{\omega_x \to 0}{\longrightarrow} U_0 \hat{N}(\hat{N} - 1), \tag{3.33}$$

which does not affect the dynamics of the isolated system. This substitution can be safely done when the next-leading terms proportional to $U^{(1)}_{i,j}$ are large in comparison to the corrections $O(\Omega)$, which is the case $\omega_x \ll E_r$, as shown in Fig. 3.4(c).

Dropping the term in (3.33) from (3.30) and taking into account equalities (3.25) and (3.26), the total Hamiltonian in the tight-binding approximation can be approximated to

$$\hat{H}_{t.b.} = \hat{H}_{\text{n.i.}} + \hat{H}_{\text{int}} \simeq \hat{H}_1 + \hat{H}_2 + \hat{J}, \tag{3.34}$$

with

$$\hat{H}_1 := U_1\Big[\hat{b}_L^\dagger\hat{b}_R^\dagger\hat{b}_M\hat{b}_M + \hat{b}_L\hat{b}_R\hat{b}_M^\dagger\hat{b}_M^\dagger + \hat{N}_R\hat{N}_M + \hat{N}_M\hat{N}_L\Big] - \tilde{\epsilon}\hat{N}_M \tag{3.35}$$

$$\hat{H}_2 := U_2\hat{N}_L\hat{N}_R, \tag{3.36}$$

$$\hat{J} := -\frac{J}{2}\left(\hat{b}_R^\dagger\hat{b}_M + \hat{b}_L^\dagger\hat{b}_M + \hat{b}_R\hat{b}_M^\dagger + \hat{b}_L\hat{b}_M^\dagger\right). \tag{3.37}$$

Here, to simplify the notation we have conveniently relabelled the left, middle and right well modes by identifiying $\left\{\hat{b}_{-1},\hat{b}_0,\hat{b}_1\right\}$ with $\left\{\hat{b}_L,\hat{b}_M,\hat{b}_R\right\}$. Furthermore, at $\delta = 0$, due to s-parity symmetry we have $U_{RM}^{(1)} = U_{LM}^{(1)} = U_{MM}^{(1)} = U_{RL}^{(1)} := U_1/2$ (see (3.32)), $J_{RM} = J_{LM} := J$ and $\epsilon_L = \epsilon_R$ (see (3.19) and (3.20)). Then, the linear term in N in (3.9) reduces to an energy offset for the central well that we parameterize with $\tilde{\epsilon} = (\epsilon_R + \epsilon_M)/2 - \epsilon_M$. We conveniently incorporate such term into $\hat{H}_1$, despite being of noninteracting origin. For convenience, the coefficient $2U_{RL}^{(2)}$ is relabelled as U_2. The operator $\hat{J}$ can be interpreted as a trapping-mediated tunneling, while $\hat{H}_1$ and $\hat{H}_2$ are the effective nearest neighbors and next-nearest neighbors interaction operators, respectively.

In this way, Hamiltonian (3.34) is a good description as long as condition (3.17) is fulfilled. Observe that the operator $\hat{H}_1$ naturally includes correlated tunneling terms proportional to $\hat{b}_L^\dagger\hat{b}_R^\dagger\hat{b}_M\hat{b}_M$ + H.c. that couple the central well mode with the left and right modes. Remarkably, these are the leading order interaction terms in the tight-binding Hamiltonian (3.34). Their presence, therefore, yield an extended Hubbard model in quasimomentum space that is richer than its position-space counterpart. Note that these terms involves more than two modes simultaneously, and thus cannot occur in the most explored spin-$\frac{1}{2}$ scenario [263]. This fundamental difference motivates the study here of the properties of the spin-1 system.

3.4 Properties of the tight-binding Hamiltonian

We now explore the properties of the tight-binding Hamiltonian (3.34) derived in the previous section, which is characterized by the presence of correlated tunneling terms that involve the bound states of the triple-well *momentum-space potential*.

3.4.1 Spectral properties of $\hat{H}_{t.b.}$

We consider first the case $J/U_1 \ll 1$. Such condition occurs at sufficiently small ω_x, since U_1 and U_2 are linear in the standard deviation σ_x (see eqs. (3.27)-(3.29)) and thus proportional to $\omega_x^{1/2}$ for $\omega_x \to 0$, while J decreases exponentially with ω_x. In this regime the interactions dominates and the dynamics is solely determined by the Raman-induced interactions. We first consider the situation where the next-nearest neighbor interactions

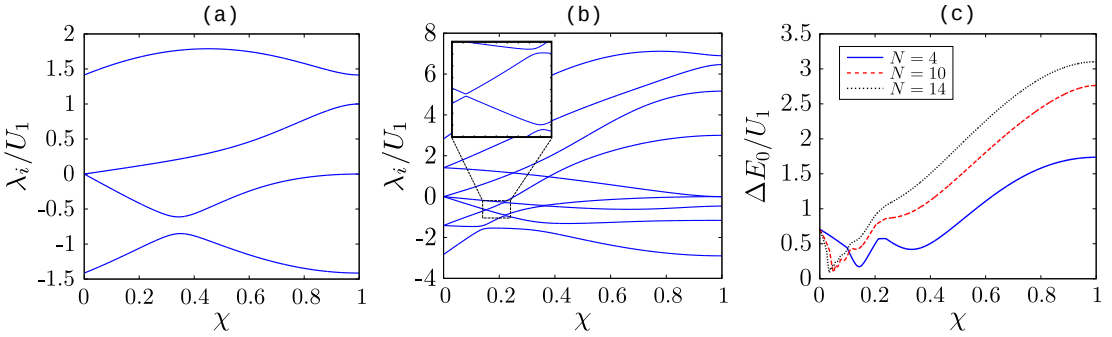

Figure 3.5: Spectrum of the tight-binding Hamiltonian I. eigenvalues λ_i of (3.34) with $\tilde{\epsilon} = 0$ and $U_2 = 0$, in the even parity subspace for (a) $N = 2$ and (b) $N = 4$, as a function of $\chi = \frac{2}{\pi}\arctan\left(\frac{U_1}{J}\right)$. The gaps at the avoided crossings are small but nonzero, as illustrated in the inset. The energy gap between the two lowest energy eigenstates is plotted in (c), for $N = 4$ (blue solid line), $N = 10$ (red dashed line) and $N = 14$ (black dotted line).

can also be neglected, that is, when $U_2 \ll U_1$, which applies for small Ω. Under these considerations

$$\hat{H}_{t.b.} \sim \hat{H}_1, \tag{3.38}$$

which simply includes the possible collision processes between adjacent well states that exchange momentum, as shown in Fig. 3.3(b). We can interpret such processes as effective spin-changing collisions, if we regard the dressed well states as effective spin degrees of freedom. The picture is especially appropriate, if we take into account that each well-state correlates strongly with the bare spin states when the Raman coupling is weak.

To make this interpretation concrete, we introduce the effective spin operators

$$\hat{L}_{x,y,z} = \sum_{\mu\nu} \hat{b}^\dagger_\mu (\hat{F}_{x,y,z})_{\mu\nu} \hat{b}_\nu. \tag{3.39}$$

It is also convenient to introduce the quadrupole tensor element

$$\hat{L}_{zz} = \sum_{\mu\nu} \hat{b}^\dagger_\mu (\hat{F}^2_z)_{\mu\nu} \hat{b}_\nu. \tag{3.40}$$

Substituting (3.39) and (3.40) into (3.35) we can reexpress $\hat{H}_1$ as

$$\hat{H}_1 = \frac{U_1}{2}\left[\hat{L}^2 - \hat{L}_z^2 + \left(\frac{2\tilde{\epsilon}}{U_1} + 1\right)\hat{L}_{zz} - \hat{N}\right]. \tag{3.41}$$

Naturally, Hamiltonian (3.41) possesses a global U(1) symmetry associated with the conservation of parity and the total number of particles N. Moreover, the effective magnetization is preserved in the collision processes, with $\left[\hat{H}_1, \hat{L}_z\right] = 0$, yielding an additional U(1) symmetry associated with the conservation of the left- and right-well population imbalance, which we label as m_z.

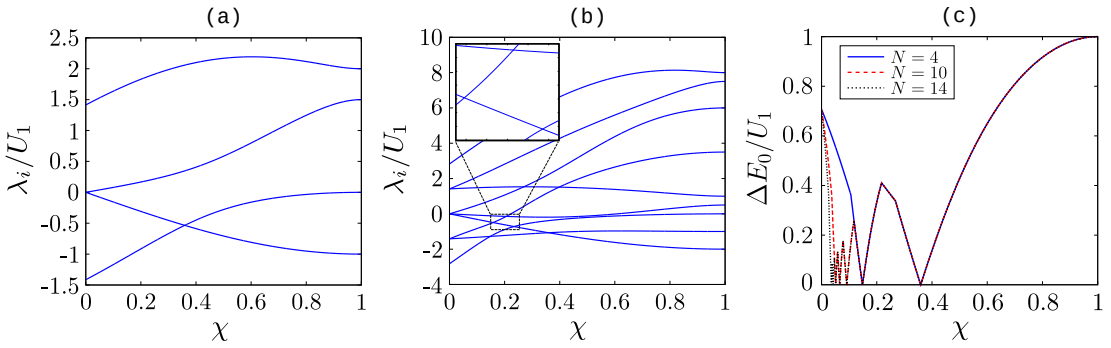

Figure 3.6: Spectrum of the tight-binding Hamiltonian II. Eigenvalues λ_i of (3.34) with $\tilde{\epsilon} = -U_1/2$ and $U_2 = 0$, in the even parity subspace for (a) $N = 2$ and (b) $N = 4$, as a function of $\chi = \frac{2}{\pi}\arctan\left(\frac{U_1}{J}\right)$. The gaps at the crossings vanish at this value of the parameter $\tilde{\epsilon}$. The energy gap between the two lowest energy eigenstates is plotted in (c), for $N = 4$ (blue solid line), $N = 10$ (red dashed line) and $N = 14$ (black dotted line).

Furthermore, Hamiltonian $\hat{H}_1$ acquires yet another U(1) symmetry and becomes integrable when $\tilde{\epsilon} = -U_1/2$. The choice $\tilde{\epsilon} = -U_1/2$ eliminates the quadrupolar-like contribution proportional to $\hat{L}_{zz}$ and leaves the expression of the Hamiltonian only in terms of the spin operators $\hat{L}_j$ and the total number of particles. The Hilbert space $\mathscr{H}$ can then be split into the orthogonal subspaces $\mathscr{H}_l^N$, corresponding to all the irreducible representations of $\mathfrak{so}(3)$ that are spanned in the subspace given by a total number of particles N, $\mathscr{H}^N$. These subspaces have dimension $2l + 1$ and are labelled by the total number of particles N and the possible values of the total angular momentum numbers l. Since the wave function must be symmetric, each subspace $\mathscr{H}^N$ realizes the $l = 0, 2, \ldots, N$ representations when N is even, and $l = 1, 3, \ldots, N$ representations when N is odd. In this most symmetric configuration, the spectrum of $\hat{H}_1$ at $\tilde{\epsilon} = -U_1/2$ is fully characterized by the additional quantum number $m_z \in \{-l, -l+1, \ldots, l\}$. The corresponding eigenvalues are given by

$$\lambda_{(N,l,m_z)} = \frac{U_1}{2}\left[l(l+1) - m_z^2 - N\right]. \tag{3.42}$$

The $\mathfrak{so}(3)$ spin structure of $\hat{H}_1$ at $\tilde{\epsilon} = -U_1/2$ is preserved if we add a nonzero tunneling contribution to the Hamiltonian (recall (3.34) and (3.37)). Effectively, the tunneling operator acts as transverse magnetic field with $\hat{J} = -\frac{J}{\sqrt{2}}\hat{L}_x$. However, in this case the U(1) symmetry associated with the conservation of magnetization breaks down to a Z_2 symmetry associated with parity conservation, and the integrability of the Hamiltonian is lost. Still, it leaves the subspaces with different total effective spin and particle number $\mathscr{H}_l^N$ uncoupled. In Fig. 3.5 we show the energy spectrum of Hamiltonian (3.34) for $N = 2$ and $N = 4$ in the symmetric subspace with $\tilde{\epsilon} = 0$ and $U_2 = 0$, plotted against $\chi = \frac{2}{\pi}\arctan\left(\frac{U_1}{J}\right)$. The parameter χ ranges from the noninteracting scenario at $\chi = 0$ to the case with suppressed tunneling at $\chi = 1$. The spectrum exhibits avoided crossings with nonvanishing level repulsion across all the $\mathscr{H}^N$ subspaces. The level

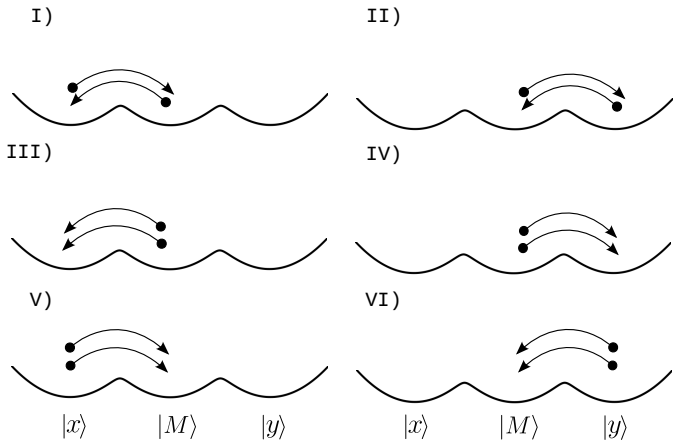

Figure 3.7: **Two coupled two-mode-Bose-Hubbard models.** Representation of all the collision processes in the transformed mode basis $\{|x\rangle, |y\rangle, |M\rangle\}$ that are included in the operator $\hat{H}_1$, where $|j\rangle = \hat{b}_j^\dagger |0\rangle$. In this basis, the problem is analogous to two identical double-well configurations with atom-pair tunnelings that share one site.

repulsion vanishes in all the crossings for $\tilde{\epsilon} = -U_1/2$, as shown in Fig. 3.6. The values of χ at which the crossings are found within a given subspace $\mathscr{H}^N$ are preserved along the subspaces $\mathscr{H}^{N'}$ with a higher number of particles $N' > N$ of the same number-parity, as illustrated for the two lowest eigenstates in Fig. 3.6(c). Naturally, this results from the block diagonalization of the Hamiltonian into the different spin representations $\mathscr{H}_l^N$ at $\tilde{\epsilon} = -U_1/2$.

A remarkably similar behavior is observed in the two-mode Bose Hubbard model with atom-pair tunneling along the boundary between phase-locking and self-trapping phases [291, 292]. This connection can be made more evident by introducing the unitary transformation

$$\hat{b}_x = \cos\theta \frac{\hat{b}_L + \hat{b}_R}{\sqrt{2}} - i \sin\theta \frac{\hat{b}_L - \hat{b}_R}{\sqrt{2}}, \tag{3.43}$$

$$\hat{b}_y = \sin\theta \frac{\hat{b}_L + \hat{b}_R}{\sqrt{2}} + i \cos\theta \frac{\hat{b}_L - \hat{b}_R}{\sqrt{2}}, \tag{3.44}$$

and reexpressing Hamiltonian (3.34) in terms of the modes $\hat{b}_x$, $\hat{b}_y^\dagger$, and setting $U_2 = 0$, yields

$$\begin{aligned} \hat{H}_{t.b.} =& U_1 \hat{N}_x \hat{N}_M + \frac{U_1}{2}\left((\hat{b}_x^\dagger)^2 \hat{b}_M^2 + \hat{b}_x^2 (\hat{b}_M^\dagger)^2\right) - \frac{J\cos\theta}{2}\left(\hat{b}_x^\dagger \hat{b}_M + \hat{b}_x \hat{b}_M^\dagger\right) - \tilde{\epsilon}\hat{N}_M \\ & U_1 \hat{N}_y \hat{N}_M + \frac{U_1}{2}\left((\hat{b}_y^\dagger)^2 \hat{b}_M^2 + \hat{b}_y^2 (\hat{b}_M^\dagger)^2\right) - \frac{J\sin\theta}{2}\left(\hat{b}_y^\dagger \hat{b}_M + \hat{b}_y \hat{b}_M^\dagger\right). \end{aligned} \tag{3.45}$$

Clearly, the tight-binding Hamiltonian (3.34) can be interpreted as the composition of two-mode Bose Hubbard systems sharing one mode, where nonlinear atom-pair tunneling processes are included, as depicted in Figure 3.7. Like in such systems, fragmentation

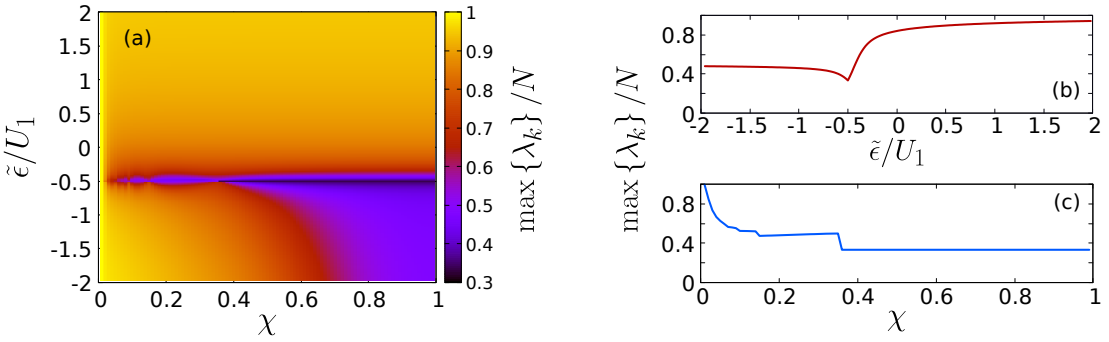

Figure 3.8: Condensed fraction of the ground state. (a) Largest eigenvalue of the one-body density matrix ρ^1, which quantifies the fragmentation of the ground state of Hamiltonian (3.34), as a function of the parameters $\chi = \frac{2}{\pi}\arctan\left(\frac{U_1}{J}\right)$ and $\tilde{\epsilon}$. (b) Largest eigenvalue of ρ^1 as function of $\tilde{\epsilon}$ while fixing $\chi = 1$, which corresponds to setting the effective transverse magnetic $\frac{J}{\sqrt{2}}\hat{L}_x$ field to zero. (c) Largest eigenvalue of ρ^1 as function of χ while fixing $\tilde{\epsilon} = -U_1/2$, which corresponds to setting the effective tensor field $\frac{2\epsilon+U_1}{2}\hat{L}_{zz}$ field to zero. In all cases we set $U_2 = 0$.

can occur in the ground state when the interactions dominate and it corresponds to the degeneracy of mean-field solution. The fragmentation can be evaluated using Penrose-Onsager criterion [293]. It is quantified by the eigenvalues λ_k of one-body density matrix, which for our system is given by $\rho^1_{ij} = \left\langle \hat{b}_i^\dagger \hat{b}_j \right\rangle$. The largest eigenvalue of ρ^1_{ij} is plotted in Fig. 3.8 as a function of χ and $\tilde{\epsilon}/U_1$. Observe that at $\tilde{\epsilon} = -U_1/2$ and large χ, the ground state becomes triply fragmented with all $\lambda_k = N/3$, as occurs in spinor gases with spin-dependent collisions [294] in the absence of an external magnetic field. Here, despite having assumed symmetric bare interactions, spin-spin interactions are effectively induced by Raman dressing. As expected, the addition of both an effective magnetic bias field through the tunneling term proportional to $J\hat{L}_x$ or the quadrupolar tensor element proportional to $\hat{L}_{zz}$ breaks the triple degeneracy.

Finally, unlike with the tunneling operator $\hat{J}$, the addition of a nonzero term $\hat{H}_2$ (3.36) breaks the U(1) symmetry associated with the charge l in the three-mode Hamiltonian (3.34). We can write

$$\hat{H}_2 = \frac{U_2}{4}\left(\hat{L}_{zz}^2 - \hat{L}_z^2\right). \tag{3.46}$$

The term proportional to $\hat{L}_{zz}^2$ in (3.46) cannot be compensated by adjusting the single-particle parameters. As $\left[\hat{L}_{zz}^2, \hat{L}^2\right] \neq 0$, $\hat{H}_2$ couples the different subspaces $\mathscr{H}_l^N$ across all parameter space. Even so, its effect remains small at weak Raman coupling (see Fig. 3.4). Moreover, it is worth mentioning that while the total spin l is not preserved by $\hat{H}_2$, the magnetization m_z is.

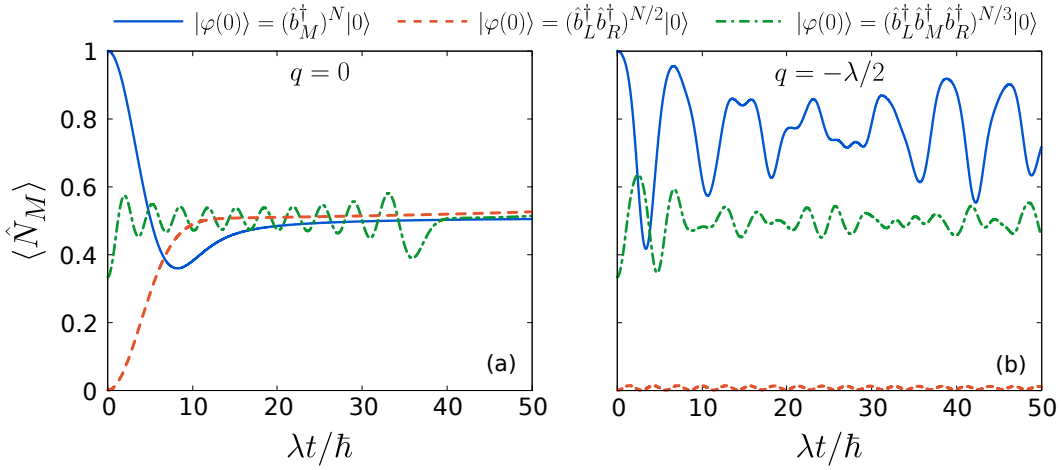

Figure 3.9: Spin mixing induced by effective spin-dependent collisions. Mean population in the middle well mode $\langle \hat{N}_M \rangle$ as a function of time for a state initially at $(\hat{b}_M^\dagger)^N|0\rangle$ (blue solid line), $(\hat{b}_L^\dagger \hat{b}_R^\dagger)^{N/2}|0\rangle$ (red dashed line) and $(\hat{b}_L^\dagger \hat{b}_M^\dagger \hat{b}_R^\dagger)^{N/3}|0\rangle$ (green dash-dotted line), with $N = 60$. The initial state is evolved under Hamiltonian (3.48) with $\lambda_2 = 0$ and $q = 0$ in (a) and $q = -\lambda/2$ in (b).

3.4.2 Dynamical properties of $\hat{H}_{t.b.}$

So far, we have seen that the interplay between Raman dressing and s-wave scattering in the atom cloud gives rise to effective spin-changing collisions that couple the dressed states at the vicinity of the lowest dispersion band minima. By truncating the Hilbert space to just the three lowest bound states of the band, these processes are captured by Hamiltonian (3.35), and the low-energy landscape can be described by the collective spin Hamiltonian

$$\hat{H}_{t.b.} \simeq \frac{U_1}{2}\left[\hat{L}^2 - \hat{L}_z^2 + \left(\frac{2\tilde{\epsilon}}{U_1} + 1\right)\hat{L}_{zz}\right] - \frac{J}{\sqrt{2}}\hat{L}_x + \frac{U_2}{4}\left(\hat{L}_{zz}^2 - \hat{L}_z^2\right), \tag{3.47}$$

where we have dropped the terms that depend only on the total number of particles. Since J increases exponentially with ω_x and U does it linearly, we can always find a regime where $J \ll U_1$, regardless of the value of Ω. We will now focus on this regime, where the effective transverse field contribution to (3.47) vanishes, and the Hamiltonian is block-diagonalized in subspaces with preserved effective magnetization, m_z. Remarkably, in the subspace of zero magnetization we have

$$\hat{H}_{t.b.} \overset{m_z=0}{\longrightarrow} \lambda\frac{\hat{L}^2}{2N} + q\hat{L}_{zz} + \frac{\lambda_2}{4N}\hat{L}_{zz}^2, \tag{3.48}$$

where we define $\lambda_1 = U_1 N$, $\lambda_2 = U_2 N$ and $q = \tilde{\epsilon} + \frac{\lambda}{2N}$. In this form, Hamiltonian (3.48) is analogous to the Hamiltonian describing the spin dynamics of a spinor BEC with spin-dependent collisions [165, 295, 296], where coherent spin-mixing is induced by nonlinear processes [295, 296], with a small correction proportional to λ_2 (remind that, since we

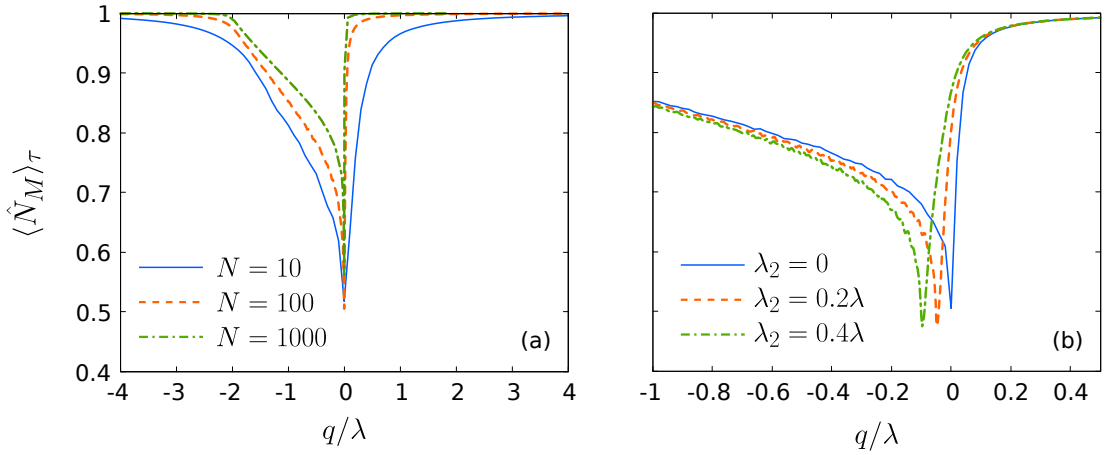

Figure 3.10: Signature of the spin-mixing dynamics. (a) Time-averaged relative occupation of the middle well mode $\langle \hat{N}_M \rangle_\tau$, as a function of q for a state initially at $(|\varphi(t=0)\rangle = \hat{b}_M)^N |0\rangle$. The state is evolved under Hamiltonian (3.48) and the values are averaged over a time τ=$10\tau_c$ for different numbers of particles: $N = 10$ (blue solid line), $N = 100$ (orange dashed line), $N = 1000$ (green dash-dotted line). (b) Corresponding values of $\langle \hat{N}_M \rangle_\tau$ for $N = 100$ and $\lambda_2 = 0$ (blue solid line), $\lambda_2 = 0.2\lambda$ (orange dashed line) and $\lambda_2 = 0.4\lambda$ (green dash-dotted line).

assume weak Raman coupling, we have $\lambda_2 \ll \lambda_1$ (see Fig. 3.4)). Indeed, at resonance, with $q = \lambda_2 = 0$, a generic state initially prepared in the $m_z = 0$ manifold undergoes nonlinear coherent spin mixing, as illustrated in Fig. 3.9(a), over times characterized by

$$\tau_c = \frac{\hbar}{\lambda} N^{1/2}. \tag{3.49}$$

In the figure, the expected value of the population in the middle well, $\langle \hat{N}_M \rangle$, is plotted as a function of time for different initial states $|\varphi(t=0)\rangle$. The macroscopic spin mixing time τ_c is a potential signature to measure the SOC-induced nonlinear spin dynamics. However, the induced spin-mixing is very sensitive to the resonance of the two-body spin-exchanging processes, as shown in Fig. 3.9(b), where the same initial states as in Fig. 3.9(a) are let evolve while setting $q = - < \lambda/2$.

Such sensitivity is illustrated in Fig. 3.10(a), where we plot the time-averaged value of the population in the middle well state, $\langle \hat{N}_M \rangle_\tau$, as a function of q, and for several values of N. The values are averaged over a time $\tau = 10\tau_c$, with the initial state prepared with all atoms in the middle well state. The profile of the drop in $\langle \hat{N}_M \rangle_\tau$ converges fast as N is increased, to a width in q that is roughly given by $\Delta q \sim \lambda$. As we will discuss in the next chapters, the onset of spin oscillations following a quench at $\tilde{\epsilon} = -2$ is related to a quantum phase transition in the most excited state of the collective spin Hamiltonian [297, 298]. In Fig. 3.10(b), we show the corresponding values of $\langle N_m \rangle_\tau$ obtained by setting $\lambda_2 \neq 0$. At first order, the addition of the term proportional to $\lambda_2 \hat{L}_{zz}^2$ to the

Hamiltonian results in a shift in the resonance of the spin-mixing by $\sim -\frac{\lambda_2}{4}$.

In an experimental implementation, the state $(\hat{b}_M)^N |0\rangle$ can be easily prepared by initially setting $q < -2\lambda$. The dynamics depicted in Fig. 3.10 can then be induced by a quench in the central well energy Δ_0 (as defined in section 3.2.1) to reach the targeted value of q. The quench can be performed without considerably populating the higher bands due to the scale separation between the gap, which, to first order, is given by Ω at the avoided crossings, and $\lambda \ll \Omega$. With this preparation, the mean population in the middle well, $\langle \hat{N}_M \rangle$, is a suitable observable to probe experimentally the correlated spin dynamics induced by the tight-binding Hamiltonian (3.34). Notice that in the weakly-coupled regime, the populations in the left, middle and right well modes are highly correlated to the populations $s = -1$, $s = 0$ and $s = 1$ bare spins, respectively. Moreover, the Rabi frequency could be adiabatically turned off in order to better the correlation between the occupation of well states and the spin states, improving the resolution in the eventual Stern-Gerlach measurement of the populations.

3.4.3 Experimental considerations

To experimentally probe the described SOC-induced spin-mixing dynamics in a quench protocol as described, we require that the region of resonance $\Delta q \sim \lambda$ is sufficiently large compared to the noise associated with q, and that $\tau_c \propto 1/\lambda$ is short compared to the characteristic times associated with the atom loss due to spontaneous emission from the Raman beams and the heating mechanisms that take place in the dressed and trapped gas. As a first approach, the optimization of both quantities relies then in having the effective spin-spin interaction strength λ as large as possible while simultaneously fulfilling the constraints that led to the derivation of the tight-binding Hamiltonian. Mainly, recall from (3.17) that the validity of the tight-binding Hamiltonian relied on an upper bound on the atom density. From (3.27), (3.28) and (3.29), it follows that $\lambda = C_{-1,1,0,0} g \langle n \rangle$. At weak couplings, we can compute $C_{-1,1,0,0}$ from the perturbative expressions of the spin compositions of the dressed states at the lowest band minima $\overrightarrow{s_0}(k_j)$, which yields $C_{-1,1,0,0} = \Omega^2/16E_r^2 + O((\Omega/E_r)^3)$, and so

$$\lambda \simeq g \langle n \rangle \frac{\Omega^2}{16E_r^2}. \tag{3.50}$$

For simplicity, let us consider harmonic trapping along the perpendicular directions, with $\hat{V}_\perp = \frac{1}{2}m(\omega_y^2 y^2 + \omega_z^2 z^2)$, and define the aspect ratios $r_y = \omega_y/\omega_x$ and $r_z = \omega_z/\omega_x$. Notice that the tight-binding condition also puts a lower bound on the transverse trapping frequencies, and so we require $r_y, r_z \geq 1$. Considering Gaussian profiles for the well modes, we obtain

$$g \langle n \rangle = gN \left(\frac{m\omega_x}{2\pi\hbar}\right)^{3/2} (r_y r_z)^{1/2}. \tag{3.51}$$

By parameterizing

$$\alpha = \frac{g \langle n \rangle}{\hbar\omega_x}, \tag{3.52}$$

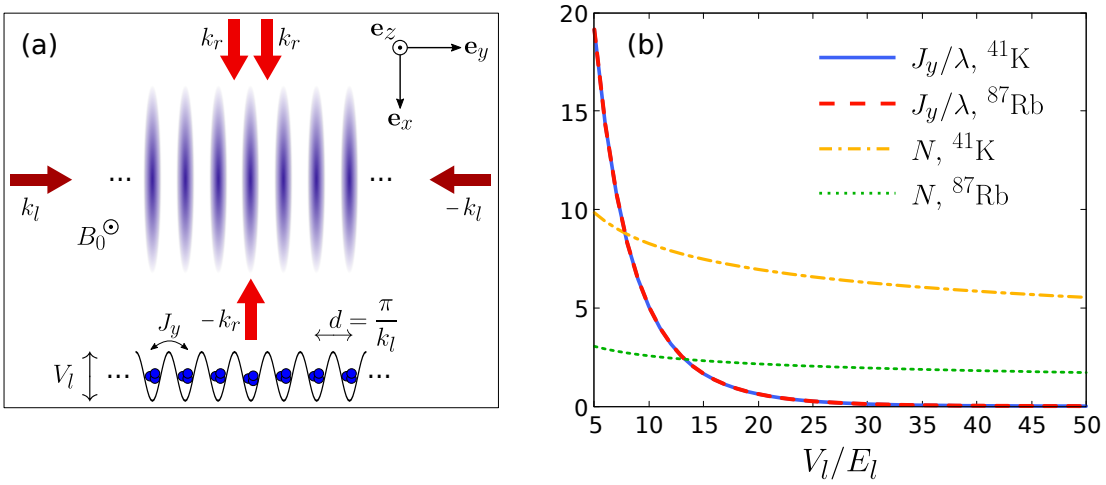

Figure 3.11: Realization of the tight-binding Hamiltonian in the few-particle regime. (a) Schematic representation of the Raman-dressed gas loaded in a deep optical lattice. (b) Number of particles per lattice site N and relative strength of the inter-site tunneling strength J_y/λ, as a function of the lattice depth V_l/E_l. The quantities are computed using equations (3.54) to (3.57), where we set $\Omega = 2E_r$ and $\alpha = \beta = 0.1$. The recoil energies of lattice beams are computed by considering $\lambda_l = 1064$ nm and by using the mass of the ^{41}K and ^{87}Rb atomic species. The respective recoil energies are computed using $\lambda_r = 769$ nm and $\lambda_r = 790$ nm, and the scattering parameter g for both species is taken from [147].

with $0 < \alpha \ll 1$, and

$$\beta = \frac{\hbar\omega_x}{E_r}, \tag{3.53}$$

with $0 < \beta \ll 1$, and using equations (3.50) and (3.51) we can write λ and N as a function of the recoil energy

$$\lambda = \alpha\beta\frac{\Omega^2}{16E_r}, \tag{3.54}$$

$$N = \frac{\alpha\hbar^3}{g\sqrt{\beta r_y r_z E_r}}\left(\frac{m}{2\pi}\right)^{-3/2}. \tag{3.55}$$

We can use expressions (3.54) and (3.55) to gain insights on the experimental viability of the tight-binding Hamiltonian presented in this chapter. As a reference, we consider ^{41}K and ^{87}Rb atoms, which have a rather large fine structure splitting and almost symmetric interaction, and use the corresponding values of a_0, a_2 given in [147]. Their large fine structure splitting results in a relatively low photon scattering rate from Raman beams (see Sec. 2.1), and thus allows for long-lived Raman-dressed gases. By setting, e.g., $\alpha = 0.1$ and $\beta = 0.1$, we see from eqs. (3.52) to (3.54) that, for both species, we can obtain λ in the order of several tens of Hz while keeping $\Omega < 4E_r$. Likewise, $\langle n \rangle$ can be kept in the order of 10^{13}cm^{-3}, which is compatible with typical dilute

ultracold gases. However, notice from (3.55) that the constraint on the density ($\alpha \ll 1$) drastically limits the number of particles in the gas. Even in the most favorable scenario of ^{41}K atoms in an isotropic trap ($r_y = r_z = 1$), the gas would be limited to maximal sizes of $\sim 10^2$ particles. While such small condensates can be technically challenging to implement, the few-particle regime could be explored by loading the condensate into a deep 1D optical lattice, displayed perpendicularly with respect to the Raman beams, as represented schematically in Fig. 3.11(a). There, we consider a 1D optical lattice along the $\mathbf{e}_y$ direction, generated by means of two counter-propagating laser beams with wave vector k_l.

In the deep lattice regime (see Sec. 2.3), where the lattice potential V_l is much larger than the recoil energy of the lattice beams $E_l = \frac{\hbar^2 k_l^2}{2m}$, we have

$$\hbar\omega_y = 2\sqrt{V_l E_l}, \tag{3.56}$$

which yields an inter-site tunneling strength for the trapped atoms of

$$J_y \simeq E_l \frac{4}{\sqrt{\pi}} (V_l/E_r)^{3/4} \exp(-2\sqrt{V_l E_l}). \tag{3.57}$$

This configuration is equivalent to set e.g. $r_y \gg 1$ in equation (3.55) (notice that λ is unaffected by the choice of r_y and r_z). Since $N \propto r_y^{-1/2}$, by setting $r_y \gg 1$ few atoms could still be placed per lattice site in the Mott insulator regime, where each site could be treated as an independent realization of the tight-binding Hamiltonian. This could be achieved while keeping a relatively large value for λ.

By considering ^{41}K and typical lattice wavelengths $\sim 10^{-6}$ m, we can easily set $J_y \ll \lambda$, with lattice depths of few tens of the recoil energy and many atoms per site. By way of example, in Fig. 3.11(b) we plot the number of atoms per site and the strength of the inter-site tunneling relative to λ as a function of the lattice depth. For both ^{41}K and ^{87}Rb atoms, we set the Raman wavelength to $\lambda_r = 790$ nm and the lattice wavelength to $\lambda_l = 1064$ nm, and fix $\Omega = 2E_r$ and $\alpha = \beta = 0.1$. With these numbers, we obtain a spin-mixing parameter of $\lambda/h \sim 20$ Hz in the case of ^{41}K, and $\lambda/h \sim 10$ Hz in the case of ^{87}Rb. The corresponding characteristic spin-mixing times obtained using (3.49) in these conditions are around $\tau_c \sim 20$ms for both species, which is compatible with the lifetime of ultracold Raman-dressed gases [244]. Note that the mixing times for the two species are similar since the optimal number of particles per site differs. The fact that the mixing times scale with $N^{1/2}$ further motivates its exploration in the few-particle regime.

It is left to compare the characteristic energy scale of the spin-mixing dynamics, λ, to the main sources of noise and uncertainty in the Raman-dressed gas. As shown in Fig. 3.10, macroscopic spin oscillations are only induced by Hamiltonian (3.48) near the resonant condition at $q = 0$, and the resonance width for the proposed observable, $\langle \hat{N}_M \rangle$, is in the order of λ. Aside from the atom loss due to spontaneous emission from the Raman beams, a major source of noise in typical experiments with Raman-dressed spinor

gases stems from the instability of the external magnetic bias field. This is particularly true in the spin-1 scheme proposed in this chapter, where a large bias field B is required in order to tune $\epsilon < 0$ in the dressed Hamiltonian (3.1), or equivalently, $q < 0$ in the spin Hamiltonian (3.48). To achieve $\epsilon < 0$, each pair of hyperfine states needs to be coupled by independent Raman transitions. In turn, this requires having a quadratic Zeeman split sufficiently large to avoid cross coupling. This effect was achieved in the experiment from [118] by employing a static bias field as large as $B \sim 35\,\mathrm{G}$.

With such strong fields, magnetic fluctuations can get significantly large even in the controlled set-ups of ultracold atom experiments [118]. For both ^{41}K and ^{87}Rb in the $F = 1$ manifold, a magnetic fluctuation of $\Delta B \sim 10^{-3}$ G induces a fluctuation of the linear Zeeman split in the order of several hundreds of Hz. Such modulation of the Zeeman energy levels translates into the addition of a fluctuating term $\delta(t)\hat{L}_z$ to the spin Hamiltonian (3.47), with an amplitude that is at least an order of magnitude larger than λ. Luckily, the protocol proposed is designed to be robust against such fluctuations at linear Zeeman level. This is clear since we prepare the initial state in the zero magnetization manifold, where $\langle \hat{L}_z \rangle = 0$. As long as δ is kept small compared to E_r, the parameters of the tight-binding Hamiltonian are not modified significantly. However, magnetic fluctuations can not be overlooked since we still need to account for the fluctuations in the quadratic contribution to the Zeeman split, albeit it is typically much smaller. Taking as a reference the values provided in [118], with $B \sim 35\,\mathrm{G}$ and $\Delta B \sim 10^{-3}$ G, the fluctuation in the quadratic Zeeman shift is in the order of few Hz, which is already below the values of λ that are obtained in the conditions described in Fig. 3.11. Actually, in [118], the largest contribution to the uncertainty of ϵ stems not from magnetic field fluctuations but from calibration error in Ω. The mechanism behind such contribution stems from the residual cross coupling between the two Raman transitions, which is proportional to Ω^2. Nonetheless, since Ω remains very stable during the lifetime of the Raman-dressed condensate, its associated error can be therefore considered a shot-to-shot calibration error rather than a source of noise and heating.

Therefore, the spin-mixing dynamics described in this chapter can in principle be resolvable in realistic experiments. We note that magnetic noise could be optimized further. For instance, recently, in [299], the root mean square value of the magnetic field noise was kept as low as a few tens of μG. There is yet another consideration that is worth mentioning. In the derivation of Hamiltonian (3.48), we have neglected the contribution from the momentum-space tunneling term proportional to $J\hat{L}_x$, which acts as a transverse magnetic field. In order to confine the many-body state within the $m_z = 0$ subspace during the dynamics, we therefore require that $|J| \ll \lambda$. This is guaranteed as ω_x approaches 0, yet since we want to maximize $\lambda \propto \beta$, it may be convenient to relax the constraint on J. In any case, this can be addressed by setting a comparatively large detuning $|\delta|$, which separates energetically the subspaces with different magnetization m_z, and sets the tunneling processes out of resonance.

To conclude, we note that in (3.54) we have not taken into account the intrinsic spin-

changing collisions that in the spinor gas arise from the non-symmetric contribution to the two-body interacting Hamiltonian, as discussed in Sec. 3.2.3. Such processes have a scattering parameter given by $g_a = 4\pi\hbar^2(a_2 - a_0)/3m$ [147]. When $|g_a| \ll g$, as is the case for ^{41}K and ^{87}Rb, its effect can be safely reintroduced simply by adding the intrinsic and SOC-induced parameters into a single parameter $g_a + \lambda$, and neglecting the corrections of order $g_a\Omega^2$. Both ^{41}K and ^{87}Rb are ferromagnetic species, which yields a negative correction to the effective spin-mixing rate. Luckily, in both cases we can easily have $|g_a| \ll \lambda$ by setting $E_r < \Omega < 4E_r$, and hence such a correction does not significantly alter the analysis made above regarding the energy and time scales. Moreover, we note that the parameters used in Fig. 3.11(b) are chosen merely to give a sense of scale, and that the implementation could in principle be further optimized in an actual experiment.

3.5 Conclusion

In this chapter, we have explored the many-body properties of Raman-dressed spinor condensates at low energies. As we have covered, spin-orbit coupling can be tailored in charge-neutral ultracold atoms by means of Raman dressing. In a Raman transition, the atomic levels are indirectly coupled via resonant two-photon processes that involve a large momentum exchange between the electromagnetic field and the atoms. With Raman beams typically in the near infrared regime, the recoil kinetic energy associated with such processes is large compared to the energies that characterize the many phenomena in the ultracold Bose gas, and it effectively induces a coupling between the momentum of the atoms and their internal state, which can be interpreted as a synthetic form of SOC. The aim of this chapter has been the study of the interplay between s-wave scattering processes and this form of SOC.

In particular, we have focused on the low-energy landscape of the weakly coupled spin-1 gas, where the lowest single-particle dispersion band exhibits a triple-well shape. Inspired by recent works on momentum-space lattices [265–267], we have regarded the weakly dressed gas as a momentum space Hubbard-like system. We have shown that, in this tight-binding regime, the SOC-mediated modulation of the scattering processes in the gas gives rise to effective correlated tunneling processes between the site modes in the momentum space lattice. Their presence supposes a marked departure from conventional position space analogies. Interestingly, these virtual processes act as spin-changing collision processes that can be tuned with the Raman intensity.

We have discussed the spectral properties of the resulting Hamiltonian, and showed that it becomes integrable in a certain region of the parameter space. In such conditions, the system can be mapped into a collective spin Hamiltonian, and the dynamics becomes analogous to the one taking place in undressed spinor BECs with spin-dependent scattering parameters [165, 295, 296]. Remarkably, we have shown that the SOC-induced spin-changing collisions can dominate the dynamics of the system in the few-particle regime. Exploiting the difference between the noninteracting and the interacting energy

scales, we have proposed a quench protocol through which all the noninteracting dynamics is frozen, effectively isolating the low-energy phenomena of interest. The visibility of the induced collective spin dynamics heavily relies on the choice of the experimental signature and the initial state, which allows the protocol to be robust against relatively large fluctuations in the bias magnetic field. Finally, we have shown that the predicted spin dynamics can be measured in state-of-the-art experiments with ultracold atoms. It is worth stressing that, in the experimental setup sketched in Sec. 3.4.3, atom-pair tunneling-like processes are expected to be the leading order contributions to the resulting effective perturbative dynamics. By contrast, in conventional Hubbard models, atom-pair hopping processes are typically much smaller than one-body tunnelings, and the latter can not be suppressed independently of the former. Already at the two-particle level, these atom-pair processes coherently couple the two-body states $|020\rangle \leftrightarrow |101\rangle$. Thus, one could exploit them to generate maximally entangled pairs in each site of the lattice. The presence of SOC would translate these quantum correlations to the external degrees of freedom of the atoms, making the problem richer.

To conclude, we note that the analogy explored in this chapter between the dressed condensate and its bare counterpart paves the way for the next two chapters in this thesis, where this connection is explored further. Despite its apparent simplicity, the collective spin dynamics in spinor condensates have been the framework of a large body of research over the last two decades involving many-body phenomena [300–310]. Its success is in part due to the large tunability of ultracold atomic gases as an experimental platform. From a practical point of view, the spin-mixing mechanism in such systems have been proposed and exploited, e.g., for the generation of macroscopic entanglement [272, 274–285, 311], to be used in metrological applications [73]. In the dressed dynamics that we have described, the induced spin-spin interactions can be tuned independently of the density of the gas by adjusting the intensity of the Raman beams. This extra degree of tunability allows for further harnessing of the spin-mixing dynamics, which opens a new avenue for its exploitation in quantum protocols. Finally, we note that the spin-1 scenario we have discussed in this chapter is the minimal spin size where the described Raman-induced spin-changing collisions manifest and can be experimentally detected. Similar and more complex processes appear at higher spins. Such terms can take place in spin-orbit-coupled Bose gases of alkali atoms such as Caesium ($F = 3$) or Lanthanide atoms such as Dysprosium [210].

CHAPTER 4

Dynamical preparation of stripe states in spin-orbit-coupled gases

In spinor Bose-Einstein condensates, nonsymmetric spin interactions are a remarkable proxy to coherently realize macroscopic many-body quantum states. In particular, spin-changing scattering processes have been exploited to generate entanglement, to study dynamical quantum phase transitions, and proposed for realizing nematic phases in atomic condensates. In the previous chapter, we showed that in a spinor gas dressed by Raman beams, the coupling between spin and momentum induces a spin dependence in the scattering processes. We explored a regime that involved the lowest-energy single-particle solutions of the dressed and trapped gas and showed that there the modulation of the collisions lead to a collective spin Hamiltonian. The derived Hamiltonian effectively described an undressed spinor gas in which the nonsymmetric spin interactions could be adjusted with the intensity of the Raman beams. This chapter explores further this description of spin-orbit-coupled gases, and show that the same collective spin physics can be generalized by considering instead the dynamics of self-consistent modes located at the vicinity of the band minima, which are perturbatively coupled by the SOC-induced nonsymmetric interactions.

The approach taken in the previous chapter to treat the Raman-induced spin-mixing dynamics stemmed from an intuitive momentum-space lattice picture in the weakly-coupled regime. While such an approach provided a simple tool to understand the processes taking place and their relative energy and time scales, it also imposed an upper bound on the density of the gas that limited the experimental accessibility of the model to the few-particle regime. In this chapter, we show that the equivalence at the quantum level of the weakly-coupled Raman-dressed gas to an *artificial* spinor gas with tunable spin-changing collisions holds away from the tight-binding regime previously considered. The understanding of the low-energy landscape of the dressed system in

these terms allow us to design a robust protocol to coherently drive a spin-orbit-coupled condensate into the experimentally elusive ferromagnetic stripe phase of the spin-1 gas. Stripe phases in spin-orbit-coupled gases have drawn significant attention due to their supersolid-like properties. Here we propose a novel preparation via crossing a quantum phase transition of the resulting effective low-energy spin model in an excited-state.

The chapter is organized as follows. We start by motivating the exploration of the stripe phase of spin-orbit-coupled gases in Sec. 4.1, where we also summarize the results presented in the chapter. In Sec. 4.2, we analytically show that the weakly-coupled regime of the Raman-dressed spinor condensate effectively describes an undressed spinor gas with tunable spin-changing collisions. We exemplify the strengths of this dressed-base description in Sec. 4.3, where we show that the dynamics of the collective pseudospin degree of freedom can be exploited to access the striped regime of the spin-orbit-coupled gas. In Sec. 4.4 we numerically assess the experimental feasibility of the protocol described in the previous section. Finally, in Sec. 4.5, we conclude the chapter by briefly reviewing the results presented and address future research directions.

4.1 Introduction

Artificial spin-orbit coupling (SOC) in ultracold atomic gases offers an excellent platform for studying quantum many-body physics [30, 84, 85]. The interplay between light dressing induced by Raman coupling [86] and atom-atom interactions can lead, for instance, to high-order synthetic partial waves [116, 117], to chiral interactions and density-dependent gauge fields [312] or to the formation of stripe phases [104]. The latter have gained significant attention over the past decade [115, 185, 189, 192, 195, 313], in great part due to its supersolid-like properties [119, 314, 315], that is, its simultaneous spontaneous breaking of translational invariance and of U(1) (global) phase symmetry, resulting in a crystalline structure that maintains off-diagonal long-range order.

Accessing the stripe regime of ultracold gases with SOC remains experimentally challenging, since its stability relies on the asymmetry between intra- and inter-spin interactions, typically small in a common spinor BECs. The predicted spatial density modulations have only been unambiguously observed in [108], using orbital states in a superlattice as pseudo-spin states, and very recently also in metastable states of a ^{87}Rb spinor gas [207] (for its realization in dipolar gases, see [316–318]). While sharing many properties with conventional supersolids, the nature of the stripe phases in gases with SOC is still debated [319], with current proposals focusing on probing its excitation spectrum. So far, most protocols to enhance the accessibility of the phase and the contrast of the stripes pursue an effective decrease of the intraspin interactions [107, 198]. Alternatively, here we propose a novel approach to access the stripe regime of a spin-1 gas with largely symmetric spin interactions, based on the coherent spin-mixing dynamics induced by Raman dressing.

The results presented in chapter 3 described a direct connection between SOC BECs

and spinor gases with spin-changing collisions. This connection is further explored in this chapter, where we show analytically that the Raman-dressed spin-1 SOC gas at low energies is equivalent, for weak Raman coupling and interactions, and zero total magnetization, to an *artificial* spin-1 gas with tunable spin-changing collisions. Such a relationship between the two systems has been previously hinted by many authors [195, 263, 286–290], but not explicitly formulated. By considering the pseudospinor gas formulation of the low-energy problem, we then follow the single-spatial-mode [165, 320] recipe commonly employed to treat the collective spin dynamics in undressed spinor gases, and adapt it to describe the psedospin dynamics in the dressed scenario. Under these conditions, the system is well described by a one-axis-twisting Hamiltonian [321]. This same Hamiltonian explains several quantum many-body phenomena in spinor condensates [147, 161], including the generation of macroscopic entanglement [272, 274–285, 311], with potential metrological applications [73], and the observation of nonequilibrium phenomena such as the formation of spin domains and topological defects [300–310]. Recently, dynamical [120] and excited-state [121] quantum phase transitions have been theoretically [322, 323] and experimentally [297, 298] studied in spin-1 BECs with spin-changing collisions. Here we exploit this map to provide a many-body protocol to access the ferromagnetic stripe phase of the SOC gas via crossing a quantum phase transition of the low-energy Hamiltonian in an excited state. This preparation enhances the accessibility of the phase, which has as the ground-state phase a very narrow region of stability [196] and has not been experimentally demonstrated so far.

4.2 The Raman-dressed gas as an artificial spinor gas

We consider a spin-1 spin-orbit-coupled Bose gas held in an isotropic harmonic potential $V_{\rm t} = \frac{1}{2}m\omega_{\rm t}^2\mathbf{r}^2$, in which the atoms interact via two-body s-wave scattering processes. The synthetic spin-1 SOC is realized by two pairs of counter-propagating laser beams in a Raman configuration as detailed in chapter 2. In a frame co-rotating and co-moving with the laser beams, the system is described by the Hamiltonian

$$\hat{H} = \int d\mathbf{r} \left[\hat{\mathbf{\Psi}}^\dagger \left(\hat{\mathcal{H}}_{\rm k} + V_{\rm t} \right) \hat{\mathbf{\Psi}} + \frac{g_s}{2} (\hat{\mathbf{\Psi}}^\dagger \hat{\mathbf{\Psi}})^2 + \frac{g_a}{2} \sum_j (\hat{\mathbf{\Psi}}^\dagger \hat{F}_j \hat{\mathbf{\Psi}})^2 \right], \tag{4.1}$$

with $\hat{\mathbf{\Psi}} = (\hat{\Psi}_{-1}, \hat{\Psi}_0, \hat{\Psi}_1)^T$ being the spinor field operator and $\{\hbar\hat{F}_x, \hbar\hat{F}_y, \hbar\hat{F}_z\}$ being the spin-1 matrices. Here $g_s = 4\pi\hbar^2(a_0 + 2a_2)/3m$ and $g_a = 4\pi\hbar^2(a_2 - a_0)/3m$, with a_0 and a_2 being the scattering lengths in the $F = 0$ and $F = 2$ channels, respectively. The dressed kinetic Hamiltonian reads

$$\hat{\mathcal{H}}_{\rm k} = \frac{\hbar^2}{2m} \left(\mathbf{k} - 2k_r \hat{F}_z \mathbf{e}_x \right)^2 + \frac{\Omega}{\sqrt{2}} \hat{F}_x + \delta \hat{F}_z + \epsilon \hat{F}_z^2, \tag{4.2}$$

where Ω is the Raman coupling strength, δ is the Raman detuning and ϵ is the effective quadrupole tensor field strength. The latter term can be controlled independently of δ by

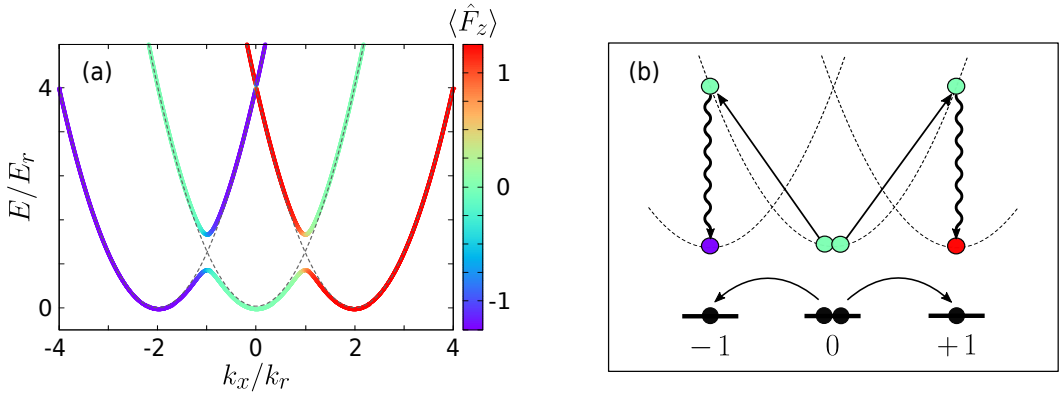

Figure 4.1: Raman-induced spin-changing collisions. (a) Dispersion bands of the dressed Hamiltonian $\hat{\mathcal{H}}_{\mathrm{k}}$ with $\Omega = 0.65E_r$, $\delta = 0$ and $\epsilon = \Omega^2/16E_r$. The color texture indicates the expected value of the spin of the dressed states, and the dashed lines show the undressed dispersion bands. (b) Schematic representation of a virtual process that acts as an effective spin-changing collision. These involve a two-body scattering process in which the two incoming particles exchange a relatively large momentum, and thus would be out of resonance in the absence of Raman dressing, but become resonant by simultaneously involving two-photon Raman photons (represented in wavy lines) that take up the momentum gained by the particles while in turn change their internal state.

.

employing two different Raman couplings between the two Zeeman pairs $\{|1,1\rangle, |1,0\rangle\}$ and $\{|1,0\rangle, |1,-1\rangle\}$, and simultaneously adjusting the Raman frequency differences [118]. We label the Raman single-photon recoil energy and momentum as $E_r = \frac{\hbar^2 k_r^2}{2m}$ and $\hbar k_r$, respectively. As discussed in chapter 3, in the weakly-coupled regime, the lowest dispersion band of $\hat{\mathcal{H}}_{\mathrm{k}}$ presents a triple-well shape along the direction of the momentum transfer, which we arbitrarily set along the $\mathbf{e}_x$ axis. Spin texture is present in the band, with the spin mixture being the largest at the vicinity of the avoided crossings (see Fig. 4.1(a)). While much smaller, the spin overlap between states located at the vicinity of adjacent minima is nonzero, and increases linearly with Ω. This overlap allows collision processes that exchange large momentum at low energies. In the previous chapter we saw how these Raman-mediated processes can act as spin-changing collisions. In Fig. 4.1(b), we schematically represent one of such virtual processes, which involve simultaneously a two-body collision process (represented with a solid line in the figure) and two-photon Raman transitions (represented with a wavy line).

In order to draw an analogy between these effective spin-changing processes and the intrinsic ones present in the gas, the Hilbert space needs to be restricted to the states in the vicinity of the band minima, so that we can identify those to the spin states in a spinor gas. To do so, in chapter 3 we considered the direct truncation of the Hilbert space to the lowest single-particle eigenstates of the dressed and trapped system, that directly lead to an effective spin Hamiltonian. Instead, in this section we will see that,

actually, the perturbative description of weakly-dressed gas, up to second order in $\Omega/4E_r$, incorporates the equivalent spin-mixing processes in a natural way.

4.2.1 Low-energy effective field theory

Let us now consider the regime where δ, ϵ, $\hbar\omega_{\mathrm{t}}$ and the interaction energy per particle are all much smaller than the recoil energy E_r. In these conditions, it is safe to assume that the low-energy landscape is well-described by an effective theory in which all the dynamics involves only the lowest free single-particle band modes around each band minima $\mathbf{k}_j \sim 2jk_r\mathbf{e}_x$, with $j \in \{-1, 0, 1\}$. Thus, we set a cut-off $\Lambda \ll \hbar k_r$ to the momentum spread p around each $\mathbf{k}_j$, so that $|p| < \Lambda$, and use second order perturbation theory to express the bare fields $\hat{\Psi}_i$ in terms of the lowest-band dressed-state fields around the band minima, which we label as $\hat{\varphi}_j$. With this notation, we can identify the operators acting in the separated regions as a pseudospinor field $\hat{\boldsymbol{\varphi}} = (\hat{\varphi}_{-1}, \hat{\varphi}_0, \hat{\varphi}_1)^T$, with $\left[\hat{\varphi}_i(\mathbf{p}), \hat{\varphi}_j^\dagger(\mathbf{p}')\right] = \delta(\mathbf{p}-\mathbf{p}')\delta_{ij}$.

For the sake of clarity, in the remainder of this section we will write all the energies and momenta scaled to the recoil energy E_r and momentum $\hbar k_r$, respectively, unless these quantities appear explicitly on the expressions. Doing so, the perturbative expression for $\hat{\Psi}_i$ in terms of $\hat{\varphi}_j$ around the center band minimum are obtained from the dressed kinetic Hamiltonian (4.2), which yield

$$\begin{aligned}
\hat{\Psi}_0(p) &= \left(1 - \frac{\Omega^2}{64}\left(1 - \frac{\epsilon}{2} + O((\Lambda + \frac{\epsilon+\delta}{4})^2)\right)\right)\hat{\varphi}_0(p) + O\left((\frac{\Omega}{8(1-\Lambda)})^3\right), \\
\hat{\Psi}_{\pm1}(p) &= -\frac{\Omega}{8}\left(1 - \frac{\epsilon \pm \delta \mp 4p}{4} + O((\Lambda + \frac{\epsilon+\delta}{4})^2)\right)\hat{\varphi}_0(p) + O\left((\frac{\Omega}{8(1-\Lambda)})^3\right).
\end{aligned} \tag{4.3}$$

Likewise, in right/left band minima we have

$$\begin{aligned}
\hat{\Psi}_{\pm1}(\pm2+p) &= \left(1 - \frac{1}{2}\left(\frac{\Omega}{8}\right)^2\left(1 + \frac{\epsilon \pm \delta \mp 4p}{2} + O((\Lambda + \frac{\epsilon+\delta}{4})^2)\right)\right)\hat{\varphi}_{\pm1}(p) \\
&\quad + O\left((\frac{\Omega}{8(1-\Lambda)})^3\right), \\
\hat{\Psi}_0(\pm2+p) &= -\frac{\Omega}{8}\left(1 + \frac{\epsilon \pm \delta \mp 4p}{4} + O((\Lambda + \frac{\epsilon+\delta}{4})^2)\right)\hat{\varphi}_{\pm1}(p) + O\left((\frac{\Omega}{8(1-\Lambda)})^3\right), \\
\hat{\Psi}_{\mp1}(\pm2+p) &= \frac{\Omega^2/16}{((16 + p^2 \pm \delta \pm 8p)\left(1 - \frac{\epsilon\mp\delta\pm4p}{4}\right)}\hat{\varphi}_{\pm1}(p) + O\left((\frac{\Omega}{8(1-\Lambda)})^3\right).
\end{aligned} \tag{4.4}$$

For simplicity, in equations (4.3) and (4.4) we have made explicit only the dependence on momentum along the direction of the recoil momentum transfer. At the same time, notice that in the lowest dressed band, the positions of the edge minima are actually

shifted from ± 2 by a small amount proportional to Ω^2. Still, up to the second order in Ω that we are considering, these shifts do not contribute to the expressions of (4.4), and hence are not included in the redefinition of momenta. Notice also that the last term of the above expressions can be neglected since it contributes to the interactions at fourth order in $\frac{\Omega}{8(1-\Lambda)}$. As we will see below, due to momentum conservation, the nontrivial contributions to the interacting Hamiltonian involve only the first order terms in the above expressions, while the second order just renormalize the symmetric interactions.

We can now substitute the expressions for the bare fields into Hamiltonian (4.1) to obtain a lowest-band-truncated pseudospinor Hamiltonian. The noninteracting contributions can be straightforwardly grouped into

$$\hat{H}_{\text{n.i.}} = \int d\mathbf{r}\, \hat{\boldsymbol{\varphi}}^\dagger \left(\frac{\mathbf{p}^2}{2m} + V_{\text{t}} + \delta \hat{F}_z + \tilde{\epsilon} \hat{F}_z^2 \right) \hat{\boldsymbol{\varphi}}. \tag{4.5}$$

In (4.5), we have introduced the coefficient $\tilde{\epsilon}$, which includes the correction to ϵ, with

$$\tilde{\epsilon} = \epsilon + \frac{\Omega^2}{16 E_r} + O((\frac{\Omega^2}{E_r})^3). \tag{4.6}$$

The interacting terms are somewhat trickier, since they will involve combinations of many four-wave operators $\hat{\varphi}_i \hat{\varphi}_j \hat{\varphi}_k \hat{\varphi}_l$. To address them, we now conveniently adopt the notation shortcuts

$$\int\int \hat{\Psi}_a^\dagger \hat{\Psi}_b^\dagger \hat{\Psi}_a \hat{\Psi}_b \equiv \int \mathrm{d}r \int \prod_{j=1}^{4} \frac{\mathrm{d}^3 k_j}{(2\pi)^3} e^{i\mathbf{r}\cdot(\mathbf{k}_1+\mathbf{k}_2-\mathbf{k}_3-\mathbf{k}_4)} \hat{\Psi}_a^\dagger(\mathbf{k}_1) \hat{\Psi}_b^\dagger(\mathbf{k}_2) \hat{\Psi}_a(\mathbf{k}_3) \hat{\Psi}_b(\mathbf{k}_4), \tag{4.7}$$

and

$$\int\int \hat{\varphi}_a^\dagger \hat{\varphi}_b^\dagger \hat{\varphi}_a \hat{\varphi}_b \equiv \int \mathrm{d}r \int_{-\Lambda}^{\Lambda} \prod_{j=1}^{4} \frac{\mathrm{d}^3 p_j}{(2\pi)^3} e^{i\mathbf{r}\cdot(\mathbf{p}_1+\mathbf{p}_2-\mathbf{p}_3-\mathbf{p}_4)} \hat{\varphi}_a^\dagger(\mathbf{p}_1) \hat{\varphi}_b^\dagger(\mathbf{p}_2) \hat{\varphi}_a(\mathbf{p}_3) \hat{\varphi}_b(\mathbf{p}_4). \tag{4.8}$$

Typically, in the alkali gases we consider, the spin-symmetric part of the interacting Hamiltonian is much larger than the nonsymmetric one, that is, $g_s \gg |g_a|$ [147]. Hence, we start by considering the perturbative contributions that stem from the symmetric interaction Hamiltonian.

$$\hat{V}_s = \sum_{a=-1,0,+1} \frac{g_s}{2} \int\int \left(\hat{\Psi}_a^\dagger \hat{\Psi}_a^\dagger \hat{\Psi}_a \hat{\Psi}_a + 2 \sum_{b>a} \hat{\Psi}_a^\dagger \hat{\Psi}_b^\dagger \hat{\Psi}_a \hat{\Psi}_b \right). \tag{4.9}$$

When the terms in (4.9) are evaluated on the low-energy states, it follows that

$$\begin{aligned}
&\int\int \hat{\Psi}_{\pm}^{\dagger}\hat{\Psi}_{\pm}^{\dagger}\hat{\Psi}_{\pm}\hat{\Psi}_{\pm} = \\
&\quad = \int\int \left(1 - \frac{\Omega^2}{32}\left(1 + \frac{\epsilon \pm \delta}{2} \mp \frac{p_1 + p_2 + p_3 + p_4}{2} + O((\Lambda + \frac{\epsilon + \delta}{4})^2)\right)\right) \hat{\varphi}_{\pm}^{\dagger}\hat{\varphi}_{\pm}^{\dagger}\hat{\varphi}_{\pm}\hat{\varphi}_{\pm} \\
&+\frac{\Omega^2}{16}\int\int \left(1 - \frac{\epsilon \pm \delta}{2} \pm (p_2 + p_4) + O((\Lambda + \frac{\epsilon + \delta}{4})^2)\right) \hat{\varphi}_{\pm}^{\dagger}\hat{\varphi}_{0}^{\dagger}\hat{\varphi}_{\pm}\hat{\varphi}_{0},
\end{aligned} \tag{4.10}$$

$$\begin{aligned}
&\int\int \hat{\Psi}_{\pm}^{\dagger}\hat{\Psi}_{\mp}^{\dagger}\hat{\Psi}_{\pm}\hat{\Psi}_{\mp} = \\
&\quad = \int\int \left(1 - \frac{\Omega^2}{32}\left(1 + \frac{\epsilon}{2} \mp \frac{p_1 - p_2 + p_3 - p_4}{2} + O((\Lambda + \frac{\epsilon + \delta}{4})^2)\right)\right) \hat{\varphi}_{\pm}^{\dagger}\hat{\varphi}_{\mp}^{\dagger}\hat{\varphi}_{\pm}\hat{\varphi}_{\mp} \\
&+\frac{\Omega^2}{64}\int\int \left(1 - \frac{\epsilon \pm \delta}{2} \pm (p_1 + p_3) + O((\Lambda + \frac{\epsilon + \delta}{4})^2)\right) \hat{\varphi}_{0}^{\dagger}\hat{\varphi}_{\mp}^{\dagger}\hat{\varphi}_{0}\hat{\varphi}_{\mp} \\
&+\frac{\Omega^2}{64}\int\int \left(1 - \frac{\epsilon \mp \delta}{2} \mp (p_2 + p_4) + O((\Lambda + \frac{\epsilon + \delta}{4})^2)\right) \hat{\varphi}_{\pm}^{\dagger}\hat{\varphi}_{0}^{\dagger}\hat{\varphi}_{\pm}\hat{\varphi}_{0} \\
&+\frac{\Omega^2}{64}\int\int \left(1 - \frac{\epsilon}{2} \pm (p_1 - p_2) + O((\Lambda + \frac{\epsilon + \delta}{4})^2)\right) \hat{\varphi}_{0}^{\dagger}\hat{\varphi}_{0}^{\dagger}\hat{\varphi}_{\pm}\hat{\varphi}_{\mp} \\
&+\frac{\Omega^2}{64}\int\int \left(1 - \frac{\epsilon}{2} \pm (p_3 - p_4) + O((\Lambda + \frac{\epsilon + \delta}{4})^2)\right) \hat{\varphi}_{\pm}^{\dagger}\hat{\varphi}_{\mp}^{\dagger}\hat{\varphi}_{0}\hat{\varphi}_{0},
\end{aligned} \tag{4.11}$$

$$\begin{aligned}
&\int\int \hat{\Psi}_{\pm}^{\dagger}\hat{\Psi}_{0}^{\dagger}\hat{\Psi}_{\pm}\hat{\Psi}_{0} = \\
&\quad = \int\int \left(1 - \frac{\Omega^2}{64}\left(3 - \frac{\epsilon \mp \delta}{2} \mp (p_1 + p_3) + O((\Lambda + \frac{\epsilon + \delta}{4})^2)\right)\right) \hat{\varphi}_{\pm}^{\dagger}\hat{\varphi}_{0}^{\dagger}\hat{\varphi}_{\pm}\hat{\varphi}_{0} \\
&+\frac{\Omega^2}{64}\int\int \left(1 - \frac{\epsilon \pm \delta}{2} \pm (p_1 + p_3) + O((\Lambda + \frac{\epsilon + \delta}{4})^2)\right) \hat{\varphi}_{0}^{\dagger}\hat{\varphi}_{0}^{\dagger}\hat{\varphi}_{0}\hat{\varphi}_{0} \\
&+\frac{\Omega^2}{64}\int\int \left(1 \pm (p_1 - p_2) + O((\Lambda + \frac{\epsilon + \delta}{4})^2)\right) \hat{\varphi}_{0}^{\dagger}\hat{\varphi}_{\pm}^{\dagger}\hat{\varphi}_{\pm}\hat{\varphi}_{0} \\
&+\frac{\Omega^2}{64}\int\int \left(1 \pm (p_3 - p_4) + O((\Lambda + \frac{\epsilon + \delta}{4})^2)\right) \hat{\varphi}_{0}^{\dagger}\hat{\varphi}_{\pm}^{\dagger}\hat{\varphi}_{0}\hat{\varphi}_{\pm} \\
&+\frac{\Omega^2}{64}\int\int \left(1 + \frac{\epsilon \pm \delta}{2} \mp (p_2 + p_4) + O((\Lambda + \frac{\epsilon + \delta}{4})^2)\right) \hat{\varphi}_{\pm}^{\dagger}\hat{\varphi}_{\pm}^{\dagger}\hat{\varphi}_{\pm}\hat{\varphi}_{\pm} \\
&+\frac{\Omega^2}{64}\int\int \left(1 + \frac{\epsilon \mp + \delta}{2} \pm (p_2 + p_4) + O((\Lambda + \frac{\epsilon + \delta}{4})^2)\right) \hat{\varphi}_{\pm}^{\dagger}\hat{\varphi}_{\mp}^{\dagger}\hat{\varphi}_{\pm}\hat{\varphi}_{\mp} \\
&+\frac{\Omega^2}{64}\int\int \left(1 \mp \delta/2 \pm (p_2 + p_3) + O((\Lambda + \frac{\epsilon + \delta}{4})^2)\right) \hat{\varphi}_{\pm}^{\dagger}\hat{\varphi}_{\mp}^{\dagger}\hat{\varphi}_{0}\hat{\varphi}_{0} \\
&+\frac{\Omega^2}{64}\int\int \left(1 \mp \delta/2 \pm (p_1 + p_4) + O((\Lambda + \frac{\epsilon + \delta}{4})^2)\right) \hat{\varphi}_{0}^{\dagger}\hat{\varphi}_{0}^{\dagger}\hat{\varphi}_{\pm}\hat{\varphi}_{\mp},
\end{aligned} \tag{4.12}$$

$$\int\int \hat{\Psi}_0^\dagger \hat{\Psi}_0^\dagger \hat{\Psi}_0 \hat{\Psi}_0 = \int\int \left(1 - \frac{\Omega^2}{16}\left(1 - \frac{\epsilon}{2} + O((\Lambda + \frac{\epsilon+\delta}{4})^2)\right)\right) \hat{\varphi}_0^\dagger \hat{\varphi}_0^\dagger \hat{\varphi}_0 \hat{\varphi}_0$$
$$+\frac{\Omega^2}{16}\int\int \left(1 + \frac{\epsilon+\delta}{2} - (p_1+p_3) + O((\Lambda + \frac{\epsilon+\delta}{4})^2)\right) \hat{\varphi}_+^\dagger \hat{\varphi}_0^\dagger \hat{\varphi}_+ \hat{\varphi}_0$$
$$+\frac{\Omega^2}{16}\int\int \left(1 + \frac{\epsilon-\delta}{2} + (p_1+p_3) + O((\Lambda + \frac{\epsilon+\delta}{4})^2)\right) \hat{\varphi}_-^\dagger \hat{\varphi}_0^\dagger \hat{\varphi}_- \hat{\varphi}_0$$
$$+\frac{\Omega^2}{32}\int\int \left(1 + \frac{\epsilon}{2} - (p_1-p_2) + O((\Lambda + \frac{\epsilon+\delta}{4})^2)\right) \hat{\varphi}_+^\dagger \hat{\varphi}_-^\dagger \hat{\varphi}_0 \hat{\varphi}_0$$
$$+\frac{\Omega^2}{32}\int\int \left(1 + \frac{\epsilon}{2} - (p_3-p_4) + O((\Lambda + \frac{\epsilon+\delta}{4})^2)\right) \hat{\varphi}_0^\dagger \hat{\varphi}_0^\dagger \hat{\varphi}_+ \hat{\varphi}_-, \quad (4.13)$$

Finally, inserting (4.10)-(4.13) into the symmetric contribution to the interacting Hamiltonian (4.9), we get

$$\hat{V}_s = \frac{g_s}{2}\int\int \left(\sum_{a=-1,0,+1}\left(\hat{\varphi}_a^\dagger \hat{\varphi}_a^\dagger \hat{\varphi}_a \hat{\varphi}_a + 2\sum_{b>a} \hat{\varphi}_a^\dagger \hat{\varphi}_b^\dagger \hat{\varphi}_a \hat{\varphi}_b\right)\right)$$
$$+g_s\frac{\Omega^2}{16}\int\int \left(\left(\hat{\varphi}_{+1}^\dagger \hat{\varphi}_{+1} + \hat{\varphi}_{-1}^\dagger \hat{\varphi}_{-1}\right)\hat{\varphi}_0^\dagger \hat{\varphi}_0 + \left(\hat{\varphi}_{+1}^\dagger \hat{\varphi}_{-1}^\dagger \hat{\varphi}_0 \hat{\varphi}_0 + \text{H.c.}\right) + O((\Lambda + \frac{\epsilon+\delta}{4})^2)\right)$$
$$+g_s\frac{\Omega^2}{32}\int\int \left((p_2 - p_1 + p_4 - p_3)\left(\hat{\varphi}_{+1}^\dagger \hat{\varphi}_0^\dagger \hat{\varphi}_{+1} \hat{\varphi}_0 - \hat{\varphi}_{-1}^\dagger \hat{\varphi}_0^\dagger \hat{\varphi}_{-1} \hat{\varphi}_0 + (\hat{\varphi}_{+1}^\dagger \hat{\varphi}_{-1}^\dagger \hat{\varphi}_0 \hat{\varphi}_0 + H.c.)\right)\right.$$
$$\left. + O((\Lambda + \frac{\epsilon+\delta}{4})^2)\right). \quad (4.14)$$

Observe that, as expected, due to momentum conservation no first order corrections appear in the expansion. The second order corrections, however, include the expected spin-changing collisions processes that preserve the total momentum, as the one depicted in Fig. 4.1(b). Note that these processes are analogous to those described for the tight-binding states in the previous chapter, with the same relative strength given by $g_s\Omega^2/16E_r^2$. The last term in (4.14) contains corrections to the spin-mixing contribution that depend linearly on the momentum. Nonetheless, their value is bounded by the cut-off in the momentum spread around the wells. Since, by assumption, $|p_i - p_j| < 2\Lambda \ll 1$, for simplicity we will neglect such momentum-dependent corrections to the interacting Hamiltonian, which will allow us to write the Hamiltonian in a simple form. Indeed, considering that, for $|p| > \Lambda$, the fields $\hat{\varphi}_j(p)$ vanish when acting on the low-energy subspace, we can formally remove the cut-off in the integration and perform the Fourier transform. By doing so, we obtain the following expression for the symmetric interacting Hamiltonian in the dressed basis

$$\hat{V}_s = \int d\mathbf{r}\left[\frac{g_s}{2}\sum_{ij} \hat{\varphi}_i^\dagger \hat{\varphi}_j^\dagger \hat{\varphi}_j \hat{\varphi}_i + \tilde{g}_a\left(\hat{\varphi}_1^\dagger \hat{\varphi}_1 + \hat{\varphi}_{-1}^\dagger \hat{\varphi}_{-1}\right)\hat{\varphi}_0^\dagger \hat{\varphi}_0\right.$$
$$\left. + \tilde{g}_a\left(\hat{\varphi}_1^\dagger \hat{\varphi}_{-1}^\dagger \hat{\varphi}_0 \hat{\varphi}_0 + \hat{\varphi}_1 \hat{\varphi}_{-1} \hat{\varphi}_0^\dagger \hat{\varphi}_0^\dagger\right)\right], \quad (4.15)$$

where we have defined the *synthetic* scattering parameter

$$\tilde{g}_a = g_s \frac{\Omega^2}{16}\left(1 + O((\Lambda + \frac{\epsilon+\delta}{4})^2)\right). \tag{4.16}$$

Remarkably, the contributions proportional to $\tilde{g}_a$ can be group into the term $\frac{\tilde{g}_a}{2}\sum_{i=x,y}(\hat{\boldsymbol{\varphi}}^\dagger \hat{F}_i \hat{\boldsymbol{\varphi}})^2$, where the structure of the resulting effective spin interaction in the dressed Hamiltonian is most evident.

Proceeding analogously with the nonsymmetric part of the interaction potential, $\hat{V}_a = \frac{g_a}{2}\int d\mathbf{r}\sum_j (\hat{\boldsymbol{\Psi}}^\dagger \hat{F}_j \hat{\boldsymbol{\Psi}})^2$, yields

$$\hat{V}_a = \frac{g_a}{2}\int d\mathbf{r}\sum_j (\hat{\boldsymbol{\varphi}}^\dagger \hat{F}_j \hat{\boldsymbol{\varphi}})^2 + O(g_a\Omega^2), \tag{4.17}$$

which includes the zero order term plus second (and higher) order corrections proportional to $g_a\Omega^2$. Since we assume $|g_a| \ll g_s$, we will safely neglect such corrections in the total Hamiltonian.

Finally, we can group all the contributions (4.5), (4.15) and (4.17) to the low-energy dressed field Hamiltonian

$$\begin{aligned}\hat{H} &= \hat{H}_{\text{n.i.}} + \hat{V}_s + \hat{V}_a \\ &= \int d\mathbf{r}\left[\hat{\boldsymbol{\varphi}}^\dagger\left(\frac{\mathbf{p}^2}{2m} + V_{\text{t}} + \delta\hat{F}_z + \tilde{\epsilon}\hat{F}_z^2\right)\hat{\boldsymbol{\varphi}} + \frac{g_s}{2}\sum_{ij}\hat{\varphi}_i^\dagger\hat{\varphi}_j^\dagger\hat{\varphi}_j\hat{\varphi}_i\right] \\ &+ \int d\mathbf{r}\left[\frac{g_a}{2}\sum_{j=x,y,z}(\hat{\boldsymbol{\varphi}}^\dagger\hat{F}_j\hat{\boldsymbol{\varphi}})^2 + \frac{\tilde{g}_a}{2}\sum_{i=x,y}(\hat{\boldsymbol{\varphi}}^\dagger\hat{F}_i\hat{\boldsymbol{\varphi}})^2\right],\end{aligned} \tag{4.18}$$

In this way, when written in terms of the pseudospinor field $\hat{\boldsymbol{\varphi}}$, the perturbative expansion of the weakly-coupled Raman-dressed spinor Hamiltonian around the single-particle band minima describes an effective undressed spinor gas. With this description, we can treat the dressed system as an undressed one, where all the relevant effects from the dressing, within the order of approximation considered, are simply incorporated into the modified nonsymmetric interactions. Notice that the presence of SOC induces an anisotropy in the spin-dependent collisions, by giving rise to an effective spin interaction that acts only in the direction transversal to the Zeeman quantization axis, $\mathbf{e}_z$. This anysotropy breaks the SO(3) symmetry of the intrinsic spin-spin interactions in the gas into a SO(2) symmetry. The degree of anisotropy will depend on the ratio between the intrinsic and SOC-induced spin parameters $\propto \tilde{g}_a/g_a$.

4.2.2 Collective spin model

In Sec. 4.2.1 we have seen that the weakly-coupled Raman-dresed spin-1 Bose gas can actually be described in terms of an *artificial* undressed spinor gas. Often, spinor gases are treated following the commonly considered single-spatial-mode approximation

[320]. When this consideration holds, the system realizes a collective spin Hamiltonian, which allows the description within a simple framework of a large variety of quantum many-body phenomena in spinor condensates [147]. For our *artificial* spinor gas, we will now consider the regime where we can take a similar approximation. To do so, we essentially require that the symmetric and the nonsymmetric contributions to dressed spinor Hamiltonian (4.18) are energetically well-separated. The former can be grouped into

$$\hat{H}_{\mathrm{S}} = \int d\mathbf{r} \left[\sum_i \hat{\varphi}_i^\dagger \left(\frac{\mathbf{p}^2}{2m} + V_{\mathrm{t}} \right) \hat{\varphi}_i + \frac{g_s}{2} \sum_{ij} \hat{\varphi}_i^\dagger \hat{\varphi}_j^\dagger \hat{\varphi}_j \hat{\varphi}_i \right], \tag{4.19}$$

while the latter are collected into

$$\hat{H}_{\mathrm{A}} = \int d\mathbf{r} \left[\frac{g_a}{2} \sum_{j=x,y,z} (\hat{\boldsymbol{\varphi}}^\dagger \hat{F}_j \hat{\boldsymbol{\varphi}})^2 + \frac{\tilde{g}_a}{2} \sum_{i=x,y} (\hat{\boldsymbol{\varphi}}^\dagger \hat{F}_i \hat{\boldsymbol{\varphi}})^2 + \hat{\boldsymbol{\varphi}}^\dagger \left(\delta \hat{F}_z + \tilde{\epsilon} \hat{F}_z^2 \right) \hat{\boldsymbol{\varphi}} \right], \tag{4.20}$$

so that $\hat{H} \simeq \hat{H}_{\mathrm{S}} + \hat{H}_{\mathrm{A}}$. By requiring that $\langle \hat{H}_{\mathrm{A}} \rangle \ll \langle \hat{H}_{\mathrm{S}} \rangle$, we can treat the low-energy landscape by simply considering the perturbative action of $\hat{H}_{\mathrm{A}}$ over the ground state solutions of $\hat{H}_{\mathrm{S}}$. The lowest energy solutions of the symmetric part of the dressed spinor Hamiltonian can then be written as superpositions of three pseudospin modes that share the same spatial wavefunction, regardless of the many-body occupation of each mode. Therefore, we will henceforth truncate the Hilbert space of the system to these three self-consistent many-body modes of $\hat{H}_{\mathrm{S}}$ and assume that the dynamics is then well described by a three-mode model. We label the three eigenmodes of $\hat{H}_{\mathrm{S}}$ as $|\phi_{-1}\rangle$, $|\phi_0\rangle$ and $|\phi_1\rangle$, and introduce the associated bosonic operators $\hat{b}_{-1}$, $\hat{b}_0$ and $\hat{b}_1$, respectively. With this definitions, we now truncate the dressed field operators to $\hat{\varphi}_i^\dagger(\mathbf{r}) \sim \phi_i^*(\mathbf{r}) \hat{b}_i^\dagger$. We call the three modes, $|\phi_j\rangle$, pseudospin states.

Note that in the dressed basis, which corotates with the dressing beams, this truncation can be regarded as the single-spatial-mode approximation of the pseudospinor gas, where the spatial wavefunctions of the solutions are independent of the pseudospin state. Yet, here, each solution is located at the vicinity of each band minimum $\mathbf{k}_j$, and the wavefunctions are modulated in the laboratory frame by a pseudospin-dependent spatial phase $\exp(i\mathbf{k}_j \cdot \mathbf{r})$ that stems from SOC. Such modulations will have a major role in the next section, where the internal properties of the collective spin Hamiltonian will be connected to the external spatial properties of the Raman-dressed gas. Therefore, to emphasize the actual distinction of the three wave-functions, we refer to the truncation we have taken as a three-mode approximation.

By construction, introducing the truncated field operators into (4.19) results in a contribution that depends only on the total number of particles, N, which we will henceforth drop. All the dynamics in the gas is therefore captured by the perturbative action of the nonsymmetric contribution to the total Hamiltonian, which we account by substituting the truncated field operators into (4.20). Doing so, we obtain the following

one-axis-twisting Hamiltonian

$$\hat{H}_{\text{eff}} = \frac{\lambda}{2N}\hat{L}^2 - \frac{\lambda - g_a\bar{n}}{2N}\hat{L}_z^2 + \delta\hat{L}_z + \left(\tilde{\epsilon} + \frac{\lambda}{2N}\right)\hat{L}_{zz}, \tag{4.21}$$

where we have introduced the collective pseudospin operators $\hat{L}_{x,y,z} = \sum_{\mu\nu}\hat{b}_\mu^\dagger(\hat{F}_{x,y,z})_{\mu\nu}\hat{b}_\nu$ and $\hat{L}_{zz} = \sum_{\mu\nu}\hat{b}_\mu^\dagger(\hat{F}_z^2)_{\mu\nu}\hat{b}_\nu$, and where we define the spin interaction parameter

$$\lambda = (\tilde{g}_a + g_a)\bar{n} = \left(g_s\frac{\Omega^2}{16E_r^2} + g_a\right)\bar{n}, \tag{4.22}$$

with $\bar{n}$ being the mean density of the gas [1].

Since $[\hat{H}_{\text{eff}}, \hat{L}_z] = 0$, the total magnetization is preserved by $\hat{H}_{\text{eff}}$. Therefore, if we prepare an initial state of the system in an eigenstate of $\hat{L}_z$, with eigenvalue m_z, the dynamics will be restricted to the subspace with magnetization $\langle\hat{L}_z\rangle = m_z$. In this situation, the second and third terms in (4.21) amount to just a global energy shift, that we can drop, and the effective Hamiltonian (4.21) reduces to

$$\hat{H}_0 = \lambda\frac{\hat{L}^2}{2N} + \tilde{\epsilon}\hat{L}_{zz}, \tag{4.23}$$

where for clarity we have also neglected the small correction to the last term in equation (4.21) given by $\frac{\lambda}{2N}\hat{L}_{zz}$, given that in this chapter we consider $N \gg 1$. Henceforth, we will restrict ourselves to the subspace with $m_z = 0$, where the dropped constant terms are, in fact, null. This restriction is reasonable from an experimental point of view, since the $m_z = 0$ subspace is the simplest to realize.

Hamiltonian (4.23) is completely analogous to the Hamiltonian that describes the nonlinear collective spin dynamics in a spin-1 BEC [165]. In the SOC-based realization of (4.23) that we propose, though, the spin-spin interaction strength λ can be adjusted by adjusting the Raman coupling strength Ω. As anticipated, the collective spin Hamiltonian derived in this section is equivalent to Hamiltonian (3.48) in chapter 3, excluding the term proportional to λ_2. Such a term corresponds here to the dressed collision processes that couple the $\hat{\varphi}_1$ and $\hat{\varphi}_{-1}$ pseudospins, which are of fourth order in Ω/E_r in the perturbative expansion of the interacting Hamiltonian, and hence have been directly neglected. However, with the approach taken in this chapter, we do not require the scale separation between the noninteracting and the interacting energy scales that was assumed in the derivation of the tight-binding model of chapter 3, which roughly demanded $g_s\bar{n} \ll \hbar\omega$. Here, the three self-consistent modes play the role of the bound well states, and the scale separation is required instead between the symmetric and the nonsymmetric interaction energies in the effective spinor Hamiltonian. In this manner, we can achieve the desired scale separation without severely constraining the density of

[1] Since the spinor modes $|\phi_j\rangle$ are determined through the symmetric Hamiltonian (4.19), we have that $|\phi_i(\mathbf{r})| = |\phi_j(\mathbf{r})|$ for all $i, j = -1, 0, 1$. Thus, within the subspace spanned by these three modes, the mean density of the gas is simply given by $\bar{n} = N\int d\mathbf{r}|\phi_0(\mathbf{r})|^4$.

the gas. This allows the realization of the same collective spin model with thousands of particles in the cloud, as we will see in the next sections.

So far, we have established the analytical equivalence, within the order of approximation considered, of the Raman-dressed gas to an undressed Bose gas with tunable spin interactions. On the one hand, this treatment of the dressed gas suggests that spin-orbit-coupled BECs can provide an alternative platform for designing entanglement protocols and studying dynamical phase transitions and nonequilibrium dynamics, where the coupling between spin and momentum and the enhanced tunability of the spin-spin interactions may offer many possibilities that go beyond those of undressed spinor gases. On the other hand, this formulation provides a simple framework to understand the quantum phases of the Raman-dressed gas and their dynamics. In the next section, we will exemplify the use of such insights by designing a protocol based on this map to prepare a supersolid-like stripe phase of the spin-1 spin-orbit-coupled gas.

4.3 Dynamical preparation of stripe states

In this section we will show that the properties of the Raman-dressed gas can be easily understood in terms of the pseudospin model. Most importantly, we will see that under suitable conditions, the map needs not be limited to describe the properties of the ground state, but can be extended to a low-lying family of energy eigenstates of the dressed condensate that comprises the whole spectrum of the collective spin model. Finally, we will see how this understanding of the low-energy landscape can be exploited to design a protocol to prepare the ferromagnetic stripe phase of the system.

4.3.1 Phase diagram of the collective spin model

The phases of the collective pseudospin Hamiltonian (4.23) derived in the previous section depend on the relative strength of the two noncommuting competing terms: one proportional to the total spin squared $\hat{L}^2$, and one proportional to the quadrupolar term $\hat{L}_{zz}$. Accordingly, these can be characterized by a single parameter, that is, the ratio $\tilde{\epsilon}/\lambda$. Hamiltonian (4.23) has two characteristic regimes depending on the sign of the spin interactions. When the interactions are of antiferromagnetic nature, i.e. $\lambda > 0$, the ground state is then either in a polar (P) phase for $\tilde{\epsilon}/\lambda > 0$, where all the atoms occupy the $|\phi_0\rangle$ state, or in a twin-Fock (TF) phase for $\tilde{\epsilon}/\lambda < 0$, in which the ground state approximates the spin-$\frac{1}{2}$ balanced Dicke state $\frac{1}{(N/2)!}(\hat{b}^\dagger_{-1})^{N/2}(\hat{b}^\dagger_1)^{N/2}|0\rangle$. In this regime, the two phases are simply favored and characterized by the noninteracting magnetic term $\hat{L}_{zz}$, with a first-order phase transition between them ocurring at $\tilde{\epsilon} = 0$, as shown in Fig. 4.2(a). The ferromagnetic regime of (4.23), with $\lambda < 0$, is richer, since the interacting term will tend to maximize the total spin. When $|\lambda|$ is sufficiently large, this spin-spin interactions favors a ground state with a non-vanishing transverse magnetization. This spontaneous breaking of the SO(2) symmetry of the system [301]

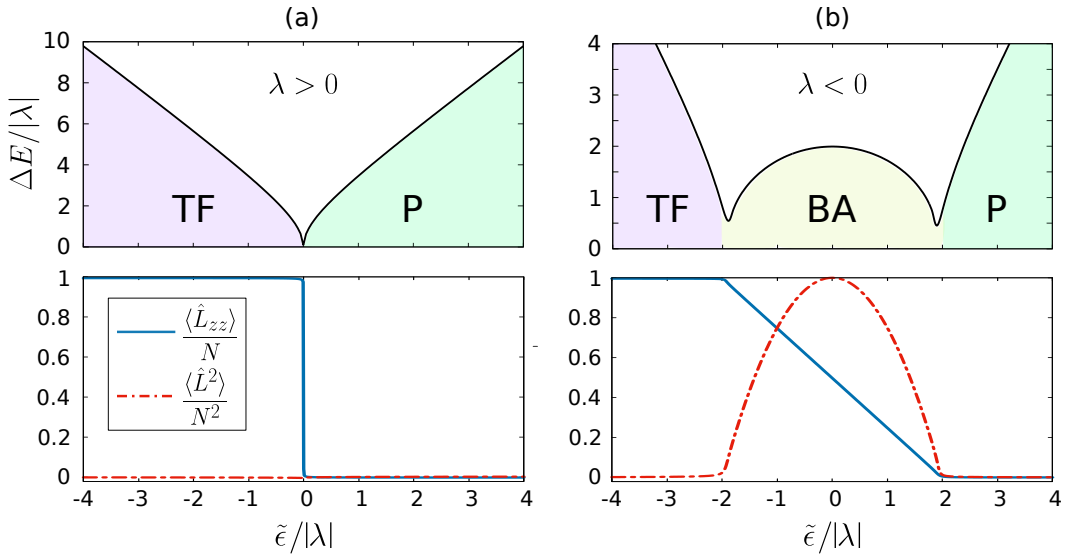

Figure 4.2: Phases of the collective spin model. (a) Upper panel: energy gap ΔE between the two lowest eigenstates of Hamiltonian (4.23) for $N = 1000$ and for $\lambda > 0$ (antiferromagnetic spin interactions) as a function of $\tilde{\epsilon}/|\lambda|$. Lower panel: corresponding expected value of the total collective pseudospin squared $\hat{L}^2$ (red dashed line) and tensor magnetization $\hat{L}_{zz}$ (blue solid line) of the ground state. Figure (b) shows the corresponding quantities for the ferromagnetic regime, with $\lambda < 0$. In both figures, the color filling is used as guide to the eye to highlight the regions that correspond to the polar (P), twin-fock (TF) and broken-axisymmetry (BA) phases.

gives rise to the so-called broken-axisymmetry (BA) phase [324] in between the TF and P phases. The phase is signaled by a nonzero total spin, with the tensor magnetization decreasing uniformingly with $\tilde{\epsilon}$ across the phase. In the thermodynamic limit, the two second-order transitions take place, respectively, at $\tilde{\epsilon} = \pm 2|\lambda|$, as depicted in Fig. 4.2(b).

The different phases are well captured by a mean-field description of model (4.23). In this limit, we assume that the solutions of the system are given by projective coherent states $|N, \mathbf{N}, \boldsymbol{\theta}\rangle = \frac{1}{\sqrt{N!}} \left(\sum_j \sqrt{N_j/N} e^{i\theta_j} b_j^\dagger \right)^N |0\rangle$, that is, a macroscopic occupation of a single single-particle state $|\phi\rangle = \sum_j \sqrt{N_j/N} e^{i\theta_j} b_j^\dagger |0\rangle$. In the thermodynamic limit, the quantum fluctuations of these solutions vanish, and the dynamics of coherent states is well described by the classical trajectories of the complex quantities $b_j = \sqrt{N_j} e^{i\theta_j}$ (see Sec. 2.2.2). Here, N_j and θ_j are, respectively, the mean occupation and phase of the mode $\hat{b}_j |0\rangle$ in the coherent state $|N, \mathbf{N}, \boldsymbol{\theta}\rangle$. The mean-field energy is retrieved then by substituting the mode operators $\hat{b}_j$ in Hamiltonian (4.23) with their expected values b_j, which yields

$$E_{\mathrm{mf}} = \frac{\lambda}{N} \left[(b_{-1}^\dagger b_1^\dagger b_0 b_0 + H.c.) + N_0(N_1 + N_{-1}) \right] + \tilde{\epsilon}(N - N_0). \tag{4.24}$$

Fixing $m_z = 0$, we have $N_1 = N_{-1} = \frac{N-N_0}{2}$, and the mean-field energy can be written as

$$E_{\rm mf} = \frac{2\lambda}{N}(N-N_0)N_0\cos^2\theta + \tilde{\epsilon}(N-N_0), \tag{4.25}$$

where we have defined the spinor phase $\theta = \theta_0 - \frac{\theta_1+\theta_{-1}}{2}$. The tensor magnetization and the total spin read

$$\langle \hat{L}_{zz}\rangle = N - N_0, \qquad \langle \hat{L}^2\rangle = 4(N-N_0)N_0\cos^2\theta. \tag{4.26}$$

Clearly, for $\lambda > 0$, the mean-field energy (4.25) is minimized when $\tilde{\epsilon} > 0$ at $N_0 = N$, and so $L^2 = \langle \hat{L}^2\rangle = 0$ and $L_{zz} = \langle \hat{L}_{zz}\rangle = 0$ (P phase). Likewise, when $\tilde{\epsilon} < 0$ the energy is minimized at $N_0 = 0$, and so $L^2 = 0$ and $L_{zz} = N$ (TF phase). Therefore, the spin-spin interacting energy in the antiferromagnetic regime is null across the whole diagram. Contrarily, the ferromagnetic regime is characterized by a nonzero interacting energy in the BA phase. When $\lambda < 0$, the energy is minimal at $\theta = \pi k$ for $0 < N_0 < N$. Then, the solutions fulfill $\frac{\partial E_{\rm mf}}{\partial N_0} = -\frac{2|\lambda|}{N}(N-2N_0) - \tilde{\epsilon} = 0$ and so we have

$$N_0 = \frac{N}{2}\left(\frac{\tilde{\epsilon}}{2|\lambda|}+1\right), \qquad \theta = \pi k, \quad k\in\mathbb{Z}, \tag{4.27}$$

for $-2|\lambda| \le \tilde{\epsilon} \le 2|\lambda|$. Therefore, in the BA phase

$$L_{zz} = \frac{N}{2}\left(1-\frac{\tilde{\epsilon}}{2|\lambda|}\right), \qquad L^2 = N^2\left(1-\frac{\tilde{\epsilon}^2}{4|\lambda|^2}\right). \tag{4.28}$$

For $|\tilde{\epsilon}| > 2|\lambda|$, the spin energy vanishes, and the system realizes the P and TF phases as in the antiferromagnetic case (see Fig. 4.2).

Despite its simplicity, model (4.23) displays thus a rich phase diagram. The interplay between the two competing contributions in the Hamiltonian has been employed in spinor gases to, e.g., generate spin-squeezed macroscopic states [73], with both the BA and the TF phases being macroscopically entangled. The platform has also been proposed recently for the exploration of dynamical and excited-state quantum phase transitions [297, 298, 322, 323].

4.3.2 Phases of the dressed gas as a pseudospin model

Let us now assume the validity of model (4.23) as a description for the Raman-dressed gas. With this assumption in mind, to be checked later on in this section, we can map the paramters of the pseudospin model, λ and $\tilde{\epsilon}$, to the parameters of the original dressed Hamiltonian, Ω and ϵ, to describe the phase diagram of the dressed system in these terms. This is illustrated in Fig. 4.3(a), where we show phase diagram of Hamiltonian (4.23) in the $\Omega-\epsilon$ plane. In the figure, we use expressions (4.6) and (4.22) for $\tilde{\epsilon}(\Omega,\epsilon)$ and $\lambda(\Omega)$, and consider ^{87}Rb, with $g_a/g_s = -0.0047$ [147], and a mean atom density of $\bar{n} = 7.5\times10^{13}$ cm^{-3}. For $\Omega > \Omega_c = 4E_r\sqrt{|g_a|/g_s}$, we have $\lambda > 0$, and the diagram is equivalent

to that of an antiferromagnetic spinor gas, which includes the P and TF phases. At $\Omega = \Omega_c$, the effective and the intrinsic spin-mixing dynamics mutually compensate, by having $\tilde{g}_a = -g_a$, which yields $\lambda = 0$. Finally, for $\Omega < \Omega_c$, the effective spin dynamics is ferromagnetic, $\lambda < 0$, and the BA phase is favored in the region $-2|\lambda| < \tilde{\epsilon}(\Omega, \epsilon) < 2|\lambda|$. The three phases meet at the tricritical point C_F, at $\Omega = \Omega_c$ and $\epsilon = g_a/g_s$. We emphasize that these phases are obtained in the zero-magnetization subspace. Without enforcing such constraint, the BA and the P phase are expected to persist, but the ground state in the two-minima regime where the macroscopically entangled TF phase is predicted would instead realize the magnetized plane-wave (PW) phase of the spin-1 spin-orbit-coupled gas. There, a global Z_2 symmetry of the Hamiltonian is spontaneously broken favoring the formation of a condensate in either of the band minimums. The PW phase is characterized by a nonzero magnetization $\sim k_{\pm 1}/k_r$, and the transition from the BA phase to the PW phase is of first-order nature. For a comprehensive discussion of the ground state phases of the dressed gas in the different regimes, see [196]. Still, as we will discuss below, the zero-magnetization manifold can be robustly prepared and explored exploiting the induced spin-mixing dynamics, which will justify the use here of the truncated pseudospin model.

Remarkably, in the Raman-dressed BEC, the collective spin phases described exhibit richer features. With the induced spin-orbit coupling, the structures appearing in the internal (spin) degrees of freedom are transferred to the external (motional) degrees of freedom. Most notably, the BA phase of the effective model corresponds to the supersolid-like ferromagnetic stripe (FS) phase of the spin-1 SOC gas diagram, described in detail in [196]. The FS phase is characterized by the presence of spatial density modulations that are proportional to Ω. The emergence of these density modulations is well understood from the mean-field limit of the pseudo-spin model. The mean-field wavefunction of the gas in the three-mode approximation reads $\boldsymbol{\psi}(\mathbf{r}) = \sum_j \sqrt{N_j}\boldsymbol{\phi}_j(\mathbf{r})e^{i\theta_j}$. Here N_j and θ_j are, respectively, the mean occupation and phase of the mode $\hat{b}_j\,|0\rangle$ in the coherent state $|N, \mathbf{N}, \boldsymbol{\theta}\rangle$, and $\boldsymbol{\phi}_j$ is the corresponding spinor spatial wavefunction. Since we consider that the three modes are tightly located at the vicinity of the respective band minima $\mathbf{k}_j$, we can approximate them by plane waves times an slowly varying envelope function, which for simplicity will omit in the following argument. Then, up to second order in $\Omega/8E_r$, and neglecting the corrections proportional to $(\epsilon + \delta)\Omega^2/E_r^3$, we can write

$$
\begin{aligned}
\boldsymbol{\phi}_1(\mathbf{r}) &\propto e^{i\mathbf{k}_1\cdot\mathbf{r}} \left(1 - \frac{1}{2}\left(\frac{\Omega}{8E_r}\right)^2, \frac{\Omega}{8E_r}, 0\right)^T, \\
\boldsymbol{\phi}_0(\mathbf{r}) &\propto e^{i\mathbf{k}_0\cdot\mathbf{r}} \left(\frac{\Omega}{8E_r}, 1 - \left(\frac{\Omega}{8E_r}\right)^2, \frac{\Omega}{8E_r}\right)^T, \\
\boldsymbol{\phi}_{-1}(\mathbf{r}) &\propto e^{i\mathbf{k}_{-1}\cdot\mathbf{r}} \left(0, \frac{\Omega}{8E_r}, 1 - \frac{1}{2}\left(\frac{\Omega}{8E_r}\right)^2\right)^T.
\end{aligned}
\tag{4.29}
$$

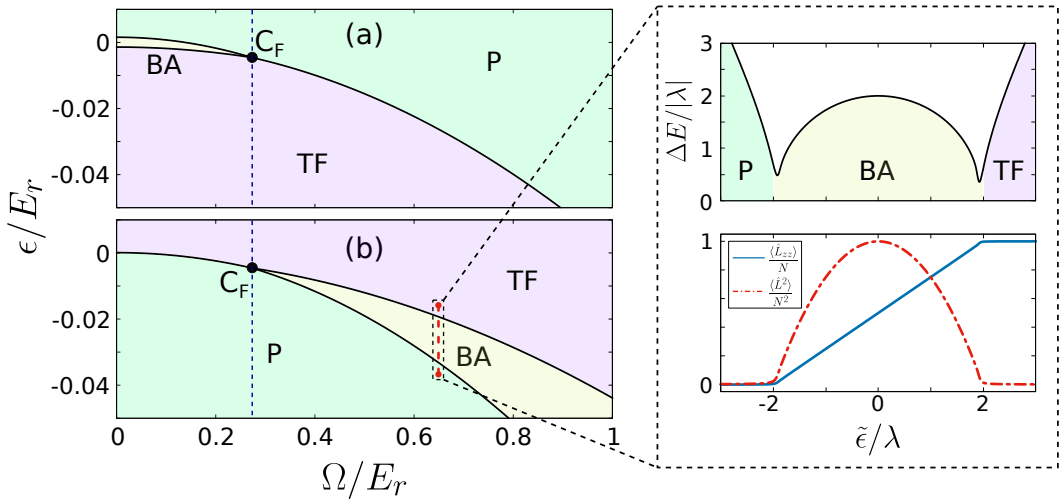

Figure 4.3: Collective pseudospin dynamics in SOC BECs. For weak Raman coupling and interactions, the dressed-state dynamics can be captured by the pseudospin Hamiltonian (4.23). (a) Phase diagram of (4.23), as a function of the Raman Rabi frequency Ω and effective quadratic Zeeman shift ϵ, for ^{87}Rb at $n = 7.5 \times 10^{13}$ cm^{-3}. The polar (P), twin-Fock (TF) and broken-axisymmetry (BA) phases meet at the tricritical point C_F (black dot). The blue dashed vertical line at $\Omega_c = 4E_r\sqrt{|g_a|/g_s}$ separates the ferromagnetic ($\lambda < 0$) and the antiferromagnetic ($\lambda > 0$) regimes of the effective Hamiltonian. (b) Corresponding phase diagram for the highest-excited eigenstate. The upper panel in the inset shows the energy gap ΔE between the two most excited eigenstates along the red dashed segment for $N = 1000$. The lower panel shows the expected value of the collective pseudospin $\hat{L}^2$ (red dashed line) and tensor magnetization $\hat{L}_{zz}$ (blue solid line).

At $m_z = 0$, the mode occupations fulfill $N_1 = N_{-1} = (N - N_0)/2$. Moreover, since we consider $\delta \ll E_r$, we have $\mathbf{k}_0 \simeq 0$ and $\mathbf{k}_1 \simeq -\mathbf{k}_{-1}$. In these conditions, the spatial density of the gas $n(\mathbf{r}) = \boldsymbol{\psi}^*(\mathbf{r}) \cdot \boldsymbol{\psi}(\mathbf{r})$ reads

$$n(\mathbf{r}) \simeq \bar{n}\left(1 + \cos(\mathbf{k}_1 \cdot \mathbf{r} - \theta_1 + \theta_{-1})\frac{\Omega}{E_r}\sqrt{\frac{N_0(N-N_0)}{2N^2}}\cos\theta + O((\Omega/8E_r)^2)\right), \quad (4.30)$$

where $\bar{n}$ is the average density.

Expression (4.30), describes a density distribution that is periodically modulated along the direction of the Raman momentum, with wavelength $\sim \pi/k_r$. The amplitude of the modulation is linearly proportional to Ω/E_r, times a factor that depends on the occupation of the central mode N_0 and on the spinor phase θ. As discussed above, in the ferromagnetic regime, the spin interactions favor the simultaneous occupation of the three modes when $|\tilde{\epsilon}| > 2|\lambda|$, with $0 < N_0 < N$, while at the same time locking the phase at $\theta = \pi k$. Inserting the values fro N_0 and θ from equation (4.27) into (4.30), we see that the amplitude of the modulations become nonzero when the ground state enters the BA phase, increasing as $|\tilde{\epsilon}|$ diminishes and reaching its maximum value at $\tilde{\epsilon} = 0$.

4.3.3 The FS phase as an excited state

We have seen that the BA phase of the pseudospin model (4.23) describes the FS phase of the dressed gas. However, in condensates of both ^{41}K and ^{87}Rb atomic species, commonly employed to realize Raman-dressed gases due to their relatively large fine structre splitting, the nonsymmetric interactions are small. This implies that the FS phase is only favored in a very narrow region in parameter space, as shown in Fig. 4.3(a), which makes its experimental realization challenging. Alternatively, the pseudospin map suggests that the ferromagnetic landscape can be probed instead in a low-lying excited state of the Raman-dressed gas that corresponds to the most-excited manifold of $\hat{H}_0$ in the antiferromagnetic regime. The ground and most excited manifolds of the ferromagnetic and antiferromagnetic regimes are directly related, as $\hat{H}_0(\lambda, \tilde{\epsilon}) = -\hat{H}_0(-\lambda, -\tilde{\epsilon})$. In Fig. 4.3(b), we show the phase diagram for the most excited state of $\hat{H}_0$. It displays the same phases as the ground state, but with the phase boundaries redefined. The inset in Fig. 4.3(b) illustrates the equivalence between the structure of the excited antiferromagnetic states and that of the ferromagnetic ground states shown in Fig. 4.2(b). Notably, in the excited-state diagram, the predicted BA phase occurs for a much broader range of parameters, which could be exploited to facilitate the preparation of the FS phase. Besides that, in the excited diagram, the BA phase –and therefore the predicted stripe phase– occurs at larger Ω. Hence, the dressed gas should exhibit there a larger contrast of the density modulations, when compared to its ground-state counterpart.

While often preparing a specific excited state can be laborious, here we propose to access the BA state in the highest excited state of the effective model by driving a fully polarized state across the P-BA quantum phase transition in the excited manifold. To do so, we can exploit the fact that, at the P-BA and BA-TF transitions, the energy gap ΔE between the two highest excited states closes slowly for increasing total number of particles (see inset in Fig. 4.3(b)), with ΔE being proportional to $\lambda N^{-1/3}$. This facilitates the quasi-adiabatic driving through both phase transitions in workable time scales even when the number of particles is large. This feature was used in [282] and [283] to generate macroscopic TF and BA states, respectively, in ^{87}Rb spinor condensates.

In this way, following the dressed-spinor description, we propose to probe the ferromagnetic phase diagram in the most excited phase diagram of the effective model by driving an initially polarized state. The loading of such a state could be easily achieved from an undressed condensate in the $m_f = 0$ bare spin state by adiabatically turning up Ω, while setting $\tilde{\epsilon} < -2\lambda$. The excited phase diagram can then be probed by varying ϵ and Ω, which allows to access the FS phase of the spin-orbit-coupled gas, in correspondence to the BA phase of the pseudospin model. Naturally, this preparation assumes the validity of the three-mode truncation that leads to Hamiltonian (4.23), and it is expected to rely on the existence of the energy gap predicted therein. Qualitatively, the truncation is expected to be the accurate for small condensates when $|\lambda|, |\tilde{\epsilon}| \ll g_s n, \hbar\omega_t$. Nonetheless, it is difficult to quantitatively estimate its accuracy. To this end, below we will assess the extent of the truncation by simulating the protocol using the Gross–Pitaevskii

equation for the full dressed gas.

4.3.4 Dynamical preparation of FS states: Gross-Pitaevskii results

By replacing the field operator $\hat{\boldsymbol{\Psi}}$ with a scalar spinor wavefunction $\boldsymbol{\psi} = (\psi_{-1}, \psi_0, \psi_1)^T$ in (4.1) we obtain the energy functional

$$E[\boldsymbol{\psi}] = \int d\mathbf{r} \left[\boldsymbol{\psi}^* \left(\hat{\mathcal{H}}_{\mathrm{k}} + V_{\mathrm{t}} \right) \boldsymbol{\psi} + \frac{g_s}{2} |\boldsymbol{\psi}|^4 + \frac{g_a}{2} \sum_j (\boldsymbol{\psi}^* \hat{F}_j \boldsymbol{\psi})^2 \right] \tag{4.31}$$

that describes the mean-field regime of the Raman-dressed BEC (see Sec. 2.2.2 for more details on the mean-field treatment of a Bose gas). The time evolution is described by the time-dependent Gross-Pitaevskii equation (GPE)

$$i\hbar \dot{\psi}_j = \delta E[\boldsymbol{\psi}] / \delta \psi_j^*. \tag{4.32}$$

To evaluate the feasibility of the preparation of the FS phase in an excited state as described in Sec. 4.3.3, we will now compute the GPE.We incorporate a time-dependent parameter $\tilde{\epsilon}(t)$, in order to simulate a quasi-adiabatic drive across the quantum phases predicted by the effective model. To retrieve the quantities relevant to the three-mode model, we calculate the three self-consistent modes $\boldsymbol{\phi}_j$ via imaginary time evolution of the GPE. The modes can be easily obtained by projecting the ground state at $\delta = \tilde{\epsilon} = 0$, which populates the three well states, into the well separated regions around each minimum of the lowest band. Given the small range of values that we consider for both ϵ and δ, we can neglect the perturbative deviations of the expressions for such modes from the ones obtained at $\delta = \tilde{\epsilon} = 0$. We can then compute $N_0 = b_0^* b_0$ and $\theta = \arg(b_0) - (\arg(b_1) + \arg(b_{-1}))/2$, using $b_j = \int d\mathbf{r} \boldsymbol{\phi}_j^*(\mathbf{r}) \cdot \boldsymbol{\psi}(\mathbf{r})$. As a reference, we will consider similar conditions to those described in [283], with small ^{87}Rb condensates in the $F = 1$ hyperfine manifold at $n \sim 7.5 \times 10^{13}$ cm^{-3}, and take $E_r/\hbar = 2\pi \times 3680$ Hz, $k_r = 7.95 \times 10^6$ m^{-1} and $g_s k_r^3 = 1.066\, E_r$.

Before discussing the results from GPE simulations, however, there is one important remark to make. In the P and TF phases of the spin Hamiltonian, the state approaches the Fock states $\frac{1}{\sqrt{N!}}(\hat{b}_0^\dagger)^N |0\rangle$ and $\frac{1}{(N/2)!}(\hat{b}_{-1}^\dagger)^{N/2}(\hat{b}_1^\dagger)^{N/2} |0\rangle$, respectively. As long as the three modes are not significantly populated, as it is the case for the states above, the mean-field dynamics is expected to be inaccurate, with the actual dynamics being dominated by quantum fluctuations [273, 325]. This can be immediately seen from expression (4.24) for the mean-field energy. The corresponding three-mode mean-field equations read

$$\begin{aligned} i\hbar \dot{b}_0 &= \delta E_{\mathrm{mf}} / \delta b_0^* = \frac{\lambda}{N} \left[2 b_1 b_{-1} b_0^* + b_1^* b_1 b_0 + b_{-1}^* b_{-1} b_0 \right] - \tilde{\epsilon} b_0, \\ i\hbar \dot{b}_{\pm 1} &= \delta E_{\mathrm{mf}} / \delta b_{\pm}^* = \frac{\lambda}{N} \left[b_{\mp 1}^* b_0 b_0 + b_0^* b_0 b_{\pm 1} \right]. \end{aligned} \tag{4.33}$$

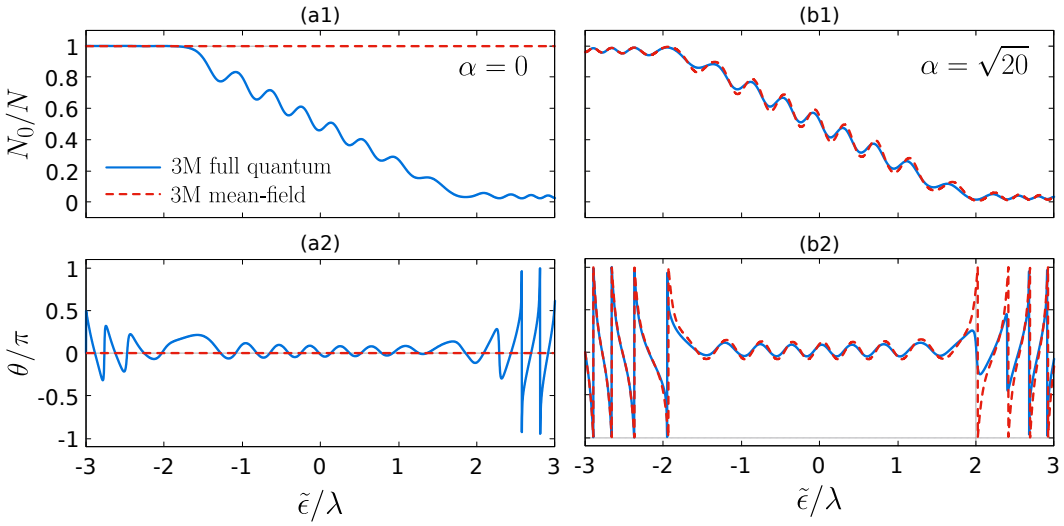

Figure 4.4: Comparison between full quantum and mean-field simulations. A state initially prepared at the coherent state with $b_{\pm1}(0) = \alpha$ and $b_0(0) = \sqrt{N - 2|\alpha|^2}$ is driven from $\tilde{\epsilon} = -3\lambda$ to $\tilde{\epsilon} = 3\lambda$ by linearly increasing $\tilde{\epsilon}$ over a time $\tau_d = 8h/\lambda$. The relative occupation of the state $|\phi_0\rangle$, N_0/N, along the drive is plotted in (a1) and (b1) for $\alpha = 0$ and $\alpha = \sqrt{20}$, respectively. In both cases $N = 1000$. The corresponding values for the spinor phase θ is plotted in (a2) and (b2). Solid blue lines show the results from full quantum simulations of Hamiltonian (4.23). Red dashed lines show the results obtained with the mean-field equations (4.33).

Clearly, initially setting $b_{\pm1} = 0$ or $b_0 = 0$ into eqs. (4.33) results in a stationary state, independently of $\tilde{\epsilon}$, in contradiction with the dynamics predicted by the quantum Hamiltonian (4.23). There, the presence of the effective spin-changing collision processes $\hat{b}_1^\dagger \hat{b}_{-1}^\dagger \hat{b}_0 \hat{b}_0$ and $\hat{b}_1 \hat{b}_{-1} \hat{b}_0^\dagger \hat{b}_0^\dagger$ prevents any Fock state from truly being an eigenstate of the Hamiltonian for finite N. Even at very large N, such small deviation from the actual eigenstate break the stationarity of the mean-field solutions at the $b_{\pm1} = 0$ and $b_0 = 0$ points. Near resonance, spin-mixing collisions exponentially amplify the quantum fluctuations, in a process that is equivalent to the photon pair creation in an optical parametric amplifier [326].

Consequently, to be able to evaluate the proposed protocol with the GPE of the dressed gas, we instead simulate an analogous drive across the P-TF-BA excited diagram in a slightly lower lying family of excited states, in which we set the initial state to a coherent state with $0 < N_{\pm1} \ll N$. In these conditions, mean-field computations quickly converge to full quantum simulations as $N_{\pm1}(t = 0)$ is increased, while the properties like the energy gap and the location of the phase boundaries do not vary significantly as long as $N_{\pm1}(t = 0)$ is kept much smaller than N. This is exemplified in Fig. 4.4, where we compare the results for a drive through both P-BA and BA-TF phases obtained from mean-field and full quantum simulations of the three-mode model. By setting a small

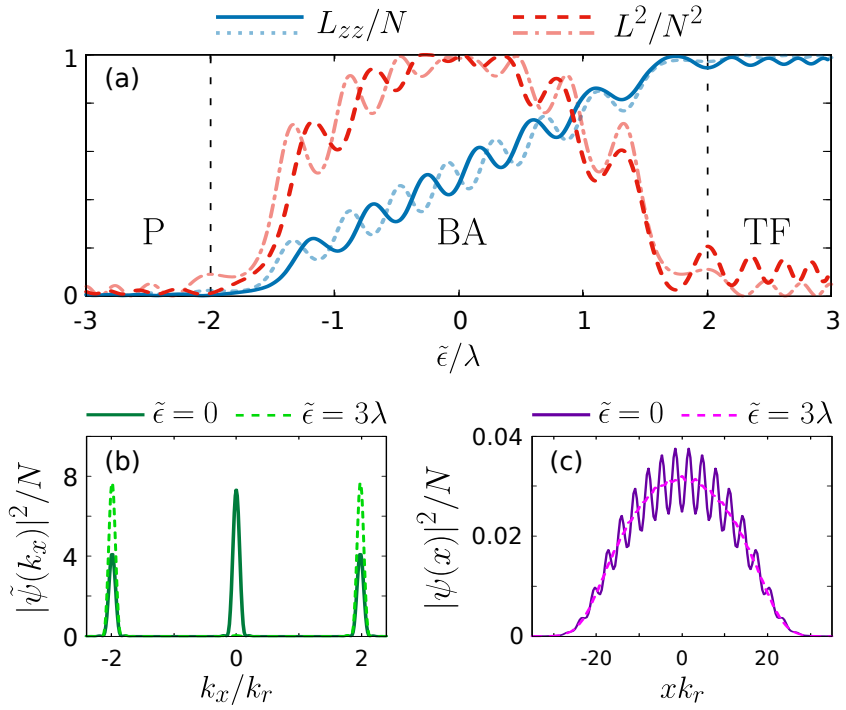

Figure 4.5: Crossing quantum phase transitions in an excited state. (a) L_{zz} (blue solid line) and L^2 (red dashed line) as a function of $\tilde{\epsilon}$ for a state initially prepared at $b_{\pm1} = \sqrt{50}$ and $b_0 = \sqrt{N-100}$, with $N(0) = 10^4$ and $\hbar\omega_t = 2\pi \times 140\,\mathrm{Hz}$.The state is evolved under the GPE while driving $\tilde{\epsilon}$ from -3λ to 3λ, keeping $\Omega = 0.65E_r$, following the red dashed path in Fig. 4.3(b). The total drive time is set to $\tau_d = 8h/\lambda$. The corresponding results obtained with simulations of the three-mode model (4.23) are shown in light colors. (b) Quasi-momentum density $|\tilde{\psi}(k_x)|^2$ of the driven state at $\tilde{\epsilon} = 0$ (dark green solid line) and $\tilde{\epsilon} = 3\lambda$ (light green dashed line). (c) Corresponding density profiles at $\tilde{\epsilon} = 0$ (purple solid line) and $\tilde{\epsilon} = 3\lambda$ (pink dashed line).

but nonzero initial occupation of the edge modes, both the mode occupation and the relative phase between the modes along the drive obtained with mean-field simulations match well the expected values predicted by Hamiltonian (4.23). At the same time, figure Fig. 4.4(a2) shows that the driven state experiences the phase-locking predicted by the mean-field solutions (see (4.27)) when crossing the BA phase, even when we set $N_{\pm1}(t = 0) = 0$, where the spin-mixing dynamics is started solely by quantum fluctuations. This reinforces the assumption that stripe state also results from the full quantum dynamics, and not only from the dynamics of coherent states.

With these considerations in mind, we simulate a drive along the red dashed vertical path drawn in the excited state diagram from Fig. 4.3(b) using the GPE (4.32). In Fig. 4.5 we show the results for such a drive obtained by setting $\delta = 0$, $\omega_t = 2\pi \times 140\,\mathrm{Hz}$, $N = 10^4$ and $\Omega = 0.65E_r$ into the GPE, and setting the initial state to $b_{\pm1} = \sqrt{50}$ and $b_0 = \sqrt{N-100}$. In Fig. 4.5(a) we plot the corresponding values of the collective pseudospin

$L^2 = \sum_j [\sum_{\mu\nu} b^*_\mu (\hat{F}_j)_{\mu\nu} b_\nu]^2$ and the tensor magnetization $L_{zz} = \sum_{\mu\nu} b^*_\mu (\hat{F}^2_z)_{\mu\nu} b_\nu$ along the drive, as a function of $\tilde{\epsilon}/\lambda$. The state is time evolved following the linear ramp $\tilde{\epsilon}(t) = 3\lambda(2t/\tau_d - 1)$, with $\tau_d = 8h/\lambda$, which should cross both P-BA and BA-TF phase transitions at $\tilde{\epsilon} \sim \pm 2\lambda$. As predicted by the collective spin model, in the region $-2\lambda < \tilde{\epsilon} < 2\lambda$, which would correspond to the most excited BA phase for a perfectly adiabatic drive, the tensor magnetization $\hat{L}_{zz}$ increases homogeneously with $\tilde{\epsilon}$. Likewise, the total spin squared $\hat{L}^2$ peaks at $\tilde{\epsilon} = 0$ and then decreases again, as was expected (see Fig.4.3(c)). For comparison, the results obtained from the direct simulation of the three-mode Hamiltonian (4.23) are shown in light colors, which highlights the very good agreement between the full dressed and trapped gas and the effective model in this regime of parameters.

As we argued in Sec. 4.3.2, in the Raman-based realization of the collective spin model, the spin and the orbital degrees of freedom are coupled. The different pseudospin modes correlate with quasimomentum-shifted band states, roughly in correspondence to the states located at the minima of the single-particle lowest band. In Fig. 4.5(b) we plot the momentum-space density at the middle and at the end of the drive, where such localization of the condensate around the band minima at $\mathbf{k}_j \sim 2jk_r\mathbf{e}_x$ is illustrated. Together with the nonothogonal bare spin compositions of the pseudopspin states, these quasimomentum shifts result into periodic density modulations of the condensate, or stripes, as described in Sec. 4.3.2. Indeed, the corresponding density profiles are shown in Fig. 4.5(c). In the excited BA phase, the prepared state exhibits large density modulations along the direction of the Raman beams. There, the relative peak-to-valley contrast of the stripes is approximately given $\mathrm{V}_{\mathrm{ptv}} \sim 0.21$, close to the theoretical value $\mathrm{V}^{\mathrm{th}}_{\mathrm{ptv}} = \frac{\max(n(\mathbf{r}))-\min(n(\mathbf{r}))}{\max(n(\mathbf{r}))+\min(n(\mathbf{r}))} = \Omega/E_r\sqrt{N_0(N-N_0)/2N^2}$ predicted by the density distribution (4.30), which was obtained considering plane-wave-like spatial modes.

Naturally, the level of agreement between the collective spin model and the GPE of the full dressed gas depends strongly on the choice of parameters. In general, with the SOC-induced spin mixing dynamics being proportional to Ω^2 (see equation (4.16)), the energy scale of the effective model is enhanced at larger Ω. On the one hand, therefore, increasing the Raman coupling strength has a clear advantage: a larger λ reduces the preparation time, proportional to $\hbar/|\lambda|$, and therefore the relative impact of the heating mechanisms and of photon scattering loss, which we will cover in the next section. On the other hand, however, the validity of the three-mode truncation that leads to Hamiltonian (4.23) is progressively more challenged as λ is increased. This is in great part due to the increased range of values for $\tilde{\epsilon}$ that is required with a larger λ, which implies that higher-excited modes become closer to being resonantly coupled along the drive. To quantify the accuracy of the approximation, we compute the projection of the time-evolved states on to the subspace spanned by the three self-consistent mode, $f_{3\mathrm{M}} = \frac{1}{N^2}\sum_j \left|\int d\mathbf{r}\boldsymbol{\phi}^*_j \cdot \boldsymbol{\psi}\right|^2$, previously obtained via imaginary time evolution. In Fig. 4.6(a1) we plot the $f_{3\mathrm{M}}$ as a function of $\tilde{\epsilon}$ for analogous linear drives along ϵ, for different values of Ω. In each case, we set the drive time to $\tau_d = 8\hbar/\lambda$. As expected, increasing Ω while leaving

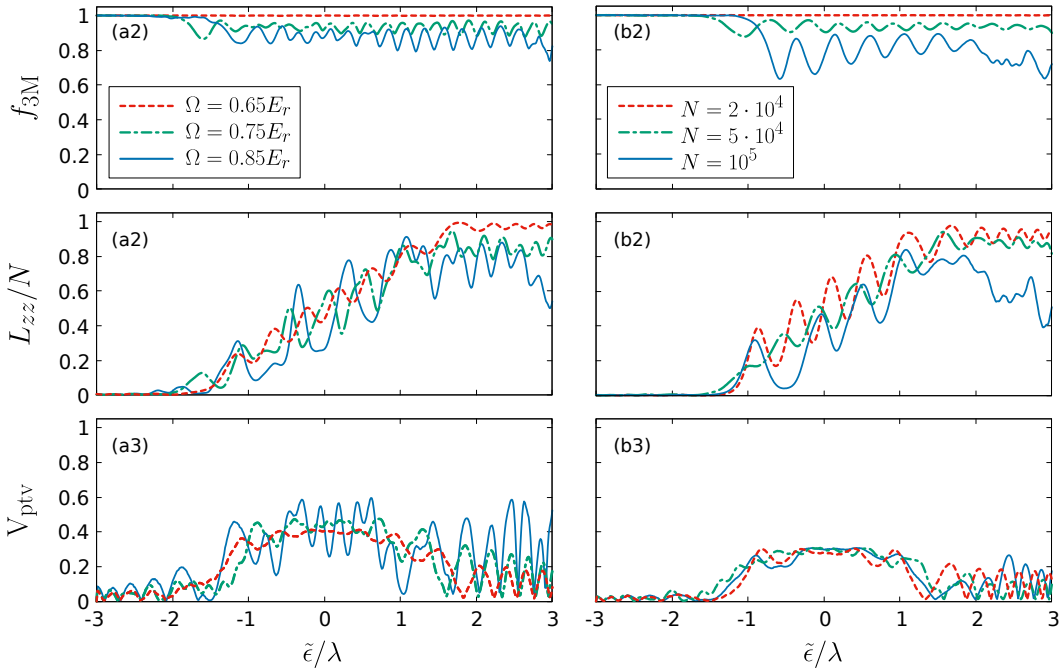

Figure 4.6: Validity of the three-mode approximation. (a1) Relative occupation of the three self-consistent modes $\boldsymbol{\phi}_{-1}$, $\boldsymbol{\phi}_0$ and $\boldsymbol{\phi}_1$, $f_{3M} = \frac{1}{N^2}\sum_j \left|\int d\mathbf{r}\boldsymbol{\phi}_j^* \cdot \boldsymbol{\psi}\right|^2$, as a function of $\tilde{\epsilon}$, for a state initially prepared at $\boldsymbol{\psi} = \alpha(\boldsymbol{\phi}_{-1} + \boldsymbol{\phi}_1) + \sqrt{N - 2|\alpha|^2}\boldsymbol{\phi}_0$, with $N = 10^4$, $\alpha = \sqrt{25}$ and $\hbar\omega_t = 2\pi \times 140\,\text{Hz}$. The state is evolved under the GPE while driving $\tilde{\epsilon}$ from -3λ to 3λ, and keeping $\Omega = 0.65E_r$ (red dashed line), $\Omega = 0.75E_r$ (green dash-dotted line) and $\Omega = 0.85E_r$ (solid blue). The total drive time is set to $\tau_d = 8h/\lambda$. Figures (a2) and (a3) show, respectively, the mean tensor magnetization $\hat{L}_{zz}$ and the relative peak-to-valley contrast V_{ptv} along the drive depicted in (a1). (b1) f_{3M} as a function of $\tilde{\epsilon}$ for a state initially prepared at $\boldsymbol{\psi} = \alpha(\boldsymbol{\phi}_{-1} + \boldsymbol{\phi}_1) + \sqrt{N - 2|\alpha|^2}\boldsymbol{\phi}_0$, with $\alpha = \sqrt{10^{-3}N}$ and $N = 2 \times 10^4$ (dashed-red), $N = 5 \times 10^4$ (green dash-dotted line) and $N = 8 \times 10^4$ (solid blue). The state is evolved under the GPE, driving $\tilde{\epsilon}$ from -3λ to 3λ, while keeping $\Omega = 0.5E_r$ and adjusting ω_t so that $\bar{n} = 10^{-14}$ cm^{-3}. The total drive time is set to $\tau_d = 8h/\lambda$. Below, (b2) and (b3) show the corresponding values for $\hat{L}_{zz}$ and V_{ptv}, respectively, along the drive depicted in (b1).

the rest of parameters unchanged leads to a rapid increase in the excitation out of the three-mode subspace. The corresponding values of L_{zz} and the relative peak-to-valley contrast of the stripes, V_{ptv}, are plotted in Fig. 4.6(a2) and Fig. 4.6(a3), respectively. The latter is averaged from the obtained longitudinal density profiles. At the same time, at any given density, the robustness of the protocol strongly depends on the number of particles, as exemplified in Fig. 4.6(b1). There, we simulate several drives where we fix the density but vary the total number of particles. Below, Fig. 4.6(b2) and Fig. 4.6(b3) show, repectively, the values L_{zz} and V_{ptv} along the drive.

It is worth pointing out that, while f_{3M} quantifies the accuracy of the few-mode truncation, the different physical quantities are affected differently by the value of f_{3M}. For instance, macroscopic entanglement preparation is expected to be very sensitive to the full quantum structure of the prepared state. Thus, even a tiny reduction of f_{3M} could result in a considerable reduction of the generated entanglement. On the contrary, the macroscopic spin transfer and the contrast of the stripes are less sensitive to the leakage of probability amplitude out of the three-mode description, as exemplified in Fig. 4.6. At larger Ω, the loss of contrast in the stripes due to the degradation of the three-mode approximation and the reduced stability of the spinor phase is partly compensated through the linear dependency of the contrast on Ω. While less stable in time, the stripes can retain to some extent a large contrast as we move away from the three-mode approximation. As a consequence, the optimal experimental parameters will be strongly dependent on the physical observables of interest.

In this way, the GPE supports the collective pseudospin description (4.23) of the low-energy landscape of Hamiltonian (4.1) for a wide range of parameters, and the idea that the stripe phase can be accessed by coherently driving the dressed condensate through a quantum phase transition in an excited state. It should be stressed that such an approach to prepare the stripe phase can not be extrapolated to the spin-$\frac{1}{2}$ gas, where spin-changing collision processes do not naturally occur and can not be induced by Raman dressing. In dressed spin-1 gases, this dynamical preparation of stripe states could in principle permit to access the phase in regimes where it would be experimentally more feasible. At the same time, doing so would greatly enhance the contrast of the spatial modulations in the gas. Yet, so far, we have simulated the GPE for an ideal spin-orbit-coupled BEC. In the next section we will evaluate further the feasibility of the protocol described in this section by accounting for the major sources of noise that would be present in its actual experimental realization.

4.4 Experimental considerations

In Sec. 4.3 we introduced a protocol to access the ferromagnetic stripe phase of the spin-1 spin-orbit-coupled gas that exploited the map of dressed gas to a collective spin model derived in Sec. 4.2. However, the feasibility of the scheme in an experiment with ultracold atoms will be subject to several sources of noise that are detrimental to the stability and contrast of the stripes prepared, most notably the fluctuations in the Zeeman levels due to the instability of the bias magnetic-field and the calibration uncertainty in the intensity of the Raman beams. To gain insights on the extent of such constraints, we now incorporate atom loss and heating mechanisms into the simulations of the GPE. As a starting point, we naively model the noise in δ and ϵ with sinusoidal signals of frequency 50 Hz and amplitude 300 Hz and 2.5 Hz, respectively. We consider Ω to be stable during the drive, but to have a calibration uncertainty of 125 Hz in each realization. These amplitudes are compatible with a magnetic bias field instability of

$\sim$ 0.5 mG and a relative uncertainty of $\pm 5\%$ in Ω, within the stabilities reached in experiments with ^{87}Rb [104, 118, 299]. At the same time, we consider a 10% uncertainty in the number of atoms initially in the condensate, and the population to decay as $N(t) = N(0)\exp(-\gamma t)$, with $\gamma = 3.33\,\mathrm{s}^{-1}$, which is compatible with the lifetime of spin-1 Raman-dressed BECs for $\Omega < E_r$ [118, 244].

In these conditions, we simulate the protocol by introducing the time-dependence and randomized parameter in the GPE (4.32). This time, instead of varying the effective quadratic Zeeman shift ϵ, we drive the state along the Ω direction in the excited phase diagram, as exemplified with the blue dash-dotted path in Fig. 4.7. The left panel in the inset show the ideal energy gap along the path, for $N = 1000$ and $n = 7.5 \times 10^{13}$ cm^{-3}, in which ϵ is kept fixed while Ω is linearly ramped up. On the right, we plot the instantaneous values of the characteristic observables of the collective spin phases.

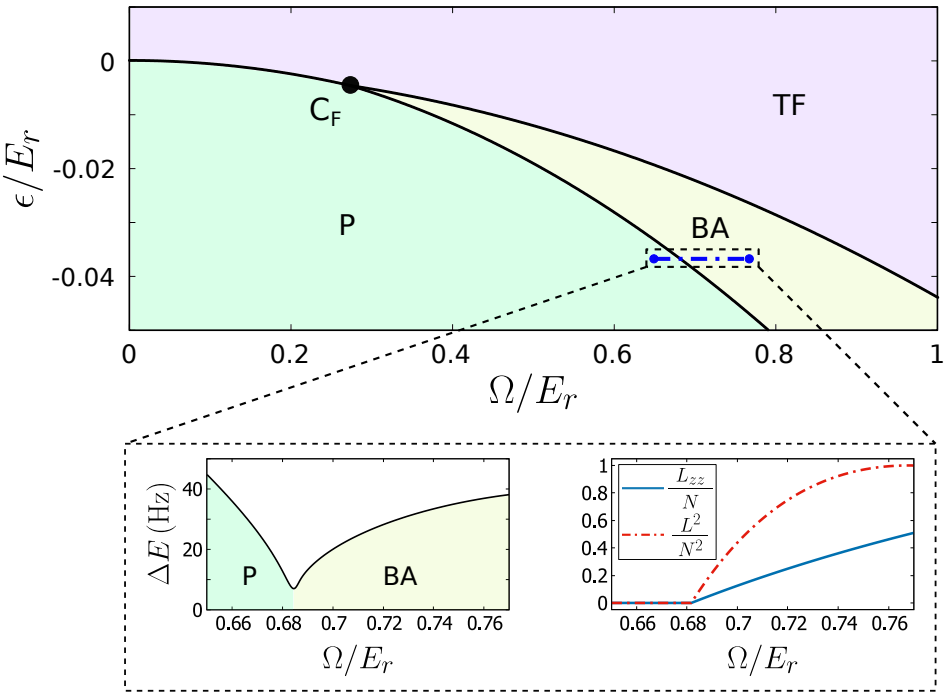

Figure 4.7: Phase diagram of the highest-excited eigenstate of (4.23), as a function of the Raman Rabi frequency Ω and effective quadratic Zeeman shift ϵ, for ^{87}Rb at $n = 7.5 \times 10^{13}$ cm^{-3}. The polar (P), twin-Fock (TF) and broken-axisymmetry (BA) phases are colored, respectively, in light green, light yellow and light purple as a guide to the eye. The three phases meet at the tricritical point C_F (black dot). The left panel in the inset below shows the energy gap ΔE between the two most excited eigenstates along the blue dash-dotted segment for $N = 1000$. The right panel shows the corresponding mean values of the collective pseudospin $\hat{L}^2$ (red dashed line) and tensor magnetization $\hat{L}_{zz}$ (blue solid line) of the highest-excited eigenstate

.

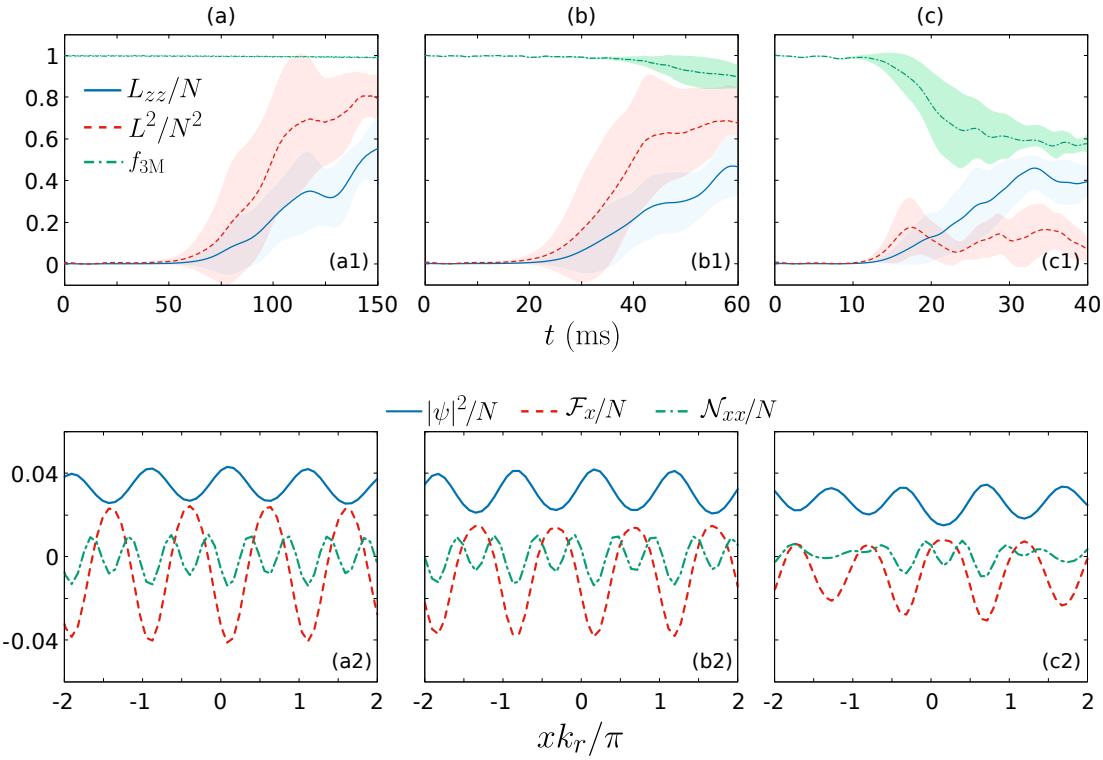

Figure 4.8: Robust preparation of FS states. (a1) L_{zz} (blue solid line), L^2 (red dashed line) and f_{3M} (green dahs-dotted line) a function of time for a state initially prepared at $b_{\pm1} = \sqrt{10}$ and $b_0 = \sqrt{N-20}$, with $N(0) = 10^4$ and $\hbar\omega_t = 2\pi \times 140\,\mathrm{Hz}$. The state is evolved under the GPE while driving $\tilde{\epsilon}$ from -3λ to 0 by linearly increasing Ω from $0.65E_r$ to $0.767E_r$, following the blue dash-dotted path drawn in the diagram from Fig. 4.7. The parameters of the GPE are subject to random fluctuations that simulate experimental noise, as described in the main text, and the values depicted are averaged over 20 realizations. The shadowed regions indicate the associated standard deviations. (a2) Longitudinal density $|\psi|^2$ (blue solid line), spin density $\mathcal{F}_x$ (red dashed line) and nematic density $\mathcal{N}_{xx}$ (green dash-dotted line) at $t = 150$ ms from a single realization of the drive, where it is expected that $\tilde{\epsilon} = 0.5\lambda$. In (b) and (c) we show the corresponding results for analogous drives from -3λ to 0, where the state is initially prepared at $\Omega(t=0) = E_r$ and $\Omega(t=0) = 1.25E_r$, respectively. The larger values of λ along the drive allow a faster preparation at the cost of a reduced robustness, which is signaled by a decrease in f_{3M} by the end of the drive.

Such a path illustrates the tunability of the SOC-mediated spin dynamics, which we can exploit to improve the preparation. Driving along Ω has two major advantages. Mainly, the spin-mixing parameter λ is increased as $\tilde{\epsilon}$ approaches to 0, which allows to reduce the preparation time while retaining a high robustness. At the same time, the drive ends at larger Ω, where the contrast of the stripes is further enhanced as long as the few-mode picture is preserved.

There is a general trade-off between the detrimental effects of the different noise sources, which all become more relevant when the energy scale of the spin dynamics is made smaller, and the amount of excitations created out of the the three-mode subspace, which has the opposite behavior. As argued in Sec. 4.3.4, the experiment should be optimized differently depending on the observables that are targeted. To be on the safe side, we first simulate the drive along the blue dash-dotted path from Fig. 4.7, considering $N = 10^4$ and $n = 7.5 \times 10^{13}$ cm^{-3}. There Ω is initially set to $0.65E_r$, which results in a very small fraction of the population excited out of the three-mode subspace. The results for such a drive are shown in Fig. 4.8(a). In Fig. 4.8(a1), we plot L_{zz}, L^2 and $f_{3\mathrm{M}} = \frac{1}{N^2}\sum_j |b_j|^2$, averaged over 20 realizations of the drive, where the GPE incorporated the randomized parameters as described above. The P-BA transition is well captured, with $f_{3\mathrm{M}} \sim 0.99$ by the end of the drives. In Fig. 4.8(a2) below we plot the longitudinal density $|\boldsymbol{\psi}|^2$, the spin density $\mathcal{F}_x = \boldsymbol{\psi}^* \hat{F}_x \boldsymbol{\psi}$ and the nematic density $\mathcal{N}_{xx} = \boldsymbol{\psi}^*(\frac{2}{3} - \hat{F}_x^2)\boldsymbol{\psi}$ at $\tilde{\epsilon} = 0$ for a single realization of the drive, randomly chosen from the sample. Note that in the latter figure the profiles are not averaged over all the realizations, since the randomness of the relative spinor phase between different realizations would unavoidably flatten the contrast in the averaged profile. Fig. 4.8(a2) shows that, indeed, as predicted by the effective model, the prepared state exhibits the characteristic properties of FS states, with large spatial modulations along the direction of the Raman beams. The FS phase can be distinguished from antiferromagnetic stripe phases from the periodicity of the modulations, with the particle density and the spin densities having periodicity $2\pi/|\mathbf{k_1}|$, and the nematic densities containing harmonic components both with period $2\pi/|\mathbf{k_1}|$ and $\pi/|\mathbf{k_1}|$ [196].

Similarly, in Fig. 4.8(b) we show the corresponding results for an analogous drive along Ω, where the state is prepared at a larger Ω, with $\Omega(t = 0) = E_r$. As discussed in the previous paragraph, in these conditions the system experiences a reduced impact from parameter fluctuations, yet we observe a larger decrease in $f_{3\mathrm{M}}$, as shown Fig. 4.8(b1). By comparing Fig. 4.8(b2) to Fig. 4.8(a2), we notice that the prepared states appear to retain to a large degree the spatial properties of the FS states. However, the spatial structures of the FS phase degrade quickly as Ω is further increased, as illustrated in Fig. 4.8(c), where we set $\Omega(t = 0) = 1.25E_r$. In this conditions, the robustness of the three-mode truncation is largely reduced and, consequently, the collective spin structure is lost. In any case, the freedom in the choice of parameters highlights the enhanced tunability of the realization of the spin model in Raman-dresed spinor gases. Our results indicate that the preparation of the FS phase in an excited state is compatible with the degree of control attained in state-of-the-art experiments with ultracold gases. As a final remark, we note that the preparation could be optimized further by employing reinforcement learning techniques, as recently demonstrated in the experiment from [327] for the same collective spin model realized in undressed spinor gases.

4.5 Conclusions

In this chapter we have presented the Raman-dressed spin-1 Bose-Einstein condensate as a versatile platform to study nonequilibrium phenomena. We have analytically demonstrated that in the weak Raman coupling regime, the dressed system is equivalent at quantum level to an artificial spinor gas with tunable spin-changing collisions. On the one hand, such formulation allows a simple description of the quantum phases of the Raman-dressed gas and of their dynamics in terms of the artificial spinor gas. On the other hand, the coupling between spin and momentum that arises from the synthtetic SOC and the degree of tunability of the nonsymmetric spin-spin interaction offer many possibilities that go beyond those of undressed spinor gases.

By way of example, we have proposed a protocol to prepare the supersolid-like FS phase of the spin-1 spin-orbit-coupled gas that is based on this map. The preparation is achieved via driving an initially polarized state across a quantum phase transition in an excited-state of the effective low-energy Hamiltonian. Remarkably, we have shown that this approach enhances the accessibility of the phase, which, to date, has not been yet experimentally demonstrated in spin-1 gases. In the excited-state phase diagram, the FS phase is broader, and both the energy gap and the contrast of the density modulations are larger. These features could enable a robust preparation of the state and ease the detection of its supersolid properties, e.g. by probing its spectrum of excitations [192, 198]. We emphasize that only through the explicit mapping, which identifies the excited-state stripe phase with the broken-axisymmetry phase of the collective spin physics of the effective spinor model, such a simple approach is made evident.

Through simulations of the GPE of the full dressed gas, we have shown the implementation of the protocol to be feasible in state-of-the-art experiments with ultracold atoms. We have benchmarked the protocol in accordance to the results reported from experiments with ^{87}Rb condensates at the National Institute of Standards and Technology. Unlike most proposals to realize striped phases in spinor gases, we show that the phase can be robustly accessed without relying on an effective decrease of the intraspin interactions. Instead, by preparing the phase in an excited-state, the characteristic parameters that stabilize the phase are scaled up, making it more robust against experimental noise. While we find the protocol compatible with ^{87}Rb experiments, this approach does not rely critically on the specific properties of interatomic interactions and could in principle be generalized across the alkali atomic species and to non-alkali atoms like ^{162}Dy. However, we note that such an approach, which is based on the SOC-induced dynamical spin-mixing processes, can not be employed to prepare the stripe phase in spin-$\frac{1}{2}$ gases.

The dressed-base description of Raman-coupled spinor gases suggests new directions for probing nonequilibrium phenomena, as in [306, 310], with light-dressed spinor gases of alkali-metal and non-alkali-metal [328] atoms. Furthermore, the FS phase corresponds to the BA entangled phase of the artificial spinor gas: its preparation may thus lead to the generation of macroscopic entanglement in momentum space (cf. [329]), with

potential applications in quantum metrology. Finally, the map also introduces gases with SOC as an alternative platform to study dynamical and excited-state quantum phase transitions. It suggests that the connection between the FS and BA phases can be extended throughout the spectrum of the effective spin model. This precise connection will be explored in the next chapter.

CHAPTER 5

Excited state quantum phase transitions in spin-orbit-coupled Bose gases

In chapter 3 we saw that spin-changing collisions emerge in Bose gases in the presence of spin-orbit coupling. In the Raman-dressing-based realization of such systems, we showed that the strength of the SOC-induced spin interactions can be conveniently adjusted with the intensity of the Raman beams. Next, in chapter 4 we went a step further in this direction, and showed that for a relatively large regime of parameters, the weakly-dressed gas can be made completely analogous to an undressed gas with tunable spin interactions. Relevantly to this chapter, we showed there that such an analogy not only provided a simple framework to understand the phases of the dressed gas, but it could actually be extended for a broad family of energy states of the Hamiltonian. In this chapter, we will make use of this equivalence throughout the energy spectrum to explore excited-state quantum phase transitions in spin-1 Raman-dressed condensates, inspired by a recent proposal that exploits spin-changing collisions in an undressed gas.

Excited-state quantum phase transitions depend on and reveal the structure of the spectrum of many-body systems. In analogy to ground-state quantum phase transitions, excited-state quantum phase transitions involve the existence of criticalities in the energy spectrum, typically involving an additional control parameter, that occur across a large set of excited energy levels. In some systems they can even extend to the whole the excitation spectra. While they are theoretically well understood, and predicted to occur in a large variety of models, finding suitable signatures and detecting them in actual experiments remains challenging. For instance, excited-state phases in spinor gases has been identified only very recently, and characterized through a topological order parameter that is challenging to measure in experiments. In this chapter, we propose the Raman-dressed spin-orbit-coupled gas as a novel platform to explore excited-state quantum phase transitions. By making use of the equivalence between the dressed system

and an undressed spinor gas developed in the previous chapter, we are able to identify excited-state phases in the former system that are in correspondence with those of the latter. In the dressed system, the excited phases are further characterized by the behavior of the spatial density modulations, or stripes, induced by spin-orbit coupling. One the one hand, a novel order parameter for the phases can be defined in these terms, which can in principle be measured in current state-of-the-art experiments with ultracold atoms and facilitate the detection of the excited phases. One the other hand, we show that the properties of the excited phases can be exploited to prepare stripe states with large and stable density modulations.

The paper is organized as follows. We start by establishing in Sec. 5.1 a theoretical and experimental background to the results presented in this chapter, where we also briefly remind the Raman-dressed spin-1 gas and its description as a collective pseudo-spin Hamiltonian with tunable spin interactions. The main result of the chapter is presented in Sec. 5.2, where we introduce the novel excited stripe phase of the Raman-dressed condensate. In turn, we show that its experimental signature can provide a new means to detect the ESQP transitions of the collective spin model, and can also provide an alternative signature of a dynamical quantum phase transition therein. In Sec. 5.3 we propose a robust protocol to prepare excited stripe states, which we benchmark numerically with simulations of the GPE. Finally, we briefly recap and draw our conclusions in Sec. 5.4.

5.1 Introduction

Harnessing quantum matter with light is at the heart of quantum technology [330, 331]. The engineering of artificial spin-orbit coupling (SOC) in charge-neutral ultracold atomic gases via Raman dressing is a prominent example [30, 84, 85] (see Sec. 2.2.3). Spinor gases dressed by Raman coupling [86, 104] interact differently [116, 117], host stripe phases [108, 207] with supersolid-like properties (see also [313], for dipolar gases realization see [316–318]), or even realize a topological gauge theory [332]. In this chapter, we propose to use Raman-dresed spin-orbit-coupled gases for studying dynamical [120] and excited [121] quantum phase transitions in spinor BECs.

5.1.1 Background and motivation

In recent years, the notion of quantum phase transition [221, 333] has been extended beyond the ground states of quantum systems. In broad terms, quantum phase transitions are characterized by a nonanalytical changes in the properties of the ground state (or a given eigenstate) of a system when a specific control parameter is varied across a critical value. Drawing an analogy to such processes, dynamical quantum phase transition refer to the existence of non-analyticities in the properties of a state as a function of time following a quench of a parameter. They have been described in many sys-

tems, and demonstrated in quench experiments with cold atoms in optical lattices [334–336] and cavities [337], trapped ions [338, 339], and with superconducting qubits [340]. At the same time, in an even closer parallelism to regular quantum phase transitions, the so-called excited-state quantum phase (ESQP) transitions describe the criticalities that occur across the spectrum of certain many-body Hamiltonians, and involve a large amount of excited states. Typically, across an excited-state quantum phase transition, both the energy and the properties of the excited states vary nonanalytically at some critical value of the energy, which in turn depends smoothly on an additional control parameter. Thus, critical boundaries are formed in the plane defined by the energy and the control parameter. These boundaries separate extended sets of eigenstates into different ESQPs. Typically, the energy gap closes at the boundary, resulting in a divergence of the density of states. ESQP transitions have been shown to occur in a variety of models [341–349], and have been observed in superconducting microwave Dirac billiards [350]. Recently, both dynamical and ESQP transitions have been theoretically [323, 351] and experimentally [297, 298] studied in spin-1 BECs with spin-changing collisions.

In chapter 4, we saw that the weakly-coupled Raman-dressed spin-1 SOC gas at low energies can be understood as an artificial spin-1 gas with tunable spin-changing collisions that can be adjusted with the intensity of the Raman beams. We further showed that, in certain conditions, the dressed system is well described by a one-axis-twisting collective spin Hamiltonian [165, 272, 321]. The realization of the same model in undressed spinor condensates has led to the observation of various quantum many-body phenomena [147], including the formation of spin domains and topological defects [300–310], and the generation of macroscopic entanglement [274–285, 311], with prospects for metrological applications [73]. The map to pseudospin degrees of freedom (see Fig. 5.1) highlights the potential advantage of SOC dressed gases for engineering quantum many-body physics: the enhanced tunability of the system and the built-in entanglement between the emerging collective spin structures and the orbital degrees of freedom. In this chapter we employ these unique features to identify a novel Excited-Stripe (ES) phase of the spin-1 SOC gas. The phase is in correspondence to the Broken-Axisymmetry (BA') excited phase of the effective collective spin model, discussed in [323], which is characterized by a topological order parameter, and can extend over the whole spectrum of the Hamiltonian. In the SOC gas, ES phase comprises the classical phase-space trajectories with nonzero time average of the spatial modulations of the density of the gas.

We exploit the relationship between the topological order parameter and the stability of the density modulations in the SOC gas to design a novel detection protocol for the ESQPs of the spinor gas. In the dressed gas, having an interferometer built-in generated by SOC makes a measurement of the contrast of the stripe equivalent to a simultaneous measurement of the amplitude and phase of the dressed spin components. Remarkably, this approach benefits from an intrinsic robustness to magnetic fluctuations, which constraint the current proposals for detecting the excited phases of the model

in spinor gases with intrinsic spin changing collisions [323]. Moreover, we also show that a type of dynamical quantum phase transition in the dressed system can also be characterized by an observable that is based on the contrast of the density modulations. Finally, through the effective model, we are able to provide a robust protocol to prepare striped states. The ES phase of the gas can be accessed from an initially unpolarized gas via crossing an ESQP transition in a two-step quench scheme. With such an approach, we show that the ES phase can be realized in current state-of-the-art experiments with spin-1 SOC gases, with the prepared states exhibiting large and stable density modulations. At the same time, the proposal introduces a novel procedure to access the striped regime of the spin-1 with SOC, which as ground-state phase has a very narrow region of stability [196] and it has yet to be experimentally demonstrated.

5.1.2 The Raman-dressed gas as an artificial spinor gas

In this chapter we consider again a spin-1 BEC of N atoms of mas m subject to synthetic SOC with equal Rashba and Dresselhaus contributions, as experimentally realized via Raman-coupling two Zeeman pairs $\{|1,1\rangle, |1,0\rangle\}$ and $\{|1,0\rangle, |1,-1\rangle\}$ independently [118]. In the presence of dressing, the kinetic Hamiltonian can be written as

$$\hat{\mathcal{H}}_{\mathrm{k}} = \frac{\hbar^2}{2m}\left(\mathbf{k} - 2k_r\hat{F}_z\mathbf{e}_x\right)^2 + \frac{\Omega}{\sqrt{2}}\hat{F}_x + \delta\hat{F}_z + \epsilon\hat{F}_z^2, \tag{5.1}$$

where $\hbar\hat{F}_j$ are the spin-1 matrices. Here, Ω quantifies the Raman coupling strength. By simultaneously adjusting the detuning from resonance of each Raman pair, the strengths of an effective quadrupole tensor field and a magnetic field term, ϵ and δ, respectively, can be independently tuned in the laboratory (see methods from [118]).

The many-body scenario for the Raman-dressed gas in the mean-field regime is captured by the energy functional

$$E[\boldsymbol{\psi}] = \int d\mathbf{r}\left[\boldsymbol{\psi}^*\left(\hat{\mathcal{H}}_{\mathrm{k}} + V_{\mathrm{t}}\right)\boldsymbol{\psi} + \frac{g_s}{2}|\boldsymbol{\psi}|^4 + \frac{g_a}{2}\sum_j(\boldsymbol{\psi}^*\hat{F}_j\boldsymbol{\psi})^2\right], \tag{5.2}$$

where $\boldsymbol{\psi} = (\psi_1, \psi_0, \psi_{-1})^T$ is the spinor condensate wavefunction, normalized to the total number of particles as $\int d\mathbf{r}\boldsymbol{\psi}^*\boldsymbol{\psi} = N$. The spin-symmetric and nonsymmetric interaction couplings are given by $g_s = 4\pi\hbar^2(a_0 + 2a_2)/3m$ and $g_a = 4\pi\hbar^2(a_2 - a_0)/3m$, where a_0 and a_2 are the scattering lengths in the $F = 0$ and $F = 2$ channels, respectively. For simplicity, we will consider that the gas is confined with an isotropic harmonic potential $V_{\mathrm{t}} = \frac{1}{2}m\omega_{\mathrm{t}}^2\mathbf{r}^2$.

In this chapter we consider again the weak Raman coupling regime, where Ω is smaller than the Raman single-photon recoil energy E_r. We label the recoil momentum as $\hbar k_r$, so that $E_r = \frac{\hbar^2 k_r^2}{2m}$. Furthermore, we will consider $E_r \gg \delta, \epsilon$. In this regime, the lowest dispersion band of $\hat{\mathcal{H}}_{\mathrm{k}}$ has three different minima $\mathbf{k}_j \sim 2jk_r\mathbf{e}_z$, with $j \in \{-1, 0, 1\}$, as illustrated in Fig. 5.1(a). As demonstrated in the previous chapter, in

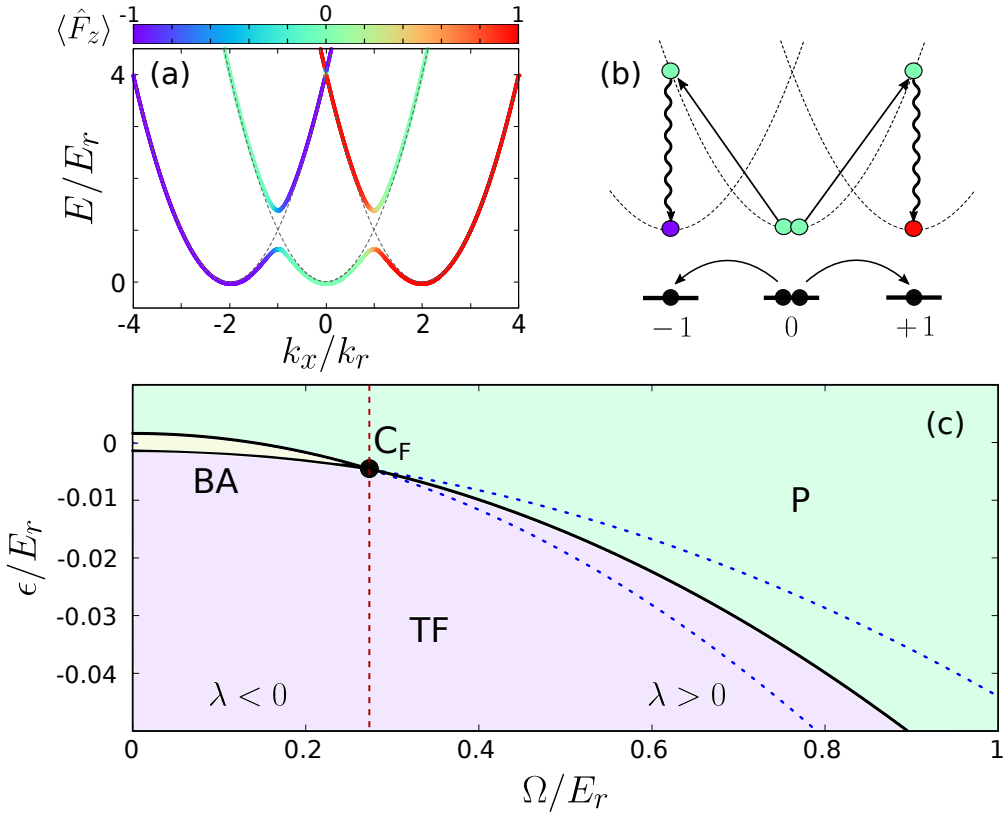

Figure 5.1: Pseudospin dynamics in SOC BECs. (a) Dispersion bands of Hamiltonian (5.1), setting $\Omega = 0.75E_r$, $\delta = 0$ and $\epsilon = \Omega^2/16E_r$. The corresponding mean value of $\hat{F}_z$ for the band states is indicated with the color texture. The undressed bands are shown in gray dashed lines. (b) Schematic representation of an effective spin-changing collision process enabled by Raman transitions (represented in wavy lines). (c) Phase diagram of the dressed spin Hamiltonian (5.3), as a function of the Raman Rabi frequency Ω and effective quadratic Zeeman shift ϵ, for ^{87}Rb at $\bar{n} = 7.5 \times 10^{13}$ cm^{-3}. The polar (P), twin-Fock (TF) and broken-axisymmetry (BA) phases meet at the tricritical point C_F (black dot). The red dashed vertical line at $\Omega_c = 4E_r\sqrt{|g_a|/g_s}$ separates the ferromagnetic ($\lambda < 0$) and the antiferromagnetic ($\lambda > 0$) regimes of the effective Hamiltonian. The blue dotted lines enclose the region of parameters around the P-TF transition where the BA' excited-state quantum phase takes place (see Sec. 5.2), with its boundaries located at $\tilde{\epsilon} = \pm 2\lambda$ in the thermodynamic limit.

these conditions the dynamics of the dressed gas is equivalent to the one of an effective spinor gas with Raman-mediated spin-changing collisions (see Fig. 5.1(b)). For small condensates, the low-energy landscape of the weakly-coupled gas can be restricted to just three self-consistent modes, and the system is then well described by a collective pseudo-spin Hamiltonian. We label the collective pseudo-spin operators as $\hat{L}_{x,y,z} = \sum_{\mu\nu} \hat{b}^\dagger_\mu (\hat{F}_{x,y,z})_{\mu\nu} \hat{b}_\nu$ and $\hat{L}_{zz} = \sum_{\mu\nu} \hat{b}^\dagger_\mu (\hat{F}^2_z)_{\mu\nu} \hat{b}_\nu$, where the bosonic operators $\hat{b}^\dagger_{-1}$, $\hat{b}^\dagger_0$ and

$\hat{b}_1^\dagger$ create a particle in the left, middle and right well mode, respectively. With this notation, we restrict ourselves to the zero "magnetization" subspace, where $\hat{L}_z = 0$, and where the effective Hamiltonian reads (see Sec. 4.2 in chapter 4 for a detailed derivation)

$$\hat{H} = \lambda \frac{\hat{L}^2}{2N} + \tilde{\epsilon}\hat{L}_{zz}. \tag{5.3}$$

Here, $\lambda = (g_a + g_s \frac{\Omega^2}{16E_r^2})\bar{n}$, where $\bar{n}$ is the mean density of the gas. The coefficient $\tilde{\epsilon}$ includes a perturbative correction to ϵ, with $\tilde{\epsilon} = \epsilon + \frac{\Omega^2}{16E_r}$.

Hamiltonian (5.3) is completely equivalent to the one describing the nonlinear coherent spin dynamics of spin-1 BECs where $g_a \ll g_s$ [165]. Note that such equivalence does not generally extend throughout the Hilbert space, where an additional term proportional to $\hat{L}_z^2$ breaks the SO(3) symmetry of the interacting Hamiltonian (see equation (4.21) in chapter 4). This fact motivates our restriction to the subspace with zero magnetization. Nonetheless, it should be noted that, as long as the spread in $\hat{L}_z$ is much smaller than N, the analogy can be straightforwardly extended to subspaces of any magnetization. In Fig. 5.1(c) we plot the phase diagram of Hamiltonian (5.3) in the $\Omega - \epsilon$ plane using the expression for $\tilde{\epsilon}(\Omega, \epsilon)$ and $\lambda(\Omega)$, and considering a mean density $\bar{n} = 7.5 \times 10^{13}$ cm^{-3} and the values for g_a and g_s for ^{87}Rb as given in [147]. The dashed vertical line at $\Omega = 4E_r\sqrt{|g_a|/g_s}$ separates the ferromagnetic ($\lambda < 0$) and the antiferromagnetic ($\lambda > 0$) regimes of the dressed-spin dynamics. The antiferromagnetic regime includes the polar (P) phase at $\tilde{\epsilon}(\Omega) > 0$, in which all the atoms occupy the middle well mode, and the twin-Fock (TF) phase for $\tilde{\epsilon}(\Omega) < 0$, where the atoms evenly occupy both edge-well states. The scenario is richer in the ferromagnetic regime, where the effective spin interactions favor the formation of a non-vanishing transverse magnetization. When the effective interaction dominates, this results in the spontaneous breaking of the SO(2) symmetry of the system [301], giving rise to the so-called broken-axisymmetry (BA) phase [324] in between the P and TF phases.

5.2 ESQPs in SOC gases

Recently, ferromagnetic spin-1 BECs, which are described by the collective spin Hamiltonian (5.3) with $\lambda < 0$, have been shown to exhibit ESQP transitions [323]. The Hamiltonian hosts three separate ESQPs that extend from the ground state phases and span across the whole energy spectrum. The ESQP diagram of (5.3) in the $\tilde{\epsilon} - \mathcal{E}$ plane is shown in Fig. 5.2(a) for $\lambda < 0$, where $\mathcal{E} = \langle H \rangle / (|\lambda| N)$ is the scaled energy per particle of the eigenstates of $\hat{H}$ and $\mathcal{E}_g$ is the one of the ground state. The phases P', BA' and TF' are labelled according to the corresponding ground state phase of (5.3), which were discussed in detail in Sec. 4.3. At the boundaries between the phases, the mean-field limit of the density of states diverges, as it is expected for an ESQP transition [121]. The boundaries are found at the critical energies $\mathcal{E}^*$, which in turn depend on the additional control parameter $\tilde{\epsilon}$ and are given by $\mathcal{E}^* = \tilde{\epsilon}/|\lambda|$ for $-2 < \tilde{\epsilon}/|\lambda| < 0$,

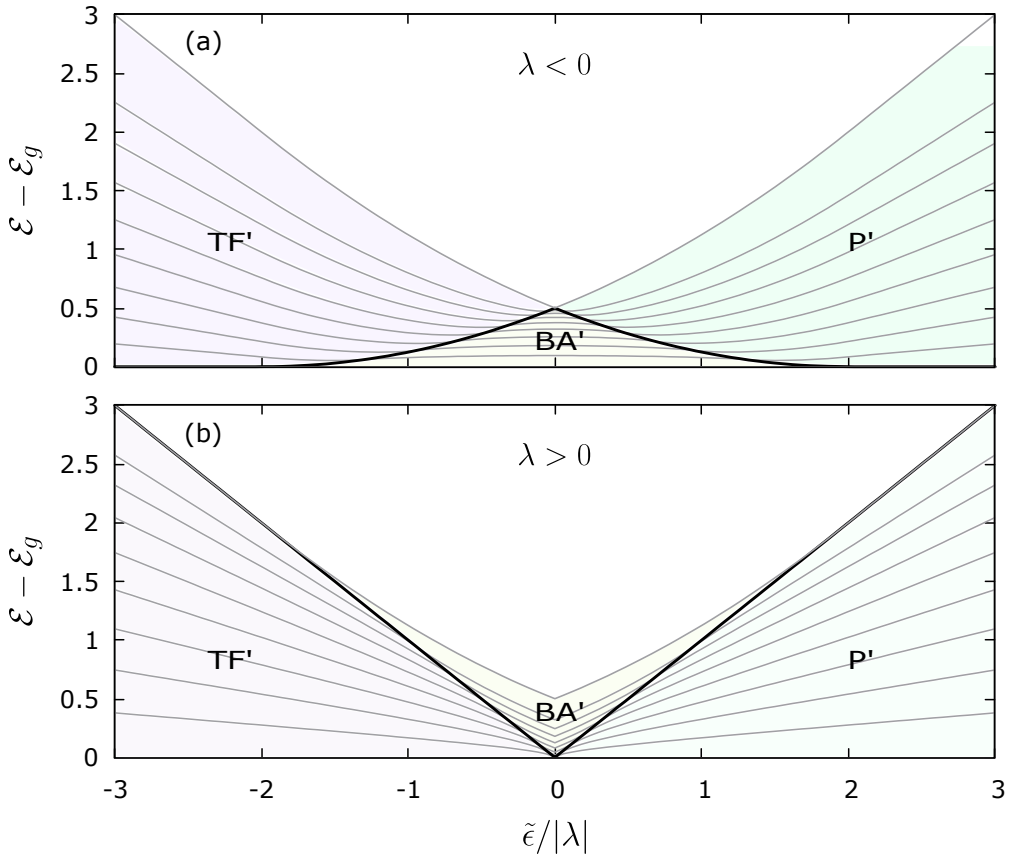

Figure 5.2: Excited-state quantum phases (ESQPs) in SOC BECs. ESQP diagram of Hamiltonian (5.3), which describes the low-energy landscape of spin-1 gases with spin-orbit coupling, for both effective ferromagnetic (a) and antiferromagnetic (b) dressed-spin interactions. The horizontal axis shows the scaled value of the effective quadratic Zeeman shift $\tilde{\epsilon}$ and the vertical axis indicates the energy of the eigenstates relative to the ground state energy. The thin gray lines show every twenty-fifth eigenvalue of the Hamiltonian for $N = 500$. The thick black line indicates the phase boundary at the critical energies $\mathcal{E}^*(\tilde{\epsilon})$.

and at $\mathcal{E}^* = 0$ for $0 < \tilde{\epsilon}/|\lambda| < 2$. Notice that, since $\hat{H}(\lambda, \tilde{\epsilon}) = -\hat{H}(-\lambda, -\tilde{\epsilon})$, the same three phases also occur for antiferromagnetic gases, but with their boundaries redefined, as shown in Fig. 5.2(b). In this regime, the critical energies are found at $\mathcal{E}^* = 0$ for $-2 < \tilde{\epsilon}/|\lambda| < 0$, and $\mathcal{E}^* = \tilde{\epsilon}/|\lambda|$ for $0 < \tilde{\epsilon}/|\lambda| < 2$.

As discussed thoroughly in [323], within these ESQPs the classical phase-space trajectories of coherent states can be classified with respect to a topological order parameter (for a similar behavior in the Rabi model, see [352]). In this section, we will show that this order parameter is directly related to the stability of the density modulations in the spin-orbit-coupled gas. We will exploit this relationship to provide a novel detection protocol for the ESQPs of the spinor gas.

As in [323], we consider now the set of coherent states $|N,\mathbf{n},\boldsymbol{\theta}\rangle = \frac{1}{\sqrt{N!}}\left(\sum_j \sqrt{n_j}e^{i\theta_j}b_j^\dagger\right)^N|0\rangle$ in the zero magnetization subspace, with $\sum_j n_j = 1$ and $n_1 = n_{-1}$. In the mean-field limit of (5.3), the scaled energy per particle is given by

$$\mathcal{E}(\mathbf{n},\boldsymbol{\theta}) = \langle N,\mathbf{n},\boldsymbol{\theta}|\,\hat{H}\,|N,\mathbf{n},\boldsymbol{\theta}\rangle\,/|\lambda|N = \mathrm{sgn}(\lambda)2(1-n_0)n_0\cos^2\theta + \frac{\tilde{\epsilon}}{|\lambda|}(1-n_0), \quad (5.4)$$

where we define the spinor phase $\theta = \theta_0 - \frac{\theta_1+\theta_{-1}}{2}$. From (5.4), we obtain the corresponding mean-field equations of motion

$$\dot{n}_0 = \frac{|\lambda|}{\hbar}\frac{\partial\mathcal{E}}{\partial\theta}, \qquad \dot{\theta} = -\frac{|\lambda|}{\hbar}\frac{\partial\mathcal{E}}{\partial n_0}. \quad (5.5)$$

The solutions of equations (5.5) are periodic, and the relationship between the periodicity of $n_0(t)$ and $\theta(t)$ varies between the different ESQPs. In the BA' phase, for each point in the $\tilde{\epsilon}-\mathcal{E}$ plane there exist two solutions with disconnected trajectories. In these solutions both $n(t)$ and $\theta(t)$ have the same periodicity. Furthermore, the values that $\theta(t)$ can take are bounded, with $-\pi/2 < \theta(t) < \pi/2$ in one solution and $\pi/2 < \theta(t) < 3\pi/2$ in the other. Conversely, in the P' and TF' phases the solution is unique at each point and the spinor phase θ is unbounded. By labelling the periodicity in $n(t)$ by τ , in the P' and TF' phases of the ferromagnetic diagram one has $\theta(t+\tau) = \theta(t) \pm \pi$ (see [295], [162] and [323] for more details). In [323], they introduce the winding number

$$w = \frac{1}{\pi}\left[\theta(\tau) - \theta(0)\right], \quad (5.6)$$

which can be interpreted as a topological order parameter that distinguishes between the three excited phases. It takes the value $w = -1, 0, 1$ for any mean-field trajectory within the P', BA' and TF' phases, respectively. In the antiferromagnetic diagram, the sign of w is flipped with respect to the ferromagnetic case.

5.2.1 The Excited-Stripe phase

So far, we have described the excited phases that occur in the collective spin model (5.3). In the spinor gases, these can be identified by their effect on the properties of the phase space trajectories in the classical limit, in particular, on the behavior of the spin population n_0 and the spinor phase θ. Remarkably, we saw in chapter 4 that in the Raman-based realization of Hamiltonian (5.3), the presence of spin-orbit coupling correlates these two quantities to the motional degrees of freedom in the gas. Specifically, in Sec. 4.3.2 we described the spatial properties of the ground state phases of the spin-orbit-coupled condensate in terms of n_0 and θ. We will now extend this relationship to the whole phase space diagram of the effective model and relate properties of the trajectories $(n_0(t), \theta(t))$ that coherent pseudospin states follow to the those of the Raman-dressed atomic cloud.

To do so, we write the mean-field wavefunction of the gas as $\boldsymbol{\psi}(\mathbf{r}) = \sqrt{N}\sum_j \sqrt{n_j}\boldsymbol{\phi}_j(\mathbf{r})e^{i\theta_j}$, where we label the three self-consistent modes around $\mathbf{k}_j$ as $\boldsymbol{\phi}_j$. As argued in Sec. 4.3.2, since we consider that $\hbar\omega_t \ll E_r$, the three modes are well located at the vicinity of the lowest dispersion band minima, and can be described by plane waves (see equation (4.29)) times a slowly varying envelope function. In these conditions, the spatial density of the gas can be approximated to

$$n(\mathbf{r},t) = \boldsymbol{\psi}^*(\mathbf{r},t)\cdot\boldsymbol{\psi}(\mathbf{r},t) \sim \bar{n}\left(1+\frac{\Delta n(x,t)}{\bar{n}}\right), \tag{5.7}$$

where

$$\Delta n(x,t) = \bar{n}\cos(k_1 x-\Delta)\frac{\Omega}{E_r}\sqrt{\frac{n_0(t)(1-n_0(t))}{2}}\cos\theta(t) + O((\Omega/8E_r)^2). \tag{5.8}$$

Here, $\Delta = \theta_1 - \theta_{-1}$ is the phase difference between the modes located at the edge band minima, which is a constant of motion if we set $\delta = 0$. In this way, the mean-field solutions of (5.3) exhibit spatial density modulations that depend both on n_0 and θ, with a relative amplitude given by

$$A(t) = \frac{\Omega}{E_r}\sqrt{\frac{n_0(t)(1-n_0(t))}{2}}\cos\theta(t). \tag{5.9}$$

Let us now evaluate the behavior of these density modulations in the different excited phases introduced above. In both the P' and TF' excited phases, the trajectories fulfill that $n_0(t+\tau) = n(t)$ and $\cos\theta(t+\tau) = -\cos\theta(t)$. Hence, it follows from (5.9) that

$$\frac{1}{2\tau}\int_0^{2\tau} dt A(t) = 0, \tag{5.10}$$

and so

$$\lim_{T\to\infty}\frac{1}{T}\int_0^{T} dt A(t) = 0, \tag{5.11}$$

for all solutions in the P' and TF' phases. Thus, while an arbitrary excited state in such phases can exhibit spatial density modulations at a given time, such modulations vanish in the time-averaged density profile.

The situation is different for the trajectories that belong to the BA' excited phase. There, for each $\tilde{\epsilon}$ and $\mathcal{E}$, there are two classical solutions that fulfill $\cos\theta(t) > 0$ and $\cos\theta(t) < 0$, respectively, for all t. Therefore

$$\lim_{T\to\infty}\left|\frac{1}{T}\int_0^{T} dt A(t)\right| > 0. \tag{5.12}$$

Thus, we can define a new observable that distinguishes a novel ESQP of the SOC spin-1 gas, which we label as Excited-Stripe phase (ES). The classical solutions exhibit a nonzero time-averaged amplitude of the spatial density modulations, or stripes, in the region of parameters that corresponds to the BA' ESQP of the effective dressed spin

model of (5.3). The topological order parameter w therein is then associated with the stability of the stripes in the Raman-dressed spin-1 gas. This stability is well understood from the locking of the relative spinor phase θ in the classical mean-field trajectories when $w = 0$, which arises from the effective dressed spin-changing collisions in the gas.

Notice that in presence of a nonzero detuning δ, the phase of the modulations, Δ, (see equation (5.8)), becomes time dependent, with $\dot{\Delta} = \dot{\theta}_1 - \dot{\theta}_{-1} = 2\delta/\hbar$. While the amplitude of the stripes remains unchanged at leading order, this time dependence of the phase results in vanishing modulations in the time-averaged density profile in the laboratory frame, regardless of the behavior of $A(t)$. Yet even in this situation, there always exists a frame co-moving with the modulation where time-averaging of modulations yields the same nonzero value as at $\delta = 0$. Such a frame can not be defined for the dressed states that correspond to excited TF' and P' states, and thus the definition of the ES phase can be conceptually generalized. In practice, though, the ES phase can be more conveniently distinguished in the presence of nonzero detuning, or even time-dependent, from the behavior of the contrast of the modulations over time. This will be discussed in detail in Sec. 5.2.3.

In the ES phase, the contrast of the stripes increases with Ω, and, thus, is larger in the antiferromagnetic regime of (5.3), where $\Omega > \Omega_c$. At the same time, for nearly-spin-symmetric gases such as ^{87}Rb, the region of parameters where the ES can exist is much broader there, as indicated with blue-dotted lines in Fig. 5.1(c). Yet in this regime the stripe phase does not occur in the ground state of the Raman-dressed gas, and one may suspect the gas to undergo a phase separation between the different spin components over time. Still, within the validity of three-mode truncation that leads to (5.3), phase separation does not occur, and thus the effective model predicts that the ES phase will persists as excited states even at $\Omega > \Omega_c$, in the same way as we showed for states in the most-excited manifold of the effective Hamiltonian in chapter 4. However, with the ES phase being defined and understood in terms of the stability of the spinor phase over time, its characterizing observable, that is, the time-averaged density profile (or the time-dependent behavior of the contrast, as we will show below), is predictably more sensitive to the validity of the three-mode truncation.

Such a three-mode truncation is equivalent to the single-spatial mode approximation in undressed antiferromagnetic spinor condensates. As the latter, it holds better the smaller the condensate and for zero total magnetization [320]. As for the latter, it is notoriously difficult to determine analytically its precise range of validity. Naturally, the physical requirement on the Hamiltonian of the gas for the single-spatial mode approximation to hold is that its nonsymmetric part has to be a perturbation of the symmetric part, so that $\lambda \ll g_s\bar{n}$ and $\lambda \ll \hbar\omega_t$. To assess the validity of the truncation in the Raman-dressed gas and the extent to which the ES phase can be realized there, we will next compare the predictions of the model with the mean-field evolution of the whole gas.

5.2.2 The ES phase: Gross-Pitaevskii results

To verify the predictions of model (5.3) for Raman-dressed SOC gases, we simulate the GPE of the whole system

$$i\hbar\dot{\psi}_j = \delta E[\boldsymbol{\psi}]/\delta\psi_j^*, \tag{5.13}$$

where $E[\psi]$ is the energy functional in (5.2). We calculate the self-consistent modes $\boldsymbol{\phi}_j$ via imaginary time evolution of the GPE and define $n_0 = b_0^* b_0$ and $\theta = \arg(b_0) - (\arg(b_1) + \arg(b_{-1}))/2$, with

$$b_j = \frac{1}{N}\int d\mathbf{r}\boldsymbol{\phi}_j^*(\mathbf{r})\cdot\boldsymbol{\psi}(\mathbf{r}). \tag{5.14}$$

We consider small ^{87}Rb condensates in the $F = 1$ hyperfine manifold, with $E_r/\hbar = 2\pi \times 3678\,\text{Hz}$, $k_r = 7.95 \times 10^6\ \text{m}^{-1}$. We use the corresponding values $a_0 = 101.8a_B$ and $a_2 = 100.4a_B$ for the scattering lengths in the different channels, taken from [147], where a_B is the Bohr radius.

In Fig. 5.3(a), we plot the relative amplitude $A(t)$ as a function of time for two different states prepared at $\Omega = 0.75E_r$, $\omega_t = 2\pi \times 140$ Hz, and $\delta = 0$ with $N = 10^4$. In both cases, we adjust ϵ so that $\tilde{\epsilon} = -0.5|\lambda|$ and set $n_0(0) = 0.5$. We then evolve the initial state with the GPE (5.13). In one trajectory (red solid line), the state is initialized at $\theta = 0.1\pi$, with a corresponding $\mathcal{E} > \mathcal{E}^* = 0$, and thus expected to be in the ES phase. Indeed, in agreement with the effective model, $A(t)$ is periodic and remains positive (or negative) at any time t, due to the spinor phase being bounded along the mean-field trajectory. Conversely, the blue dashed line corresponds to a trajectory with $\theta(0) = 0.3\pi$, and so $\mathcal{E} < \mathcal{E}^*$, thus out of the ES phase (see Fig. 5.2(b)). In this case the amplitude oscillates between positive and negative values, averaging to 0 over a period. In Fig. 5.3(b) we show the corresponding time-averaged density profile of the condensate, given by

$$\langle n(x)\rangle_T = \frac{1}{T}\int_{t_0}^{t_0+T} dt \int dydz|\boldsymbol{\psi}(\mathbf{r})|^2, \tag{5.15}$$

and averaged over a time $T = 500$ ms. As expected, $\langle n\rangle_T$ exhibits large modulations when $\mathcal{E} > \mathcal{E}^* = 0$, while these vanish for $\mathcal{E} < \mathcal{E}^* = 0$. In Fig. 5.3(c) we plot the fraction of atoms that remain within the three-mode subspace, or fidelity, $f_{3M} = \frac{1}{N^2}\sum_j \left|\int d\mathbf{r}\boldsymbol{\phi}_j^*\cdot\boldsymbol{\psi}\right|^2$, as a function of time, which highlights the accuracy of the approximation in this regime of parameters.

As exemplified by the results shown in Fig. 5.3, the GPE analysis of the Raman-dressed gas supports the predictions of the dressed spin model in a broad, and experimentally accessible, range of parameters. We stress that the stripe phase as an ESQP is only well defined and understood within the three-mode subspace, where the robustness of the spatial density modulations is enabled by the collective spin structure of the effective Hamiltonian. The contrast of the modulations in $\langle n(x)\rangle_T$ is very sensitive on the

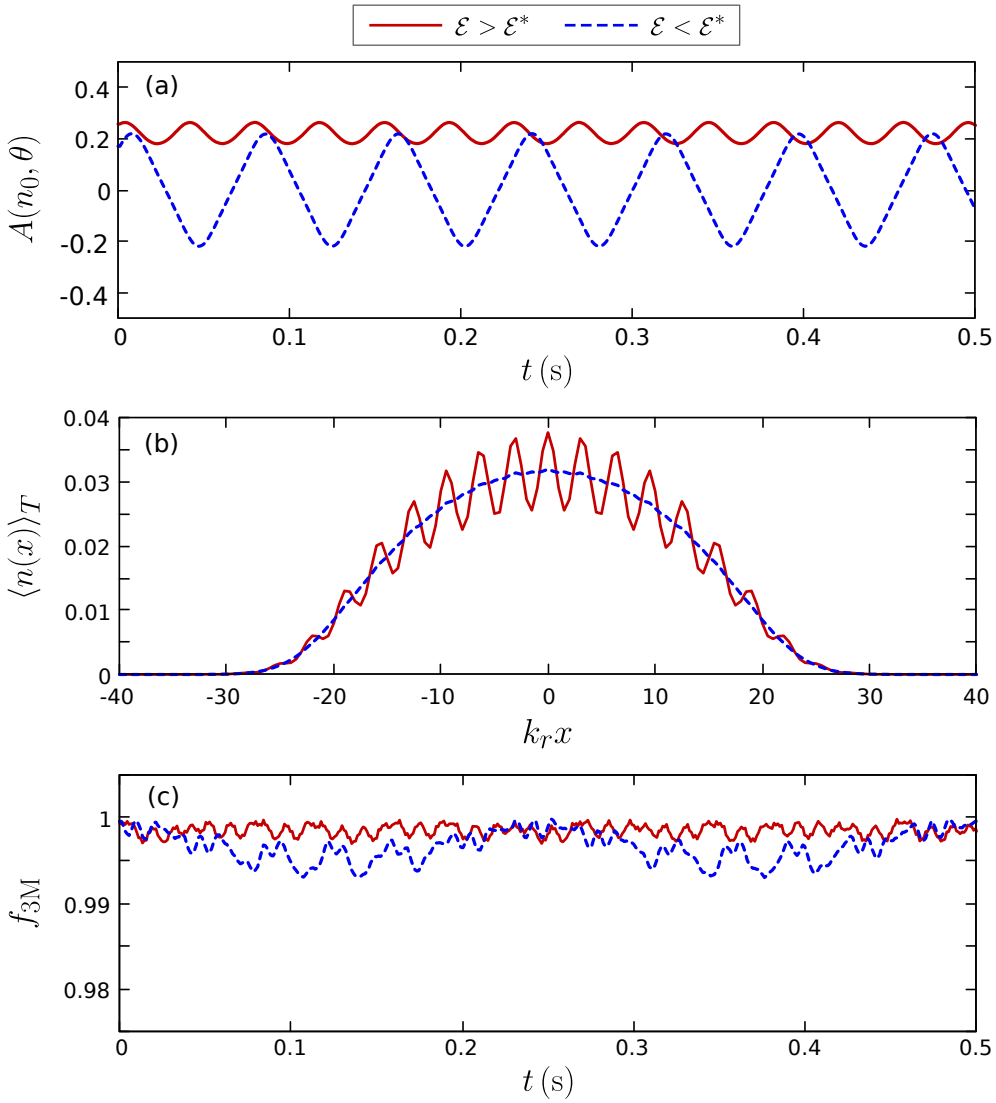

Figure 5.3: Signature of the excited-state stripe phase. (a) Relative amplitude $A(t)$ of the spatial modulations for a dressed condensate of $N = 10^4$ particles prepared with $\Omega = 0.75E_r$, $\omega_t = 2\pi \times 140$ Hz, $\delta = 0$ and $\tilde{\epsilon} = -0.5|\lambda|$, computed using the GPE (5.13). Red solid line: $A(t)$ for a state initially at $n_0(0) = 0.5$ and $\theta = 0.1\pi$, with $\mathcal{E} > \mathcal{E}^*$ (ES phase). Blue dashed line: $A(t)$ for an initial state at $n_0(0) = 0.5$ and $\theta = 0.3\pi$, with $\mathcal{E} < \mathcal{E}^*$ (T' phase). (b) Corresponding time-averaged density profile of the condensate, $\langle n(x) \rangle_T$, averaged over $T = 0.5$s. When $\mathcal{E} > \mathcal{E}^*$, the spatial modulation in $\langle n(x) \rangle_T$ does not vanish with increasing T. (c) Fraction of the condensate that remains within the subspace spanned by the self-consistent modes $\boldsymbol{\phi}_j$.

degree of accuracy of the truncation, which in turn depends both on the strength of the effective spin interaction coefficient $|\lambda|$ and on the total number of particles.

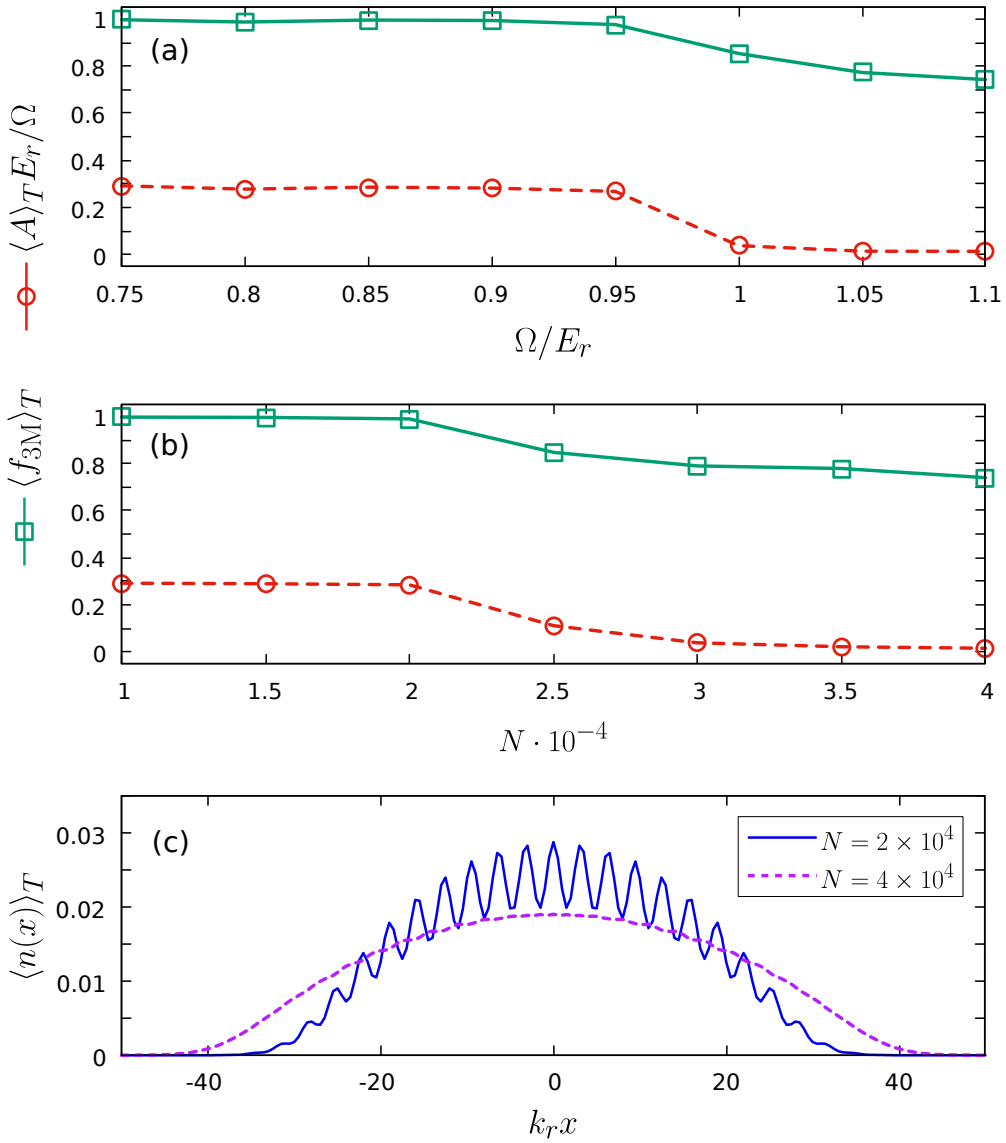

Figure 5.4: Robustness of the ES phase. (a) Time-averaged relative amplitude, $\langle A\rangle_T$ (red circles), and fidelity of the three-mode truncation, $\langle f_{3M}\rangle_T$ (green squares), as a function of Ω for a dressed condensate of $N = 10^4$ particles. The state is prepared with $n_0(0) = 0.5$ and $\theta = 0.1\pi$, and evolved using (5.13) with $\tilde{\epsilon} = -0.5|\lambda|$. (b) $\langle A\rangle_T$ and $\langle f_{3M}\rangle_T$ as a function of N for a state prepared at $n_0(0) = 0.5$ and $\theta = 0.1\pi$, with $\Omega = 0.75E_r$ and $\tilde{\epsilon} = -0.5|\lambda|$. (c) Time-averaged density profile for the corresponding trajectories with $N = 2\times10^4$ (blue solid line) and $N = 4\times10^4$ (purple dashed line) from (b). In all cases, the state is evolved for $T = 500\,\mathrm{ms}$ and ω_t is adjusted to have $\bar{n} = 7.5\times10^{13}\,\mathrm{cm}^{-3}$.

This sensitivity is illustrated in Fig. 5.4, where we show the values of the time-averaged amplitude $\langle A\rangle_T = \frac{1}{T}\int_0^T dt A(t)$ and fidelity $\langle f_{3M}\rangle_T = \frac{1}{T}\int_0^T dt f_{3M}(t)$ for a state

initialized at $n_0 = 0.5$ and $\theta = 0.1\pi$ and evolved under eq. (5.13), for several values of Ω in Fig. 5.4(a), and for a varying total number of particles in Fig. 5.4(b). In all cases, ω_t is adjusted so that $\bar{n} = 7.5 \times 10^{13}\,\mathrm{cm}^{-3}$, and the quantities are averaged over a total time $T = 500\,\mathrm{ms}$. In Fig. 5.4(a) we set $N = 10^4$, and in Fig. 5.4(b) $\Omega = 0.75E_r$. While, according to the effective model (5.3), the state is prepared within the BA' phase, with $\mathcal{E} > \mathcal{E}^*$, the contrast of the time-averaged density modulations rapidly vanishes as soon as the fidelity of the three-mode truncation degrades. This is exemplified in Fig. 5.4(c), where we plot the time-averaged density profile for the corresponding trajectories with $N = 2 \times 10^4$ and $N = 4 \times 10^4$ from Fig. 5.4(b). In the latter case, the stripes are absent in the time-averaged density profile, despite having considered the same Raman dressing parameters and atom density than in the former, and the same initial relative spin populations.

It is clear, then, that the collective spin structure is fundamental to the nature of the ES phase. Still, we are able to identify a wide range of parameters for which the few-mode description is accurate, and the behavior of the dressed gas understood in these terms. Furthermore, the direct connection between the ES phase of the Raman-dressed gas and the BA' phase of the effective spin model can provide a powerful tool for the detection of the ESQPs of the spinor gas.

5.2.3 Signature of the BA' ESQP

In [323], the authors propose an experimental scheme to detect the BA' ESQP of a spinor gas. The protocol relies on an interferometric scheme to measure the absolute value of the winding number of (5.6), $|w|$, where the spins are coupled via an internal-state beam splitter after the state is evolved for a period T. Such a scheme faces a major difficulty: the visibility of the projected measurement is very sensitive to the accumulated phase difference between the ± 1 modes, and hence, to the magnetic field fluctuations in the experiment.

We now show that the realization of the same effective Hamiltonian in the Raman-dressed spinor gas can in principle avoid such a drawback. As discussed in Sec. 5.2.1, the amplitude of the spatial density modulations in the dressed gas does not depend at first order in Ω/E_r on the relative phase Δ, and so neither does the contrast or visibility of the modulations. Using expressions (5.7) to (5.9) for the density of the gas, we can define a theoretical value for the peak-to-valley contrast of the stripes

$$\mathrm{V}_{\mathrm{ptv}}^{\mathrm{th}}(t) = \frac{\max(n) - \min(n)}{\max(n) + \min(n)} = |A(t)| = \frac{\Omega}{E_r}\sqrt{\frac{n_0(t)(1-n_0(t))}{2}}\,|\cos\theta(t)|. \tag{5.16}$$

We conveniently define the scaled contrast $\tilde{\mathrm{V}}$ as

$$\tilde{\mathrm{V}}(t) = \mathrm{V}_{\mathrm{ptv}}^{\mathrm{th}} E_r/\Omega = \sqrt{\frac{n_0(t)(1-n_0(t))}{2}}\,|\cos\theta(t)|. \tag{5.17}$$

The measurement of the contrast of the stripes involves, therefore, a simultaneous measurement of the population n_0 and the phase θ. From the behavior of the contrast alone,

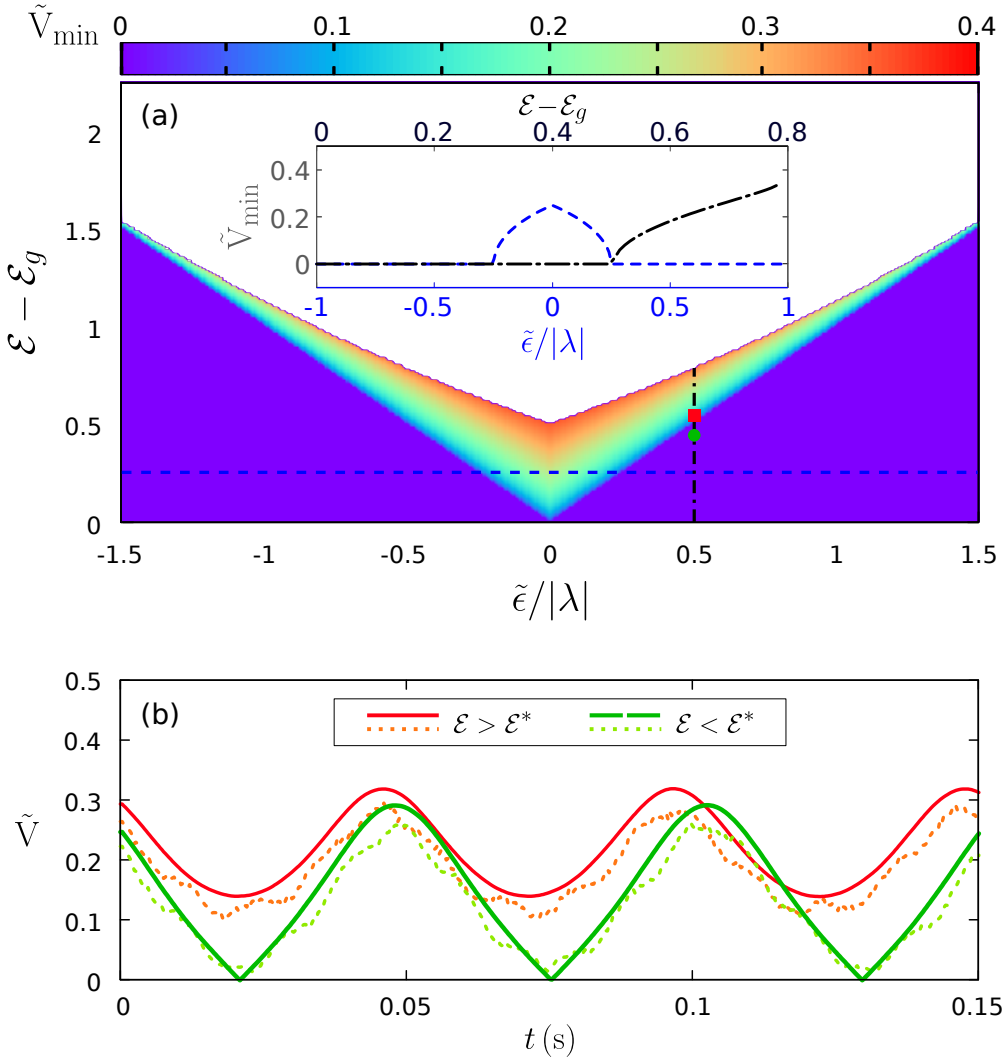

Figure 5.5: Stripe contrast as signature of the BA' ESQP. (a) Minimum value $\tilde{V}_{min}$ of the scaled contrast $\tilde{V} = \sqrt{2n_0(1-n_0)}|\cos\theta|$ along the classical trajectories given by equations (5.5), as a function of $\tilde{\epsilon}$ and $\mathcal{E}$, computed using eq. (5.18). The inset shows $\tilde{V}$ for constant $\mathcal{E} - \mathcal{E}_g = 0.25$ (blued dashed line) and $\tilde{\epsilon}/|\lambda| = 0.5$ (black dash-dotted line). (b) $\tilde{V}$ as a function of time for two classical trajectories at $\tilde{\epsilon}/|\lambda| = 0.5$, in and out of the BA'(ES) phase, indicated in (a) by the red and green square dots, respectively. The red solid line corresponds to $n_0(0) = 0.6$ and $\phi(0) = 0.174$, with $\mathcal{E} > \mathcal{E}^*$. The green dashed line corresponds to $n_0(0) = 0.6$ and $\phi(0) = 0.243$, with $\mathcal{E} < \mathcal{E}^*$. The corresponding values for the peak-to-valley scaled contrast of the solutions of the GPE (5.13) are shown in dotted lines. The values are obtained for a condensate of $N = 10^4$ and $\bar{n} = 7.5 \times 10^{13}\,\mathrm{cm}^{-3}$, setting $\Omega = 0.75E_r$.

we can infer the absolute value of the winding number of (5.6), $|w|$, and, thus, detect the BA' phase of the pseudospin gas –the ES phase of the dressed gas– regardless of the

values taken by $\Delta(t)$.

The contrast $\tilde{\mathrm{V}}$ is a positive semidefinite quantity and for generic n_0 can reach zero only when θ reaches $(2k+1)\pi/2$, with $k \in \mathbb{Z}$. This obviously occurs in the P' and TF' phases, where θ is unbounded, but never occurs in the BA' phase where $|\theta| \leq \theta_{\max} < \pi/2$. Thus, the minimum value $\tilde{\mathrm{V}}_{\min}$ of the scaled contrast (5.17) is a proxy of $|w|$ as it is nonzero only in the BA' phase, as illustrated in Fig. 5.5(a), where we plot $\tilde{\mathrm{V}}_{\min}$ along the classical trajectories as a function of $\tilde{\epsilon}$ and $\mathcal{E}$. The onset of nonzero $\tilde{\mathrm{V}}_{\min}$ is found at the critical energy $\mathcal{E}^*$. The behavior of $\tilde{\mathrm{V}}_{\min}$ along the direction of both the energy and the control parameter $\tilde{\epsilon}$ is illustrated in the inset of Fig. 5.5(a), which undergoes nonanalytical changes at the boundary of the ESQP transition. We exemplify the behavior of the contrast in the different excited phases in Fig. 5.5(b), where we plot $\tilde{\mathrm{V}}$ as a function of time along two trajectories at $\tilde{\epsilon}/|\lambda| = 0.5$. We choose the parameters to have one trajectory within the BA' phase, with $\mathcal{E}$ slightly above $\mathcal{E}^*$, and the other in the TF' phase, with $\mathcal{E} < \mathcal{E}^*$. For comparison, in the figure we show in dotted lines the corresponding results from the GPE equation of the dressed and trapped gas (5.13). In this case, the contrast is computed from the averaged relative peak-to-valley difference in the condensate density profile along the direction of the Raman dressing. As predicted, in the trajectory slightly above the critical energy, the contrast of the stripes oscillates periodically but does not vanish at any time.

We note that values of the minimal contrast shown Fig. 5.5(a) are obtained analytically using (5.17). By taking the time derivative of expression (5.17) and using (5.5), it is clear that, in the BA' phase, $\tilde{\mathrm{V}}$ can only be minimal (or maximal) at $\theta = 0$. We then use (5.4) and (5.17) with $\theta = 0$ to retrieve the analytical expression for $\tilde{\mathrm{V}}_{\min}$ in terms of the mean-field energy density and the control parameter $\tilde{\epsilon}$, which reads

$$\tilde{\mathrm{V}}_{\min} = \sqrt{\mathcal{E} - \frac{\frac{\tilde{\epsilon}}{\lambda}\left(\frac{\tilde{\epsilon}}{\lambda}+2\right) + \frac{|\tilde{\epsilon}|}{\lambda}\sqrt{\left(\frac{\tilde{\epsilon}}{\lambda}-2\right)^2 - 8\left(\mathcal{E} - \frac{\tilde{\epsilon}}{\lambda}\right)}}{4}}. \tag{5.18}$$

Such a derivation, however, assumes that the condensates are perfectly located at the three minima of the dispersion band. The presence of trapping leads to a momentum spread of the wavepackets, decreasing the actual contrast of the stripes in the cloud. This can be observed in Fig. 5.5(b), where the peak-to-valley contrast evaluated in the condensate wavefunction is slightly lower than the value predicted by eq. (5.17). Nonetheless, for relatively small trapping frequencies the behavior of the gas in the distinct ESQPs is qualitatively well described by eq. (5.17).

In this way, we have shown that the realization of the collective spin Hamiltonian (5.3) with a Raman-dressed artificial spinor gas can provide an alternative approach to the detection of the ESQP transition therein. In the dressed system, we propose to exploit the built-in interferometer that arises from Raman-dressing, where the three quasimomentum-shifted dressed states can spatially interfere due to their nonzero spin overlap. The behavior of the density modulations arising from such interference signals the value of the topological order parameter that characterizes the BA' phase of the

effective spin system introduced in [323]. Our proposal, thus, does not rely on any external interferometric measurement, which results in an intrinsic robustness to magnetic fluctuations. In such a scheme, the precision to delimit the boundary of the BA' phase is subject to the experimental sensitivity associated with the measurements of the density modulations. Remarkably, $\tilde{\mathrm{V}}_{\mathrm{min}}$ increases abruptly at the boundary, and the modulations of the ES states remain large at any time of the trajectory even for states close to the transition, as exemplified with the trajectory shown in solid red in Fig. 5.5(b). This behavior can be understood from the fact that, in the classical limit, $\tilde{\mathrm{V}}_{\mathrm{min}}$ plays the role of the order parameter of a second order phase transition. From (5.18) we can see that its susceptibility diverges as

$$\frac{\partial \tilde{\mathrm{V}}}{\partial \mathcal{E}} \simeq \frac{\sqrt{C}}{2}(\mathcal{E}-\mathcal{E}_*)^{-1/2}, \tag{5.19}$$

where $C = 1 + \frac{|\epsilon/\lambda|}{2-|\epsilon/\lambda|}$.

5.2.4 Quench excitation of stripe states as a dynamical quantum phase transition

We conclude this section by studying the behavior of the spatial modulations in the gas in the quench response of the system. In quantum many-body systems, a type of dynamical quantum phase transition has been defined, in which the time-average of the dynamical response of system following a quantum quench in a control parameter is regarded as the order parameter [120, 353]. In this class of critical phenomena, such an order parameter vanishes or undergoes a nonanalytical change at a critical value of the control parameter. These behaviors have been shown to occur in spin chains with long range interactions [354, 355]. Notice that the collective spin model (5.3) can be interpreted as a N-spin-1 chain with an effective infinite-range interaction, and, indeed, this type of dynamical phase transitions have been described [356] and experimentally identified with spinor gases [297, 298].

Naturally, when described by Hamiltonian (5.3), the dressed gas is expected to exhibit the same dynamical behavior (see Sec. 3.4.2 from chapter 3). Yet, again, in the dressed gas we can rethink these critical phenomena of the model in terms of the spatial degrees of freedom. We consider now the time evolution of the fully polarized state $(\hat{b}_0^\dagger)^N|0\rangle$, which is the ground state for $\tilde{\epsilon}\to\infty$, after an instantaneous quench to a finite value of $\tilde{\epsilon}$. In these conditions, in Fig. 5.6 we plot the time-averaged scaled contrast of the stripes, $\langle\hat{\mathrm{V}}\rangle_\tau$, together with the time-averaged relative occupation of the central well, $\langle\hat{n}_0\rangle_\tau$, as a function of $\tilde{\epsilon}$ and for several total number of particles. The quantities are averaged over a time $\tau = 10\tau_c$, where $\tau_c = \sqrt{N}\hbar/\lambda$ is the characteristic spin-mixing time defined for the same model in Sec. 3.4.2. Here, we have defined the quantum operators $\hat{n}_0 = \frac{1}{N}\hat{b}_0^\dagger\hat{b}_0$, $\hat{\theta} = \frac{1}{2}\arg\left(\hat{b}_1^\dagger\hat{b}_{-1}^\dagger\hat{b}_0\hat{b}_0\right)$ and $\hat{\tilde{\mathrm{V}}} = \sqrt{\hat{n}_0(1-\hat{n}_0)/2}|\cos\hat{\theta}|$.

Observe that for both the time-averaged fringe contrast and pseudospin population, a nonanalytical change in their values as a function of $\tilde{\epsilon}$ can be inferred in the thermo-

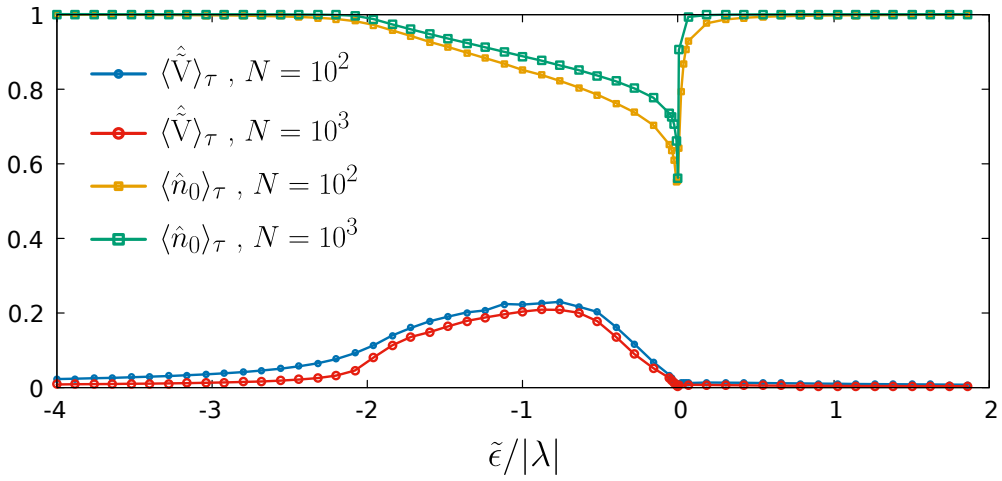

Figure 5.6: Signature of a dynamical quantum phase transition. Time-averaged relative scaled contrast of the stripes $\langle\hat{\tilde{V}}\rangle_\tau$ and time-averaged relative occupation of the middle well mode $\langle\hat{n}_0\rangle_\tau$ as a function of $\tilde{\epsilon}$, for a state initially at $|\varphi(t=0)\rangle = (\hat{b}_M^\dagger)^N |0\rangle$. The state is evolved under Hamiltonian (5.3) for $N = 100$ and $N = 1000$, and the values are averaged over a time $\tau = 10\tau_c$.

dynamic limit at $\tilde{\epsilon} = -2\lambda$ and $\tilde{\epsilon} = 0$. Given the shortened lifetime of a Raman-dressed BEC, the described long-time-averaged behavior of the gas is challenging to observe in an experiment. However, as experimentally demonstrated in [298], the dynamical phase transition can be alternatively probed by a finite-time observable. There, the authors characterize the transition with the behavior of the time averages taken over a time span that includes only the first peak (or valley) in the evolution of the observables, which appears in a short time. It should be noted though, that, unlike in the study of ESQP transitions, here the order parameter related to the spatial degrees of freedom (the contrast of the stripes) does not appear to provide any experimental advantage when compared to the one related to the internal degrees of freedom, i.e., the spin populations. Indeed, the latter can be easily detected in an experiment following a Stern-Gerlach-like measurement. Still, it is worth noting that, in some sense, the dynamical response for both order parameters appears to be qualitatively different, and therefore worth looking into it. At $\tilde{\epsilon} = 0$, the dynamical phase transition in the spin population is of first order, showing a discontinuity in the order parameter, and can be connected to the ground state quantum phase transition that takes place at this value of the control parameter. Contrarily, the change in the amplitude of the stripes decreases smoothly to zero as $\tilde{\epsilon}$ approaches $\tilde{\epsilon} = 0$ from $\tilde{\epsilon} < 0$, and the ground-state transition there does not involve the appearance of stripes. This difference further highlights the role of the spinor phase θ in the spatial structures of the excited stripe states.

In this way, in this section we have shown that, through its map to bare spin dynamics, the Raman-dressed Bose gas can provide an alternative platform to study dynamical

and ESQP transitions. This is of special relevance for the latter, where we have argued that the SOC-induced spatial properties of Raman gases could in principle provide an advantage when it comes to the detection of such excited phases. At the same time, the properties of both the quench dynamics described by the spin model and the mean-field phase space trajectories in the excited-state phase diagram can be exploited to facilitate the accessibility of stripe states in experiments with spin-orbit-coupled gases. With these insights, in the next section, we describe a quench protocol to prepare ES states in a spin-1 spinor gas.

5.3 Quench excitation of ES states via coherent spin-mixing

The pseudospin Hamiltonian (5.3) gives a simple framework to understand the collective behavior of SOC condensates. So far, in this chapter we have used this framework to identify excited-state phases in Raman-dressed Bose-Einstein condensate. Through this description, we have shown that Raman dressing can improve the accessibility of the excited-state phases of spinor gases, which in the dressed gas are characterized by the behavior of the density modulations they display. Conversely, in this section we will use the predictions of the spin model to propose a protocol that allows a robust and fast preparation of supersolid-like ES states. We will benchmark the proposal with simulations of the GPE and discuss its feasibility in state-of-the-art experiments.

5.3.1 Two-step quench scheme: few-mode predictions

By comparing the rescaled contrast (5.17) and classical energy (5.5), we notice that we can write the squared scaled contrast in terms of the mean-field energy as

$$\tilde{V}^2 = \mathrm{sgn}(\lambda)(\mathcal{E} - \tilde{\epsilon}/|\lambda|(1 - n_0)). \tag{5.20}$$

From (5.20), it immediately follows that, at $\tilde{\epsilon} = 0$, $\tilde{V}$ becomes a constant of motion of the classical trajectories as it is proportional to the square root of the classical energy. With this in mind, we propose a two-step quench scheme to access ES states that exhibit large and stable density modulations.

We consider that the system is initially in the fully polarized state with $n_0 = 1$, where all the atoms occupy the middle-well mode. Experimentally, this scenario is very convenient: such a state can be prepared from an undressed polarized condensate in the $m_f = 0$ spin state simply by adiabatically turning up Ω while keeping $\tilde{\epsilon} > 2|\lambda|$. The preparation is followed by a first quench in $\tilde{\epsilon}$ into the range $-2 < \tilde{\epsilon}/\lambda < 0$. According to the classical equations of motion (5.5), such a polarized initial state is a stationary point of the Hamiltonian at all values of $\tilde{\epsilon}$. However, as we discussed in Sec. 4.3.4 in the previous chapter, at finite N quantum fluctuations start a coherent spin-mixing dynamics that breaks the stationarity of the state [273, 325, 351]. Most importantly, as shown in 5.2.4, such a quench will lead to the excitation of stripe states, with a nonzero time

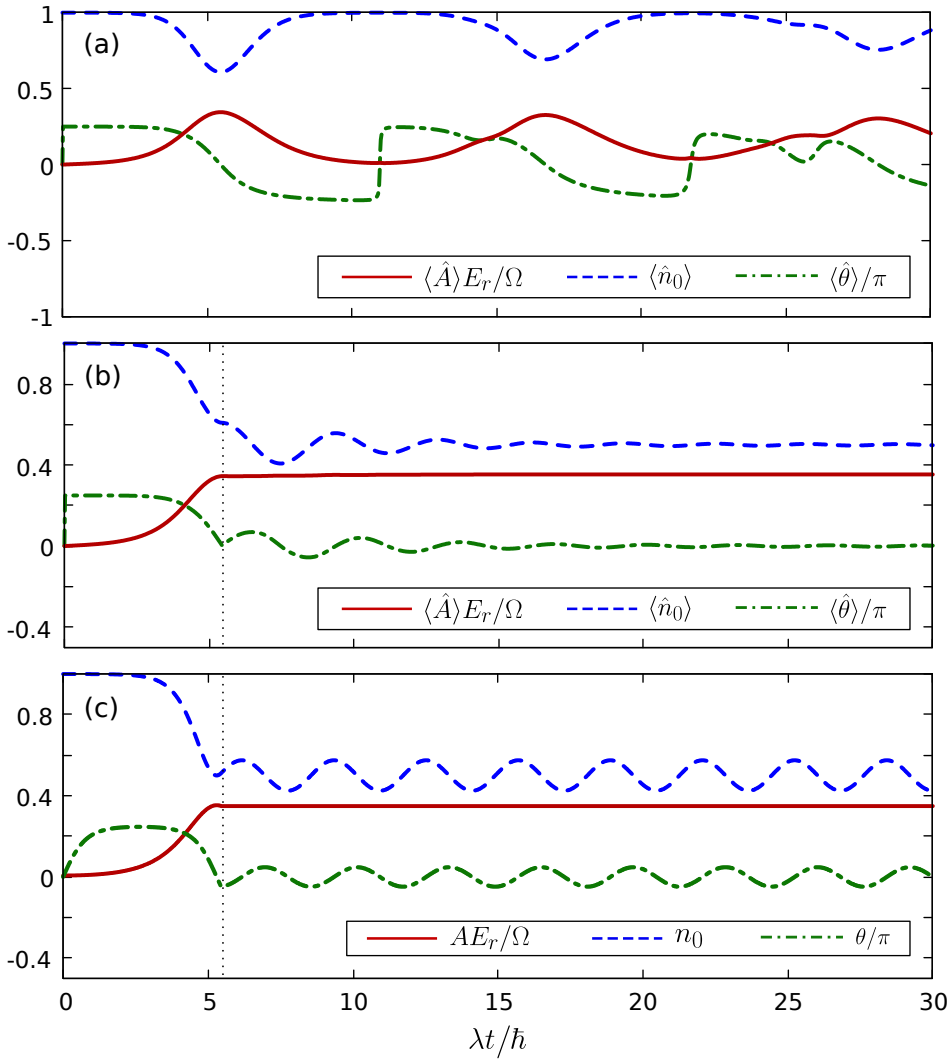

Figure 5.7: Excitation of ES states via coherent spin mixing: few-mode predictions. (a) Expected value of $\hat{n}_0$ (blue dashed line), $\hat{\theta}$ (dashed-dotted green) and $\hat{A}$ (solid red) as a function of time for a state prepared at $t = 0$ in $|\psi\rangle\,(t = 0) = (\hat{b}_0^\dagger)^N\,|0\rangle$, with $N = 10^4$ and evolved under Hamiltonian (5.3), setting $\tilde{\epsilon}/\lambda = -1$ and $\lambda > 0$. (b) The same initial state is evolved with $\tilde{\epsilon}/\lambda = -1$ for a time $t_1 = 5.5\hbar/\lambda$ (indicated with the vertical dotted gray line), where $\tilde{\epsilon}$ is quenched to 0. Following the quench, $\langle\hat{A}\rangle$ stabilizes near to its maximum value. (c) Classical trajectories for the state $n_0(0) = 0.9998$ and $\theta(0) = 0$ evolved under equations (5.5), setting $\tilde{\epsilon}/\lambda = -1$ for $t \leq t_1 = 5.5\hbar/\lambda$, and $\tilde{\epsilon} = 0$ for $t > t_1$.

average of the contrast. If the quantum evolution that the system follows some time after the quench resembles the predictions of the classical phase space trajectories, the density modulations could be stabilized with a subsequent quench to $\tilde{\epsilon} = 0$, as suggested by equation (5.20).

This is exemplified in Fig. 5.7. In Fig. 5.7(a), where we plot a quantum trajectory for an initial state $(\hat{b}_0^\dagger)^N |0\rangle$, with $N = 10^4$, evolved under Hamiltonian (5.3) with $\tilde{\epsilon}/\lambda = -1$ and $\lambda > 0$. We show the expected values of the relative occupation of the middle-well mode $\hat{n}_0 = \frac{1}{N}\hat{b}_0^\dagger \hat{b}_0$, the spinor phase $\hat{\theta} = \frac{1}{2}\arg\left(\hat{b}_1^\dagger \hat{b}_{-1}^\dagger \hat{b}_0 \hat{b}_0\right)$ and the relative amplitude $\hat{A} = (\Omega/E_r)\sqrt{\hat{n}_0(1-\hat{n}_0)/2}\cos(\hat{\theta})$ as a function of time. After some time, the expected amplitude $\langle \hat{A} \rangle$ reaches a local maximum. For a coherent state, performing a second quench to $\tilde{\epsilon} = 0$ when the maximum is reached would leave $\langle \hat{A} \rangle$ locked at this value, as it is clear from equation (5.20). Naturally, the quantum trajectories of (5.3) for noncoherent states and away from the thermodynamic limit may depart from the classical predictions. Nonetheless, we numerically find a qualitative agreement between classical and quantum trajectories, as shown in Fig. 5.7(b). In the figure, the initial state $(\hat{b}_0^\dagger)^N |0\rangle$ is evolved under Hamiltonian (5.3) with $\tilde{\epsilon} = -\lambda$ for a time $t_1 = 5.5\hbar/\lambda$, where the Hamiltonian is quenched to $\tilde{\epsilon} = 0$. Following the second quench, the relative amplitude $\langle A(t) \rangle$ is rapidly stabilized very near its maximum value $\frac{1}{2\sqrt{2}}\Omega/E_r$. For comparison, in Fig. 5.7(c) we show the analogous results for a mean-field trajectory obtained using equations (5.5). To avoid the classical stationary point at $n_0 = 1$, the state is initially in a coherent state with a very small fraction of atoms in the edge well states, with $n_0(0) = 0.9998$ in this example.

5.3.2 Excitation of ES states: Gross-Pitaevskii results

Again, we assess further the validity of the two-step scheme with the GPE of the Raman-dressed gas. In order to obtain wide and stable density modulations, we take relatively large values of Ω, and consider small condensates to be safely in the three-mode approximation. Fig. 5.8 shows a simulation of the protocol with a condensate of $N = 10^4$ particles, $\bar{n} = 7.5 \times 10^{13}\,\mathrm{cm}^{-3}$ and $\Omega = 0.75E_r$. In Fig. 5.8(a) we plot n_0, θ, and $A(t)$ as a function of time for a state initially prepared at $n_0 = 0.9998$ and time-evolved with the GPE (5.13). The state is evolved with $\tilde{\epsilon}/\lambda = -1$ for a time $t_1 = 5.5\hbar/\lambda$, where $\tilde{\epsilon}$ is quenched to 0. As expected, $A(t)$ is stabilized after the quench, despite that n_0 and θ keep oscillating with time. With the contrast stabilized, the time-averaged density profile exhibits very large density modulations, with over 20% contrast of the stripes, as shown in Fig. 5.8(b). In Fig. 5.8(c) we plot the values of $f_{3\mathrm{M}}$ during the evolution, which remains very close to 1 for the chosen parameters.

With the two-step quench scheme described, a state with near-maximal density modulations (at a given value of Ω) can be reached in a robust and fast manner. In the example shown in Fig. 5.8, we have $\lambda/\hbar \simeq 2\pi \times 17.9\,\mathrm{Hz}$, many times larger than the intrinsic spin-mixing rate in an undressed ^{87}Rb $F = 1$ spinor gas. The peak in $A(t)$ is reached in about 50 ms. The mean-field treatment of the dressed spinor gas, thus, appears to support the protocol we present. However, the feasibility of the scheme in an actual experiment is subject to the stability of the parameters of the GPE. Several sources of noise can be detrimental to the stability and contrast of the stripes prepared,

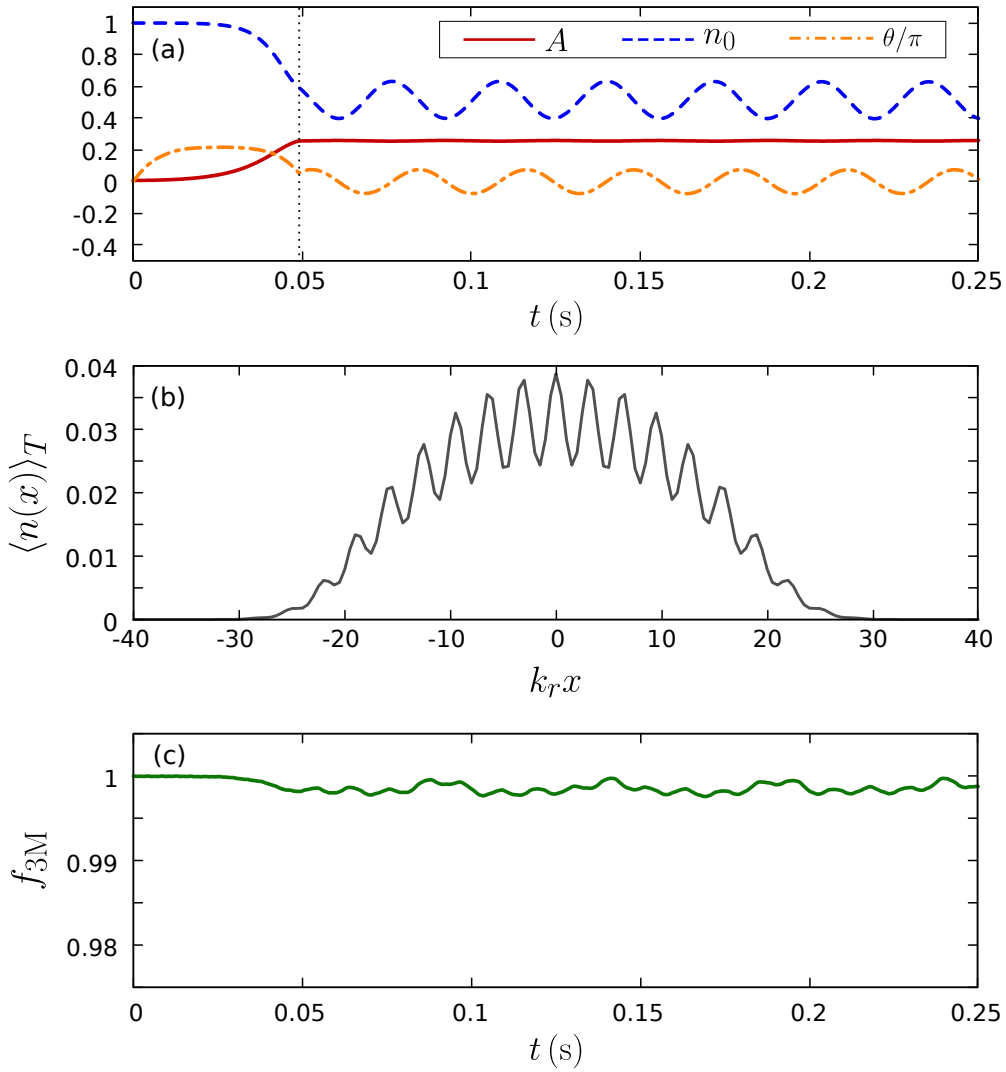

Figure 5.8: Excitation of ES states via coherent spin mixing: GPE results. (a) n_0 (blue dashed line), θ (dotted-dashed orange) and $A(t)$ (solid red) as a function of time for a state initially prepared at $n_0 = 0.9998$ and $\theta = 0$. The state is evolved with the GPE (5.13), for $N = 10^4$, $\Omega = 0.75E_r$ and ω_t adjusted to have $\bar{n} = 7.5 \times 10^{13}\,\mathrm{cm}^{-3}$. For $t \leq t_1 = 5.5\hbar/\lambda$, we set $\tilde{\epsilon}/\lambda = -1$. At $t = t_1$ (dotted vertical line) $\tilde{\epsilon}$ is quenched to 0. (b) Corresponding density profile $\langle n(x)\rangle_T$, time-averaged from $t = t_1$ to $t = 0.25\,\mathrm{s}$. (c) Relative occupation of the three-mode subspace, f_{3M}, along the preparation.

most notably the fluctuations in the Zeeman levels due to magnetic-field fluctuations and the calibration uncertainty in the intensity of the Raman beams.

To conclude this section we now briefly address the robustness of the protocol by incorporating fluctuating and randomized parameters to the simulations of the GPE, in order to mimic the effects of the main sources of noise. To account for atom loss, we

continuously renormalize the condensate wavefunction to $N(t) = N(0)\exp(-\gamma t)$, with $\gamma = 3.33\,\mathrm{s}^{-1}$, which is compatible with the lifetime of spin-1 Raman-dressed BECs in the considered regimes [244]. Furthermore, we consider a 10% Gaussian uncertainty in $N(0)$. The background magnetic noise is accounted via sinusoidal modulations of δ and ϵ at a frequency of 50 Hz. We set their amplitudes, respectively, to 700 Hz and 5 Hz, which roughly correspond to a magnetic bias field of $B \sim 35\,\mathrm{G}$ with ~ 1 mG instability in experiments with $F = 1$ ^{87}Rb atoms. We consider a Gaussian uncertainty of $\pm 5\%$ in Ω, to match the systematic uncertainty reported in [118]. Finally, a finite bias field unavoidably results in a residual cross coupling between the two Raman-dressed Zeeman state pairs. This cross coupling is translated into an effective shift in the value of ϵ that depends on Ω, which can be computed from Floquet theory. We use the polynomial expression for the shift as given in Methods from [118].

With all these considerations, we reproduce the protocol described in this section while incorporating now the uncertainties in the parameters. In Fig. 5.9(a1) we plot the corresponding mean value and standard deviation of $A(t)$, n_0 and $f_{3\mathrm{M}}$ as a function of time, evaluated from a sample of 20 realizations. Despite the addition of noise, the preparation still yields large and stable modulations in the density profile for the parameters chosen. As discussed in the previous section, the tunability of the Raman-mediated spin-mixing allows the realization of the protocol in larger condensates. This can be achieved by setting a lower Ω (see Fig. 5.4), but at the expense of a smaller contrast of the stripes, as well as of detrimental effects from noise and atom loss. This is exemplified in Fig. 5.9(a2), where we plot the results for an analogous preparation with $N(0) = 10^5$ and $\Omega = 0.5E_r$. The trap frequency is adjusted to initially have $\bar{n} = 7.5 \times 10^{13}\,\mathrm{cm}^{-3}$. While smaller, the amplitude $A(t)$ is stabilized in less than 200 ms, with over half the atoms remaining in the condensate.

In Fig. 5.9(b) we plot the longitudinal density $|\boldsymbol{\psi}|^2$, the spin density $\mathcal{F}_x = \boldsymbol{\psi}^* \hat{F}_x \boldsymbol{\psi}$ and the nematic density $\mathcal{N}_{xx} = \boldsymbol{\psi}^*(2/3 - \hat{F}_x^2)\boldsymbol{\psi}$ at $t = t_1$, right after the quench to $\tilde{\epsilon} = 0$. The quantities are computed for a randomly chosen realization from the samples used in Fig. 5.9(a). The values shown are not time-averaged since the instability in δ induces a back-and-forth displacement of the stripes. However, as discussed in Sec. 5.2, the width of the stripes remains stable over time, according to (5.9). In the prepared ES states, the periodicity of the spatial modulations match those of the ground-state ferromagnetic stripe phase [196], with the particle density and the spin densities having periodicity $2\pi/|\mathbf{k_1}|$, and the nematic densities containing harmonic components both with period $2\pi/|\mathbf{k_1}|$ and $\pi/|\mathbf{k_1}|$. Remarkably, this preparation of stripe states via crossing an ESQP transition of the effective model compares favorably, both in its robustness and in the contrast achieved, to the quasiadiabatic preparation through a quantum phase transition we described in the previous chapter. As it was also the case for the latter, the preparation proposed in this chapter can not be implemented in the spin-$\frac{1}{2}$ gas: the protocol highlights once again the structural differences between spin-$\frac{1}{2}$ and spin-1 gases.

We conclude by stressing that, as we discussed in Sec. 5.2, due to the instability in the

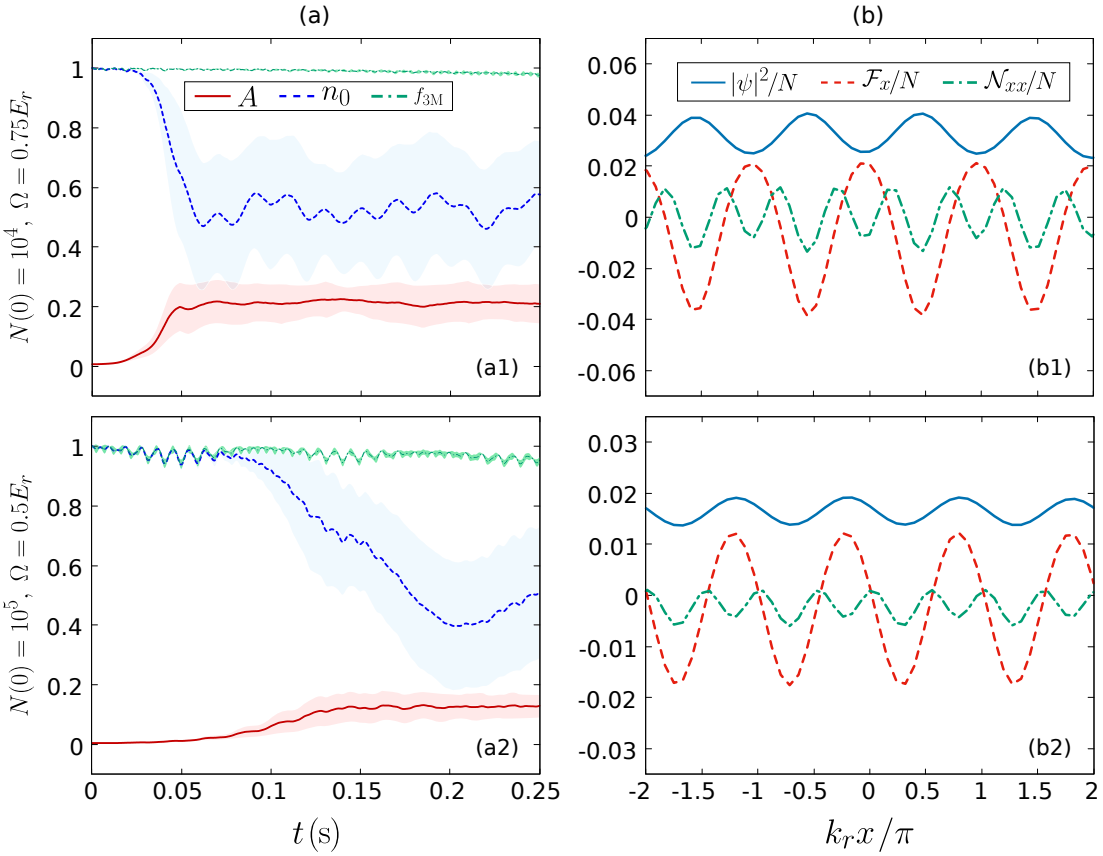

Figure 5.9: Robust excitation of ES states. (a) Mean value of $A(t)$ (red solid line), n_0 (blue dashed line) and f_{3M} (green dash-dotted line) as a function of time, for a state with $n_0(0) = 0.9998$ and $\theta(0) = 0$. The state is evolved under the GPE (5.13), with $N(t) = N(0)\exp(-\gamma t)$ and including randomized parameters to account for atom loss and experimental noise (see main text). In (a1), we set $N(0) = 10^4$ and $\Omega = 0.75E_r$. In (a2), we set $N(0) = 10^5$ and $\Omega = 0.5E_r$. In both cases $\gamma = 3.33$, and $\tilde{\epsilon}/\lambda = -1$ for $t \leq t_1 = 5.5\hbar/\lambda$ and $\tilde{\epsilon} = 0$ for $t > t_1$. The trap frequency ω_t is adjusted to have $\bar{n}(0) = 7.5 \times 10^{13}\,\mathrm{cm}^{-3}$. The averages are computed from a sample of 20 realizations in each case, with the light-colored shadowed regions indicating the associated standard deviation. (b) Longitudinal density $|\psi|^2$ (blue solid line), spin density $\mathcal{F}_x$ (red dashed line) and nematic density $\mathcal{N}_{xx}$ (green dash-dotted line) at $t = t_1$, evaluated for a single realization from the samples used in (a).

relative phase Δ between the modes $b_{\pm 1}$, it is not possible to distinguish experimentally positive and negative values of $A(t)$. However, in the states prepared, the contrast of the stripes $V \sim |A|$ remains stable over time and does not vanish at any given time, which is the distinct feature of the ES phase. At the same time, this stability provides a direct measurement of the winding number w that characterizes the BA' ESQP of the effective spin Hamiltonian. In an experimental implementation, the periodic density modulations

in the gas could be measured using optical Bragg scattering [357], as described in [207].

5.4 Conclusions

In this chapter we have studied the emergence of excited-state quantum phases in Raman-dressed SOC spin-1 condensates. To do so, we have relied on the description of the weakly-coupled Raman-dressed BEC as an artificial spinor gas with tunable spin-changing collisions, which was introduced in chapter 4. Through this simple yet insightful description, we have identified the existence of ESQPs in the dressed gas by direct correspondence to those recently described in the bare spinor condensates. Moreover, due to the coupling between internal (spin) and external (motional) degrees of freedom in the presence of SOC, the excited phases in the dressed scenario exhibit richer features, and are characterized by the behavior of the spatial density modulations, or stripes. Most relevantly, we have defined a novel ESQP in the dressed system, the ES phase, where the atomic cloud exhibits stable density modulations that do not vanish over time. The nature of the phase is understood from the topological order parameter that characterizes the ESQPs of the spinor gas in the regime where the system is described by a collective spin Hamiltonian.

We have numerically assessed the predictions of the effective model with simulations of the GPE of the dressed condensate. We have found that, indeed, the collective spin structure plays a fundamental role to the existence of the ES phase, with its signature quickly vanishing when the few-mode truncation that leads to the effective Hamiltonian is significantly challenged. While such a sensitivity supposes a restriction to its experimental realization, we have shown that the large tunability of the system allows a wide regime of parameters for which the phase is supported. At the same time, we have shown that the realization of the spin Hamiltonian in the dressed condensate can be advantageous when it comes to the detection of the ESQP transitions of the system. So far, the proposal to measure the topological order parameter in undressed quantum gases [323] relies on an interferometric protocol that is very sensitive to magnetic field fluctuations. In contrast, in the Raman-dressed gas, the same information can be obtained from direct measurements of the density profile of the atomic cloud, with an order parameter, the minimum contrast of the spatial modulations, that is insensitive to fluctuations of the bias field at leading order. In turn, we have also shown that the time-averaged contrast of the stripes can signal a type of dynamical phase transition in the dressed system.

Notably, in the chapter we have used the map to pseudospin degrees of freedom bidirectionally. On the one hand, we provide an alternative and potentially advantageous framework to explore dynamical and ESQP transitions. On the other hand, the work also exemplifies the use of ESQP transitions as a tool to engineer quantum states of interest. The analytical understanding of the excited-state phase diagram has allowed us to propose a feasible protocol for preparing the excited-state ferromagnetic stripe phase of the spin-1 spin-orbit-coupled gas. By crossing an excited-state quantum phase

transition of the effective low-energy Hamiltonian in a two-step quench scheme, we can access any supersolid-like excited state with stable stripes belonging to the phase, which we identify with the broken-axisymmetry phase of the artificial-spinor-gas description. We have numerically supported the viability of such a preparation using as a reference the results reported from experiments with ^{87}Rb condensates at the National Institute of Standards and Technology. Our results indicate that the proposal can be implemented directly in state-of-the-art experiments with ultracold atoms.

As it was also the case for the protocol described in chapter 4, the characteristic parameters that stabilize the phase are scaled up in the excited state diagram, compared to ground state stripe phase, even in the case of symmetric spin interactions. At the same time, the contrast of the supersolid fringes is increased. Unlike for the scheme in chapter 4, though, the preparation proposed in this chapter is not restricted to the most-excited state manifold of the effective model, and does not rely on its quasi-adiabatic following. This results in a comparatively reduced preparation time, which can be of especial relevance given the shortened lifetime of the Raman-dressed condensate.

The pseudospin description of the Raman-dressed gas across the whole spectrum of the collective spin Hamiltonian suggests alternative directions for achieving macroscopic entanglement in momentum space [329]. The squeezing and quantum correlations generated by our two-step quench scheme can be calculated for a mesoscopic number of particles by including the effect of atoms' losses in the single-mode quantum description by wave-function Monte Carlo [358], as recently done in [285]. Beyond the single-mode approximation, the properties of the quantum correlations in the system could be explored for few particles, for instance in connection to the two-particle solutions of the model, as done in [359] for the spin-$\frac{1}{2}$ scenario.

With this chapter, we conclude the part of this thesis devoted to the study of the interplay between Raman dressing and weak interatomic interactions in spin-1 Bose gases, in particular of the emergence and the harnessing of the SOC-induced spin-mixing dynamics. So far, we have exploited a simple but powerful idea: the Raman-dressed spinor gas as an artificial spinor gas with tunable spin-changing collision. Simple because accessible to any physicist, and powerful because it has a significant impact on the understanding of the system. Through this understanding, we have proposed the Raman-dressed gas as an alternative platform for the exploration of nonequilibrium dynamics in experiments with ultracold atoms. In the next chapter, we will shift our focus from the spin-1 to the spin-$\frac{1}{2}$ gas. While the many-body spin-changing processes that we have discussed so far can not be tailored in the latter system, we will see that, there, the interplay between two-body collisions and Raman dressing can give rise to interesting many-body phenomena in a strongly correlated regime. To do so, we will follow a similar approach, which will involve a lowest-band description of the dressed gas loaded in an optical lattice.

CHAPTER 6

Effective frustrated quantum magnetism in a synthetic ladder

In line with the research presented in the previous three chapters of the thesis, this chapter will explore further the emergence of nontrivial behavior in interacting many-body systems when dressed by Raman beams. We will now consider a dressed spin-$\frac{1}{2}$ gas loaded into a one dimensional optical lattice. In the lattice, the strength of the interatomic interactions and the Rabi couplings can be made larger relative to the suppressed kinetic energy, while retaining a large degree of robustness. At the same time, the presence of the lattice involves an additional characteristic length scale, related to the wavelength of the lattice beams. As we will see, the interplay between such a scale and the one established by the Raman recoil momentum can give rise to frustration effects in the system. In this chapter, we will propose to employ Raman dressing as a flexible tool to study frustrated quantum magnetism with ultracold atoms.

The interplay between geometric frustration and interactions plays a key role in the emergence of quantum phases in quantum magnetism. Here, we will show that the Raman-based realization of a semi-synthetic flux ladder can hold frustrated quantum phases in strongly-correlated regimes that are in reach of state-of-the-art experiments. Following a lowest-band truncation of the Hamiltonian in the strong Raman coupling regime, equivalent to the large inter-leg hopping regime of the flux ladder, the system can be mapped into an effective two-leg triangular Bose ladder with staggered flux. The effective flux and the ratio of the tunneling strengths can be independently tuned over a wide range of values by adjusting the properties of the Raman beams. Guided by this map, we numerically show that the Hamiltonian is able to explore three different phases, a superfluid, a bond-ordered-wave and a chiral superfluid, which are characteristic of a large class of Heisenberg models in presence of geometric frustration. Remarkably, these regimes remain stable in a large region of parameters and are accessible in currently

available experiments with Raman-dressed ultracold ^{41}K and ^{87}Rb atoms. The results presented in this chapter offer an alternative approach to simulate frustrated quantum magnetism.

The chapter is organized as follows. In Sec. 6.1, we review the theoretical and experimental context of the work presented in this chapter, and motivate the exploration of frustrated quantum magnetism with Raman-dressed spinor gases. Next, in Sec. 6.2 we introduce the Raman-dressed lattice system and its natural interpretation as a semi-synthetic flux ladder. We then show that the low-energy landscape of the flux ladder can be described in terms of an effective 1D lattice model for a quasi particle with complex tunneling terms of various ranges. In Sec. 6.3, we specialize in the simplest spin-$\frac{1}{2}$ scenario, where the system realizes a two-leg flux ladder. There, only first- and second-neighbor tunnelings become relevant for a wide regime of parameters, and the system can be mapped into an interacting triangular ladder with staggered flux. Through this map, we are able to identify in Sec. 6.4 the existence of frustrated many-body phases in the strongly interacting regime of the effective triangular system, which are analogous to magnetic phases predicted in frustrated quantum spin models. In Sec. 6.5, we show that these phases can be in principle accessed in state-of-the-art experiments with ultracold atoms, and present a detection protocol that exploits the tunability of the dressed-based realization of the model that we propose in this chapter. Finally, we summarize our results and comment about future developments in Sec. 6.6.

6.1 Introduction

Raman-induced spin-orbit coupling (SOC) in Bose and Fermi gases, both in the bulk or loaded in optical lattices, provides a flexible playground for studying many-body physics and quantum phase transitions in a controlled manner. By entangling internal and external degrees of freedom, the SOC produced by Raman beams [86, 104] leads already at the single-particle or at the mean-field levels to spatially-dependent dressed states with modified dispersion relation and spatially dependent interactions [208]. Such behavior can be interpreted in terms of a synthetic gauge field [84, 85] that can be also density dependent [360]. The successful experimental demonstrations of the last decade of synthetic one-dimensional and two-dimensional SOC [199, 202, 204, 206] have opened interesting perspectives. In the bulk, SOC can stabilize exotic phases like the stripe phase [108, 186, 207], where translation invariance is spontaneously broken [361], in analogy with supersolids very recently realized in dipolar gases [249–251] (see also [362] for the realization of supersolid-like state in a cavity). Also in the bulk, SOC may lead to modified scattering properties in the gas [116], which may lead to a variety of collective phenomena in the mean-field regime, as has been extensively discussed in the previous chapters in this thesis for $F = 1$ BECs. Interestingly, SOC combined with radio-frequency dressing offers a novel mechanism to achieve subwavelength optical lattices [244]. When loaded into an optical lattice, the Raman-dressed gas effectively

realizes a quasi-1D flux ladder, a paradigmatic model to study quantum magnetism. In this chapter we will explore the interplay between interactions and Raman-induced SOC in 1D optical lattices, and show that such an interplay can give rise to frustrated quantum magnetism phenomena.

6.1.1 Quantum magnetism in semi-synthetic flux ladders

Combining SOC and optical lattices makes it easier to access the strongly coupled regimes, where the connection to quantum magnetism appears. On the one hand, the lattice quenches the kinetic term and allows for relatively large interactions and Rabi couplings with negligible losses [30]. On the other hand, the lattice introduces another length scale $1/k_l$, where k_l is the lattice beam wavevector, in addition to the inverse of the Raman momentum kick $1/k_r$, and thus may favor frustration. Such an effect becomes evident when the atomic spin states are interpreted as different sites of the lattice along a synthetic dimension [92, 237]. Raman-coupled spin states in 1D spin independent optical lattices experience a synthetic magnetic flux proportional to k_r/k_l that leads to the appearance of edge states in narrow Hofstadter slabs [93], as experimentally demonstrated in [94, 95, 254, 255] (also with atomic momentum states [266] and with photons [363]). Remarkably, the correspondence between the Hofstadter model [97] in 2D lattices and quasi-1D systems extends also to its topological properties and quantum Hall response [364] as experimentally demonstrated in [96]. Even more strikingly, this correspondence extends under proper conditions also when interactions are included [365, 366].

Bosonic flux ladders are the simplest quasi-1D systems that realize such a correspondence, since they allow orbital motions around the planar loops. Two-dimensional effects such as phase frustration can therefore emerge in these systems. The presence of magnetic fields in this scenario can give rise to interesting effects. Already at the single-particle level, they provide a toy model of type-II superconductors [367–369] and display Meissner and vortex phases –the latter being related to the stripe phase in the bulk– as first experimentally demonstrated in real-space ladders in [238]. The interplay between the magnetic flux, the rung vs leg tunnelings, and interactions in real and synthetic ladders leads to a variety of interesting phases and have been extensively studied, especially for strong interactions [240, 370–379]. For similar studies in fermionic ladders see for instance [380–384].

In this chapter we will look at the synthetic flux ladders formed by Raman-dressed spin-1/2 atoms in 1D optical lattices from a different perspective. Following a similar approach to the one taken in the previous chapters to study spin-orbit-coupled gases in the bulk, our starting point here is a lowest-band truncation of the single-particle Hamiltonian. Remarkably, in the lattice, compared to the bulk, we can further manipulate the properties of the single-particle bands by tuning the magnetic flux, that is, the ratio k_r/k_l. Exploiting this enhanced flexibility, we can establish a hierarchy of energy scales. The interband band gap, the interacting energy and the intraband bandwidth

can be adjusted independently and set them well-separated from each other. This energy separation allows, for instance, to preserve the many-wells structure of the lowest band for arbitrarily strong Raman couplings, and realize a strongly-correlated regime therein. With these considerations, a map of the dressed system into a two-leg triangular ladder with staggered flux and on-site interactions is made evident. Through such a map, this low-energy treatment of the semi-synthetic flux ladder suggests that Raman-dressed gases can be employed to study frustrated quantum magnetism [228]. For alternative theoretical proposals of synthetic triangular and zigzag lattices see [385, 386]. Likewise, for an experimental realization in synthetic lattices in momentum space with constant fluxes see [387].

6.1.2 Frustrated quantum magnetism in bosonic ladders

The interplay between geometrical frustration and quantum fluctuations connects some of the most intriguing concepts in many-body quantum systems [388]. In this context, frustrated quantum magnets, where a macroscopic number of quasi-degenerate states compete with each other, provide an ideal playground to capture exotic phenomena like resonating valence bonds [389] and quantum spin liquid [390]. The most common building block where frustrated magnetism reveals its complexity is usually represented by Heisenberg models on a square lattice with nearest-neighbors (NN) and next-nearest-neighbors (NNN) antiferromagnetic couplings that can be alternatively modeled as NN Heisenberg model on triangular geometries [391]. There, for instance, a part from intriguing properties related to deconfined quantum critical points [392, 393] and anyonic liquid [394], the appearance of spontaneous dimerization [395–397], and chiral order [398, 399] has been predicted.

Lattices and ladders with triangular geometries have been widely studied in ultracold atoms [400] especially in connection to supersolidity [401, 402] and frustrated quantum magnetism. In triangular translational-invariant configurations, the presence of complex tunnelings naturally gives rise to staggered fluxes, for instance equal to π. In optical lattices, they can be generated, e.g., by accelerating the lattice potential along a closed orbit, and employed to study classical magnetism in experiments with ultracold bosons [403]. In the presence of strong interactions, such systems offer a promising route towards the realization of quantum spin liquid phases [404], both in homogeneous gases [405] and in the presence of an harmonic trapping [406]. Fully frustrated, i.e., π-flux, triangular ladders have been theoretically studied in the strongly-interacting regime in [407–409].

Although in solid state physics several materials are well modeled by spin models on triangular geometries [410–415], the typical temperature in such systems has prevented efficient investigations of the chiral order. Only very recently one experiment achieved an important step in this direction [416]. The temperature poses a crucial issue also in the context of quantum simulations of frustrated quantum systems with ultracold atoms. The Floquet procedures proposed to achieve the π flux needed [225, 403, 404] result

in an undesirably large heating, which renders such modulation schemes unrealistic. To address this issue, different strategies that do not involve fast driving modulations, like laser assisted tunneling [417] or Raman couplings [92, 93], have been proved to be powerful tools to generate synthetic gauge fields. The latter method has been revealed particularly remarkable when applied on ladder geometries, allowing for the experimental study of aspects of quantum Hall physics [94, 95, 418, 419]. This flexibility in generating gauge fields combined with the impressive level of parameters control and detection techniques typical of ultracold atomic setups [64] has further motivated theoretical effort to establish ladder geometries as fundamental tools to explore intriguing problems in many-body quantum physics. Relevantly in this context, Meissner [367, 370, 372, 420, 421] and vortex phases [422–425], Laughlin-like states [365, 366, 373, 375, 376, 426], Hall physics [240, 427–429] and Z_2 lattice gauge theories [430] have been proposed.

In this chapter we present a further contribution in this direction, and propose the Raman-dressed ultracold gas in a 1D lattice as an alternative platform for the simulation of frustrated quantum magnetism. In our Raman-based realization of the frustrated triangular ladder, the parameters of the effective model, namely, the rung and longitudinal tunnelings and the strength of the flux, can be widely adjusted by tuning the laser dressing parameters. Irrespective of the interactions between the spin states, the interactions in the effective ladder can be made local. Notably, in the experimentally accessible regime of large separation between the bandwidth and the bandgap, we can access both the weakly and the strongly interacting regimes of the triangular ladder within the validity of the mapping. Despite its simplicity, the triangular map allows to identify specific regimes of the flux ladder where quantum frustration may play an important role. We will demonstrate numerically the agreement between the ladder model and the effective Hamiltonian across a wide range of parameters. We will show that the system is indeed able to realize analogous phases to those appearing in the frustrated quantum XX model [431], that is, a gapless superfluid, a bond order wave and a chiral superfluid phase. Notably, we find that the predicted frustrated phases persist even in regimes where the mapping is less accurate.

In the previous chapters, we showed that the collective pseudospin physics realized in Raman-dressed gases exhibited richer features through its relationship between internal (spin) and external (motional) degrees of freedom. These were made evident in the bare basis description of the system, in the form of, e.g., the appearance of spatial density modulations. Remarkably, they were even proposed as a proxy to experimentally detect structures of the embedded spin model. Similarly, the frustrated magnetic structures that arise in the effective model introduced in this chapter, that is, the dimerized and chiral orders of the dressed states, present further interesting properties when considered back in terms of the bare, or undressed, basis. We will see that the structures in the currents and densities of undressed bosons in the original square ladder geometry correlate well with the magnetic phases of interest. Exploiting this correspondence, the phase diagram of the frustrated model could in principle be realized and detected in state-of-the-art

experiments with ultracold atoms.

6.2 Tunable ladder physics in 1D lattices with SOC

We consider a spin-F spinor gas loaded in a 1D spin-independent optical lattice, in the configuration described in Sec. 2.3.3: the lattice is generated with a pair of far-detuned counter-propagating laser beams of wavelength λ_l that intersect with an opening angle θ_l, with the trapped atoms being further dressed by an additional pair of laser beams in a Raman configuration of wavelength λ_r and an opening angle θ_r. A bias magnetic field lifts the degeneracy between the different spin states (see Fig. 2.7(a) for a sketch of the experimental layout). In general, effective spin-S sizes can be achieved by coupling $2S+1$ of the $2F+1$ states $|F, m_F\rangle$ within the given hyperfine manifold of total angular momentum F, rendering the non-coupled states off-resonant via the quadratic Zeeman shift. The wavelength of the lattice beams defines the lattice spacing $a = \pi/k_l$, with $k_l = 2\pi\cos(\theta_l)/\lambda_l$ being the single-photon recoil momentum. The Raman wavelength gives an associated Raman recoil momentum $k_r = 2\pi\cos(\theta_r)/\lambda_r$. We consider a potential depth V_l sufficiently deep so as to consider the tight-binding approximation, yet shallow enough to avoid the suppression of nearest-neighbor tunneling. This condition can be achieved roughly when $5E_l < V_l < 10E_l$, where $E_l = \hbar^2 k_l^2/2m$ is the recoil energy, with m being the atomic mass. In the absence of interatomic interactions, the system can be described by the Hamiltonian [93]

$$H_{\text{n.i.}} = \sum_{n,m} \Big(-t a^\dagger_{n+1,m} + \Omega_{m+1} e^{-i\gamma n} a^\dagger_{n,m+1} + \frac{1}{2}\Delta_m a^\dagger_{n,m} \Big) a_{n,m} + \text{H.c.}, \tag{6.1}$$

where $a^\dagger_{n,m}$ and $a_{n,m}$ are the bosonic creation and annihilation operators, respectively, for the Wannier modes at the lattice site n with spin state m. Here, t is the tunneling rate between the nearest-neighbor modes, Ω_m is the Raman coupling strength between levels m and $m+1$, Δ_m is an onsite energy shift that depends on the detuning of the Raman lasers from resonance, and $\gamma = 2k_r a = 2\pi k_r/k_l$. The strength of the Raman dressing is constrained by the tight-binding approximation. To be consistent, the coupling strengths Ω_m are required to be much smaller than the energy splitting between the tightly-bound states and the rest of single-particle states, roughly given by $\epsilon_{\text{t.b.}} \sim 2\sqrt{V_l E_l}$. As noted in [93], and elaborated in Sec. 2.3.3, such a system is equivalent to a 2D (quasi 1D) flux ladder, where the internal spin states act as sites along a synthetic transverse dimension. Moreover, the atoms pick up a position dependent phase $n\gamma$ when hopping along the synthetic dimension, due to the spatial dependence of the Raman coupling, which mimics the effect of a magnetic flux γ piercing each plaquette of the ladder (see Fig. 2.7(b)).

Hamiltonian (6.1) realizes the Hofstadter model on a slab and reproduces the main features of magnetic lattice systems, such as the fractal Hofstadter-butterfly spectrum and the chiral edge states of the associated Chern insulating phases. However, interatomic interactions in synthetic dimensions have naturally a long-range character as

particles with different spins interact locally when they occupy the same site in the actual 1D lattice. To some extent, such a long-range behavior can be altered or even suppressed, e.g., displacing spatially the spin states as originally proposed in [92], or considering non-SU(F) interactions for the spin states as obtained from Feshbach resonance (see for instance [257]) or by properly modulating the scattering length as recently proposed in [432]. By contrast, here we show that, following a truncation of the single-particle Hilbert space, interesting quasi 1D ladder structures can be obtained where the interactions and tunnelings can be controlled simply by adjusting the dressing parameters.

6.2.1 Effective quasi-particle from Raman dressing

As typically done to treat the spin-orbit-coupled bulk-gas problem, the Hamiltonian can be made simpler by rewriting it in a position-independent form. This is achieved by applying the gauge transformation $a'_{n,m} = a_{n,m}e^{i\gamma nm}$ that relates the laboratory frame to the frame co-rotating with the laser fields. Doing so, the phase terms that appeared in (6.1) are transferred to the hopping amplitudes along the physical direction, yielding:

$$H_{\text{n.i.}} = \sum_{n,m} \Big(-te^{-i\gamma m}{a'_{n+1,m}}^{\dagger} + \Omega_m {a'_{n,m+1}}^{\dagger} + \frac{1}{2}\Delta_m {a'_{n,m}}^{\dagger}\Big) a'_{n,m} + \text{H.c.}. \tag{6.2}$$

From now on, we will stick to this gauge choice, and omit for the sake of clarity the primed labelling of the bosonic operators. In the rotated basis, Hamiltonian (6.2) is now block diagonal in orthogonal quasimomentum subspaces, and can be written as

$$H_{\text{n.i.}} = \sum_q H_q, \tag{6.3}$$

with

$$H_q = \sum_m \big(-2t\cos(q+\gamma m) + \Delta_m\big)\tilde{a}^{\dagger}_{q,m}\tilde{a}_{q,m} + \sum_m \Big(\Omega_{m+1}\tilde{a}^{\dagger}_{q,m+1}\tilde{a}_{q,m} + \text{H.c.}\Big), \tag{6.4}$$

where we have introduced the Fourier transformed modes $\tilde{a}^{\dagger}_{q,m} = \frac{1}{\sqrt{L}}\sum_n e^{iqn}a^{\dagger}_{n,m}$, with L being the total number of sites in the lattice. Hamiltonian (6.3) has $2S+1$ energy bands, which we label as $\epsilon_{q,m'}$, with $m' \in \{0,1,...,2S\}$ ($\epsilon_i \leq \epsilon_j$ for $i<j$), and with associated band modes

$$\tilde{b}^{\dagger}_{q,m'} = \sum_m \mathrm{U}_{m',m}(q)\tilde{a}^{\dagger}_{q,m} \tag{6.5}$$

that diagonalize the corresponding orthogonal block H_q. Here,

$$\mathrm{U}(q) = \sum_{m_1,m_2} \mathrm{U}_{m_1+F,m_2}(q)\big(\tilde{a}^{\dagger}_{q,m_2}|0\rangle\big)\big(\langle 0|\,\tilde{a}_{q,m_1}\big) \tag{6.6}$$

is the unitary transformation that relates the dressed eigenbasis $\{\tilde{b}^{\dagger}_{q,m'}|0\rangle\}_{m'}$ with the uncoupled hyperfine state basis $\{\tilde{a}^{\dagger}_{q,m}|0\rangle\}_m$, and where $\mathrm{U}_{m',m}(q) = \langle 0|\,\tilde{a}_{q,m}\tilde{b}^{\dagger}_{q,m'}|0\rangle$. Without loss of generality, we can assume the coefficients $\mathrm{U}_{ij}(q)$ to be real.

We now restrict ourselves to the regime where the lowest band can be well separated from the higher energy bands. This occurs for sufficiently large coupling coefficients Ω_m, with a band gap that depends also on the value of the phase γ. Under these circumstances, the low-energy landscape of the system is well described by the truncated Hamiltonian

$$H_{\text{n.i.}} \simeq \sum_q \epsilon_{q,0} \tilde{b}^\dagger_{q,0} \tilde{b}_{q,0}, \tag{6.7}$$

where only the lowest band mode operators are included.

This simple truncation in momentum space can have interesting effects that are made clearer by rotating back the dressed basis into position space. We introduce the inverse-Fourier-transformed dressed mode operators

$$b^\dagger_n := \frac{1}{\sqrt{L}} \sum_q e^{-iqn} \tilde{b}^\dagger_{q,0} = \frac{1}{L} \sum_{m,q,n'} e^{iq(n'-n)} U_{0,m}(q) a^\dagger_{n',m}, \tag{6.8}$$

and substitute their expressions into the truncated Hamiltonian (6.7), which yields

$$H_{\text{n.i.}} \simeq \sum_n \sum_l t_l b^\dagger_{n+l} b_n, \tag{6.9}$$

where

$$t_l = \frac{1}{L} \sum_q e^{-iql} \epsilon_{q,0}. \tag{6.10}$$

The lowest dispersion band $\epsilon_{q,0}$ has a shape that depends on the total spin size S and that can be tailored by adjusting Ω_m, γ and Δ_m. Therefore, the strength and relative phase of the different tunneling coefficients in the dressed picture, t_l, can be tuned with the parameters of the Raman dressing.

With these considerations in mind, we now account for interatomic interactions by writing them in terms of the dressed states. As long as the energy per particle is much smaller than the gap between the two bands, we can neglect the terms in the interaction Hamiltonian that involve higher band states, and restrict to its action onto the truncated dressed basis $\left\{ b^\dagger_n |0\rangle \right\}_n$. For simplicity we will assume SU(F) symmetric interactions, which is a good approximation, for instance, for $F = 1$ ^{87}Rb and $F = 1$ ^{41}K, although a generalization of this is straightforward. In the lattice, the tight-binding interaction Hamiltonian reads

$$H_{\text{int}} = \frac{U}{2} \sum_n N_n (N_n - 1), \tag{6.11}$$

with

$$N_n = \sum_m a^\dagger_{n,m} a_{n,m}, \tag{6.12}$$

where U is the onsite interaction energy per particle pair and N is the total number of particles. From (6.5) and (6.8), we obtain the truncated expression of the bare basis

operators

$$a^\dagger_{n,m} = \frac{1}{\sqrt{L}}\sum_q e^{-iqn}\tilde{a}^\dagger_{q,m} \simeq \frac{1}{\sqrt{L}}\sum_q e^{-iqn}\mathrm{U}_{0,m}(q)\tilde{b}^\dagger_{q,0}$$
$$= \frac{1}{L}\sum_l \left(\sum_q e^{iq(l-n)}\mathrm{U}_{0,m}(q)\right) b^\dagger_l = \sum_l \lambda^{(l)}_m b^\dagger_{n+l}. \tag{6.13}$$

In the last equality, we have defined the coefficients

$$\lambda^{(l)}_m := \frac{1}{L}\sum_q e^{iql}\mathrm{U}_{0,m}(q), \tag{6.14}$$

which correspond to the amplitudes of the modes $b^\dagger_n|0\rangle$ at sites $n+l$. With the truncated expressions (6.13) for the lattice operators, we can now rewrite N_n as

$$N_n = \sum_{l,l'} C_{l,l'} b^\dagger_{n+l} b_{n+l'}, \tag{6.15}$$

where $C_{l,l'} = \sum_m \lambda^{(l)}_m (\lambda^{(l')}_m)^*$.

For weakly coupled gases, the spread of the truncated modes can be significant, while they become tightly localized in the strong coupling limit. Thus, at weak couplings the density-density terms in the interaction Hamiltonian (6.11) may include significant higher order terms in the truncated basis. In practice, though, the lowest-band truncation demands relatively large Ω_m, and in many situations we will be able to safely neglect such contributions and write

$$H \simeq \sum_n \sum_l \left(t_l b^\dagger_{n+l} b_n + \frac{U}{2}\sum_{l'} C_{0,0} C_{l,l'} b^\dagger_n b_n b^\dagger_{n+l} b_{n+l'} \right). \tag{6.16}$$

In this way, when written in terms of dressed bosons, the Raman-dressed lattice Hamiltonian can be thought of as a Hubbard-like model for a quasiparticle with modified properties, which may include long-range complex tunneling terms and non-trivial interactions. For the remainder of this chapter, we will focus on the simplest of these scenarios, namely the spin-1/2 Hamiltonian. In the next section, we will see that in the case of $S = \frac{1}{2}$, the effective Hamiltonian (6.16) describes a triangular ladder model with tunable staggered flux. As elaborated in Sec. 6.1.2, triangular configurations have attracted a great deal of attention as a natural route to geometrical frustration, which plays a major role in the emergence of frustrated quantum magnetic phases. Therefore, it is worth studying their implementation with Raman-dressed Bose gases.

6.3 The spin-1/2 case: an effective triangular ladder with staggered flux

The spin-$\frac{1}{2}$ can be realized by having only two states of a hyperfine manifold coupled by Raman transitions, with the rest being set off resonance via the quadratic Zeeman

shift [104]. In this case, the Hamiltonian can be interpreted as a semi-synthetic two-leg flux ladder charged with N bosons in $2L$ lattice sites, as schematically represented in Fig. 6.2, which reads

$$H_{1/2} = \sum_{j=1}^{L} \sum_{\sigma=\pm\frac{1}{2}} \left(-te^{-\imath\gamma\sigma} a^{\dagger}_{j+1,\sigma} + \frac{\Omega}{2} a^{\dagger}_{j,\bar{\sigma}} + \sigma\delta a^{\dagger}_{j,\sigma} \right) a_{j,\sigma} + \text{H.c.}$$
$$+ \sum_{j=1}^{L} \sum_{\sigma=\pm\frac{1}{2}} \left(\frac{U_{\sigma\sigma}}{2} n_{j\sigma}(n_{j\sigma}-1) + \frac{U_{\sigma\bar{\sigma}}}{2} n_{j,\sigma} n_{j\bar{\sigma}} \right). \tag{6.17}$$

Here, Ω is the Raman coupling strength between the two levels involved, which we set to $\Omega > 0$, and δ is the detuning from Raman resonance which yields a uniform potential between the upper and lower leg of the ladder. The second line in eq. (6.17) describes the general form for the inter- and intra-leg onsite interactions, with $\bar{\sigma}$ labelling the site of the opposite leg from σ. For simplicity, we will restrict ourselves to the SU(2) symmetric scenario, and set $U_{\sigma,\sigma} = U_{\sigma,\bar{\sigma}} = U$. As argued in Sec. 6.2, the resulting nonlocal behavior of the interactions along the synthetic dimension is often not desired, since it breaks the immediate analogies to systems in solid state physics. Yet, as we will see later on in this chapter, such a behavior will actually be favorable for our purposes, which contributes to further support the realization of the model in Raman dressed systems.

We will now consider for this $S = \frac{1}{2}$ case the lowest band recipe presented in the previous section. From (6.4), we have

$$H_q = \left(2t \sin\left(\frac{\gamma}{2}\right) \sin(q) + \frac{\delta}{2} \right) \sigma_z - 2t \cos\left(\frac{\gamma}{2}\right) \cos(q) + \Omega\sigma_x, \tag{6.18}$$

where σ_i are the Pauli matrices. The two energy bands are given by

$$\epsilon_{q,\pm} = \pm\Omega\sqrt{1 + (\tilde{q} + \tilde{\delta}/2)^2} - 2t \cos\left(\frac{\gamma}{2}\right) \cos(q), \tag{6.19}$$

and the unitary transformation that relates the bare and the dressed basis reads $\mathrm{U} = e^{i\sigma_y\theta_q/2}$, with $\cos(\theta_q) = \frac{\tilde{q}+\tilde{\delta}/2}{\sqrt{1+(\tilde{q}+\tilde{\delta}/2)^2}}$, $0 \leq \theta_q \leq \pi$. Here, we have relabelled the upper and lower band indices, respectively, by $m = \pm$, and have conveniently defined the scaled quantities $\tilde{q} := \frac{2t\sin(\gamma/2)\sin(q)}{\Omega}$ and $\tilde{\delta} := \delta/\Omega$.

Rewriting U explicitly in terms of $\tilde{q}$ and $\tilde{\delta}$, we have

$$\mathrm{U}_{-,\pm} = \pm\frac{1}{\sqrt{2}} \sqrt{1 \pm \frac{\tilde{q} + \tilde{\delta}/2}{\sqrt{1 + (\tilde{q} + \tilde{\delta}/2)^2}}}. \tag{6.20}$$

The two bands and are represented in Fig. 6.1(a) for $\Omega = 2t$, $\gamma = 0.9\pi$ and $\delta = 0$. We label the energy gap separating the two bands as $\Delta\epsilon$, and the bandwidth of the lowest band as $\delta\epsilon$. The latter is directly related to the strength of the effective tunnelings t_l in the lowest band model. Together with the tight-binding energy $\epsilon_{\text{t.b.}}$, these quantities

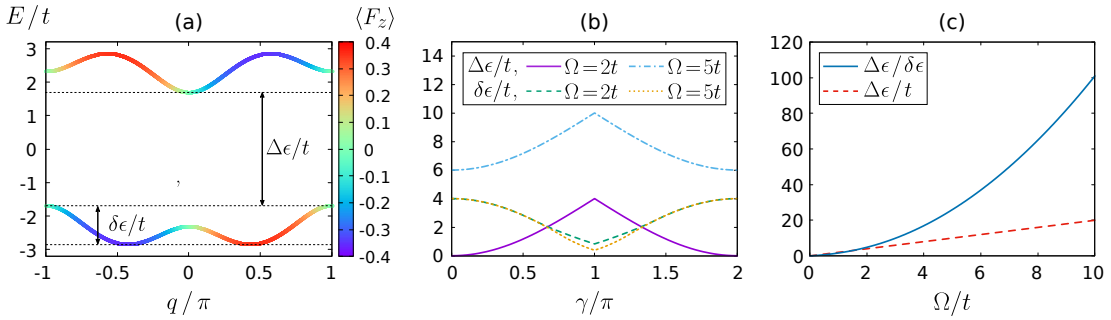

Figure 6.1: Noninteracting energy scales: (a) Energy bands (6.19) of Hamiltonian (6.17) for $\Omega = 2t$, $\gamma = 0.9\pi$. The arrows indicate the bandwidth $\delta\epsilon$, which is related to the tunneling strength of the effective dressed particle, and the band-gap $\Delta\epsilon$ that separates the two bands. The color texture represents the expected value of the spin of the band states. (b) $\Delta\epsilon$ and $\delta\epsilon$ as a function of γ for $\Omega = 2t$ and $\Omega = 5t$. (c) $\Delta\epsilon$ and $\Delta\epsilon/\delta\epsilon$ as a function of Ω at $\gamma = \pi$. In all figures, we set $\delta = 0$.

set the three different energy scales of the effective system at the single-particle level. In Fig. 6.1(b) and Fig. 6.1(c) we plot $\Delta\epsilon$ as a function of γ and Ω, respectively. The bandgap $\Delta\epsilon$ increases with both Ω and the flux γ, and is maximal at $\gamma = \pi$. Contrarily, the bandwidth $\delta\epsilon$, is a decreasing function of Ω, and it is minimized at $\gamma = \pi$, as shown in Fig. 6.1(b). In this way, the ratio between $\Delta\epsilon$ and $\delta\epsilon$ increases fast as Ω is made larger, as shown in Fig. 6.1(c).

By using expressions (6.19) and (6.20), we can retrieve the analytical expressions for the quantities relevant to the lowest-band model in the spin-$\frac{1}{2}$ case. Since we want the three energy scales well separated, we will assume moderate-to-large values for Ω and truncate the expansion of the parameters to first order in t/Ω. By introducing (6.20) into (6.8), we obtain the following expression for the dressed mode operators $b_n^\dagger$ in the bare basis $a_{n,m}^\dagger$

$$b_n^\dagger = \sqrt{\frac{1}{2} + \frac{\tilde{\delta}}{2\sqrt{4+\tilde{\delta}^2}}}\, a_{n,+}^\dagger - \sqrt{\frac{1}{2} - \frac{\tilde{\delta}}{2\sqrt{4+\tilde{\delta}^2}}}\, a_{n,-}^\dagger \tag{6.21}$$
$$+ i\frac{4t\sin(\gamma/2)}{\sqrt{2}(4+\tilde{\delta}^2)^{3/2}\Omega}\left(\frac{a_{n+1,+}^\dagger + a_{n+1,-}^\dagger}{\sqrt{1+\frac{\tilde{\delta}}{\sqrt{4+\tilde{\delta}^2}}}} - \frac{a_{n-1,+}^\dagger + a_{n-1,-}^\dagger}{\sqrt{1-\frac{\tilde{\delta}}{\sqrt{4+\tilde{\delta}^2}}}}\right) + O\left((t/\Omega)^2\right).$$

Similarly, we can expand the expression for the effective tunneling coefficients t_l. From

$$\epsilon_{q,-} = -\Omega\left(\sqrt{1+\tilde{\delta}^2/4} + \frac{\tilde{\delta}\tilde{q}}{\sqrt{4+\tilde{\delta}^2}} + \frac{4\tilde{q}^2}{(4+\tilde{\delta}^2)^{3/2}} + O(\tilde{q}^3)\right) - 2t\cos(\gamma/2)\cos(q), \tag{6.22}$$

and by taking the limit $L \to \infty$, it follows that

$$t_k = -\left(\Omega\sqrt{1+\frac{\delta^2}{4\Omega^2}} + \frac{8t^2\sin^2(\gamma/2)}{\Omega(4+\delta^2/\Omega^2)^{3/2}}\right)\delta_{k,0} - \left(t\cos(\gamma/2) \mp i\frac{t\delta\sin(\gamma/2)}{\Omega\sqrt{4+(\delta/\Omega)^2}}\right)\delta_{k,\pm1} + \frac{4t^2\sin^2(\gamma/2)}{\Omega(4+\delta^2/\Omega^2)^{3/2}}\delta_{k,\pm2} + O((t/\Omega)^3). \tag{6.23}$$

Up to second order in t/Ω, the noninteracting dressed Hamiltonian (6.9) can therefore be written as

$$H_{n.i.} = \sum_i (t_1 b_i^\dagger b_{i+1} + t_2 b_i^\dagger b_{i+2} + \text{H.c.}) + O((t/\Omega)^3), \tag{6.24}$$

where we drop the constant term $t_0 N$. Notice that only the NN and NNN coupling coefficients are nonzero at this order of approximation. Hamiltonian (6.24) is equivalent to a triangular ladder with gauge-invariant staggered flux

$$\Phi = 2\phi_1 - \phi_2, \tag{6.25}$$

with $\phi_1 = \arg(-t_1)$ and $\phi_2 = \arg(-t_2)$. Remarkably, see from (6.23) that, in the chosen gauge, the NN tunneling coefficient t_1 has a nonzero imaginary contribution that is linearly proportional to the Raman detuning δ. To first order in δ/Ω, and to second order in t/Ω, we then have

$$\phi_1 = -\frac{\delta\tan(\gamma/2)}{2\Omega}, \quad \phi_2 = \pi. \tag{6.26}$$

Hence, at linear order in δ/Ω around $\delta = 0$, we can tune the staggered flux Φ while leaving $|t_1|$ and t_2 unchanged. Near fully frustration, the sensitivity of the effective staggered flux Φ to δ is given by

$$\left|\frac{\partial\Phi}{\partial(\delta/t)}\right| \simeq 2\left|\frac{\partial\phi_1}{\partial(\delta/t)}\right| \simeq 2\left|\frac{t\tan(\gamma/2)}{2\Omega}\right| \overset{\gamma\sim\pi,\delta\sim0}{\simeq} 2|t_2/t_1|. \tag{6.27}$$

Setting now $\delta = 0$, the ladder is fully frustrated, with $|\Phi| = \pi$, and the tunneling coefficients read

$$t_1 = -t\cos(\gamma/2) + O\left((t/\Omega)^3\right), \tag{6.28}$$

$$t_2 = \frac{t^2\sin^2(\gamma/2)}{2\Omega} + O\left((t/\Omega)^3\right). \tag{6.29}$$

Notice that the ratio $|t_2/t_1|$ can be tuned with both γ and Ω. This means that, even when $\Omega \gg t$, the system can in principle realize all the regimes of the frustrated triangular ladder. As we will see in the next section, this key feature will allow us to access strongly-correlated frustrated magnetic phases.

Finally, if the interacting energy per particle is much smaller than the band gap, that is $U \ll \Delta\epsilon = 2\Omega\left(1 - 2\cos(\gamma/2)\frac{t}{\Omega} + O\left((t/\Omega)^2\right)\right)$, interatomic interactions can be

truncated to the lowest band, and we can use (6.15) to write the interacting Hamiltonian in the dressed basis. Notice that the dependency on Ω only appears in the expression of N_n through the coefficients $C_{l,l'}$, which can be expanded to

$$C_{l,l'} = \frac{1}{L^2}\sum_{q,q'} e^{i(ql-q'l')} \sum_m U_{-,m}(q)U^*_{-,m}(q') = \frac{1}{L^2}\sum_{q,q'} e^{i(ql-q'l')}\frac{1}{2}\left(1+\frac{\tilde{q}\tilde{q}'}{2}\right). \quad (6.30)$$

Hence, by introducing the truncated expression (6.30) for the density operators in the dressed basis into (6.15) and (6.11), it follows that

$$H_{\rm int} \simeq \frac{U}{2}\sum_n b_n^\dagger b_n (b_n^\dagger b_n - 1) + O((t/\Omega)^2. \quad (6.31)$$

This is remarkable, since it implies that, to first order in t/Ω, the system is described by the effective Hamiltonian

$$H_\triangle = \sum_{l=1,2} t_l \sum_i (b_i^\dagger b_{i+l} + \text{H.c.}) + \frac{U}{2}\sum_i \tilde{n}_i(\tilde{n}_i - 1). \quad (6.32)$$

The Hamiltonian written in the dressed basis is therefore analogous to a triangular ladder configuration with tunable onsite interactions, tunnelings and staggered flux, as schematically represented in Fig. 6.2.

Hamiltonian (6.32) has been extensively studied, since it is the simplest model where frustrated physics can naturally emerge. Bosons in triangular configurations have been explored mainly at unit filling [433, 434] and at low densities [409]. Other possible implementations of the model have been proposed [385, 386], and an experimental realization in a different gauge sector has been achieved [400]. It is worth stressing that, in comparison to the various proposals that use synthetic dimensions to achieve frustration, in our realization of the model the interactions are directly of local nature, and no state-dependent lattice potential of any sorts is required. As discussed in Sec. 2.1, state-dependent potentials in alkali atoms can be realized by exploiting the vector contribution of the dipole light shifts. As it is the case for Raman dressing, in this situation both the spontaneous emission rate and the dipole coupling strength scale with the inverse squared of the detuning from resonance. Thus, the heating rate from photon scattering can not be arbitrarily suppressed in spin-dependent dipole potentials. This limits their practical application [84, 85], even more so when considering the deep lattice regime.

Special attention has been devoted to Hamiltonian (6.32) in the hard-core-boson limit, i.e. for $U \to \infty$, and at half-filling $\tilde{n} = N/L = 1/2$ [407, 408, 431]. There, double occupancies in the triangular ladder are suppressed, and one can identify $(b_i^\dagger, b_j) \to (S_i^+, S_j^-)$, which leads to

$$H_\triangle \overset{t_l/U\to 0}{\longrightarrow} \sum_j \left(t_1 S_j^- S_{j+1}^+ + t_2 S_j^- S_{j+2}^+ + \text{H.c.}\right). \quad (6.33)$$

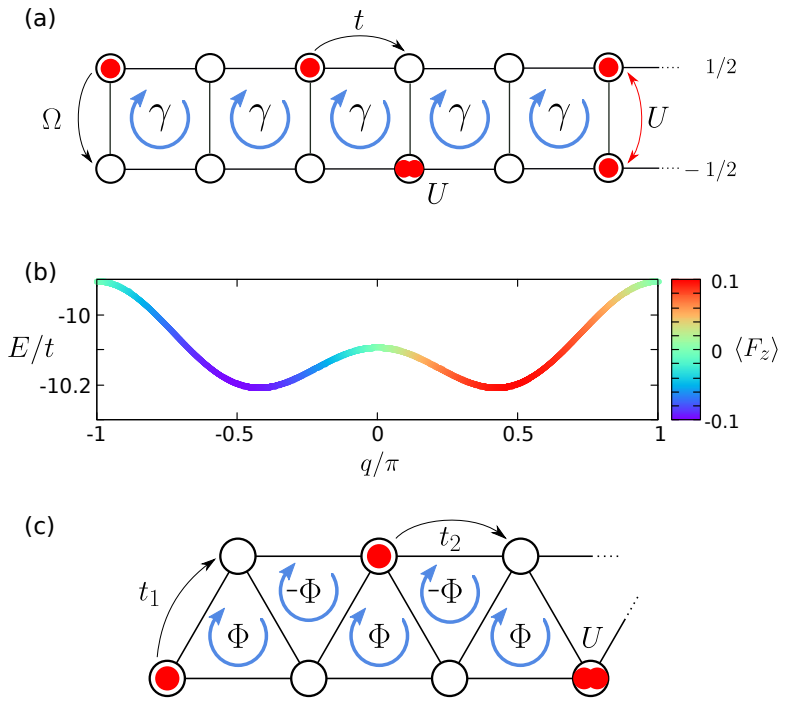

Figure 6.2: Effective triangular ladder from Raman-dressed bosons in a lattice. (a) Schematic representation of the semi-synthetic flux ladder model (6.17). (b) Lowest single-particle dispersion band for $\Omega = 10t$ and $\gamma = 0.97\pi$. The color texture indicates the expected value of the spin of the band states. Observe that, despite having $\Omega \gg t$, the double-well structure can be preserved at large γ. (c) Schematic representation of the truncated lowest-band Hamiltonian (6.32), which describes an effective triangular ladder with staggered flux and onsite interactions.

If we set $\delta = 0$, or equivalently $\Phi = \pi$, such a hard-core-boson Hamiltonian describes a t_1-t_2 spin-$\frac{1}{2}$ XX-chain

$$H_{\triangle}(\Phi = \pi) \overset{t_l/U \to 0}{\longrightarrow} \sum_j \left(t_1 S_j^x S_{j+1}^x + t_1 S_j^y S_{j+1}^y \right) + \sum_j \left(t_2 S_j^x S_{j+2}^x + t_2 S_j^y S_{j+2}^y \right), \quad (6.34)$$

which is a particular case of long-range interacting spin chains. The above Hamiltonian has been studied in detail in [392] as a 1D analogue of the deconfined quantum criticality [393] (for an extension to power-law decay couplings see [435]). From equation (6.29), we see that $t_2 > 0$. In model (6.34), frustration effects take place when $t_2 > 0$, and an interesting phase diagram, where a gapless Superfluid (SF) phase, a gapped bond-ordered-wave (BOW) and a gapless chiral superfluid (CSF), can be found at different values of the ratio between the NN and NNN couplings, $|t_2/t_1|$. For small values of $|t_2|$, the system realizes the gapless SF phase, which can be straightforwardly detected, for instance, by the long range behavior of the one-body density matrix $g^1(|i-j|) = \langle b_i^\dagger b_j \rangle$,

or by the vanishing of the single-particle excitation gap in the thermodynamic limit

$$G_L = E(L, N+1) + E(L, N-1) - 2E(L, N), \tag{6.35}$$

where $E(L, N)$ is the energy of the ground state for a ladder of L sites and N particles. For intermediate values of $|t_2|$, the system favors a dimer order, the BOW phase, characterized by the spontaneous breaking of the inversion symmetry. It is signaled, therefore, by nonzero values of the following two points operator

$$O_{BO} = \frac{1}{L}\sum_i (-1)^i \langle (b_i^\dagger b_{i+1} + b_i b_{i+1}^\dagger)\rangle, \tag{6.36}$$

Additionally, the BOW phase is an insulating phase phase, and exhibits a finite gap $G_{L\to\infty}$ and thus an exponential decay of $g^1(|i-j|)$. Finally, for larger $|t_2/t_1|$ values a chiral phase has been predicted. Indeed, on the contrary to the usual SF characterized by a single minimum in the dispersion relation, the CSF phase presents two non-equivalent minima. There, the interplay between geometric frustration and interatomic interactions favors the occupation of either of the two minima, yielding two degenerate solutions that spontaneously break a Z_2 symmetry and exhibit a finite chirality $k_i = 2\imath(b_i b_{i+1}^\dagger - b_i^\dagger b_{i+1})$. The phase is well captured by the long-range behavior of the chiral correlation function

$$k^2(|i-j|) = \langle k_i k_j \rangle. \tag{6.37}$$

In the remainder of the chapter, we will focus on these strongly-correlated regimes of Hamiltonian (6.32), which have a direct analogy to the physics in Heisenberg models. We should stress, though, that in the realization of the model that we propose, that is, as the low-energy theory embedded within the frustrated flux ladder model, the hard-core-boson condition is hard to meet in realistic experimental conditions. The triangular structure of the effective Hamiltonian emerges from the properties of the lowest-band, and the validity of the lowest-band truncation requires by construction a finite U. Yet, as we have argued in this section, the three characteristic energy scales of the Raman-dressed lattice gas can in principle be arbitrarily separated. It is worth wondering, therefore, if there actually exists a suitable regime of parameters that realizes frustrated magnetic phases that characterize model (6.34), such as the BOW. In the next section we will numerically tackle this question by performing density-matrix-renormalization-group (DMRG) calculations [36, 166, 436] of the whole semi-synthetic flux ladder model (6.17).

6.4 Frustrated quantum magnetism with dressed ultracold atoms

In the previous section, we have proposed an alternative realization of the triangular flux ladder (6.32), based on the low-energy description of the spin-$\frac{1}{2}$ semi-synthetic flux

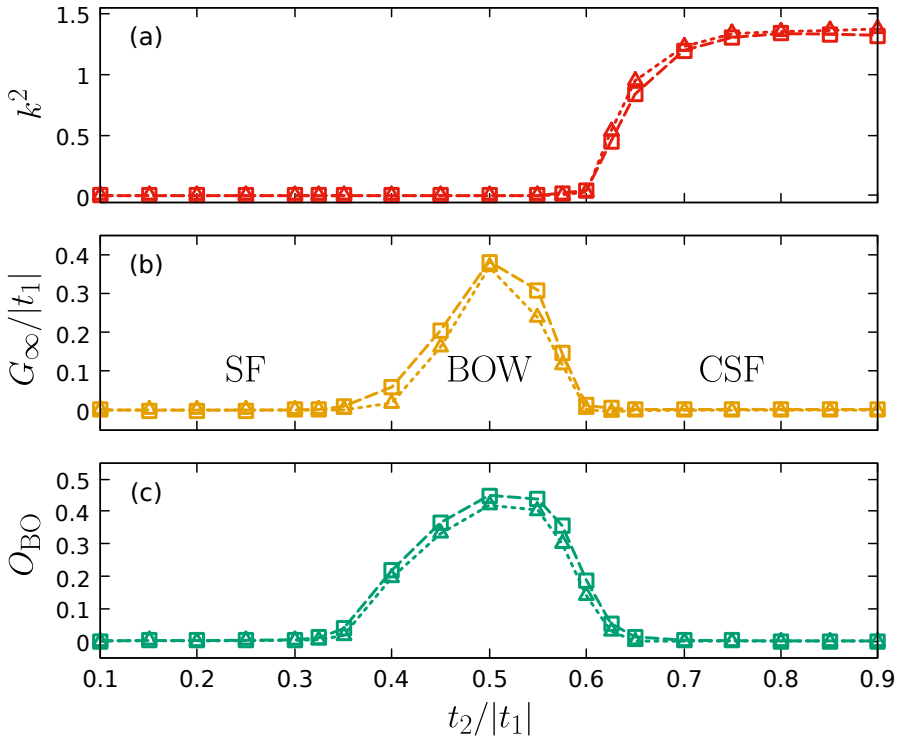

Figure 6.3: Effective triangular ladder from Raman-dressed bosons in a lattice: numerical results. Expected values of the long range chiral correlator $k^2(|i-j|\to\infty)$ (a), the single-particle excitation gap $G_{L\to\infty}$ (b) and the bond-order operator O_{BO} (c) as a function of $t_2/|t_1|$. In all cases, the triangle refer to the results obtained for the ground state of the effective model (6.32) at half filling, with $U = 10|t_1|$ and $\Phi = \pi$, and the squares refer to those obtained for the ground state of Hamiltonian (6.17) at quarter filling and $\delta = 0$. For the latter, we have fixed $\Omega = 10t$, and γ and U have been adjusted by using (6.23) in order to match the corresponding values of t_2/t_1 and U/t_1. All the quantities are extracted to the thermodynamic limit by doing a finite size extrapolation to $L\to\infty$ with systems lengths up to $L = 80$, and setting $N = L/2$.

ladder (6.17). We have seen that strongly-interacting bosons loaded in such a triangular geometry can realize physics that is analogous to that of frustrated quantum Heisenberg models. In the hard-core-boson limit, the Hamiltonian is expected to hold the three phases that take place in a frustrated t_1-t_2 spin-$\frac{1}{2}$ XX chain, namely, the SF, the BOW and the CSF phases described in the previous section. In order to analyze whether these three phases still occur for finite U, we will now explore the range of validity of the effective model by means of DMRG calculations.

We start by exploring the strong Raman coupling regime of the square ladder model, and set $\Omega = 10t$. In Fig. 6.3, we show the expected values of $G_{L\to\infty}$, O_{BO} and $k^2(|i-j|\to\infty)$ (see equations (6.35) to (6.37)) as a function of $|t_1/t_2|$, for the ground states of both the effective triangular Hamiltonian (6.32) at half-filling and the original square ladder

Hamiltonian (6.17) at quarter-filling. For the latter, the value of γ is adjusted while keeping $\Omega = 10t$, so as to obtain the theoretical value of $|t_1/t_2| = \frac{|t\sin(\gamma/2)\tan(\gamma/2)|}{2\Omega}$ predicted by equations (6.28) and (6.29). The expected values in the original ladder are computed using the expression for the dressed modes (6.21) in the bare basis. In both cases, the interaction strength is set to $U = 10|t_1|$, to realize a strongly-interacting regime of the effective triangular ladder. Indeed, Fig. 6.3 shows a very good agreement between the two models in this regime of parameters. The phase diagram predicted in the hard-core boson limit (6.34) of the effective model (6.32) appears to be preserved for large, but finite, values of U. A SF phase, uniquely captured by a vanishing gap appears at small $|t_2|$. There, the bosons quasi-condense in the unique minimum present in the dispersion relation and a finite interaction is able to give rise to superfluidity. For higher ratios between the NN and the NNN hopping, the one-body density matrix g^1 loses the long range order and G_∞ takes nonzero values, which highlights the appearance of the gapped BOW phase. The predicted dimer nature of such an insulating phase is captured by the finite value of the bond-order operator O_{BO}. Finally, when $t_2/|t_1|$ is further increased, the system eventually favors an additional CSF phase, recovering again a finite value of g^1 and a vanishing G_∞, and with chiral order as detected by the long-range ordered chirality-chirality correlation k^2.

The BOW phase is characterized by the spontaneous dimerization of the ground state. In the thermodynamic limit, two degenerate ground states correspond to the even-to-odd and the odd-to-even pairing of the triangular lattice sites, with one atom per dimer and a vanishing current between them, and the system spontaneously breaks the inversion symmetry of the Hamiltonian. Similarly, in the CSF phase, the ground state of the system consists of an equal superposition between superfluid states with two possible relative phases given by an effective Z_2 symmetry. This leads to a spontaneous Z_2 symmetry breaking in the thermodynamic limit. Within the triangular map, the degenerate states are characterized by staggered current patterns. The loop currents around each effective plaquette behave as vortices and form a vortex-antivortex crystal with effective antiferromagnetic order (for a schematic representation of the two phases see Fig. 6.6 in the next section). These structures of the effective model and the way by which they are related to structures in the original square ladder will be covered in more detail in the next section, with special attention to their experimental signatures. As we will see, the BOW phase of the effective model is related to a vortex lattice insulator in the square flux ladder at quarter filling. In turn, the SF and CSF phases correspond, respectively, to the Meissner and biased-ladder superfluid phases therein. The former persist for a similar range of fluxes as interactions are increased, while the latter is suppressed to a large extent in favor of the dimer insulating phase. Still, according to the map to a frustrated spin chain, the chiral regime should survive up to the hard-core-boson limit, albeit the transition there is found at $t_2/|t_1| \sim 1.25$ [431]. At $\Omega = 10t$, e.g., this value for the boundary corresponds to $\gamma \sim 0.975\pi$. Note that this prediction is valid for U large with respect to the band width $\propto t^2/\Omega$, but small with respect to Ω. For $U\Omega$

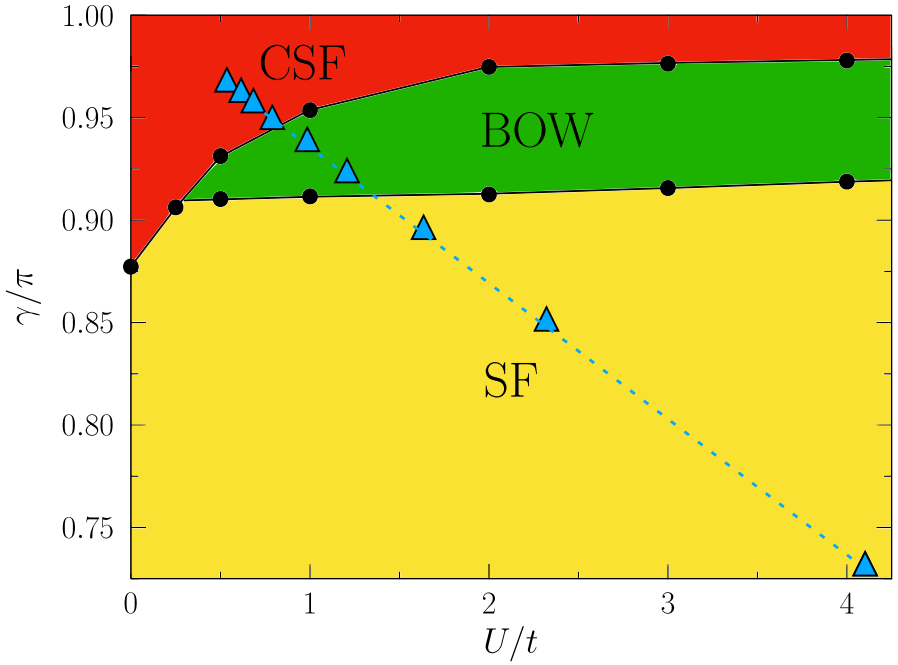

Figure 6.4: Frustrated quantum phases in semi-synthetic flux ladders. Phase diagram of Hamiltonian (6.17) at quarter filling and for $\Omega = 10t$ and $\delta = 0$. The black circles refer to the transition points detected via DMRG simulations. The blue triangles denote, from left to the right, the set of points where $U = 10t\cos(\gamma/2)$ and the ratio of the tunnelings that appear in the effective model (6.32), $|t_2/t_1|$, takes values from 0.9 to 0.1 (with an increase of 0.1 at each step), according to expressions (6.28)) and (6.29).

the predictions of the lowest band model are expected to fail because the lowest-band truncation does not apply.

The phase diagram of Hamiltonian (6.17) in the $U - \gamma$ plane is shown in Fig. 6.4 for $\Omega = 10t$ and at quarter filling. In the figure, the blue triangles cover the trajectory that fixes $U/t_1 = -10$, in correspondence to Fig. 6.3. Notably, the nontrivial BOW and CSF phases persist in large regions in parameter space. Generally speaking, both the CSF and the BOW phase appear for γ is close to π. In agreement with the triangular ladder picture, for a fixed strength of the gauge field, the system undergoes a CSF to BOW KT phase transition when U is increased. Likewise, the insulating BOW phase appears to persist for large values of U. As expected, smaller values of γ, and so of $|t_2/t_1|$, supporting the presence of a gapless SF state. In particular we observe a CSF-SF transition through a Lifshitz point when U is small and a KT transition between a BOW and a superfluid when U is larger. For stronger interactions, where a lowest-band truncation is no longer accurate, we eventually expect the charge density wave phase discussed in [372, 374] to be favored in place of both the BOW and the CSF phases, with the Meissner superfluid surviving to the HCB limit of the flux ladder.

The derivation of the effective model Eq. (6.32) was based on a series of approxima-

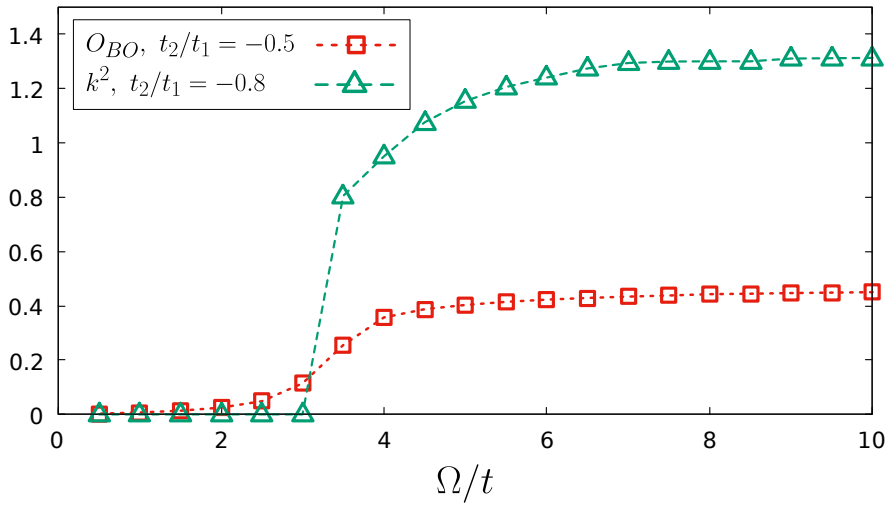

Figure 6.5: Extent of the frustrated phases. In red squares, expected value of O_{BO} as a function of Ω, for the ground state of Hamiltonian (6.17) at quarter filling. We fix $\delta = 0$ and adjust γ and U so that $t_2/|t_1| = 0.5$ and $U = 10|t_1|$. In green triangles, expected value of $k^2(L \to \infty)$ as a function of Ω, adjusting γ and U so that $t_2/|t_1| = 0.8$ and $U = 10|t_1|$. All the quantities are extrapolated to the thermodynamic limit by considering system sizes up $L = 80$.

tions applied to Hamiltonian (6.17). It is crucial, therefore, to assess the extent to which the ladder model in presence of a gauge field is able to support the presence of the phases appearing in the frustrated XX model. Not only from a theoretical understanding, but rather for the experimental implications that such an extent may have. As we will discuss in the next section, to be able to relax such constraints on the Raman parameters will be fundamental to the realization and detection of magnetic phases. So far in this section, and as a first approach in this direction, we have fixed the inter-leg hopping amplitude to the fairly large value of $\Omega/t = 10$, where truncation of the perturbative expressions from (6.32), (6.28) and (6.29) are expected to be accurate. It seems natural, then, to wonder whether the BOW and CSF are still able to occur when Ω is smaller and the lowest-band truncation of (6.17) is challenged. Again, we numerically address this question via DMRG simulations of the ladder for smaller Raman couplings (rung couplings). In Fig. 6.5 we plot O_{BO} as a function of Ω, and adjust γ to keep $|t_2/t_2| = 0.5$, where the BOW phase is expected to take place. Likewise, we plot the values of k^2 while fixing $|t_2/t_1| = 0.8$, where the CSF phase is predicted by the effective model (6.32). In both cases, we set $U = 10|t_1|$ and $t_1 < 0$. As expected, both quantities start to decrease fast when $\Omega < 4t$, where the single-particle bandgap is roughly $\sim 3U$, and no longer separates well the lowest band states, yet both phases appear to be robust for larger values of Ω. Interestingly, the BOW phase appears to persist to some extent down to values of $\Omega \sim t$, where the lowest-band truncation is not expected to be accurate.

The results presented in this section confirm that a semi-synthetic flux ladder is able

to capture all the possible regimes of the frustrated XX model by realizing the phases therein in the strongly-interacting regime of the effective triangular boson ladder, and that it does so for a wide range of parameters. These results suggest, therefore, that intriguing phases induced by the combination of geometrical frustration and quantum fluctuations, such as the BOW and CSF, could be realized in a Raman-dressed bose gas loaded in a 1D optical lattice. In the next section, we will develop further the understanding of the described phases in terms of the original square flux ladder. In particular, we will be interested in the response of the system to the explicit symmetry breaking of the symmetries that are spontaneously broken at each phase. We will see that Raman-dressed bosons in an optical lattice allow for a flexible realization of the model, where such a response can be exploited for the detection of the different phases.

6.5 Experimental implementation and detection of the frustrated phases

In this section we will argue that a Raman-based implementation of Hamiltonian (6.32) can facilitate the experimental accessibility and detection of the distinct phases that the model realizes. As we introduced in the previous section, these phases can be characterized by the three observables from equations (6.35), (6.36) and (6.37). Keep in mind, though, that such observables were defined in terms of the truncated dressed basis. While we have shown so far that the dressed system can in principle realize the frustrated physics of interest, it is crucial, then, to relate these quantities to experimental signatures that can be experimentally accessed in the original semi-synthetic flux ladder. To this end, we will now show that, in the original basis of Hamiltonian (6.17), the phases can be understood in simple terms by the current and density structures of the undressed bosons. We will see that the chirality and dimerization in the triangular ladder are directly related to the square ladder magnetization and to the dimerization of the currents, respectively. With such an understanding, we will next introduce a simple protocol to detect the different phases that exploits the tunability of the dressed system. Finally, we will briefly discuss the experimental viability of the model in an actual experiment with Raman-dressed ultracold ^{41}K atoms in an optical lattice.

6.5.1 Current structures of the frustrated phases

The BOW as a vortex crystal

To gain insights on the nature of the BOW insulating phase in the original square ladder, we now look at the properties of the ground state in the parameter regime that corresponds to the Majumdar-Ghosh point of the XX spin model (6.33), that is, at $t_2 = -t_1/2 > 0$ and $t_1/U \to 0$, where the system is solvable [437]. There, the ground state of the Hamiltonian is twofold degenerate in the thermodynamic limit, each

breaking the inversion symmetry of the Hamiltonian. The two ground states are given by dimerized product states of triplet spin states defined on pairs of consecutive sites

$$|\psi_{\mathrm{e,o}}\rangle = \bigotimes_{j\in\text{even/odd}} \frac{|\uparrow_j\downarrow_{j+1}\rangle + |\downarrow_j\uparrow_{j+1}\rangle}{\sqrt{2}} = \prod_{j\in\text{even/odd}} \frac{b_j^\dagger + b_{j+1}^\dagger}{\sqrt{2}} |0\rangle\,. \tag{6.38}$$

Without loss of generality, we use $|\psi_{\mathrm{e}}\rangle$ for the computations. The ground state $|\psi_{\mathrm{e}}\rangle$ can be written as

$$|\psi_{\mathrm{e}}\rangle = \prod_{j=0}^{L-1} D_j^\dagger |0\rangle\,, \tag{6.39}$$

where we have defined the operators

$$D_j^\dagger = \frac{b_{2j}^\dagger + b_{2j+1}^\dagger}{\sqrt{2}}, \tag{6.40}$$

which fulfill $\left[D_j, D_k^\dagger\right] = \delta_{j,k}$. At $\delta = 0$, we conveniently reexpress the dressed mode operators (6.21), truncated to first order in t/Ω, as

$$b_n^\dagger \simeq \cos\alpha c_{n,-}^\dagger + i\sin\alpha \frac{c_{n+1,+}^\dagger - c_{n-1,+}^\dagger}{\sqrt{2}}, \tag{6.41}$$

where we have defined $c_{n,\pm}^\dagger = \frac{a_{n,+}^\dagger \pm a_{n,-}^\dagger}{\sqrt{2}}$ and $\alpha = \arctan\left(\frac{t\sin(\gamma/2)}{\sqrt{2}\Omega}\right)$. By substituting the approximate expression (6.41) for the modes b_j into (6.40), we can write D_j in the bare basis $\left\{c_{j,m}^\dagger |0\rangle\right\}$ as

$$D_j^\dagger \simeq \cos\alpha \frac{c_{2j,-}^\dagger + c_{2j+1,-}^\dagger}{\sqrt{2}} + i\sin\alpha \frac{c_{2j+2,+}^\dagger + c_{2j+1,+}^\dagger - c_{2j,+}^\dagger - c_{2j-1,+}^\dagger}{2}. \tag{6.42}$$

We now compute the circular currents in the paired sites. We start by computing the expected value of the total rung current in the $2k$ plaquette, $j_{2k}^{(r)}$, defined as

$$\begin{aligned} j_{2k}^{(r)} &= i\Omega\left(a_{2k,+}a_{2k,-}^\dagger - a_{2k,+}^\dagger a_{2k,-}\right) - i\Omega\left(a_{2k+1,+}a_{2k+1,-}^\dagger - a_{2k+1,+}^\dagger a_{2k+1,-}\right) \\ &= -i\Omega\left(c_{2k,+}c_{2k,-}^\dagger - c_{2k,+}^\dagger c_{2k,-}\right) + i\Omega\left(c_{2k+1,+}c_{2k+1,-}^\dagger - c_{2k+1,+}^\dagger c_{2k+1,-}\right). \end{aligned}$$

By using expression (6.39) and the commutation relations of operators D_j, it is easy to show that

$$\begin{aligned} \langle\psi_{\mathrm{e}}| j_{2k}^{(r)} |\psi_{\mathrm{e}}\rangle &= \langle 0| D_{k-1}D_kD_{k+1} j_{2k}^{(r)} D_{k-1}^\dagger D_k^\dagger D_{k+1}^\dagger |0\rangle \\ &= \langle 0| D_{k-1}D_kD_{k+1}\left[j_{2k}^{(r)}, D_{k-1}^\dagger\right] D_k^\dagger D_{k+1}^\dagger |0\rangle \\ &+ \langle 0| D_{k-1}D_kD_{k+1}D_{k-1}^\dagger\left[j_{2k}^{(r)}, D_k^\dagger\right] D_{k+1}^\dagger |0\rangle \\ &+ \langle 0| D_{k-1}D_kD_{k+1}D_{k-1}^\dagger D_k^\dagger\left[j_{2k}^{(r)}, D_{k+1}^\dagger\right] |0\rangle\,. \end{aligned} \tag{6.43}$$

Finally, inserting (6.42) into eq. (6.43) and (6.47) yields

$$\langle\psi_{\rm e}|\, j^{(r)}_{2k}\,|\psi_{\rm e}\rangle = -\sqrt{2}\Omega\sin\alpha\cos\alpha = -t\sin(\gamma/2) + O((t/\Omega)^3). \tag{6.44}$$

Similarly, we now compute the leg currents

$$j^{\pm}_k = it\left(e^{\mp i\gamma/2}a_{k,\pm}a^\dagger_{k+1,\pm} - e^{\pm i\gamma/2}a^\dagger_{k,\pm}a_{k+1,\pm}\right). \tag{6.45}$$

In the $c^\dagger_{j,m}$ basis, the total leg current in the $2k$ plaquette reads

$$\begin{aligned} j^{(a)}_k := j^-_k - j^+_k = &-t\left(c_{k,+}c^\dagger_{k+1,+} + c_{k,-}c^\dagger_{k+1,-}\right)\sin(\gamma/2) \\ &-it\left(c_{k,+}c^\dagger_{k+1,-} + c_{k,-}c^\dagger_{k+1,+}\right)\cos(\gamma/2) + \text{H.c.} \end{aligned} \tag{6.46}$$

Again, we can write

$$\begin{aligned} \langle\psi_{\rm e}|\, j^{(a)}_{2k}\,|\psi_{\rm e}\rangle &= \langle 0|\, D_{k-1}D_kD_{k+1}j^{(a)}_{2k}D^\dagger_{k-1}D^\dagger_kD^\dagger_{k+1}\,|0\rangle \\ &= \langle 0|\, D_{k-1}D_kD_{k+1}\left[j^{(a)}_{2k}, D^\dagger_{k-1}\right]D^\dagger_kD^\dagger_{k+1}\,|0\rangle \\ &+ \langle 0|\, D_{k-1}D_kD_{k+1}D^\dagger_{k-1}\left[j^{(a)}_{2k}, D^\dagger_k\right]D^\dagger_{k+1}\,|0\rangle \\ &+ \langle 0|\, D_{k-1}D_kD_{k+1}D^\dagger_{k-1}D^\dagger_k\left[j^{(a)}_{2k}, D^\dagger_{k+1}\right]|0\rangle\,. \end{aligned} \tag{6.47}$$

which after inserting (6.42) results in

$$\begin{aligned} \langle\psi_{\rm e}|\, j^{(a)}_{2k}\,|\psi_{\rm e}\rangle &= -t\cos(\gamma/2)\sqrt{2}\sin\alpha\cos\alpha - t\sin(\gamma/2)\left(\cos^2\alpha - \frac{1}{2}\sin^2\alpha\right) \\ &= -t\sin(\gamma/2)\left(1 + \frac{t\cos(\gamma/2)}{\Omega} + O((t/\Omega)^2)\right). \end{aligned} \tag{6.48}$$

Observe that, to zero order in (t/Ω), we have $j^{(a)}_{2k} = j^{(r)}_{2k}$. This result can be extended to the $|\psi_{\rm o}\rangle$ solution by just shifting each lattice site from j to $j+1$. Therefore, the ground state solutions at the solvable Majumdar-Ghosh point consist, in the original square ladder, on two vortex crystals with one particle per vortex plaquette, with a circular current $j^{(c)}_j = j^{(a)}_j + j^{(r)}_j$ on the dimerized plaquettes given by

$$\langle\psi_{\rm e}|\, j^{(c)}_{2k}\,|\psi_{\rm e}\rangle = \langle\psi_{\rm o}|\, j^{(c)}_{2k+1}\,|\psi_{\rm o}\rangle = -2t\sin(\gamma/2) + O(t/\Omega). \tag{6.49}$$

The first order correction to these solutions includes a small current $\propto t\cos(\gamma/2)/\Omega$ between the dimerized plaquettes that vanishes both for $t/\Omega \to 0$ and $\gamma \to \pi$. Notice that both solutions have a nonzero chiral current

$$j_c = \imath t\frac{2}{L}\sum_i\sum_{\sigma=\pm1/2}\sigma(e^{-\imath\gamma\sigma}a^\dagger_{i+1,\sigma}a_{i,\sigma} - e^{\imath\gamma\sigma}a_{i+1,\sigma}a^\dagger_{i,\sigma}). \tag{6.50}$$

In particular, we have

$$\langle\psi_{\rm e,o}|\, j_c\,|\psi_{\rm e,o}\rangle = t\sin(\gamma/2)/2 + O(t/\Omega). \tag{6.51}$$

This net edge current is induced by the static gauge field that breaks the time-reversal symmetry in the Hamiltonian (6.17). We emphasize that these results have been derived assuming a hard-core-boson limit within the effective model, which can not be realized in the actual flux ladder Hamiltonian (6.17) (due to either the band separation being finite or the intraband scale vanishing). Thus, deviations should be expected for finite U. Still, we numerically find a very good agreement in the considered range of parameters, with $U \gtrsim 10t_1$, and a good qualitative agreement for even smaller Ω. The current distribution in the BOW state is schematically represented in Fig. 6.6(a), both in the effective model and in the semi-synthetic flux ladder model. For the latter, the arrows representing the currents are scaled according to the values found numerically. In this case, we have set $\Omega = 5t$, $\delta = 0$ and $\gamma = 0.877\pi$, for which $t_2/|t_1| \sim 0.5$. The leg currents on the dimer sites are found to be $j_{2k}^{(a)} \simeq -0.93t$, while equation (6.42) predicts $j_{2k}^{(a)} \simeq -1.02t$. The BOW phase predicted on the effective model, therefore, is identified with a vortex lattice insulator phase of the flux ladder at quarter filling and with maximal vortex density. An interesting property of the phase is that, finding its origin in the interplay between frustration and filling factor of the effective triangular model, the onset of the insulating phase can be found at notably low interaction strengths as the rung tunneling Ω is increased. Remarkably, such a vortex lattice is found in a regime that has been overlooked in many other works that have explored the flux ladder (see [374] for a detailed classification of various superfluid and insulating vortex lattice phases). This is probably due to the particular requirement of both large inter-leg hoppings and comparatively smaller interactions for its stabilization. Note that, while the exploration of such a regime is inviting in the semi-synthetic implementation of the flux ladder, where large inter-leg tunnelings are straightforwardly achieved, its realization along two spatial dimensions would be challenging. To achieve very large rung tunnelings there, the depth of the potential barrier along the rung direction would need to be reduced, eventually leaving the tight-binding regime. By contrast, very strong rung couplings can be achieved in the synthetic dimension before challenging the tight-binding approximation.

The CSF as a biased ladder superfluid

Similarly, the CSF phase has two degenerate solutions that spontaneously break the Z_2 symmetry of the Hamiltonian. In each solution, local interatomic interactions favor the occupation of quasimomentum states around either the left or the right minimum of the band. In fact, the weakly-interacting regime of the CSF in the flux ladder is related to the plane-wave phase of the spin-orbit-coupled bulk-gas. There, non-zero SU(2) spin interactions favor the formation of a condensate with non-zero quasimomentum when the single-particle band is in the two-minima regime. In the semi-synthetic flux ladder, a similar behavior is thus expected, and the current structure of the phase is straightforwardly understood by taking the noninteracting limit of the two solutions $|\psi_{\mathrm{L,R}}\rangle$, which are then simply given by the collective occupation of the band states located the left and right band minima, respectively.

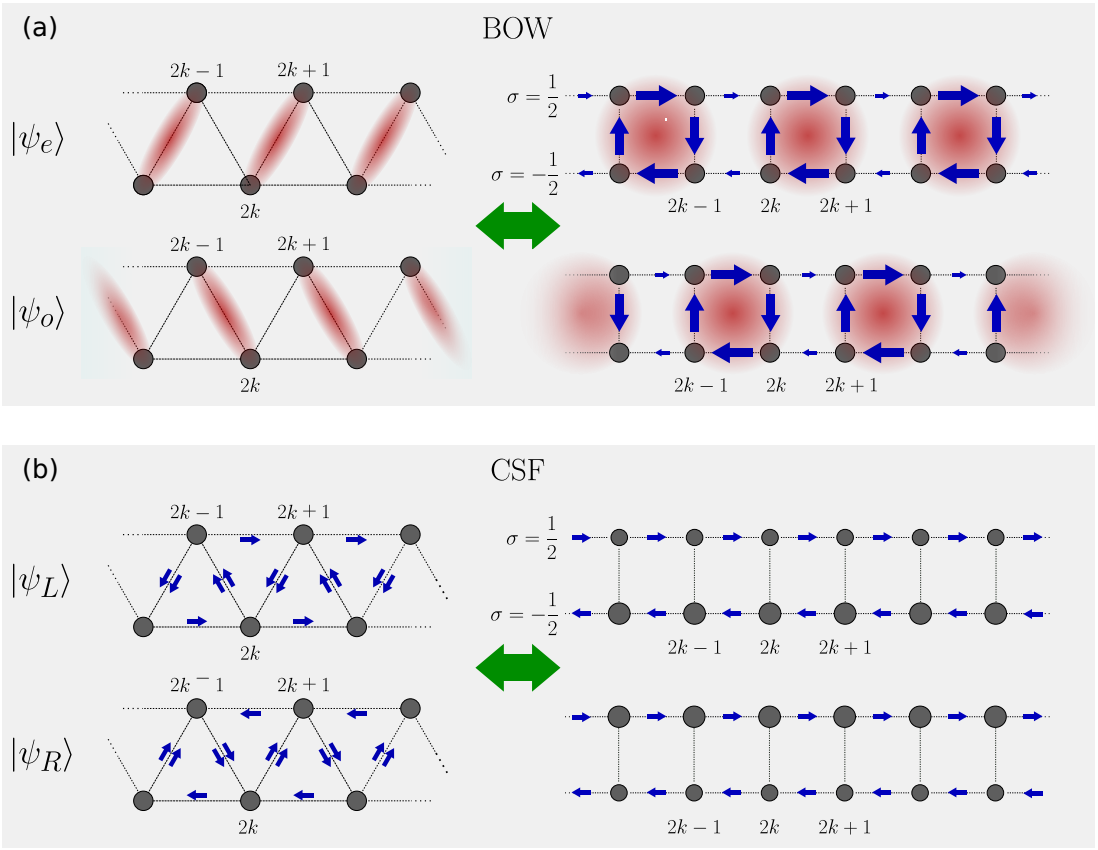

Figure 6.6: Current and density structures of the frustrated phases. Schematic representations of the current and density structures of the degenerate ground states in (a) the dimer BOW phase and in (b) the CSF phase. In the BOW state, the red shadowed sites represent the dimers. In both cases, the left panel represents the state in the triangular ladder and the right panel the corresponding state in the original square flux ladder. Within the triangular model, the densities and currents in the two phases are uniform. In the original ladder howver, the BOW translates into a vortex crystal with staggered arm currents and dimerized leg currents. In turn, the CSF translated into a biased ladder superfluid with a density imbalance between the two arms. The area of the dots and arrows representing the densities and currents of the square flux ladder (right) are scaled according to their numerical values determined at $\Omega = 5$ and $\delta = 0$, with γ and U adjusted so that $t_2/|t_1| = 0.5$ and $U = 10|t_1|$.

In the single-particle band modes all have a vanishing rung current. For a bandstate

at q, it follows

$$\begin{aligned}\langle 0|\,\tilde{b}_{q,-}\,j_k^{(r)}\,\tilde{b}_{q,-}^\dagger\,|0\rangle &= \frac{i\Omega}{L}\sum_{nn'mm'}\langle 0|\,e^{-iqn'}\,e^{iqn}U_{-,m'}^*(q)U_{-,m}(q)a_{n',m'}a_{k,-}a_{k,+}^\dagger a_{n,m}^\dagger\,|0\rangle + \text{H.c.}\\ &= -\frac{2\Omega}{L}\,\text{Im}\left(U_{-,-}^*(q)U_{-,+}(q)\right) = 0.\end{aligned} \tag{6.52}$$

At the same time, the arm current is given by

$$\begin{aligned}\langle 0|\,\tilde{b}_{q,-}\,j_k^{\pm}\,\tilde{b}_{q,-}^\dagger\,|0\rangle &= \frac{it}{L}\sum_{nn'mm'}\langle 0|\,e^{\mp i\gamma/2}e^{-iqn'}\,e^{iqn}U_{-,m'}^*(q)U_{-,m}(q)a_{n',m'}a_{k,\pm}a_{k+1,\pm}^\dagger a_{n,m}^\dagger\,|0\rangle\\ &\quad + \text{H.c.}\\ &= -\frac{2}{L}\,\text{Im}\left(te^{-i(q\pm\gamma/2)}U_{-,\pm}^*(q)U_{-,\pm}(q)\right) = \frac{2t}{L}\sin(q\pm\gamma/2)|U_{-,\pm}(q)|^2,\end{aligned} \tag{6.53}$$

which yields a nonzero edge current

$$\langle 0|\,\tilde{b}_{q,-}\,j_c\,\tilde{b}_{q,-}^\dagger\,|0\rangle = \frac{2t}{L}\sin(q+\gamma/2)|U_{-,+}(q)|^2 - \frac{2t}{L}\sin(q-\gamma/2)|U_{-,-}(q)|^2. \tag{6.54}$$

We now set $\delta = 0$, where $U_{-,\pm}(q) = \frac{1}{\sqrt{2}}\left(1 \pm t\sin(\gamma/2)\sin(q)/\Omega\right) + O(\tilde{q}^2)$ (see eq. (6.20)), and thus

$$\langle 0|\,\tilde{b}_{q,-}\,j_c\,\tilde{b}_{q,-}^\dagger\,|0\rangle = \frac{2t}{L}\left(\sin(\gamma/2)\cos(q) + \frac{t}{\Omega}\sin(\gamma)\sin(q)^2 + O((t/\Omega)^2)\right). \tag{6.55}$$

For $|\gamma| < |\gamma_c| = \left|4\tan^{-1}\left(\sqrt{\frac{\sqrt{(\Omega/t)^2+16}-4}{\Omega/t}}\right)\right|$, the lowest dispersion band exhibits a single minimum at $q_m = 0$, and the solutions correspond to the noninteracting limit of the Meissner phase: indeed, in this regime the chiral current increases with γ as $\langle j_c\rangle \propto \sin(\gamma/2)$, effectively screening the applied flux. For $|\gamma| > \gamma_c$, the band splits into two degenerate minima at $q_{R,L} = \pm\cos^{-1}\left(\frac{\Omega\sqrt{1+(2t\sin(\gamma/2)/\Omega)^2}}{2t\tan(\gamma/2)}\right)$, and the chiral current for the corresponding states $|\psi_{\text{R,L}}\rangle$ starts to decrease with an increasing flux γ. In the absence of interactions, the change is nonanalytical in the thermodynamic limit, signalling a second order phase transition. This response in the flux screening is shared by the vortex superfluid phase of the flux ladder. However, in the CSF phase predicted by the effective model, the spontaneous breaking of the Z_2 symmetry prevents the formation of vortices and instead gives rise to a population imbalance between the two legs. The CSF phase, thus, corresponds to a biased-ladder superfluid phase [374, 424, 438]. The current distribution in the CSF regime is schematically represented in Fig. 6.6(b).

The presence of interatomic interactions smooth out the single-minima to two-minima transition by favoring a spread momentum distribution in the ground state that carries on into the two minima regime of the single-particle energy band. As interactions are

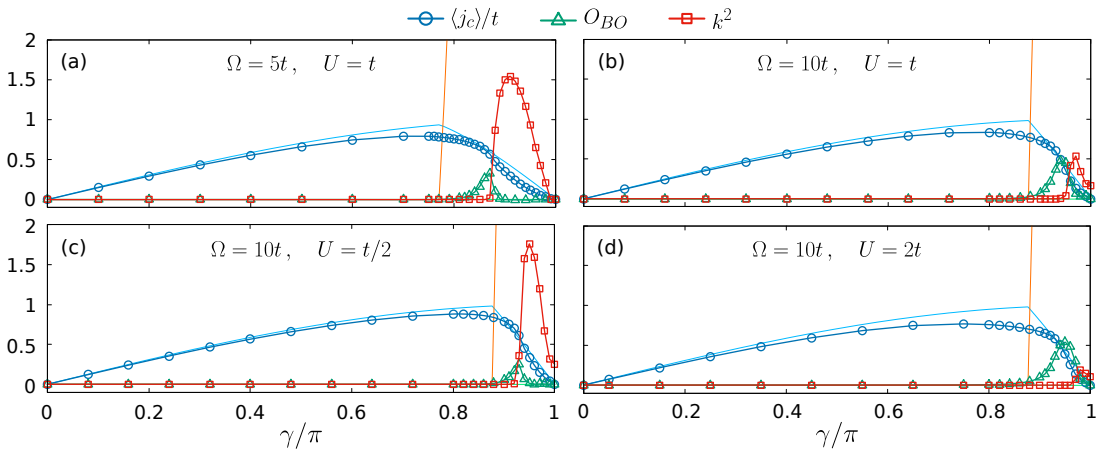

Figure 6.7: Expected value of the chiral current j_c (blue circles), the bond-order operator O_{BO} (green triangles) and the triangular ladder chiral correlation function $k^2(L)$ (red squares) as a function of γ for the ground state of Hamiltonian (6.17) at quarter filling and $\delta = 0$. We set $\Omega = 5t$ and $U = t$ in (a), $\Omega = 10t$ and $U = t$ in (b), $\Omega = 10t$ and $U = 0.5t$ in (c), and $\Omega = 10t$ and $U = 2t$ in (d). Light-colored thin solid lines show the corresponding values at the noninteracting limit. In all cases, the values are obtained from a finite size extrapolation considering sizes up to $L = 80$.

increased, the Meissner to biased-ladder superfluid transition is eventually lost in favor of the additional vortex lattice insulator phase in-between, that corresponds to the BOW dimer phase in the effective model (see Fig. 6.4). In figure Fig. 6.7 we plot the expected values of the chiral current $\langle j_c\rangle$, O_{BO} and $k^2(L)$ for the ground state at quarter filling as a function of γ for different values of U and Ω. In light-colored solid thin lines we show the corresponding values obtained for the noninteracting flux ladder. Notice how the presence of interactions the changes the nonanalytical behavior of the chiral current that characterizes the noninteracting transition. Still, even for strong interactions, the system is able to screen the external magnetic field at weak fluxes. At large γ, nonzero values of $O_{BO}(L)$ and $k^2(L)$ for $L \to \infty$ signal the onset of the BOW and CSF phases, respectively. We note that, since the values are extrapolated from finite-size samples, the degeneracy in the BOW phase is lifted by finite size effects and the extrapolated values correspond to one of the two actual ground states. Observe that the BOW phase is favored at larger Ω and U. As we have shown above, at large U and Ω, the BOW phase exhibits a vortex crystal structure with circular currents that depends weakly on these parameters (see (6.49)). This can facilitate its experimentally accessibility, since the phase is expected to exhibit a dimerized leg current of $\sim t\sin(\gamma/2)$ between the sites of the dimers, even when U and Ω are made large. Contrarily, in the CSF phase, k^2 is largely suppressed by atom-atom interactions and decreases with the rung tunneling strength. Still, the phase persists at fluxes $\gamma \sim \pi$ even for $U \gg |t_1|, |t_2|$, as is predicted by the hard-core-boson limit of the lowest-band triangular model. In Fig. 6.7(d), k^2

takes nonzero values roughly when $\gamma \gtrsim 0.97\pi$. This is consistent with the predictions of the spin-chain model (6.34), since, at this regime of parameters we have $U > 40t_1, 40t_2$, and the hard-core-boson approximation is expected to be accurate.

6.5.2 Measuring the observables of the effective model

Through the understanding of how the frustrated phases of the triangular model translate into the original square ladder model, we can connect the characterizing signatures of the phases in the former model to experimentally suitable observables defined in the latter. We now show that, indeed, the SF, the BOW and the CSF phases can be detected by measuring the response of the system to the explicit breaking of the Z_2 spin and inversion symmetries of the Hamiltonian.

We start by relating the effective current density of the triangular model to the magnetization in the square ladder. The zig-zag current between nearest neighbors in the triangular ladder is given by

$$j_1 = \frac{\partial H}{\partial \phi_1}_{|_{|t_1|,t_2}} = -\sum_i 2\,\mathrm{Im}(t_1 b_i b_{i+1}^\dagger). \tag{6.56}$$

We can directly retrieve the corresponding expression for j_1 in the original ladder by using expression (6.27), which relates the staggered flux ϕ_1 to the detuning δ. From (6.27) and (6.56), it follows that

$$\langle j_1 \rangle = \frac{\partial(\delta/t)}{\partial \phi_1}|_{|t_1|,t_2} \frac{\partial \langle H \rangle}{\partial(\delta/t)}|_{|t_1|,t_2} = -\frac{2\Omega}{t\tan(\gamma/2)} \frac{\partial E}{\partial(\delta/t)}|_{|t_1|,t_2} \tag{6.57}$$

Note that since $|t_1|$ and t_2 are independent of δ at linear order (see Eqs. (6.23)), around $\delta = 0$ we have

$$\partial_{\delta/t} E|_{|t_1|,t_2} = \partial_{\delta/t} E|_{\Omega,\gamma} \tag{6.58}$$

and thus j_1 can be calculated over the original model simply from $\langle j_1 \rangle = -\frac{2\Omega}{t\tan(\gamma/2)} \frac{\partial E}{\partial(\delta/t)}|_{\Omega,\gamma}$. Furthermore, from (6.17), it follows that

$$\partial_{\delta/t} E|_{\Omega,\gamma} = \frac{\partial \langle H \rangle}{\partial(\delta/t)}|_{\Omega,\gamma} = t \sum_{i,\sigma} \langle \sigma a_{i,\sigma}^\dagger a_{i,\sigma} \rangle. \tag{6.59}$$

Hence, near $\delta = 0$, the current in the effective triangular ladder directly maps into the mean magnetization in the original square ladder, with

$$\langle j_1 \rangle \simeq -\frac{2\Omega}{\tan(\gamma/2)} N m_z, \tag{6.60}$$

where we have defined the mean magnetization as

$$m_z = \frac{1}{N} \sum_{i,\sigma} \langle \sigma a_{i,\sigma}^\dagger a_{i,\sigma} \rangle. \tag{6.61}$$

With this expression we can relate the effective current density within the triangular model, $\frac{1}{L}\langle j_1\rangle/|t_1|$, to the magnetization of the ground state in the original ladder. By using (6.60) and (6.23), and considering the system at quarter filling, with $N = L/2$, we obtain:

$$\frac{1}{L}\langle j_1\rangle/|t_1| = -\frac{\Omega}{t\sin(\gamma/2)}m_z \overset{\gamma\simeq\pi}{\simeq} -\frac{\Omega}{t}m_z. \tag{6.62}$$

In this way, the effective current density in the triangular ladder model is proportional to the magnetization of the whole lattice. The CSF has as ground state two degenerate solutions each with nonzero and opposite current j_1, as schematically represented in Fig. 6.6, that spontaneously break the Z_2 symmetry of the Hamiltonian. In the square ladder, this is translated into a different value of m_z for each solution, and the phase can be probed by the behavior of the magnetization against the explicit symmetry breaking of such a symmetry. In the semi-synthetic flux ladder, this can be achieved simply by varying the Raman detuning δ around $\delta = 0$. In these conditions, we expect the magnetization to exhibit a nonanalytic behavior at $\delta = 0$ when the system is in the CSF phase. Contrarily, in the SF and BOW phases, we expect m_z to smoothly decrease to zero as we take δ to zero. In Fig. 6.8(a) we plot the mean relative polarization m_z of the ground state as a function of δ for $\Omega = 10t$. We adjust γ to different values of t_2/t_1 and keep $U = 10t_1$. As expected, for the CSF state at $|t_2/t_1| = 0.8$ (see Fig. 6.3), the spontaneous breaking of the Z_2 symmetry of the ground state in the CSF phase is indeed signaled by a discontinuity in m_z around $\delta = 0$, which is not observed in the case of the SF or BOW states at $|t_2/t_1| = 0.3$ and $|t_2/t_1| = 0.5$, respectively. This would translate into a hysteresis behavior for the CSF states when adiabatically driven across $\delta = 0$.

We can use a similar approach to distinguish the BOW phase. As discussed in Sec. 6.5.1, the two degenerate ground states in the BOW phase exhibit a spontaneous dimerization. We can, therefore, characterize the phase by the behavior of the system against the explicit breaking of the inversion symmetry. The symmetry breaking could be implemented in the square ladder by modulating the 1D optical lattice to generate a superlattice, where the nearest-neighbors tunnelings are dimerized. We parameterize such modulation by introducing a position dependent tunneling strength $t_j = t(1 + \Delta(-1)^j)$ between sites j and $j+1$ in Hamiltonian (6.17). The rung tunnelings are unaffected by such an explicit dimerization, and for $\Delta \ll 1$, we can neglect the second order corrections Δ^2 to the flux at each plaquette. Doing so, we obtain the following dimerized Hamiltonian

$$\begin{aligned} H(\Delta) = &\sum_{j,\sigma}\left(-t(1+\Delta(-1)^j)e^{-\imath\gamma\sigma}a^\dagger_{j+1,\sigma} + \frac{\Omega}{2}a^\dagger_{j,\bar\sigma} + \sigma\delta a^\dagger_{j,\sigma}\right)a_{j,\sigma} + \text{H.c.} \\ &+\sum_{j,\sigma}\left(\frac{U_{\sigma\sigma}}{2}n_{j\sigma}(n_{j\sigma}-1) + \frac{U_{\sigma\bar\sigma}}{2}n_{j,\sigma}n_{j\bar\sigma}\right). \end{aligned} \tag{6.63}$$

To first order, the addition of an infinitesimal Δ results in the dimerization of the effective triangular ladder

$$H_\triangle(\Delta) \simeq \sum_j (t_1(1+\Delta(-1)^j)b^\dagger_j b_{j+1} + t_2 b^\dagger_j b_{j+2} + \text{H.c.}) + \frac{U}{2}\sum_i \tilde n_i(\tilde n_i - 1), \tag{6.64}$$

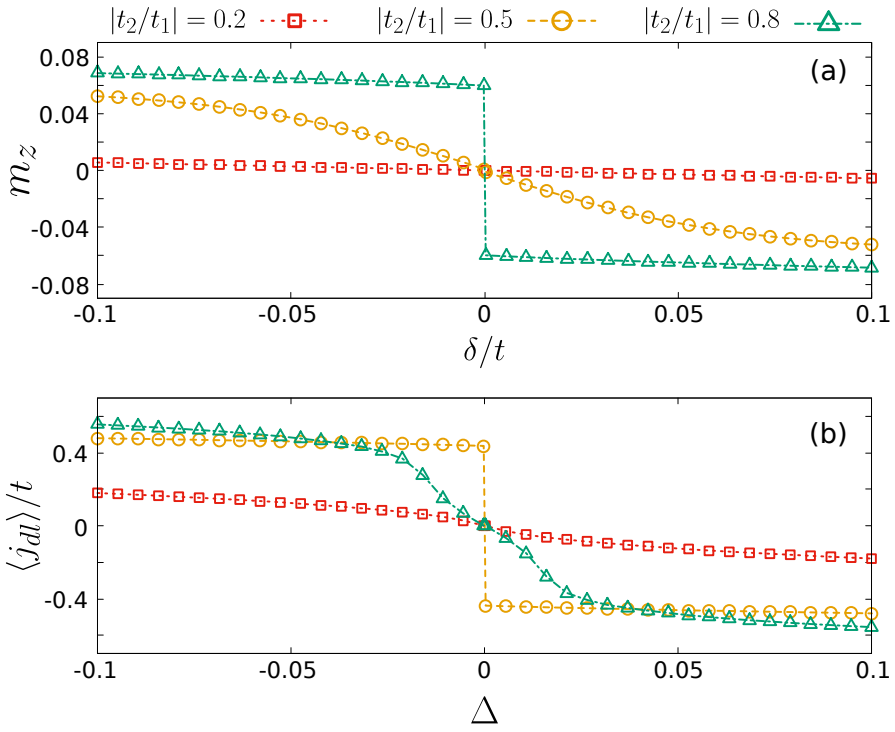

Figure 6.8: Signature of the frustrated phases. (a) Expected value of the magnetization m_z as a function of δ, for the ground state of Hamiltonian (6.17) at quarter filling, with $\Omega = 10t$ and adjusting γ and U so that $U = 10|t_1|$ and $t_2/|t_1| = 0.2$ (red squares), 0.5 (yellow circles), 0.8 (green triangles), with $t_1 < 0$. (b) Expected value of the staggered leg current j_{dl} (see main text) as a function of Δ and fixing $\delta = 0$. All quantities are extrapolated to the thermodynamic limit by considering system sizes up to $L = 80$.

that allows us to write the O_{BO} observable in the original basis as

$$O_{BO} = \frac{1}{Lt_1}\frac{\partial H_{\triangle}}{\partial \Delta} \simeq \frac{1}{Lt_1}\frac{\partial H}{\partial \Delta} = -\frac{t}{Lt_1}\sum_{j,\sigma}(-1)^j 2\,\mathrm{Re}\left(e^{-\imath\gamma\sigma}a^{\dagger}_{j+1,\sigma}a_{j,\sigma} + H.c.\right). \quad (6.65)$$

Analogously as discussed before for the current j_1, in the BOW phase we expect the O_{BO} operator to behave nonanalytically around $\Delta = 0$, and not to do so for states that belong to the SF and CSF phases. Furthermore, as we have shown in Sec. 6.5.1, the dimers in the BOW phase of the effective triangular ladder correspond to vortices in the square ladder. With this in mind, it can be experimentally more convenient to probe the dimerization of the system simply by measuring the dimerized leg currents. By measuring the response of the following current

$$j_{dl} = \frac{1}{L}\sum_{j,\sigma}(-1)^j 4\sigma\,\mathrm{Im}\left(te^{-\imath\gamma\sigma}a^{\dagger}_{j+1,\sigma}a_{j,\sigma} + H.c.\right) \quad (6.66)$$

against the variation of Δ around $\Delta = 0$, the BOW phase can be distinguished from the SF and CSF phases. In Fig. 6.8(b) we show the expected value of the staggered leg

current j_{dl} as a function of Δ. Again, we set $\Omega = 10t$ and adjust γ to achieve different values of the ratio t_2/t_1, while setting $U = 10t_1$. For the ground state at $|t_2/t_1| = 0.5$, where the system is expected to be in the BOW phase, the spontaneous dimerization of the ground state results in the discontinuity of j_{dl} around $\Delta = 0$. As predicted, this behavior differentiates the BOW phase from the SF and CSF phases.

In this way, we have shown that the whole phase diagram of a strongly-interacting frustrated triangular ladder model could in principle be probed in the Raman-based realization of a semi-synthetic flux ladder. Our results suggest that the SF, BOW and CSF phases of the frustrated model could be efficiently detected by the response of the system to controlled perturbations that explicitly break the Z_2 symmetries that are spontaneously broken in the frustrated phases. The approach that we propose exploits the degree of tunability that the experimental platform offers, which could be advantageous to the detection of the phases. Naturally, in an actual experimental implementation of Hamiltonian (6.17), the system is subject to heating mechanisms and atom loss, which are detrimental to the realization and detection of the frustrated phases described in this chapter. To conclude this section, we will now discuss the energy scales that characterize the proposed implementation of the triangular model (6.32), and the viability of its realization with Raman-dressed ultracold atoms.

6.5.3 Comment on experimental scales

As discussed above, the SF and the CSF phases of the effective model correspond, in the weakly-interacting regime, to the Meissner and biased-ladder superfluid of the flux ladder, and are continuously connected to their corresponding strong interacting limits. The BOW phase, however, emerges via the interplay between geometric frustration and strong interactions, and is essentially a strongly-correlated phase without a noninteracting limit (see the phase diagram from Fig. 6.4). While this condition makes the phase inherently interesting, to realize strong interactions within the effective model requires both a large band gap and a small bandwidth, and thus larger values of Ω, as illustrated in Fig. 6.1. This results, in turn, in smaller energy scales of the effective model and in an increase of the heating and the atom loss rate from the Raman beams. The realization and detection of the BOW phase in the semi-synthetic flux ladder, therefore, is expected to be more challenging, and will be the focus of this discussion.

Given these constraints, in order to observe the dimer order it is convenient to choose the smallest suitable values of Ω for which the insulating phase persist. Taking as a reference the results shown in Fig. 6.5, let us fix $t_2/|t_1| = 0.5$ and $U = 10|t_1|$, where we notice that O_{BO} remains large for $\Omega \gtrsim 4t$. To gain further insights, in Fig. 6.9(a) we plot the corresponding values of the gap $G_{L\to\infty}$ of the ground state as a function of Ω. The insulating character of the phase, as signalled by the size of the gap G_∞, is maximized somewhere in between $\Omega = 6t$ and $\Omega = 7t$, but is maintained at near-maximal values for Ω as low as $\Omega \sim 5t$. Let us consider, therefore, $\Omega = 5t$ to find a loose approximation

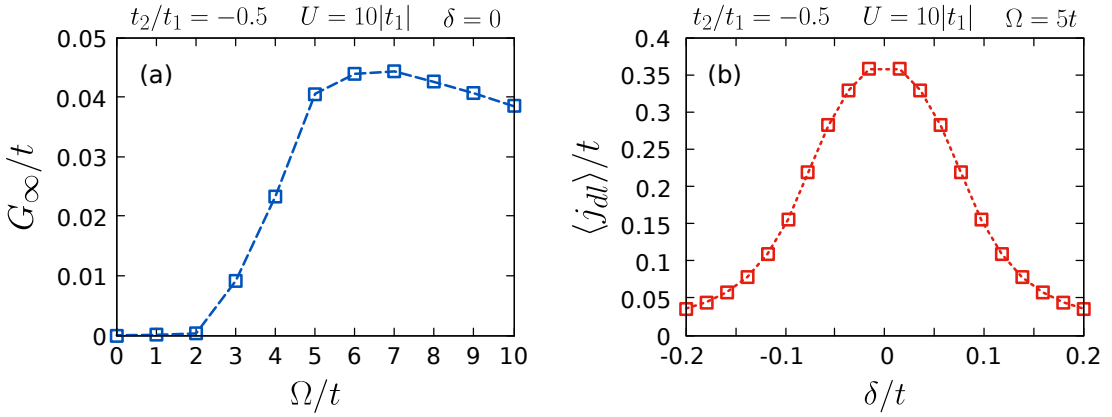

Figure 6.9: Experimental scales. (a) Expected value of single-particle excitation gap $G_{L\to\infty}$ as a function of Ω for the ground state of Hamiltonian (6.17), fixing $\delta = 0$ and adjusting γ and U so that $U = 10|t_1|$ and $t_2/|t_1| = 0.5$. (b) Expected value of staggered leg current j_{dl} as a function of δ, fixing $\Omega = 5t$ and adjusting γ and U so that $U = 10|t_1|$ and $t_2/|t_1| = 0.5$. All quantities are extrapolated to the thermodynamic limit by considering system sizes up to $L = 80$.

of the optimal energy scales of the effective model. At $\Omega = 5t$, we find $t_2/|t_1| = 0.5$ at $\gamma \simeq 0.877\pi$, and so an effective tunneling strength $|t_1| = t\cos(\gamma/2) \sim 0.192t$. Hence, a rough approximation of the optimal energy scale of the effective model in the BOW phase is about one fifth of the tunneling energy t, with a $G_\infty \sim 0.04t$. Besides the effective energy scales, another important consideration is to be made. Along the chapter, we have been concerned about the phases that appear at $\delta = 0$, where the effective staggered flux Φ (6.25) in the triangular model (6.32) is set to π, and the effects of geometric frustration are maximized. In an actual experiment, however, the degree to which δ can be stabilized around zero is technically limited. Hence, the robustness of the dimer order against fluctuations of δ needs to be considered. To this aim, we computed the expected values of the staggered leg current j_{dl} as a function of δ, which are shown in Fig. 6.9(b). As expected, j_{dl} decreases fast as δ departs from zero, or equivalently when Φ departs from π. It is therefore, important that the tunneling t is made large enough, while at the same time keeping the lattice sufficiently deep so that Hamiltonian (6.17) holds. To this end, the choice of atomic species and the lattice configuration are of relevance.

In the remainder of the discussion, we will consider ^{41}K atoms. This bosonic isotope of potassium is indeed a natural choice for the implementation of the model. Its relatively low mass ensures a large recoil energy E_l and thus large values of t, while its fairly wide fine-structure splitting limits to some extent the detrimental effects of spontaneous emission photon scattering from the Raman beams. Remarkably, the ground state of ^{41}K has two internal states connected to $|F = 1, m_F = -1\rangle$ and $|F = 1, m_F = 0\rangle$ at zero magnetic field that can be rendered immune to magnetic field fluctuations at the linear order by setting a strong bias field to an optimal value found in the order

of few hundreds of G. Doing so, δ can be stabilized with an uncertainty below 10^2 Hz [439]. Regarding the lattice configuration, in order to enhance the effective scale it could be convenient to use blue-detuned beams to generate the lattice, instead of the more usual red-detuned configuration, so that the recoil energy scale is increased. By considering the lattice generated by retro-reflected beams ($\theta_l = 0$) of wavelength of $\lambda_l = 532$ nm at a depth of $V = 5E_l$, a tunneling strength of $t/\hbar \simeq 0.0658 E_l/\hbar \simeq 2\pi \times 1126$ Hz is obtained for ^{41}K atoms. According to the discussion above, this translates, at $\Omega = 5t$, to an effective tunneling strength of $|t_1/\hbar| \sim 2\pi \times 216$ Hz. As done in the previous chapters, we will consider Raman beams at the tune-out wavelength, where their contribution to the trapping potential is negligible. For ^{41}K it is found at $\lambda_r = 769$ nm. To generate the required flux $\gamma \simeq 0.877\pi$, the Raman beams need to be angled at $\theta_r = \cos^{-1}(\frac{\gamma}{2\pi}\frac{\lambda_r}{\lambda_l}) \simeq 0.281\pi$, roughly at 50.7° (see the schematic representation of the implementation of synthetic flux ladders in Fig. 2.7 from Sec. 2.3.3). With this choice of parameters, the resulting characteristic scales are comparable to the typical ones in ultracold atoms in optical lattices, and the stability in the δ would be compatible with the full width half maximum of the curve $j_{dl}(\delta)$ shown in Fig. 6.9(b). Finally, the considered Raman coupling strength $\Omega/\hbar = 5t \simeq 2\pi \times 5.6$ kHz is roughly 0.68 times the single-photon recoil frequency of the Raman transition $\omega_r = \frac{4\pi^\hbar}{2m\lambda_r^2} \simeq 2\pi \times 8.2$ kHz. At such a weak coupling regimes, one could expect a lifetime of about 275 ms with 41K atoms in the configuration described [439], which is a about a hundred times larger than the characteristic tunneling times of the effective model. With these prospects, the realization of the effective model appears to be in reach of experiments with ultracold ^{41}K atoms.

To realize the BOW we have also to control with precision the filling factor. Its dimer structure is expected to be critically sensitive to the value of the filling factor at $N/L = 1/2$ (quarter filling of the flux ladder), with particles or holes in excess destroying the gapped phase. Prior to the turning-on of the Raman beams, the system can be efficiently initialized at half-filling by preparing first a Mott insulator at unit filling in a deep lattice of wavelength 1064 nm, with has a lattice spacing of $2a$, to be adiabatically loaded next into the lattice at 532, yielding $N/L = 0.5$. This process can be done robustly with minimal atom losses. In the last step, the intensity of Raman beams would be adiabatically ramped from 0 to the targeted value of Ω. In contrast to the loading of the lattice, significant atom loss can occur along this last preparation step, despite considering relatively long-lived ^{41}K gases. Such atom loss could be overcome by post-selection of the images with the correct filling.

It should be stressed that, a proper optimization of the experimental signature would demand a deeper analysis of the different regimes available. In general, there is a trade off between having larger effective scales and lower losses from photon scattering at smaller Ω, and the robustness of the BOW phase and strength of its signature at larger Ω, and the optimal choice would depend on the specifics of the experiment. Time-dependent simulations of the adiabatic ramp in Ω can be helpful to gain insights on the optimal

ramp times. At the same time, while the ground state for fillings different than one half lose their insulating nature, it would be worth investigating the response of the dimer state following quenches in the filling factor, to determine whether relevant information can be extracted from samples where atoms are lost. Similarly, the probing of the dynamics after a quench ramp in the intra-leg tunnelings Ω, instead of an adiabatic one, could be explored for indirect signatures of the phases, as discussed in [440] for different regimes of parameters of the flux ladder. These aspects could be relevant in order to determine the limiting factors and optimal parameters of the experiment. Beyond these numerical studies, several options could be investigated to overcome the main limitations. One could consider the realization of the model in ^{87}Rb instead, which has a significantly larger fine structure splitting, and the lifetime of the Raman-dressed gas can be extended several times longer than with ^{41}K. However, the extended lifetime would come at the expenses of a reduced recoil energy scale. Also, the regime where the Zeeman split becomes insensitive to the magnetic field variations at first order is not accessible with ^{87}Rb, and harder efforts should be made to mitigate the fluctuations in δ. In this regard, a possibility would be to use dynamical decoupling [441]. Another direction that could be worth exploring is the possibility of using a blue Raman scheme with ^{41}K [442], where the targeted excited states in the next electronic level manifold have a linewidth that is approximately five times smaller [442].

6.6 Conclusions

In this chapter we have investigated the emergence of frustrated quantum phases in a Raman-dressed Bose gas loaded into a one-dimensional optical lattice, which describes a two-leg flux ladder with a synthetic dimension. Being among the simplest systems where magnetic phenomena can be described, flux ladders have been extensively studied. Here we have followed an alternative direction to investigate the system. In the spirit of the previous chapters, we have derived an effective model following a lowest-band truncation of the single-particle Hamiltonian, and later reintroducing the interactions in terms of the lowest-band dressed states. For strong Raman coupling, the resulting effective model describes a two-leg triangular ladder with staggered flux and onsite interactions, which can be tuned over a wide range of parameters by adjusting the intensity, the angle of incidence and the detuning of the Raman beams. Through this identification, we have been able to predict regimes of the flux ladder where the interplay between inter-atomic interactions, the filling factor and geometric frustration may play an important role.

In particular, the HCB limit of the triangular ladder at half filling (quarter filling of the original ladder) describes a frustrated XX Heisenberg spin-$\frac{1}{2}$ chain with NN and NNN interactions, for which a SF, an insulating BOW, and a CSF phase have been described. While this regime is hard to achieve in the original square ladder, we expected the phases to persist in regimes of large enough separation between the bandwidth and the bandgap. We have numerically investigated their realization in the square flux ladder

at quarter filling for both finite interactions and a finite band gap. We have found that, indeed, the three phases persist for a wide range of parameters, and the nature of the phases in the original ladder and their extent has been discussed. The SF and CSF of the triangular model correspond, respectively, to a Meissner and a biased-ladder superfluid phase in the original ladder. In turn, the BOW phase has been shown to correspond to an insulating vortex lattice phase. Remarkably, these phases are identified with current and density structures that could be probed in the Raman-based implementation of the semi-synthetic flux ladder, which offer an alternative way to explore strongly-correlated frustrated magnetic phases in experiments with ultracold atoms. Finally, we have discussed relevant experimental considerations. We have shown that the wide tunability of the semi-synthetic flux ladder allows us to find suitable regimes of parameters where the phases of the effective model can be realized. Possible ways to mitigate the experimental limitation have been suggested, including studying the potential realization of the model in blue Raman schemes with ^{41}K atoms or the use of synthetic clock transitions in longer-lived ^{87}Rb gases.

To conclude, we emphasize that, despite that interacting two-leg bosonic flux ladders have been extensively studied over the last years, the regimes we have addressed here are different than those covered in most of these studies [240, 370–379, 440], typically focusing in regimes with stronger interactions and/or weaker values of the inter-leg tunneling rates. Here, by contrast, we have explored the regime where the inter-leg hopping term is much stronger than both the interactions and the intra-leg hopping energies, and at quarter filling. The appeal of such a regime becomes evident only after the map to a frustrated triangular geometry is made. It is worth noting that the Raman-based implementation of the flux ladder with synthetic dimensions is very convenient, and it naturally invites the exploration of this regime of strong inter-leg couplings. There, these couplings can be easily realized simply by increasing the intensity of the Raman beams without challenging the tight-binding approximation of the optical lattice, while at the same time keeping the scales of the low-energy model sufficiently large. The success of the effective model in predicting many-body phases of the Raman-dressed lattice suggests extending the approach to other, more complex, configurations of semi-synthetic ladders.

CHAPTER 7

Conclusions and outlook

By way of a summary, in this concluding chapter we discuss the main results presented in the dissertation, and outline possible future related research perspectives.

This thesis has been concerned with the study of the interplay between Raman coupling and interatomic interactions in ultracold Bose gases. Over the last decades, Raman dressing has been proven a powerful tool to manipulate the properties of ultracold atomic systems. Most notably, it has been extensively employed to emulate the action of electrostatic and magnetostatic fields on the otherwise neutral atoms, and to engineer spin-orbit-like interactions, two prominent additions to the versatile toolbox available for quantum simulation in this popular platform. Already at the noninteracting level, the engineering of gauge-like phase terms in the gas allows the simulation of phenomena such as the Hall, anomalous Hall and spin-Hall effects. Not surprisingly, then, the interplay between these synthetic forms of static gauge fields and interatomic interactions can give rise to a wealth of interesting phenomena. For instance, the emergence of a novel supersolid-like stripe phase in the gas, that arises from the interplay between synthetic SOC, interatomic interactions and the quantum statistics of bosonic particles, has drawn a significant amount of theoretical and experimental attention. Most notably, the possibility to access strong magnetic field regimes in 2D or quasi-2D strongly interacting systems paves the way, for instance, for the exploration of the topological order of the fractional quantum Hall effect and quantum magnetism with ultracold atoms. Amid the huge body of research devoted to such Raman-dressed atomic gases, this thesis has taken an alternative route and has explored theoretically two regimes where these systems are well described in terms of the interactions of low-energy dressed states. On the one hand, in chapters 3 to 5 we have investigated the emergence and the harnessing of Raman-induced coherent spin-mixing dynamics in weakly-dressed and weakly-interacting spin-1

bulk Bose gases. On the other hand, in chapter 6 we have focused instead on a strongly correlated regime of a Raman-dressed gas. In particular, we have studied the emergence of phenomena in connection to frustrated quantum magnetism in a spin-$\frac{1}{2}$ gas loaded in a one-dimensional optical lattice. In both scenarios we have proceeded in analogous ways. Essentially, we have pursued the derivation of effective truncated models that describe the low-energy physics in which many-body physics of interest is easily identified – the collective spin dynamics in the former and frustrated magnetic regimes in the latter. Through such identifications we have been able to locate the suitable regimes of parameters where the original systems exhibit these phenomena, and explore their potential observability in realistic experimental implementations.

In the block of chapters covering the first of these two regimes, we have shown that spin-symmetric two-body elastic collisions can resonantly couple the low energy dressed states of the Raman-dressed gas in a way that mimics the behavior of non-symmetric spin collisions in spinor gases. These coherent couplings are understood in simple terms as virtual processes where collisions that exchange large momentum are brought into resonance by spin-flipping two-photon Raman processes. Their amplitude, therefore, can be tuned with the intensity of the Raman beams. We have taken two different approaches in order to isolate the nonsymmetric couplings that result from these processes. In chapter 3, we have considered the whole interacting Hamiltonian as a perturbation, and truncated the dynamics to the three lowest single-particle states following a tight-binding-like approximation in momentum space. There, we have discussed a regime where the effective spin-changing processes can dominate the dynamics, acting like atom-pair tunneling processes in a momentum-space three-site Hubbard-like model. With such an approach, however, the experimentally accessible regimes are reduced to the few-particle problem. By contrast, chapter 4 extends the analogy of the dressed gas to an undressed spinor gas with tunable spin interactions to the low energy landscape of the many-body field Hamiltonian. There, we have restricted the system to the low energy solutions of the symmetric part of the many-body Hamiltonian, and considered their perturbative coupling by the nonsymmetric terms that include the spin-mixing processes. Doing so, the system is effectively described by a macroscopic spin degree of freedom, through which the many-body phases of the Raman dressed gas are understood in simple terms. We have used these insights to design two robust protocols to coherently drive the dressed condensate into the elusive ferromagnetic stripe (FS) phase. In chapter 4, we have proposed the preparation of the FS phase in a low-lying excited state following a quasi-adiabatic ramp of the Raman parameters, where the state is prepared via crossing a quantum phase transition of the effective model. In chapter 5, instead, we have proposed a faster and more robust two-step quench scheme that exploits the understanding of the excited-state quantum phases throughout the spectrum of the effective model. Finally, in chapter 5 we have further shown that the spatial properties of the spin-orbit-coupled gas could be exploited to detect an excited-state quantum phase transition that has been recently identified in undressed spinor gas. It is worth mentioning that, while less

practical from an experimental point of view, the approach discussed in chapter 3 could be advantageous when it comes to the observation of the discussed spin-mixing dynamics. In the scheme proposed there, the transverse lattice breaks down the condensate into pockets of few-particles each. Since the characteristic spin-mixing times after a quench scale with the square root of the number of particles, the dynamics is expected to be faster in the fragmented gas than in the bulk gas of chapters 4 and 5. Even higher values of Ω can be chosen without challenging the few-mode picture, which could enhance the spatial correlations in a few-particle striped state. On the other hand, the realization of the spin model in the bulk condensate allows the exploration of quantum phase transitions close to the thermodynamic limit, and to probe the supersolid-like properties of the striped states prepared. In turn, the macroscopic entanglement achieved there could find metrological applications.

Moving away from the weakly-correlated regimes of the Raman-dressed gas, in chapter 6 we have applied the lowest-band recipe to strongly-correlated regimes of the system loaded in a deep optical lattice. In the lattice, the Raman-dressed gas realizes an effective two-leg flux ladder where the spin degree of freedom is interpreted as a synthetic dimension. Similarly as done in the previous chapters, we have considered the many-body Hamiltonian that results from a single-particle lowest-band truncation. We have shown that, for strong Raman coupling, the truncated Hamiltonian effectively describes spinless bosons in a triangular ladder with staggered flux and local interactions. This simple map has facilitated the identification of a regime of parameters of the original square flux ladder where geometric frustration plays an important role. Indeed, in a regime of large separation between the bandwidth and the bandgap scales and intermediate interactions, we have shown that the system at quarter-filling is able to reproduce the phase diagram of a frustrated quantum XX spin model with nearest and next-nearest neighbors interactions, which includes a gapless superfluid (SF), a bond order wave (BOW) insulator and a chiral superfluid (CSF) phase. We have numerically studied the extent of these phases, and found them to persist for a significantly wide range of parameters. The frustrated phases of the triangular model are identified with density and current structures in the flux ladder, thus providing an alternative way to explore such strongly-correlated frustrated magnetic phases in experiments with ultracold atoms. Specifically, the SF and the CSF phases have been identified with a Meissner and a biased-ladder superfluid phases of the flux ladder, and the BOW phase with an insulating vortex crystal that is stabilized at quarter-filling due to the interplay of geometric frustration and interatomic interactions that are strong relative to the single-particle bandwidth. Finally, we have discussed the experimental feasibility of the frustrated model. We have noticed that the use of synthetic dimensions in the flux ladder is crucial for the realization of the phases in regimes that are experimentally accessible, where the rung currents are to be tuned to very large values with the intensity of the Raman beams. That being said, the dimer order is critically dependent on the filling factor. Its detection is thus found to be sensitive to atom losses due to spontaneous photon scattering, albeit that could be overcome

on post-selection.

Outlook and future directions

In broad terms, the thesis has exemplified, with examples in both bulk and lattice Raman-dressed systems, how the use of low-energy effective theories can provide a new understanding of the models in simple terms, and successfully point out phenomena of interest that can be easily overlooked otherwise. Such a recipe is rather generic, and can be useful to investigate a large variety of models with quantum gases of both bosonic and fermionic species, as well as across the different platforms for quantum simulations.

More specific follow-up directions to the results presented in the first block of chapters include a deeper exploration of the dynamical phase transitions in the bulk spin-orbit-coupled gas, and to study thermalization processes therein, such as the appearance of quantum scars. Likewise, it would be worth quantifying the usefulness of the macroscopic entanglement that can be prepared in the quenched protocols described. The properties of the quantum correlations in the system could also be addressed in the few-particle regime discussed in chapter 3. Finally, it would be of interest to explore configurations with nonsymmetric spin interactions and spin sizes, and different regimes of the dressing parameters. For instance, in the spin-$\frac{1}{2}$ strongly coupled gas, an emergent topological gauge theory has been recently identified in terms of the lowest-band dressed states [443].

In regards to the frustrated regimes of the semi-synthetic flux ladder, an immediate follow-up direction could be the design of both realization and detection schemes that may lead to a reduction of the detrimental impact of photon scattering. For instance, the realization of the model in a blue Raman scheme with ^{41}K atoms is expected to reduce the photon scattering relative to the coupling strength. Alternatively, the use of synthetic clock transitions in longer-lived ^{87}Rb gases could be investigated. Likewise, performing time-dependent simulations could shed light on the optimal regimes for preparing the phases of interest, and perhaps help finding indirect, more convenient quench signatures. Beyond addressing these immediate questions, we have seen that the addition of a periodic potential not only grants access to strongly-correlated regimes in the Raman-dressed gas, but the competition of two different scales allows to explore new situations, such as having simultaneously a multi-minima structure of the lowest band and strong Raman coupling. Many direct extensions of the model here investigated could be explored, where more complex configurations of semi-synthetic ladders could be treated in a similar fashion. One obvious direction would be to consider the inclusion of additional spin sites. Likewise, ladders with nonuniform fluxes could be realized by employing two different Raman pairs. The derivation of effective models of dressed particles could be useful to understand these systems, as well as to engineer novel ones.

Bibliography

[1] R. P. Feynman, Int. J. Theor. Phys. **21**, 467 (1982).

[2] S. Lloyd, Science **273**, 1073 (1996).

[3] I. M. Georgescu, S. Ashhab, and F. Nori, Rev. Mod. Phys. **86**, 153 (2014).

[4] S. Trotzky, Y.-A. Chen, A. Flesch, I. P. McCulloch, U. Schollwöck, J. Eisert, and I. Bloch, Nature Phys. **8**, 325 (2012).

[5] J. Eisert, M. Friesdorf, and C. Gogolin, Nature Phys. **11**, 124 (2015).

[6] A. M. Kaufman, M. E. Tai, A. Lukin, M. Rispoli, R. Schittko, P. M. Preiss, and M. Greiner, Science **353**, 794 (2016).

[7] D. A. Abanin, E. Altman, I. Bloch, and M. Serbyn, Rev. Mod. Phys. **91**, 021001 (2019).

[8] M. Cheneau, P. Barmettler, D. Poletti, M. Endres, P. Schauß, T. Fukuhara, C. Gross, I. Bloch, C. Kollath, and S. Kuhr, Nature **481**, 484 (2012).

[9] S. Braun, M. Friesdorf, S. S. Hodgman, M. Schreiber, J. P. Ronzheimer, A. Riera, M. del Rey, I. Bloch, J. Eisert, and U. Schneider, Proc. Natl. Acad. Sci. , 201408861 (2015).

[10] J. Zhang, G. Pagano, P. W. Hess, A. Kyprianidis, P. Becker, H. Kaplan, A. V. Gorshkov, Z.-X. Gong, and C. Monroe, Nature **551**, 601 (2017).

[11] P. Jurcevic, H. Shen, P. Hauke, C. Maier, T. Brydges, C. Hempel, B. P. Lanyon, M. Heyl, R. Blatt, and C. F. Roos, Phys. Rev. Lett. **119**, 080501 (2017).

[12] M. F. Parsons, A. Mazurenko, C. S. Chiu, G. Ji, D. Greif, and M. Greiner, Science **353**, 1253 (2016).

[13] A. Mazurenko, C. S. Chiu, G. Ji, M. F. Parsons, M. Kanász-Nagy, R. Schmidt, F. Grusdt, E. Demler, D. Greif, and M. Greiner, Nature **545**, 462 (2017).

[14] T. A. Hilker, G. Salomon, F. Grusdt, A. Omran, M. Boll, E. Demler, I. Bloch, and C. Gross, Science **357**, 484 (2017).

[15] E. Altman, K. R. Brown, G. Carleo, L. D. Carr, E. Demler, C. Chin, B. DeMarco, S. E. Economou, M. A. Eriksson, K.-M. C. Fu, M. Greiner, K. R. Hazzard, R. G. Hulet, A. J. Kollár, B. L. Lev, M. D. Lukin, R. Ma, X. Mi, S. Misra, C. Monroe, K. Murch, Z. Nazario, K.-K. Ni, A. C. Potter, P. Roushan, M. Saffman, M. Schleier-Smith, I. Siddiqi, R. Simmonds, M. Singh, I. Spielman, K. Temme, D. S. Weiss, J. Vučković, V. Vuletić, J. Ye, and M. Zwierlein, PRX Quantum **2**, 017003 (2021).

[16] F. Arute, K. Arya, R. Babbush, D. Bacon, J. C. Bardin, R. Barends, S. Boixo, M. Broughton, B. B. Buckley, D. A. Buell, B. Burkett, N. Bushnell, Y. Chen, Z. Chen, B. Chiaro, R. Collins, W. Courtney, S. Demura, A. Dunsworth, E. Farhi, A. Fowler, B. Foxen, C. Gidney, M. Giustina, R. Graff, S. Habegger, M. P. Harrigan, A. Ho, S. Hong, T. Huang, W. J. Huggins, L. Ioffe, S. V. Isakov, E. Jeffrey, Z. Jiang, C. Jones, D. Kafri, K. Kechedzhi, J. Kelly, S. Kim, P. V. Klimov, A. Korotkov, F. Kostritsa, D. Landhuis, P. Laptev, M. Lindmark, E. Lucero, O. Martin, J. M. Martinis, J. R. McClean, M. McEwen, A. Megrant, X. Mi, M. Mohseni, W. Mruczkiewicz, J. Mutus, O. Naaman, M. Neeley, C. Neill, H. Neven, M. Y. Niu, T. E. O'Brien, E. Ostby, A. Petukhov, H. Putterman, C. Quintana, P. Roushan, N. C. Rubin, D. Sank, K. J. Satzinger, V. Smelyanskiy, D. Strain, K. J. Sung, M. Szalay, T. Y. Takeshita, A. Vainsencher, T. White, N. Wiebe, Z. J. Yao, P. Yeh, and A. Zalcman, Science **369**, 1084 (2020).

[17] J. I. Cirac and P. Zoller, Nature Phys. **8**, 264 (2012).

[18] J. Clarke and F. K. Wilhelm, Nature **453**, 1031 (2008).

[19] A. A. Houck, H. E. Türeci, and J. Koch, Nature Phys. **8**, 292 (2012).

[20] F. Arute, K. Arya, R. Babbush, D. Bacon, J. C. Bardin, R. Barends, R. Biswas, S. Boixo, F. G. Brandao, D. A. Buell, *et al.*, Nature **574**, 505 (2019).

[21] M. Kjaergaard, M. E. Schwartz, J. Braumüller, P. Krantz, J. I.-J. Wang, S. Gustavsson, and W. D. Oliver, Annual Review of Condensed Matter Physics **11**, 369 (2019).

[22] D. Porras and J. I. Cirac, Phys. Rev. Lett. **92**, 207901 (2004).

[23] K. Kim, M.-S. Chang, S. Korenblit, R. Islam, E. E. Edwards, J. K. Freericks, G.-D. Lin, L.-M. Duan, and C. Monroe, Nature **465**, 590 (2010).

[24] B. P. Lanyon, C. Hempel, D. Nigg, M. Müller, R. Gerritsma, F. Zähringer, P. Schindler, J. T. Barreiro, M. Rambach, G. Kirchmair, M. Hennrich, P. Zoller, R. Blatt, and C. F. Roos, Science **334**, 57 (2011).

[25] R. Blatt and C. F. Roos, Nature Phys. **8**, 277 (2012).

[26] M. Saffman, T. G. Walker, and K. Mølmer, Rev. Mod. Phys. **82**, 2313 (2010).

[27] H. Bernien, S. Schwartz, A. Keesling, H. Levine, A. Omran, H. Pichler, S. Choi, A. S. Zibrov, M. Endres, M. Greiner, V. Vuletić, and M. D. Lukin, Nature **551**, 579 (2017).

[28] S. de Léséleuc, V. Lienhard, P. Scholl, D. Barredo, S. Weber, N. Lang, H. P. Büchler, T. Lahaye, and A. Browaeys, Science **365**, 775 (2019).

[29] I. Bloch, J. Dalibard, and S. Nascimbene, Nature Phys. **8**, 267 (2012).

[30] M. Lewenstein, A. Sanpera, and V. Ahufinger, *Ultracold Atoms in Optical Lattices: Simulating quantum many-body systems* (Oxford University Press, 2012).

[31] C. Gross and I. Bloch, Science **357**, 995 (2017).

[32] P. Hauke, F. M. Cucchietti, L. Tagliacozzo, I. Deutsch, and M. Lewenstein, Rep. Prog. Phys. **75**, 082401 (2012).

[33] D. Leibfried, Nature **463**, 608 (2010).

[34] H. Q. Lin, Phys. Rev. B **42**, 6561 (1990).

[35] R. Orús, Annals of Physics **349**, 117 (2014).

[36] U. Schollwöck, Annals of Physics **326**, 96 (2011), january 2011 Special Issue.

[37] F. Verstraete and J. I. Cirac, Phys. Rev. B **73**, 094423 (2006).

[38] L. Pitaevski and S. Stringari, *Bose-Einstein Condensation and Superfluidity* (Oxford University Press, 2016).

[39] R. G. Parr, Annual Review of Physical Chemistry **34**, 631 (1983).

[40] W. M. C. Foulkes, L. Mitas, R. J. Needs, and G. Rajagopal, Rev. Mod. Phys. **73**, 33 (2001).

[41] D. Deutsch, Proceedings of the Royal Society of London. A. Mathematical and Physical Sciences **400**, 97 (1985).

[42] J. Preskill, "Quantum computing 40 years later," (2021), arXiv:2106.10522 [quant-ph] .

[43] C. L. Degen, F. Reinhard, and P. Cappellaro, Rev. Mod. Phys. **89**, 035002 (2017).

[44] V. Giovannetti, S. Lloyd, and L. Maccone, Science **306**, 1330 (2004).

[45] V. Giovannetti, S. Lloyd, and L. Maccone, Nature Photon. **5**, 222 (2011).

[46] L. Pezze' and A. Smerzi, "Quantum theory of phase estimation," (2014), arXiv:1411.5164 [quant-ph] .

[47] N. Gisin, G. Ribordy, W. Tittel, and H. Zbinden, Rev. Mod. Phys. **74**, 145 (2002).

[48] V. Scarani, H. Bechmann-Pasquinucci, N. J. Cerf, M. Dušek, N. Lütkenhaus, and M. Peev, Rev. Mod. Phys. **81**, 1301 (2009).

[49] C. Cohen-Tannoudji, Physics Reports **219**, 153 (1992).

[50] W. Ketterle and N. V. Druten, Advances In Atomic, Molecular, and Optical Physics, **37**, 181 (1996).

[51] S. Hofferberth, I. Lesanovsky, B. Fischer, T. Schumm, and J. Schmiedmayer, Nature **449**, 324 (2007).

[52] A. Polkovnikov, K. Sengupta, A. Silva, and M. Vengalattore, Rev. Mod. Phys. **83**, 863 (2011).

[53] F. Schäfer, T. Fukuhara, S. Sugawa, Y. Takasu, and Y. Takahashi, Nature Rev. Phys. **2**, 411 (2020).

[54] A. Görlitz, J. M. Vogels, A. E. Leanhardt, C. Raman, T. L. Gustavson, J. R. Abo-Shaeer, A. P. Chikkatur, S. Gupta, S. Inouye, T. Rosenband, and W. Ketterle, Phys. Rev. Lett. **87**, 130402 (2001).

[55] H. Moritz, T. Stöferle, M. Köhl, and T. Esslinger, Phys. Rev. Lett. **91**, 250402 (2003).

[56] C. Becker, P. Soltan-Panahi, J. Kronjäger, S. Dörscher, K. Bongs, and K. Sengstock, New J. Phys. **12**, 065025 (2010).

[57] L. Tarruell, D. Greif, T. Uehlinger, G. Jotzu, and T. Esslinger, Nature **483**, 302 (2012).

[58] G.-B. Jo, J. Guzman, C. K. Thomas, P. Hosur, A. Vishwanath, and D. M. Stamper-Kurn, Phys. Rev. Lett. **108**, 045305 (2012).

[59] S. Taie, H. Ozawa, T. Ichinose, T. Nishio, S. Nakajima, and Y. Takahashi, Science Advances **1**, e1500854 (2015).

[60] S. Inouye, M. Andrews, J. Stenger, H.-J. Miesner, D. M. Stamper-Kurn, and W. Ketterle, Nature **392**, 151 (1998).

[61] J. L. Roberts, N. R. Claussen, J. P. Burke, C. H. Greene, E. A. Cornell, and C. E. Wieman, Phys. Rev. Lett. **81**, 5109 (1998).

[62] P. O. Fedichev, Y. Kagan, G. V. Shlyapnikov, and J. T. M. Walraven, Phys. Rev. Lett. **77**, 2913 (1996).

[63] M. Theis, G. Thalhammer, K. Winkler, M. Hellwig, G. Ruff, R. Grimm, and J. H. Denschlag, Phys. Rev. Lett. **93**, 123001 (2004).

[64] I. Bloch, J. Dalibard, and W. Zwerger, Rev. Mod. Phys. **80**, 885 (2008).

[65] M. Lewenstein, A. Sanpera, V. Ahufinger, B. Damski, A. Sen(De), and U. Sen, Adv. Phys. **56**, 243 (2007).

[66] L. Tarruell and L. Sanchez-Palencia, Comptes Rendus Physique **19**, 365 (2018).

[67] I. Bloch, J. Dalibard, and W. Zwerger, Rev. Mod. Phys. **80**, 885 (2008).

[68] C. A. Regal, M. Greiner, and D. S. Jin, Phys. Rev. Lett. **92**, 040403 (2004).

[69] T. Bourdel, L. Khaykovich, J. Cubizolles, J. Zhang, F. Chevy, M. Teichmann, L. Tarruell, S. J. J. M. F. Kokkelmans, and C. Salomon, Phys. Rev. Lett. **93**, 050401 (2004).

[70] S. Krinner, T. Esslinger, and J.-P. Brantut, J. Condens. Matter Phys. **29**, 343003 (2017).

[71] M. J. H. Ku, A. T. Sommer, L. W. Cheuk, and M. W. Zwierlein, Science **335**, 563 (2012).

[72] T. Langen, S. Erne, R. Geiger, B. Rauer, T. Schweigler, M. Kuhnert, W. Rohringer, I. E. Mazets, T. Gasenzer, and J. Schmiedmayer, Science **348**, 207 (2015).

[73] L. Pezzè, A. Smerzi, M. K. Oberthaler, R. Schmied, and P. Treutlein, Rev. Mod. Phys. **90**, 035005 (2018).

[74] M. C. Bañuls, R. Blatt, J. Catani, A. Celi, J. I. Cirac, M. Dalmonte, L. Fallani, K. Jansen, M. Lewenstein, S. Montangero, *et al.*, Euro. Phys. J. D **74**, 1 (2020).

[75] E. Zohar, J. I. Cirac, and B. Reznik, Rep. Prog. Phys. **79**, 014401 (2015).

[76] M. Aidelsburger, L. Barbiero, A. Bermudez, T. Chanda, A. Dauphin, D. González-Cuadra, P. R. Grzybowski, S. Hands, F. Jendrzejewski, J. Jünemann, *et al.*, Phil. Trans. R. Soc. A. **380**, 20210064 (2022).

[77] C. Schweizer, F. Grusdt, M. Berngruber, L. Barbiero, E. Demler, N. Goldman, I. Bloch, and M. Aidelsburger, Nature Phys. **15**, 1168 (2019).

[78] A. Mil, T. V. Zache, A. Hegde, A. Xia, R. P. Bhatt, M. K. Oberthaler, P. Hauke, J. Berges, and F. Jendrzejewski, Science **367**, 1128 (2020).

[79] B. Yang, H. Sun, R. Ott, H.-Y. Wang, T. V. Zache, J. C. Halimeh, Z.-S. Yuan, P. Hauke, and J.-W. Pan, Nature **587**, 392 (2020).

[80] A. L. Fetter, Rev. Mod. Phys. **81**, 647 (2009).

[81] K. W. Madison, F. Chevy, W. Wohlleben, and J. Dalibard, Phys. Rev. Lett. **84**, 806 (2000).

[82] J. R. Abo-Shaeer, C. Raman, J. M. Vogels, and W. Ketterle, Science **292**, 476 (2001).

[83] M. W. Zwierlein, J. R. Abo-Shaeer, A. Schirotzek, C. H. Schunck, and W. Ketterle, Nature **435**, 1047 (2005).

[84] J. Dalibard, F. Gerbier, G. Juzeliūnas, and P. Öhberg, Rev. Mod. Phys. **83**, 1523 (2011).

[85] N. Goldman, G. Juzeliūnas, P. Öhberg, and I. B. Spielman, Rep. Prog. Phys. **77**, 126401 (2014).

[86] Y.-J. Lin, R. L. Compton, K. Jiménez-García, J. V. Porto, and I. B. Spielman, Nature **462**, 628 (2009).

[87] A. Eckardt, Rev. Mod. Phys. **89**, 011004 (2017).

[88] M. Aidelsburger, M. Atala, M. Lohse, J. T. Barreiro, B. Paredes, and I. Bloch, Phys. Rev. Lett. **111**, 185301 (2013).

[89] H. Miyake, G. A. Siviloglou, C. J. Kennedy, W. C. Burton, and W. Ketterle, Phys. Rev. Lett. **111**, 185302 (2013).

[90] D. Jaksch and P. Zoller, New J. Phys. **5**, 56 (2003).

[91] M. Aidelsburger, M. Atala, S. Nascimbène, S. Trotzky, Y.-A. Chen, and I. Bloch, Phys. Rev. Lett. **107**, 255301 (2011).

[92] O. Boada, A. Celi, J. I. Latorre, and M. Lewenstein, Phys. Rev. Lett. **108**, 133001 (2012).

[93] A. Celi, P. Massignan, J. Ruseckas, N. Goldman, I. Spielman, G. Juzeliūnas, and M. Lewenstein, Phys. Rev. Lett. **112**, 043001 (2014).

[94] B. K. Stuhl, H.-I. Lu, L. M. Aycock, D. Genkina, and I. B. Spielman, Science **349**, 1514 (2015).

[95] M. Mancini, G. Pagano, G. Cappellini, L. Livi, M. Rider, J. Catani, C. Sias, P. Zoller, M. Inguscio, M. Dalmonte, and L. Fallani, Science **349**, 1510 (2015).

[96] D. Genkina, L. M. Aycock, H.-I. Lu, M. Lu, A. M. Pineiro, and I. Spielman, New J. Phys. **21**, 053021 (2019).

[97] D. R. Hofstadter, Phys. Rev. B **14**, 2239 (1976).

[98] M. Aidelsburger, M. Lohse, C. Schweizer, M. Atala, J. T. Barreiro, S. Nascimbène, N. Cooper, I. Bloch, and N. Goldman, Nature Phys. **11**, 162 (2015).

[99] M. Lohse, C. Schweizer, O. Zilberberg, M. Aidelsburger, and I. Bloch, Nature Phys. **12**, 350 (2016).

[100] S. Nakajima, T. Tomita, S. Taie, T. Ichinose, H. Ozawa, L. Wang, M. Troyer, and Y. Takahashi, Nature Phys. **12**, 296 (2016).

[101] N. R. Cooper, J. Dalibard, and I. B. Spielman, Rev. Mod. Phys. **91**, 015005 (2019).

[102] G. Jotzu, M. Messer, R. Desbuquois, M. Lebrat, T. Uehlinger, D. Greif, and T. Esslinger, Nature **515**, 237 (2014).

[103] F. D. M. Haldane, Phys. Rev. Lett. **61**, 2015 (1988).

[104] Y.-J. Lin, K. Jiménez-García, and I. B. Spielman, Nature **471**, 83 (2011).

[105] P. Wang, Z.-Q. Yu, Z. Fu, J. Miao, L. Huang, S. Chai, H. Zhai, and J. Zhang, Phys. Rev. Lett. **109**, 095301 (2012).

[106] L. W. Cheuk, A. T. Sommer, Z. Hadzibabic, T. Yefsah, W. S. Bakr, and M. W. Zwierlein, Phys. Rev. Lett. **109**, 095302 (2012).

[107] J. Li, W. Huang, B. Shteynas, S. Burchesky, F. Ç. Top, E. Su, J. Lee, A. O. Jamison, and W. Ketterle, Phys. Rev. Lett. **117**, 185301 (2016).

[108] J.-R. Li, J. Lee, W. Huang, S. Burchesky, B. Shteynas, F. Ç. Top, A. O. Jamison, and W. Ketterle, Nature **543**, 91 (2017).

[109] J. Sinova, D. Culcer, Q. Niu, N. A. Sinitsyn, T. Jungwirth, and A. H. MacDonald, Phys. Rev. Lett. **92**, 126603 (2004).

[110] M. Z. Hasan and C. L. Kane, Rev. Mod. Phys. **82**, 3045 (2010).

[111] X.-L. Qi and S.-C. Zhang, Rev. Mod. Phys. **83**, 1057 (2011).

[112] M. Sato and Y. Ando, Rep. Prog. Phys. **80**, 076501 (2017).

[113] V. Galitski and I. B. Spielman, Nature **494**, 49 (2013).

[114] H. Zhai, Rep. Prog. Phys. **78**, 026001 (2015).

[115] C. Wang, C. Gao, C.-M. Jian, and H. Zhai, Phys. Rev. Lett. **105**, 160403 (2010).

[116] R. A. Williams, L. J. LeBlanc, K. Jimenez-Garcia, M. C. Beeler, A. R. Perry, W. D. Phillips, and I. B. Spielman, Science **335**, 314 (2012).

[117] R. A. Williams, M. C. Beeler, L. J. LeBlanc, K. Jiménez-García, and I. B. Spielman, Phys. Rev. Lett. **111**, 095301 (2013).

[118] D. L. Campbell, R. M. Price, A. Putra, A. Valdés-Curiel, D. Trypogeorgos, and I. B. Spielman, Nature Revmun. **7**, 10897 (2016).

[119] M. Boninsegni and N. V. Prokof'ev, Rev. Mod. Phys. **84**, 759 (2012).

[120] M. Heyl, Rep. Prog. Phys. **81**, 054001 (2018).

[121] P. Cejnar, P. Stránský, M. Macek, and M. Kloc, J. Phys. A: Math. Theor. **54**, 133001 (2021).

[122] J. Cabedo, J. Claramunt, A. Celi, Y. Zhang, V. Ahufinger, and J. Mompart, Phys. Rev. A **100**, 063633 (2019).

[123] J. Cabedo, J. Claramunt, and A. Celi, Phys. Rev. A **104**, L031305 (2021).

[124] J. Cabedo and A. Celi, Phys. Rev. Research **3**, 043215 (2021).

[125] J. Cabedo, J. Claramunt, J. Mompart, V. Ahufinger, and A. Celi, Euro. Phys. J. D **74**, 1 (2020).

[126] W. D. Phillips, Rev. Mod. Phys. **70**, 721 (1998).

[127] C. N. Cohen-Tannoudji, Rev. Mod. Phys. **70**, 707 (1998).

[128] S. Chu, Rev. Mod. Phys. **70**, 685 (1998).

[129] M. H. Anderson, J. R. Ensher, M. R. Matthews, C. E. Wieman, and E. A. Cornell, Science **269**, 198 (1995).

[130] K. B. Davis, M. O. Mewes, M. R. Andrews, N. J. van Druten, D. S. Durfee, D. M. Kurn, and W. Ketterle, Phys. Rev. Lett. **75**, 3969 (1995).

[131] C. C. Bradley, C. A. Sackett, J. J. Tollett, and R. G. Hulet, Phys. Rev. Lett. **75**, 1687 (1995).

[132] G. Grynberg, A. Aspect, C. Fabre, and C. Cohen-Tannoudji, *Introduction to Quantum Optics: From the Semi-classical Approach to Quantized Light* (Cambridge University Press, 2010).

[133] D. A. Steck, "Alkali D Line Data," (https://steck.us/alkalidata/).

[134] C. Schwartz, Phys. Rev. **97**, 380 (1955).

[135] P. Juncar, J. Pinard, J. Hamon, and A. Chartier, Metrologia **17**, 77 (1981).

[136] H. J. Metcalf and P. Van der Straten, *CRC Handbook of Chemistry and Physics*, 84th ed. (CRC Press, Boca Raton, 2003).

[137] N. N. Klausen, J. L. Bohn, and C. H. Greene, Phys. Rev. A **64**, 053602 (2001).

[138] E. Brion, L. H. Pedersen, and K. Mølmer, Journal of Physics A: Mathematical and Theoretical **40**, 1033 (2007).

[139] H.-I. Yoo and J. Eberly, Physics Reports **118**, 239 (1985).

[140] D. Walls and G. Milburn, *Quantum Optics* (Springer, 2008).

[141] R. Grimm, M. Weidemüller, and Y. B. Ovchinnikov, Advances In Atomic, Molecular, and Optical Physics, **42**, 95 (2000).

[142] D. E. Pritchard, Phys. Rev. Lett. **51**, 1336 (1983).

[143] H. J. Metcalf and P. Van der Straten, *Laser cooling and trapping of neutral atoms* (Springer-Verlag New York, 1999).

[144] S. K. Schnelle, E. D. van Ooijen, M. J. Davis, N. R. Heckenberg, and H. Rubinsztein-Dunlop, Opt. Express **16**, 1405 (2008).

[145] K. Henderson, C. Ryu, C. MacCormick, and M. G. Boshier, New. J. Phys. **11**, 043030 (2009).

[146] D. M. Stamper-Kurn, M. R. Andrews, A. P. Chikkatur, S. Inouye, H.-J. Miesner, J. Stenger, and W. Ketterle, Phys. Rev. Lett. **80**, 2027 (1998).

[147] D. M. Stamper-Kurn and M. Ueda, Rev. Mod. Phys. **85**, 1191 (2013).

[148] B. Arora, M. S. Safronova, and C. W. Clark, Phys. Rev. A **84**, 043401 (2011).

[149] T. Hänsch and A. Schawlow, Optics Communications **13**, 68 (1975).

[150] P. D. Lett, W. D. Phillips, S. L. Rolston, C. E. Tanner, R. N. Watts, and C. I. Westbrook, J. Opt. Soc. Am. B **6**, 2084 (1989).

[151] W. D. Phillips and H. Metcalf, Phys. Rev. Lett. **48**, 596 (1982).

[152] E. L. Raab, M. Prentiss, A. Cable, S. Chu, and D. E. Pritchard, Phys. Rev. Lett. **59**, 2631 (1987).

[153] Y. Castin, H. Wallis, and J. Dalibard, Journal of the Optical Society of America B **6**, 2046 (1989).

[154] J. Dalibard and C. Cohen-Tannoudji, J. Opt. Soc. Am. B **6**, 2023 (1989).

[155] C. N. Cohen-Tannoudji and W. D. Phillips, Physics Today **43**, 33 (1990).

[156] P. D. Lett, R. N. Watts, C. I. Westbrook, W. D. Phillips, P. L. Gould, and H. J. Metcalf, Phys. Rev. Lett. **61**, 169 (1988).

[157] D. C. Aveline, J. R. Williams, E. R. Elliott, C. Dutenhoffer, J. R. Kellogg, J. M. Kohel, N. E. Lay, K. Oudrhiri, R. F. Shotwell, N. Yu, *et al.*, Nature **582**, 193 (2020).

[158] E. A. Cornell and C. E. Wieman, Rev. Mod. Phys. **74**, 875 (2002).

[159] W. Ketterle, Rev. Mod. Phys. **74**, 1131 (2002).

[160] J. Dalibard, in *Bose-Einstein Condensation in Atomic Gases* (IOS Press, 1999) pp. 321–349.

[161] T.-L. Ho, Phys. Rev. Lett. **81**, 742 (1998).

[162] Y. Kawaguchi and M. Ueda, Phys. Rep. **520**, 253 (2012).

[163] W. Pauli, Phys. Rev. **58**, 716 (1940).

[164] V. S. Shchesnovich, "The second quantization method for indistinguishable particles (lecture notes in physics, ufabc 2010)," (2013), arXiv:1308.3275 [cond-mat.quant-gas] .

[165] C. K. Law, H. Pu, and N. P. Bigelow, Phys. Rev. Lett. **81**, 5257 (1998).

[166] U. Schollwöck, Rev. Mod. Phys. **77**, 259 (2005).

[167] S. Stringari, Comptes Rendus de l'Académie des Sciences - Series IV - Physics **2**, 381 (2001).

[168] E. T. Jaynes, Phys. Rev. **106**, 620 (1957).

[169] F. Dalfovo, S. Giorgini, L. P. Pitaevskii, and S. Stringari, Rev. Mod. Phys. **71**, 463 (1999).

[170] B. DeMarco and D. S. Jin, Science **285**, 1703 (1999).

[171] M. Greiner, C. A. Regal, and D. S. Jin, Nature **426**, 537 (2003).

[172] S. Jochim, M. Bartenstein, A. Altmeyer, G. Hendl, S. Riedl, C. Chin, J. H. Denschlag, and R. Grimm, Science **302**, 2101 (2003).

[173] J. Bardeen, L. N. Cooper, and J. R. Schrieffer, Phys. Rev. **108**, 1175 (1957).

[174] J. R. Ensher, D. S. Jin, M. R. Matthews, C. E. Wieman, and E. A. Cornell, Phys. Rev. Lett. **77**, 4984 (1996).

[175] M.-O. Mewes, M. R. Andrews, N. J. van Druten, D. M. Kurn, D. S. Durfee, and W. Ketterle, Phys. Rev. Lett. **77**, 416 (1996).

[176] E. P. Gross, Il Nuovo Cimento (1955-1965) **20**, 454 (1961).

[177] L. P. Pitaevskii, Sov. Phys. JETP **13**, 451 (1961).

[178] Y. A. Bychkov and E. I. Rashba, Journal of Physics C Solid State Physics **17**, 6039 (1984).

[179] I. Žutić, J. Fabian, and S. Das Sarma, Rev. Mod. Phys. **76**, 323 (2004).

[180] Y.-J. Lin, R. L. Compton, A. R. Perry, W. D. Phillips, J. V. Porto, and I. B. Spielman, Phys. Rev. Lett. **102**, 130401 (2009).

[181] I. B. Spielman, Phys. Rev. A **79**, 063613 (2009).

[182] Y.-J. Lin, R. L. Compton, K. Jimenez-Garcia, W. D. Phillips, J. V. Porto, and I. B. Spielman, Nature Phys. **7**, 531 (2011).

[183] M. Aidelsburger, S. Nascimbene, and N. Goldman, Comptes Rendus Physique **19**, 394 (2018), quantum simulation / Simulation quantique.

[184] X.-J. Liu, M. F. Borunda, X. Liu, and J. Sinova, Phys. Rev. Lett. **102**, 046402 (2009).

[185] T.-L. Ho and S. Zhang, Phys. Rev. Lett. **107**, 150403 (2011).

[186] Y. Li, L. P. Pitaevskii, and S. Stringari, Phys. Rev. Lett. **108**, 225301 (2012).

[187] G. Juzeliūnas, J. Ruseckas, and J. Dalibard, Phys. Rev. A **81**, 053403 (2010).

[188] D. L. Campbell, G. Juzeliūnas, and I. B. Spielman, Phys. Rev. A **84**, 025602 (2011).

[189] G. I. Martone, Y. Li, L. P. Pitaevskii, and S. Stringari, Phys. Rev. A **86**, 063621 (2012).

[190] B. M. Anderson, G. Juzeliūnas, V. M. Galitski, and I. B. Spielman, Phys. Rev. Lett. **108**, 235301 (2012).

[191] B. M. Anderson, I. B. Spielman, and G. Juzeliūnas, Phys. Rev. Lett. **111**, 125301 (2013).

[192] Y. Li, G. I. Martone, L. P. Pitaevskii, and S. Stringari, Phys. Rev. Lett. **110**, 235302 (2013).

[193] W. Zheng, Z.-Q. Yu, X. Cui, and H. Zhai, Journal of Physics B: Atomic, Molecular and Optical Physics **46**, 134007 (2013).

[194] X.-J. Liu, K. T. Law, and T. K. Ng, Phys. Rev. Lett. **112**, 086401 (2014).

[195] Z. Lan and P. Öhberg, Phys. Rev. A **89**, 023630 (2014).

[196] G. I. Martone, F. V. Pepe, P. Facchi, S. Pascazio, and S. Stringari, Phys. Rev. Lett. **117**, 125301 (2016).

[197] B.-Z. Wang, Y.-H. Lu, W. Sun, S. Chen, Y. Deng, and X.-J. Liu, Phys. Rev. A **97**, 011605 (2018).

[198] K. T. Geier, G. I. Martone, P. Hauke, and S. Stringari, Phys. Rev. Lett. **127**, 115301 (2021).

[199] J.-Y. Zhang, S.-C. Ji, Z. Chen, L. Zhang, Z.-D. Du, B. Yan, G.-S. Pan, B. Zhao, Y.-J. Deng, H. Zhai, S. Chen, and J.-W. Pan, Phys. Rev. Lett. **109**, 115301 (2012).

[200] M. C. Beeler, R. A. Williams, K. Jimenez-Garcia, L. J. LeBlanc, A. R. Perry, and I. B. Spielman, Nature **498**, 201 (2013).

[201] C. Hamner, C. Qu, Y. Zhang, J. Chang, M. Gong, C. Zhang, and P. Engels, Nature Revmun. **5**, 1 (2014).

[202] S.-C. Ji, L. Zhang, X.-T. Xu, Z. Wu, Y. Deng, S. Chen, and J.-W. Pan, Phys. Rev. Lett. **114**, 105301 (2015).

[203] C. Hamner, Y. Zhang, M. A. Khamehchi, M. J. Davis, and P. Engels, Phys. Rev. Lett. **114**, 070401 (2015).

[204] Z. Wu, L. Zhang, W. Sun, X.-T. Xu, B.-Z. Wang, S.-C. Ji, Y. Deng, S. Chen, X.-J. Liu, and J.-W. Pan, Science **354**, 83 (2016).

[205] M. Khamehchi, K. Hossain, M. Mossman, Y. Zhang, T. Busch, M. M. Forbes, and P. Engels, Phys. Rev. Lett. **118**, 155301 (2017).

[206] W. Sun, B.-Z. Wang, X.-T. Xu, C.-R. Yi, L. Zhang, Z. Wu, Y. Deng, X.-J. Liu, S. Chen, and J.-W. Pan, Phys. Rev. Lett. **121**, 150401 (2018).

[207] A. Putra, F. Salces-Cárcoba, Y. Yue, S. Sugawa, and I. B. Spielman, Phys. Rev. Lett. **124**, 053605 (2020).

[208] J. Higbie and D. M. Stamper-Kurn, Phys. Rev. Lett. **88**, 090401 (2002).

[209] Y. Zhang, M. E. Mossman, T. Busch, P. Engels, and C. Zhang, Frontiers of Physics **11**, 118103 (2016).

[210] N. Q. Burdick, Y. Tang, and B. L. Lev, Phys. Rev. X **6**, 031022 (2016).

[211] Z. Fu, L. Huang, Z. Meng, P. Wang, L. Zhang, S. Zhang, H. Zhai, P. Zhang, and J. Zhang, Nature Phys. **10**, 110 (2014).

[212] L. Huang, Z. Meng, P. Wang, P. Peng, S.-L. Zhang, L. Chen, D. Li, Q. Zhou, and J. Zhang, Nature Phys. **12**, 540 (2016).

[213] M. Greiner, O. Mandel, T. Esslinger, T. W. Hänsch, and I. Bloch, Nature **415**, 39 (2002).

[214] J. Hubbard, Proceedings of the Royal Society of London. Series A. Mathematical and Physical Sciences **281**, 401 (1964).

[215] A. Altland and B. D. Simons, *Condensed matter field theory* (Cambridge university press, 2010).

[216] P. W. Anderson, Science **235**, 1196 (1987).

[217] W. Hofstetter, J. I. Cirac, P. Zoller, E. Demler, and M. D. Lukin, Phys. Rev. Lett. **89**, 220407 (2002).

[218] P. W. Anderson, P. A. Lee, M. Randeria, T. M. Rice, N. Trivedi, and F. C. Zhang, J. Phys.: Condens. Matter **16**, R755 (2004).

[219] K. L. Hur and T. Maurice Rice, Ann. Phys. **324**, 1452 (2009).

[220] M. P. A. Fisher, P. B. Weichman, G. Grinstein, and D. S. Fisher, Phys. Rev. B **40**, 546 (1989).

[221] S. Sachdev, *Quantum Phase Transitions*, 2nd ed. (Cambridge University Press, Cambridge, England, 2011).

[222] D. Jaksch, C. Bruder, J. I. Cirac, C. W. Gardiner, and P. Zoller, Phys. Rev. Lett. **81**, 3108 (1998).

[223] P. Windpassinger and K. Sengstock, Rep. Prog. Phys. **76**, 086401 (2013).

[224] J. Sebby-Strabley, M. Anderlini, P. S. Jessen, and J. V. Porto, Phys. Rev. A **73**, 033605 (2006).

[225] J. Struck, C. Ölschläger, R. Le Targat, P. Soltan-Panahi, A. Eckardt, M. Lewenstein, P. Windpassinger, and K. Sengstock, Science **333**, 996 (2011).

[226] J. Struck, C. Ölschläger, M. Weinberg, P. Hauke, J. Simonet, A. Eckardt, M. Lewenstein, K. Sengstock, and P. Windpassinger, Phys. Rev. Lett. **108**, 225304 (2012).

[227] N. Fläschner, B. S. Rem, M. Tarnowski, D. Vogel, D.-S. Lühmann, K. Sengstock, and C. Weitenberg, Science **352**, 1091 (2016).

[228] C. Lacroix, P. Mendels, and F. Mila, *Introduction to frustrated magnetism: materials, experiments, theory*, Vol. 164 (Springer Science & Business Media, 2011).

[229] R. A. Hart, P. M. Duarte, T.-L. Yang, X. Liu, T. Paiva, E. Khatami, R. T. Scalettar, N. Trivedi, D. A. Huse, and R. G. Hulet, Nature **519**, 211 (2015).

[230] P. N. Jepsen, J. Amato-Grill, I. Dimitrova, W. W. Ho, E. Demler, and W. Ketterle, Nature **588**, 403 (2020).

[231] D. McKay and B. DeMarco, New J. Phys. **12**, 055013 (2010).

[232] W. S. Bakr, J. I. Gillen, A. Peng, S. Fölling, and M. Greiner, Nature **462**, 74 (2009).

[233] J. F. Sherson, C. Weitenberg, M. Endres, M. Cheneau, I. Bloch, and S. Kuhr, Nature **467**, 68 (2010).

[234] E. Haller, J. Hudson, A. Kelly, D. A. Cotta, B. Peaudecerf, G. D. Bruce, and S. Kuhr, Nature Phys. **11**, 738 (2015).

[235] M. Boll, T. A. Hilker, G. Salomon, A. Omran, J. Nespolo, L. Pollet, I. Bloch, and C. Gross, Science **353**, 1257 (2016).

[236] J. Vijayan, P. Sompet, G. Salomon, J. Koepsell, S. Hirthe, A. Bohrdt, F. Grusdt, I. Bloch, and C. Gross, Science **367**, 186 (2020).

[237] T. Ozawa and H. M. Price, Nature Rev. Phys. **1**, 349–357 (2019).

[238] M. Atala, M. Aidelsburger, M. Lohse, J. T. Barreiro, B. Paredes, and I. Bloch, Nature Phys. **10**, 588 (2014).

[239] M. E. Tai, A. Lukin, M. Rispoli, R. Schittko, T. Menke, D. Borgnia, P. M. Preiss, F. Grusdt, A. M. Kaufman, and M. Greiner, Nature **546**, 519 (2017).

[240] S. Greschner, M. Filippone, and T. Giamarchi, Phys. Rev. Lett. **122**, 083402 (2019).

[241] M. Buser, S. Greschner, U. Schollwöck, and T. Giamarchi, Phys. Rev. Lett. **126**, 030501 (2021).

[242] M. Buser, U. Schollwöck, and F. Grusdt, "Snapshot based characterization of particle currents and the hall response in synthetic flux lattices," (2021), arXiv:2110.14952 [cond-mat.quant-gas] .

[243] O. Boada, A. Celi, J. Rodríguez-Laguna, J. I. Latorre, and M. Lewenstein, New J. Phys. **17**, 045007 (2015).

[244] R. P. Anderson, D. Trypogeorgos, A. Valdés-Curiel, Q.-Y. Liang, J. Tao, M. Zhao, T. Andrijauskas, G. Juzeliūnas, and I. B. Spielman, Phys. Rev. Research **2**, 013149 (2020).

[245] M. Galassi, *GNU Scientific Library Reference Manual*, 3rd ed.

[246] G. R. Dennis, J. J. Hope, and M. T. Johnsson, Comput. Phys. Commun. **184**, 201–208 (2013).

[247] M. Fishman, S. R. White, and E. M. Stoudenmire, "The ITensor Software Library for Tensor Network Calculations," (2020), arXiv:2007.14822 .

[248] T. M. Bersano, J. Hou, S. Mossman, V. Gokhroo, X.-W. Luo, K. Sun, C. Zhang, and P. Engels, Phys. Rev. A **99**, 051602(R) (2019).

[249] L. Tanzi, E. Lucioni, F. Famà, J. Catani, A. Fioretti, C. Gabbanini, R. N. Bisset, L. Santos, and G. Modugno, Phys. Rev. Lett. **122**, 130405 (2019).

[250] F. Böttcher, J.-N. Schmidt, M. Wenzel, J. Hertkorn, M. Guo, T. Langen, and T. Pfau, Phys. Rev. X **9**, 011051 (2019).

[251] L. Chomaz, D. Petter, P. Ilzhöfer, G. Natale, A. Trautmann, C. Politi, G. Durastante, R. M. W. van Bijnen, A. Patscheider, M. Sohmen, M. J. Mark, and F. Ferlaino, Phys. Rev. X **9**, 021012 (2019).

[252] M. A. Khamehchi, Y. Zhang, C. Hamner, T. Busch, and P. Engels, Phys. Rev. A **90**, 063624 (2014).

[253] G. F. Dresselhaus and M. S. Dresselhaus, Carbon **3**, 325 (1965).

[254] L. F. Livi, G. Cappellini, M. Diem, L. Franchi, C. Clivati, M. Frittelli, F. Levi, D. Calonico, J. Catani, M. Inguscio, and L. Fallani, Phys. Rev. Lett. **117**, 220401 (2016).

[255] S. Kolkowitz, S. L. Bromley, T. Bothwell, M. L. Wall, G. E. Marti, A. Koller, X. Zhang, A. M. Rey, and J. Ye, Nature **542**, 66 (2017).

[256] D. S. Petrov, Phys. Rev. Lett. **115**, 155302 (2015).

[257] C. R. Cabrera, L. Tanzi, J. Sanz, B. Naylor, P. Thomas, P. Cheiney, and L. Tarruell, Science **359**, 301 (2018).

[258] P. Cheiney, C. R. Cabrera, J. Sanz, B. Naylor, L. Tanzi, and L. Tarruell, Phys. Rev. Lett. **120**, 135301 (2018).

[259] G. Semeghini, G. Ferioli, L. Masi, C. Mazzinghi, L. Wolswijk, F. Minardi, M. Modugno, G. Modugno, M. Inguscio, and M. Fattori, Phys. Rev. Lett. **120**, 235301 (2018).

[260] H. Kadau, M. Schmitt, M. Wenzel, C. Wink, T. Maier, I. Ferrier-Barbut, and T. Pfau, Nature **530**, 194 (2016).

[261] M. Schmitt, M. Wenzel, F. Böttcher, I. Ferrier-Barbut, and T. Pfau, Nature **539**, 259 (2016).

[262] L. Chomaz, S. Baier, D. Petter, M. J. Mark, F. Wächtler, L. Santos, and F. Ferlaino, Phys. Rev. X **6**, 041039 (2016).

[263] J. Higbie and D. M. Stamper-Kurn, Phys. Rev. A **69**, 053605 (2004).

[264] B. Gadway, Phys. Rev. A **92**, 043606 (2015).

[265] E. J. Meier, F. A. An, and B. Gadway, Phys. Rev. A **93**, 051602(R) (2016).

[266] F. A. An, E. J. Meier, and B. Gadway, Science Advances **3** (2017), 10.1126/sciadv.1602685.

[267] E. J. Meier, F. A. An, A. Dauphin, M. Maffei, P. Massignan, T. L. Hughes, and B. Gadway, Science **362**, 929 (2018).

[268] F. A. An, E. J. Meier, J. Ang'ong'a, and B. Gadway, Phys. Rev. Lett. **120**, 040407 (2018).

[269] T.-L. Ho, Phys. Rev. Lett. **81**, 742 (1998).

[270] C. J. Myatt, N. R. Newbury, R. W. Ghrist, S. Loutzenhiser, and C. E. Wieman, Optics Letters **21**, 290 (1996).

[271] Q. Zhu, Q. Zhang, and B. Wu, Journal of Physics B Atomic Molecular and Optical Physics **48**, 045301 (2015).

[272] L.-M. Duan, A. Sørensen, J. I. Cirac, and P. Zoller, Phys. Rev. Lett. **85**, 3991 (2000).

[273] C. Klempt, O. Topic, G. Gebreyesus, M. Scherer, T. Henninger, P. Hyllus, W. Ertmer, L. Santos, and J. J. Arlt, Phys. Rev. Lett. **104**, 195303 (2010).

[274] E. M. Bookjans, C. D. Hamley, and M. S. Chapman, Phys. Rev. Lett. **107**, 210406 (2011).

[275] B. Lücke, M. Scherer, J. Kruse, L. Pezzé, F. Deuretzbacher, P. Hyllus, O. Topic, J. Peise, W. Ertmer, J. Arlt, L. Santos, A. Smerzi, and C. Klempt, Science **334**, 773 (2011).

[276] C. Gross, H. Strobel, E. Nicklas, T. Zibold, N. Bar-Gill, G. Kurizki, and M. K. Oberthaler, Nature **480**, 219 (2011).

[277] C. D. Hamley, C. S. Gerving, T. M. Hoang, E. M. Bookjans, and M. S. Chapman, Nature Phys. **8**, 305 (2012).

[278] Z. Zhang and L.-M. Duan, Phys. Rev. Lett. **111**, 180401 (2013).

[279] M. Gabbrielli, L. Pezzè, and A. Smerzi, Phys. Rev. Lett. **115**, 163002 (2015).

[280] I. Peise, J.and Kruse, K. Lange, B. Lücke, L. Pezzè, J. Arlt, W. Ertmer, K. Hammerer, L. Santos, A. Smerzi, and C. Klempt, Nature Revmun. **6**, 8984 (2015).

[281] T. M. Hoang, H. M. Bharath, M. J. Boguslawski, M. Anquez, B. A. Robbins, and M. S. Chapman, Proc. Natl. Acad. Sci. U. S. A. **113**, 9475—9479 (2016).

[282] X.-Y. Luo, Y.-Q. Zou, L.-N. Wu, Q. Liu, M.-F. Han, M. K. Tey, and L. You, Science **355**, 620 (2017).

[283] Y.-Q. Zou, L.-N. Wu, Q. Liu, X.-Y. Luo, S.-F. Guo, J.-H. Cao, M. K. Tey, and L. You, PNAS **115**, 6381 (2018).

[284] P. Kunkel, M. Prüfer, H. Strobel, D. Linnemann, A. Frölian, T. Gasenzer, M. Gärttner, and M. K. Oberthaler, Science **360**, 413 (2018).

[285] L. Pezzè, M. Gessner, P. Feldmann, C. Klempt, L. Santos, and A. Smerzi, Phys. Rev. Lett. **123**, 260403 (2019).

[286] J. Lian, L. Yu, J.-Q. Liang, G. Chen, and S. Jia, Sci. Rep. **3**, 3166 (2013).

[287] Y. Huang and Z.-D. Hu, Sci. Rep. **5**, 8006 (2015).

[288] X. Y. Huang, F. X. Sun, W. Zhang, Q. Y. He, and C. P. Sun, Phys. Rev. A **95**, 013605 (2017).

[289] L. Chen, Y. Zhang, and H. Pu, Phys. Rev. A **102**, 023317 (2020).

[290] D. Lao, C. Raman, and C. A. R. S. de Melo, Phys. Rev. Lett. **124**, 173203 (2020).

[291] D. Rubeni, J. Links, P. S. Isaac, and A. Foerster, Phys. Rev. A **95**, 043607 (2017).

[292] D. Agboola, P. S. Isaac, and J. Links, J. Phys. B: At. Mol. Opt. Phys. **51**, 145301 (2018).

[293] O. Penrose and L. Onsager, Phys. Rev. **104**, 576 (1956).

[294] E. J. Mueller, T.-L. Ho, M. Ueda, and G. Baym, Phys. Rev. A **74**, 033612 (2006).

[295] W. Zhang, D. L. Zhou, M.-S. Chang, M. S. Chapman, and L. You, Phys. Rev. A **72**, 013602 (2005).

[296] M.-S. Chang, Q. Qin, W. Zhang, L. You, and M. S. Chapman, Nature Phys. **1**, 111 (2005).

[297] H.-X. Yang, T. Tian, Y.-B. Yang, L.-Y. Qiu, H.-Y. Liang, A.-J. Chu, C. B. Dağ, Y. Xu, Y. Liu, and L.-M. Duan, Phys. Rev. A **100**, 013622 (2019).

[298] T. Tian, H.-X. Yang, L.-Y. Qiu, H.-Y. Liang, Y.-B. Yang, Y. Xu, and L.-M. Duan, Phys. Rev. Lett. **124**, 043001 (2020).

[299] X.-T. Xu, Z.-Y. Wang, R.-H. Jiao, C.-R. Yi, W. Sun, and S. Chen, Rev. Sci. Instrum. **90**, 054708 (2019).

[300] J. Stenger, S. Inouye, D. M. Stamper-Kurn, H.-J. Miesner, A. P. Chikkatur, and W. Ketterle, Nature **396**, 345 (1998).

[301] L. E. Sadler, J. M. Higbie, S. R. Leslie, M. Vengalattore, and D. M. Stamper-Kurn, Nature **443**, 312 (2006).

[302] E. M. Bookjans, A. Vinit, and C. Raman, Phys. Rev. Lett. **107**, 195306 (2011).

[303] A. Vinit, E. M. Bookjans, C. A. R. S. de Melo, and C. Raman, Phys. Rev. Lett. **110**, 165301 (2013).

[304] T. M. Hoang, M. Anquez, B. A. Robbins, X. Y. Yang, B. J. Land, C. D. Hamley, and M. S. Chapman, Nature Commun. **7**, 11233 (2016).

[305] M. Anquez, B. A. Robbins, H. M. Bharath, M. Boguslawski, T. M. Hoang, and M. S. Chapman, Phys. Rev. Lett. **116**, 155301 (2016).

[306] M. Prüfer, P. Kunkel, H. Strobel, S. Lannig, D. Linnemann, C.-M. Schmied, J. Berges, T. Gasenzer, and M. K. Oberthaler, Nature **563**, 217 (2018).

[307] Z. Chen, T. Tang, J. Austin, Z. Shaw, L. Zhao, and Y. Liu, Phys. Rev. Lett. **123**, 113002 (2019).

[308] S. Kang, S. W. Seo, H. Takeuchi, and Y. Shin, Phys. Rev. Lett. **122**, 095301 (2019).

[309] K. Jiménez-García, A. Invernizzi, B. Evrard, C. Frapolli, J. Dalibard, and F. Gerbier, Nature Commun. **10**, 1422 (2019).

[310] M. Prüfer, T. V. Zache, P. Kunkel, S. Lannig, A. Bonnin, H. Strobel, J. Berges, and M. K. Oberthaler, Nature Phys. **16**, 1012 (2020).

[311] A. Qu, B. Evrard, J. Dalibard, and F. Gerbier, Phys. Rev. Lett. **125**, 033401 (2020).

[312] L. Tarruell, "Engineering chiral solitons and density-dependent gauge fields in raman-coupled Bose-Einstein condensates," (2020), online talk.

[313] J. Hou, X.-W. Luo, K. Sun, T. Bersano, V. Gokhroo, S. Mossman, P. Engels, and C. Zhang, Phys. Rev. Lett. **120**, 120401 (2018).

[314] G. V. Chester, Phys. Rev. A **2**, 256 (1970).

[315] A. J. Leggett, Phys. Rev. Lett. **25**, 1543 (1970).

[316] L. Tanzi, E. Lucioni, F. Famà, J. Catani, A. Fioretti, C. Gabbanini, R. N. Bisset, L. Santos, and G. Modugno, Phys. Rev. Lett. **122**, 130405 (2019).

[317] F. Böttcher, J.-N. Schmidt, M. Wenzel, J. Hertkorn, M. Guo, T. Langen, and T. Pfau, Phys. Rev. X **9**, 011051 (2019).

[318] L. Chomaz, D. Petter, P. Ilzhöfer, G. Natale, A. Trautmann, C. Politi, G. Durastante, R. M. W. van Bijnen, A. Patscheider, M. Sohmen, M. J. Mark, and F. Ferlaino, Phys. Rev. X **9**, 021012 (2019).

[319] J. Hofmann and W. Zwerger, Journal of Statistical Mechanics: Theory and Experiment **2021**, 033104 (2021).

[320] S. Yi, O. E. Müstecaplıoğlu, C. P. Sun, and L. You, Phys. Rev. A **66**, 011601 (2002).

[321] M. Kitagawa and M. Ueda, Phys. Rev. A **47**, 5138 (1993).

[322] C. B. Dağ, S.-T. Wang, and L.-M. Duan, Phys. Rev. A **97**, 023603 (2018).

[323] P. Feldmann, C. Klempt, A. Smerzi, L. Santos, and M. Gessner, Phys. Rev. Lett. **126**, 230602 (2021).

[324] K. Murata, H. Saito, and M. Ueda, Phys. Rev. A **75**, 013607 (2007).

[325] B. Evrard, A. Qu, J. Dalibard, and F. Gerbier, Phys. Rev. A **103**, L031302 (2021).

[326] R. E. Slusher, L. W. Hollberg, B. Yurke, J. C. Mertz, and J. F. Valley, Phys. Rev. Lett. **55**, 2409 (1985).

[327] S.-F. Guo, F. Chen, Q. Liu, M. Xue, J.-J. Chen, J.-H. Cao, T.-W. Mao, M. K. Tey, and L. You, Phys. Rev. Lett. **126**, 060401 (2021).

[328] T. Chalopin, T. Satoor, A. Evrard, V. Makhalov, J. Dalibard, R. Lopes, and S. Nascimbene, Nature Phys. **16**, 1017 (2020).

[329] F. Anders, A. Idel, P. Feldmann, D. Bondarenko, S. Loriani, K. Lange, J. Peise, M. Gersemann, B. Meyer-Hoppe, S. Abend, N. Gaaloul, C. Schubert, D. Schlippert, L. Santos, E. Rasel, and C. Klempt, Phys. Rev. Lett. **127**, 140402 (2021).

[330] C. Gardiner and P. Zoller, *The Quantum World of Ultra-Cold Atoms and Light Book II: The Physics of Quantum-Optical Devices* (IMPERIAL COLLEGE PRESS, 2015) https://www.worldscientific.com/doi/pdf/10.1142/p983 .

[331] A. Celi, A. Sanpera, V. Ahufinger, and M. Lewenstein, Physica Scripta **92**, 013003 (2017).

[332] R. Ramos, A. Frölian, C. Chisholm, E. Neri, C. Cabrera, A. Celi, and L. Tarruell, Bulletin of the American Physical Society (2021).

[333] M. Vojta, Rep. Prog. Phys. **66**, 2069 (2003).

[334] N. Fläschner, D. Vogel, M. Tarnowski, B. S. Rem, D.-S. Lühmann, M. Heyl, J. C. Budich, L. Mathey, K. Sengstock, and C. Weitenberg, Nature Phys. **14**, 265–268 (2018).

[335] W. Sun, C.-R. Yi, B.-Z. Wang, W.-W. Zhang, B. C. Sanders, X.-T. Xu, Z.-Y. Wang, J. Schmiedmayer, Y. Deng, X.-J. Liu, S. Chen, and J.-W. Pan, Phys. Rev. Lett. **121**, 250403 (2018).

[336] S. Smale, P. He, B. A. Olsen, K. G. Jackson, H. Sharum, S. Trotzky, J. Marino, A. M. Rey, and J. H. Thywissen, Sciences Advances **5**, eaax1568 (2019).

[337] J. A. Muniz, D. Barberena, R. J. Lewis-Swan, D. J. Young, J. R. K. Cline, A. M. Rey, and J. K. Thompson, Nature **580**, 602 (2020).

[338] P. Jurcevic, H. Shen, P. Hauke, C. Maier, T. Brydges, C. Hempel, B. P. Lanyon, M. Heyl, R. Blatt, and C. F. Roos, Phys. Rev. Lett. **119**, 080501 (2017).

[339] J. Zhang, G. Pagano, P. W. Hess, A. Kyprianidis, P. Becker, H. Kaplan, A. V. Gorshkov, Z.-X. Gong, and C. Monroe, Nature **551**, 601 (2017).

[340] K. Xu, Z.-H. Sun, W. Liu, Y.-R. Zhang, H. Li, H. Dong, W. Ren, P. Zhang, F. Nori, D. Zheng, H. Fan, and H. Wang, Sciences Advances **6**, eaba4935 (2020).

[341] F. Leyvraz and W. D. Heiss, Phys. Rev. Lett. **95**, 050402 (2005).

[342] P. Ribeiro, J. Vidal, and R. Mosseri, Phys. Rev. Lett. **99**, 050402 (2007).

[343] M. Caprio, P. Cejnar, and F. Iachello, Ann. Phys. (N. Y.) **323**, 1106 (2008).

[344] D. Larese, F. Pérez-Bernal, and F. Iachello, J. Mol. Struct. **1051**, 310 (2013).

[345] T. Brandes, Phys. Rev. E **88**, 032133 (2013).

[346] P. Stránský, M. Macek, and P. Cejnar, Annals of Physics **345**, 73 (2014).

[347] L. F. Santos, M. Távora, and F. Pérez-Bernal, Phys. Rev. A **94**, 012113 (2016).

[348] T. Opatrný, L. Richterek, and M. Opatrný, Sci. Rep. **8**, 1984 (2018).

[349] M. Macek, P. Stránský, A. Leviatan, and P. Cejnar, Phys. Rev. C **99**, 064323 (2019).

[350] B. Dietz, F. Iachello, M. Miski-Oglu, N. Pietralla, A. Richter, L. von Smekal, and J. Wambach, Phys. Rev. B **88**, 104101 (2013).

[351] C. B. Dağ, S.-T. Wang, and L.-M. Duan, Phys. Rev. A **97**, 023603 (2018).

[352] A. L. Corps and A. Relaño, Phys. Rev. Lett. **127**, 130602 (2021).

[353] B. Sciolla and G. Biroli, Phys. Rev. Lett. **105**, 220401 (2010).

[354] J. Zhang, G. Pagano, P. W. Hess, A. Kyprianidis, P. Becker, H. Kaplan, A. V. Gorshkov, Z.-X. Gong, and C. Monroe, Nature **551**, 601 (2017).

[355] B. Žunkovič, M. Heyl, M. Knap, and A. Silva, Phys. Rev. Lett. **120**, 130601 (2018).

[356] C. B. Dağ, S.-T. Wang, and L.-M. Duan, Phys. Rev. A **97**, 023603 (2018).

[357] H. Miyake, G. A. Siviloglou, G. Puentes, D. E. Pritchard, W. Ketterle, and D. M. Weld, Phys. Rev. Lett. **107**, 175302 (2011).

[358] K. Mølmer, Y. Castin, and J. Dalibard, JOSA B **10**, 524 (1993).

[359] C. Zhu, L. Dong, and H. Pu, J. Phys. B: At. Mol. Opt. Phys. **49**, 145301 (2016).

[360] M. J. Edmonds, M. Valiente, G. Juzeliūnas, L. Santos, and P. Öhberg, Phys. Rev. Lett. **110**, 085301 (2013).

[361] Y. Li, G. I. Martone, and S. Stringari, in *Annual review of cold atoms and molecules* (World Scientific, 2015) pp. 201–250.

[362] J. Léonard, A. Morales, P. Zupancic, T. Esslinger, and T. Donner, Nature **543**, 87 (2017).

[363] E. Lustig, S. Weimann, Y. Plotnik, Y. Lumer, M. A. Bandres, A. Szameit, and M. Segev, Nature **567**, 356 (2019).

[364] S. Mugel, A. Dauphin, P. Massignan, L. Tarruell, M. Lewenstein, C. Lobo, and A. Celi, SciPost Phys. **3**, 012 (2017).

[365] E. Cornfeld and E. Sela, Phys. Rev. B **92**, 115446 (2015).

[366] M. Calvanese Strinati, S. Sahoo, K. Shtengel, and E. Sela, Phys. Rev. B **99**, 245101 (2019).

[367] E. Orignac and T. Giamarchi, Phys. Rev. B **64**, 144515 (2001).

[368] E. Granato, Phys. Rev. B **72**, 104521 (2005).

[369] A. Tokuno and A. Georges, New J. Phys. **16**, 073005 (2014).

[370] A. Petrescu and K. Le Hur, Phys. Rev. Lett. **111**, 150601 (2013).

[371] M. Di Dio, S. De Palo, E. Orignac, R. Citro, and M.-L. Chiofalo, Phys. Rev. B **92**, 060506 (2015).

[372] M. Piraud, F. Heidrich-Meisner, I. P. McCulloch, S. Greschner, T. Vekua, and U. Schollwöck, Phys. Rev. B **91**, 140406 (2015).

[373] A. Petrescu and K. Le Hur, Phys. Rev. B **91**, 054520 (2015).

[374] S. Greschner, M. Piraud, F. Heidrich-Meisner, I. P. McCulloch, U. Schollwöck, and T. Vekua, Phys. Rev. A **94**, 063628 (2016).

[375] M. Calvanese Strinati, E. Cornfeld, D. Rossini, S. Barbarino, M. Dalmonte, R. Fazio, E. Sela, and L. Mazza, Phys. Rev. X **7**, 021033 (2017).

[376] A. Petrescu, M. Piraud, G. Roux, I. P. McCulloch, and K. Le Hur, Phys. Rev. B **96**, 014524 (2017).

[377] R. Citro, S. De Palo, M. Di Dio, and E. Orignac, Phys. Rev. B **97**, 174523 (2018).

[378] S. Greschner and F. Heidrich-Meisner, Phys. Rev. A **97**, 033619 (2018).

[379] S. Greschner and T. Vekua, Phys. Rev. Lett. **119**, 073401 (2017).

[380] S. Barbarino, L. Taddia, D. Rossini, L. Mazza, and R. Fazio, Nature Commun. **6**, 1 (2015).

[381] S. Barbarino, L. Taddia, D. Rossini, L. Mazza, and R. Fazio, New J. Phys. **18**, 035010 (2016).

[382] J. Jünemann, A. Piga, S.-J. Ran, M. Lewenstein, M. Rizzi, and A. Bermudez, Phys. Rev. X **7**, 031057 (2017).

[383] S. K. Ghosh, S. Greschner, U. K. Yadav, T. Mishra, M. Rizzi, and V. B. Shenoy, Phys. Rev. A **95**, 063612 (2017).

[384] A. Haller, M. Rizzi, and M. Burrello, New J. Phys. **20**, 053007 (2018).

[385] E. Anisimovas, M. Račiūnas, C. Sträter, A. Eckardt, I. B. Spielman, and G. Juzeliūnas, Phys. Rev. A **94**, 063632 (2016).

[386] D. Suszalski and J. Zakrzewski, Phys. Rev. A **94**, 033602 (2016).

[387] F. A. An, E. J. Meier, and B. Gadway, Phys. Rev. X **8**, 031045 (2018).

[388] L. Balents, Nature **464**, 199 (2010).

[389] P. Anderson, Materials Research Bulletin **8**, 153 (1973).

[390] C. Lacroix, P. Mendels, and F. Mila, *Introduction to Frustrated Magnetism: Materials, Experiments, Theory*, Springer Series in Solid-State Sciences 164 (Springer-Verlag Berlin Heidelberg, 2011).

[391] H. T. Diep, *Frustrated Spin Systems* (World Scientific, 2004).

[392] S. Jiang and O. Motrunich, Phys. Rev. B **99**, 075103 (2019).

[393] T. Senthil, A. Vishwanath, L. Balents, S. Sachdev, and M. P. Fisher, Science **303**, 1490 (2004).

[394] A. Rahmani, A. E. Feiguin, and C. D. Batista, Phys. Rev. Lett. **113**, 267201 (2014).

[395] C. Majumdar and D. Ghosh, J MATH PHYS **10**, 1388 (1969).

[396] F. D. M. Haldane, Phys. Rev. B **25**, 4925 (1982).

[397] K. Okamoto and K. Nomura, Physics Letters A **169**, 433 (1992).

[398] S. R. White and I. Affleck, Phys. Rev. B **54**, 9862 (1996).

[399] A. A. Nersesyan, A. O. Gogolin, and F. H. L. Eßler, Phys. Rev. Lett. **81**, 910 (1998).

[400] C. Becker, P. Soltan-Panahi, J. Kronjäger, S. Dörscher, K. Bongs, and K. Sengstock, New J. Phys. **12**, 065025 (2010).

[401] R. G. Melko, A. Paramekanti, A. A. Burkov, A. Vishwanath, D. N. Sheng, and L. Balents, Phys. Rev. Lett. **95**, 127207 (2005).

[402] S. Wessel and M. Troyer, Phys. Rev. Lett. **95**, 127205 (2005).

[403] J. Struck, M. Weinberg, C. Ölschläger, P. Windpassinger, J. Simonet, K. Sengstock, R. Höppner, P. Hauke, A. Eckardt, M. Lewenstein, and L. Mathey, Nature Phys. **9**, 738 (2013).

[404] A. Eckardt, P. Hauke, P. Soltan-Panahi, C. Becker, K. Sengstock, and M. Lewenstein, EPL **89**, 10010 (2010).

[405] P. Hauke, T. Roscilde, V. Murg, J. Ignacio Cirac, and R. Schmied, New J. Phys. **12**, 053036 (2010).

[406] A. Celi, T. Grass, A. J. Ferris, B. Padhi, D. Raventós, J. Simonet, K. Sengstock, and M. Lewenstein, Phys. Rev. B **94**, 075110 (2016).

[407] T. Mishra, R. V. Pai, S. Mukerjee, and A. Paramekanti, Phys. Rev. B **87**, 174504 (2013).

[408] T. Mishra, R. V. Pai, and S. Mukerjee, Phys. Rev. A **89**, 013615 (2014).

[409] S. Greschner and T. Mishra, Phys. Rev. B **100**, 144405 (2019).

[410] S.-L. Drechsler, O. Volkova, A. N. Vasiliev, N. Tristan, J. Richter, M. Schmitt, H. Rosner, J. Málek, R. Klingeler, A. A. Zvyagin, and B. Büchner, Phys. Rev. Lett. **98**, 077202 (2007).

[411] C. de Graaf, I. de P. R. Moreira, F. Illas, O. Iglesias, and A. Labarta, Phys. Rev. B **66**, 014448 (2002).

[412] A. U. B. Wolter, F. Lipps, M. Schäpers, S.-L. Drechsler, S. Nishimoto, R. Vogel, V. Kataev, B. Büchner, H. Rosner, M. Schmitt, M. Uhlarz, Y. Skourski, J. Wosnitza, S. Süllow, and K. C. Rule, Phys. Rev. B **85**, 014407 (2012).

[413] H.-J. Grafe, S. Nishimoto, M. Iakovleva, E. Vavilova, L. Spillecke, A. Alfonsov, M.-I. Sturza, S. Wurmehl, H. Nojiri, H. Rosner, J. Richter, U. K. Rößler, S.-L. Drechsler, V. Kataev, and B. Büchner, Scientific Reports **7**, 6720 (2017).

[414] A. Orlova, E. L. Green, J. M. Law, D. I. Gorbunov, G. Chanda, S. Krämer, M. Horvatić, R. K. Kremer, J. Wosnitza, and G. L. J. A. Rikken, Phys. Rev. Lett. **118**, 247201 (2017).

[415] H. Ueda, S. Onoda, Y. Yamaguchi, T. Kimura, D. Yoshizawa, T. Morioka, M. Hagiwara, M. Hagihala, M. Soda, T. Masuda, T. Sakakibara, K. Tomiyasu, S. Ohira-Kawamura, K. Nakajima, R. Kajimoto, M. Nakamura, Y. Inamura, N. Reynolds, M. Frontzek, J. S. White, M. Hase, and Y. Yasui, Phys. Rev. B **101**, 140408 (2020).

[416] C. P. Grams, D. Brüning, S. Kopatz, T. Lorenz, P. Becker, L. Bohatý, and J. Hemberger, "Observation of chiral solitons in the quantum spin liquid phase of licuvo$_4$," (2019), arXiv:1912.04705 [cond-mat.mtrl-sci] .

[417] A. R. Kolovsky, EPL (Europhysics Letters) **93**, 20003 (2011).

[418] S. Kolkowitz, S. Bromley, T. Bothwell, M. Wall, G. Marti, A. Koller, X. Zhang, A. Rey, and J. Ye, Nature **542**, 66 (2017).

[419] J. H. Han, J. H. Kang, and Y. Shin, Phys. Rev. Lett. **122**, 065303 (2019).

[420] D. Hügel and B. Paredes, Phys. Rev. A **89**, 023619 (2014).

[421] M. Di Dio, S. De Palo, E. Orignac, R. Citro, and M.-L. Chiofalo, Phys. Rev. B **92**, 060506 (2015).

[422] A. Dhar, M. Maji, T. Mishra, R. V. Pai, S. Mukerjee, and A. Paramekanti, Phys. Rev. A **85**, 041602 (2012).

[423] A. Dhar, T. Mishra, M. Maji, R. V. Pai, S. Mukerjee, and A. Paramekanti, Phys. Rev. B **87**, 174501 (2013).

[424] S. Greschner, M. Piraud, F. Heidrich-Meisner, I. P. McCulloch, U. Schollwöck, and T. Vekua, Phys. Rev. Lett. **115**, 190402 (2015).

[425] E. Orignac, R. Citro, M. Di Dio, and S. De Palo, Phys. Rev. B **96**, 014518 (2017).

[426] F. Grusdt and M. Höning, Phys. Rev. A **90**, 053623 (2014).

[427] P. Prelovšek, M. Long, T. Markež, and X. Zotos, Phys. Rev. Lett. **83**, 2785 (1999).

[428] X. Zotos, F. Naef, M. Long, and P. Prelovšek, Phys. Rev. Lett. **85**, 377 (2000).

[429] M. Filippone, C.-E. Bardyn, S. Greschner, and T. Giamarchi, Phys. Rev. Lett. **123**, 086803 (2019).

[430] L. Barbiero, C. Schweizer, M. Aidelsburger, E. Demler, N. Goldman, and F. Grusdt, Science advances **5**, eaav7444 (2019).

[431] M. Sato, S. Furukawa, S. Onoda, and A. Furusaki, Modern Physics Letters B **25**, 901 (2011).

[432] L. Barbiero, L. Chomaz, S. Nascimbene, and N. Goldman, Phys. Rev. Research **2**, 043340 (2020).

[433] S. Greschner, L. Santos, and T. Vekua, Phys. Rev. A **87**, 033609 (2013).

[434] M. P. Zaletel, S. A. Parameswaran, A. Rüegg, and E. Altman, Phys. Rev. B **89**, 155142 (2014).

[435] S. Yang, D.-X. Yao, and A. W. Sandvik, (2020), arXiv:2001.02821 [physics.comp-ph] .

[436] S. R. White, Phys. Rev. Lett. **69**, 2863 (1992).

[437] C. K. Majumdar, J. Phys. C: Solid State Physics **3**, 911 (1970).

[438] R. Wei and E. J. Mueller, Phys. Rev. A **89**, 063617 (2014).

[439] A. Froelian, *Simulating a topological gauge theory in a Raman-dressed Bose-Einstein condensate* (Ph.D. thesis, Institute of Photonic Sciences, Universitat Politècnica de Catalunya, 2022).

[440] M. Buser, C. Hubig, U. Schollwöck, L. Tarruell, and F. Heidrich-Meisner, Phys. Rev. A **102**, 053314 (2020).

[441] D. Trypogeorgos, A. Valdés-Curiel, N. Lundblad, and I. B. Spielman, Phys. Rev. A **97**, 013407 (2018).

[442] D. C. McKay, D. Jervis, D. J. Fine, J. W. Simpson-Porco, G. J. A. Edge, and J. H. Thywissen, Phys. Rev. A **84**, 063420 (2011).

[443] C. S. Chisholm, A. Frölian, E. Neri, R. Ramos, L. Tarruell, and A. Celi, to appear (2022).